

Drift Reduction for Inertial Sensor Based Orientation and Position Estimation in the Presence of High Dynamic Variability During Competitive Skiing and Daily-Life Walking

THÈSE N° 7803 (2017)

PRÉSENTÉE LE 7 JUILLET 2017

À LA FACULTÉ DES SCIENCES ET TECHNIQUES DE L'INGÉNIEUR
LABORATOIRE DE MESURE ET D'ANALYSE DES MOUVEMENTS
PROGRAMME DOCTORAL EN GÉNIE ÉLECTRIQUE

ÉCOLE POLYTECHNIQUE FÉDÉRALE DE LAUSANNE

POUR L'OBTENTION DU GRADE DE DOCTEUR ÈS SCIENCES

PAR

Benedikt FASEL

acceptée sur proposition du jury:

Prof. D. Atienza Alonso, président du jury
Prof. K. Aminian, directeur de thèse
Prof. A. Cereatti, rapporteur
Prof. V. Senner, rapporteur
Prof. R. Gassert, rapporteur



ÉCOLE POLYTECHNIQUE
FÉDÉRALE DE LAUSANNE

Suisse
2017

*'Siehst Du, Momo', sagte er dann zum Beispiel,
'es ist so: Manchmal hat man eine sehr lange Strasse vor
sich. Man denkt, die ist so schrecklich lang; das kann man
niemals schaffen, denkt man.'*

*Er blickte eine Weile schweigend vor sich hin,
dann fuhr er fort:
'Und dann fängt man an, sich zu eilen. Und man eilt sich
immer mehr. Jedes Mal, wenn man aufblickt, sieht man,
dass es gar nicht weniger wird, was noch vor einem liegt.
Und man strengt sich noch mehr an, man kriegt es mit der
Angst zu tun und zum Schluss ist man ganz ausser Puste
und kann nicht mehr. Und die Strasse liegt immer noch
vor einem. So darf man es nicht machen!'*

*Er dachte einige Zeit nach. Dann sprach er weiter:
'Man darf nie an die ganze Strasse auf einmal denken,
verstehst du? Man muss immer nur an den nächsten
Schritt denken, an den nächsten Atemzug, an den nächsten
Besenstrich. Und immer wieder nur den nächsten.'*

*Wieder hielt er inne und überlegte, ehe er hinzufügte:
'Dann macht es Freude; das ist wichtig, dann macht man
seine Sache gut. Und so soll es sein.'*

*Und abermals nach einer langen Pause fuhr er fort:
'Auf einmal merkt man, dass man Schritt für Schritt die
ganze Strasse gemacht hat. Man hat gar nicht gemerkt
wie, und man ist nicht ausser Puste.'*

*Er nickte vor sich hin und sagte abschliessend:
'Das ist wichtig.'*

Abstract

Nowadays inertial sensors are extensively used for gait analysis. They can be used to perform temporal event detection (i.e. step detection) and to estimate the orientation of the feet and other body segments to determine walking speed and distance. Usually, orientation is estimated from integration of the measured angular velocity. Prior to integration of measured acceleration to obtain speed, the gravity component has to be estimated and removed. During each integration small measurement errors accumulate and result in so-called drift. Since the first uses of inertial sensors for gait analysis methods have been presented to model, estimate and remove the drift. The proposed methods worked well for relatively slow movements and movements taking place in the sagittal plane. Many methods also relied on periodically occurring static phases such as the stance phase during walking to correct the drift.

Inertial sensors could also be used to track higher dynamic movements, for example in sports. Potential applications focus on two aspects: performance analysis and injury prevention. To better explain and predict performance, in-field measurements to assess the coordination, kinematics, and dynamics are key. While traditional movement analysis (e.g. video analysis) can answer most of the questions related to both performance and injury, they are cumbersome and complex to use in-field. Inertial sensors, however, are perfectly suited since they allow to measure the movement in any environment and are not restricted to certain capture volumes. Nevertheless, most sports have very high movement dynamics (e.g. fast direction changes, high speeds) and are therefore challenging for computing reliable estimates of orientation, speed and position. The inertial measurements are compromised by noise and movements oftentimes don't provide static or slow phases used in gait analysis for drift correction.

Therefore, the present thesis aimed to propose and validate new methods to model, estimate and remove drift in sports and for movements taking place outdoors in uncontrolled environments. Three different strategies were proposed to measure the movement of classical cross-country skiing and ski mountaineering, alpine ski racing, and outdoor walking over several kilometres. For each activity specific biomechanical constraints and movement dynamics were exploited. The proposed methods rely only on inertial sensors and magnetometers and are able to provide orientation, speed, and position information with an accuracy and precision close to existing gold standards. The most complete system was designed in alpine ski racing, probably one of the most challenging sports for movement analysis. Extreme vibrations, high speeds of over 120 km/h and a timing

resolution below 0.01 seconds require maximum accuracy and precision. The athlete's posture and the kinematics of his centre of mass both in a relative athlete-centred frame and in a global Earth-fixed frame could be obtained with high accuracy and precision. Where 3D video analysis requires a very complex experimental setup and takes several hours of post processing to analyse a single turn of a skier, the proposed system allows to measure multiple athletes and complete runs within minutes. Thus, new experimental designs to assess performance and injury risk in alpine ski racing became feasible, greatly helping to gain further knowledge about this highly complex and risky sport.

Key words: drift correction; inertial sensors; inertial measurement unit; accelerometer; gyroscope; magnetometer; sensor fusion; kinematics; speed; position; measurement; performance; sports; alpine ski racing; cross-country skiing; walking

Zusammenfassung

Heutzutage werden Inertialsensoren vor allem für die Ganganalyse eingesetzt. Zeitliche Ereignisse können erkannt werden (z.B. Detektieren von Schritten) und über die Orientierung der Füße oder anderer Segmente kann die Gehgeschwindigkeit und Schrittdistanz berechnet werden. In den meisten Anwendungen werden Orientierung und Geschwindigkeit durch Integration der gemessenen Signale bestimmt. Während der Integration häufen sich aber kleine Messungenauigkeiten an und bilden die sogenannte Drift. Schon seit dem erstmaligen Gebrauch der Inertialsensoren für die Ganganalyse wurden verschiedene Methoden zum Modellieren, Abschätzen und Korrigieren der Drift vorgestellt. Diese Methoden können die Drift für langsame und zweidimensionale Bewegungen relativ gut korrigieren. Dazu verwenden viele der Methoden periodisch auftretende statische Phasen, wie zum Beispiel die Standphase während des Gehens.

Inertialsensoren könnten auch gebraucht werden, um dynamischere Bewegungen, wie sie im Sport oftmals auftreten, zu messen. Potentielle Anwendungen betreffen zwei Bereiche: Leistungsanalyse und Unfallverhütung. Um die Leistung eines Athleten besser erklären zu können, sind Messungen der Koordination, Kinematik und Dynamik zentral. Solche Analysen können von traditionellen Messsystemen (z.B. mit Videoanalysis) durchgeführt werden, sind für Messungen im Freien aber mit grossem Aufwand verbunden. Im Gegensatz dazu scheinen Inertialsensoren ideal geeignet: Sie können Bewegungen in jeder Umgebung messen und ihr Messvolumen ist nicht beschränkt. Das Auftreten von sehr schnellen Bewegungen im Sport (z.B. schnelle Richtungswechsel und hohe Geschwindigkeiten) stellt aber hohe Anforderungen an ein exaktes Bestimmen von Orientierung, Geschwindigkeit und Position. Die Bewegungen beinhalten oftmals keine statische oder langsame Phasen, die wie in der Ganganalyse zur Driftkorrektur verwendet werden könnten.

Diese Doktorarbeit hatte deshalb als Ziel, neue Methoden zum Modellieren, Abschätzen und Korrigieren von Sensordrift für Messungen im Sport und im Freien in unkontrollierter Umgebung zu entwickeln und zu validieren. Dazu wurden drei verschiedene Strategien vorgeschlagen, um Langlauf, Skitouren, Ski Alpin, und Gehen im Freien über mehrere Kilometer zu messen. Für jede Aktivität wurden biomechanische Bedingungen und die vorherrschende Bewegungsdynamik ideal ausgenutzt. Die vorgeschlagenen Methoden basieren nur auf Inertialsensoren und Magnetometer. Orientierung, Geschwindigkeit und Position können mit einer Genauigkeit nahe derer der Referenzsysteme berechnet werden. Die fortgeschrittenste Methode wurde für Ski Alpin entwickelt, einer der kompliziertesten

Sportarten zum Analysieren. Extreme Vibrationen, Geschwindigkeiten von über 120 km/h und eine Zeitauflösung von unter 0.01 Sekunden stellen maximale Ansprüche an ein Messsystem. Die Postur des Athleten und die Kinematik seines Körperschwerpunktes konnten in einem körperbezogenen relativen und erdbezogenen absoluten Koordinatensystem berechnet werden. Währenddem eine 3D Videoanalyse eines einzelnen Schwungs einen sehr komplexen Versuchsaufbau und etliche Stunden Nachprozessieren erfordert, kann das vorgeschlagene System mehrere Athleten und Fahrten innerhalb von nur wenigen Minuten messen und analysieren. Dieses Messsystem erlaubt nun neue Analysestrategien in denen Leistung und Unfallrisiko besser und mit grösseren Stichproben gemessen werden können.

Stichwörter: Driftkorrektur; Intertialsensoren; IMU; Beschleunigungssensor; Gyroskop; Magnetometer; Sensorfusion; Kinematik; Geschwindigkeit; Position; Messung; Leistung; Sport; Ski Alpin; Langlauf; Gehen

Acknowledgements

I would like to thank Professor Kamiar Aminian for his support and guidance throughout my thesis. Despite my initial intentions, he was able to convince me to do a PhD degree in his lab. He gave me a lot of liberty and I was even allowed to change my PhD research topic to alpine ski racing after two years of working on wrist-based activity monitoring. He also gave me the opportunity to work on a range of very interesting and always challenging side-projects (Paralympic cross-country sit-skiing, skating cross-country skiing, ski mountaineering, cohort activity analysis) with other research groups (University of Salzburg (AUT), University of Freiburg (GER), University of Jyväskylä (FIN), University of Lausanne, Centre Hospitalier Universitaire Vaudois (CHUV), etc.).

I would like to address a big thank to the Department of Sport Science and Kinesiology of the University of Salzburg under the direction of Prof. Erich Müller. Without their implication and support I would never have been able to perform so many in-field measurement campaigns with professional skiing athletes. I especially thank Jörg Spörri and Josef Kröll who spent a lot of their time to help me design efficient measurement protocols and explain me which parameters are relevant to quantify in alpine ski racing. They also spent countless hours critically revising my many articles and providing precious feedback that finally allowed me to publish my articles in outstanding scientific journals. Thanks also go to the Laboratory for Movement Biomechanics under the direction of PD Dr. Silvio Lorenzetti who agreed to contribute with the Vicon reference system for the indoor skiing validation measurements.

The wrist-based activity monitoring project was generously supported by the research division of a certain Swiss watch company and the help of the ESPLAB with special thanks to Prof. Pierre-André Farine, Dr. Sara Grassi, Flavien Bardyn, and Martin Savary.

All my countless measurement campaigns involved a great many volunteers. Thank you for your participation and the skiers for allowing me to join your trainings in various places in Switzerland, Austria, and Finland. A special thanks also to Swiss-Ski, especially Peter Lämpfli and Björn Bruhin, and their willingness to support my research and advertising it at the various coaches in both the skiing and snowboarding disciplines.

I thank the jury members of my thesis: Prof. Atienza, Prof. Cereatti, Prof. Senner, and Prof. Gassert. They showed a genuine interest in my thesis and were able to provide a very helpful external and independent view and opinion of my work.

Acknowledgements

There was rarely a day I was not motivated to go to work and this is for sure also thanks to the fantastic present and past colleagues, members, and friends of the laboratory of movement analysis and measurement.

Many thanks to my friends from school, university, sports and firefighting and to my family and my very patient and understanding Maude. A special thank also to my grandparents and mum who for the only certainty in life could not see this thesis started and finished but definitely contributed to it through their education and way of living.

The thesis could not have been performed without financial contribution from various funding bodies, the two most important being the Swiss Commission for Technology and Innovation (CTI, grant number 14787.1 PFNM-NM) and the Swiss Federal Office of Sport (OFSP, grant number 15-01; VM10052).

Lausanne, June 1 2017

B. F.

Contents

Abstract	i
Zusammenfassung	iii
Acknowledgements	v
List of figures	xiii
List of tables	xvii

I Introduction and Background	1
--------------------------------------	----------

1 Introduction	3
-----------------------	----------

1.1 Measuring Human Motion	3
1.2 Thesis structure	5
1.2.1 Part I – Drift reduction based on static constraints	6
1.2.2 Part II – Drift correction based on dynamic constraints and periodic reference updates	7
1.2.3 Part III – Movement speed estimation based on signal feature mapping	9
1.2.4 General discussion and conclusion	10
1.3 Graphical summary	11

2 State of the Art	13
---------------------------	-----------

2.1 Inertial sensors	13
2.1.1 Accelerometer measurement principle	13
2.1.2 Gyroscope measurement principle	14
2.1.3 Measurement errors	16
2.1.4 Example signals	18
2.2 Drift	21
2.2.1 Origins of orientation drift	22
2.2.2 Origins of velocity drift	25
2.2.3 Summary	28

Contents

2.3	Proposed drift correction methods for human movement analysis	29
2.3.1	First studies and drift-free computation of lower limb angles	29
2.3.2	The common approach for orientation drift correction	33
2.3.3	Kinematic chains for orientation drift correction	36
2.3.4	Drift-free orientation for periodic signals	38
2.3.5	Velocity and position drift correction	39
2.4	Conclusion	40
II	Static Drift Correction	43
3	Spatio-Temporal Analysis of Classical Cross-Country Skiing	45
3.1	Introduction	46
3.2	Methods	47
3.2.1	Definition of the diagonal stride events and phases	47
3.2.2	Measurement protocol	48
3.2.3	Reference System	49
3.2.4	Pole event detections by IMU	50
3.2.5	Estimation of spatio-temporal parameters for the ski IMU	52
3.2.6	Data analysis	52
3.3	Results	53
3.4	Discussion	55
4	Spatio-Temporal Analysis of Ski-Mountaineering	59
4.1	Introduction	60
4.2	Methods	60
4.2.1	Protocol	60
4.2.2	Materials	60
4.2.3	Definition of the parameters	61
4.2.4	Parameter computation with the inertial unit	62
4.2.5	Reference parameter computation	63
4.2.6	Statistical analysis	63
4.3	Results	63
4.4	Discussion	64
III	Dynamic Drift Correction	67
5	Joint Drift Reduction for Alpine Ski Racing	69
5.1	Introduction	70
5.2	Methods	72
5.2.1	Protocol	72
5.2.2	Wearable system	72

5.2.3	Reference system	77
5.2.4	Error analysis	77
5.3	Results	78
5.4	Discussion	79
6	Joint Drift Correction Improvements and Indoor Validation	85
6.1	Introduction	86
6.2	Methods	88
6.2.1	Measurement Protocol	88
6.2.2	Reference System	88
6.2.3	Wearable system	89
6.2.4	Validation	95
6.3	Results	96
6.3.1	Functional Calibration	96
6.3.2	3D Joint Angles	97
6.4	Discussion	98
6.4.1	Functional Calibration	98
6.4.2	3D Joint Angles	100
6.4.3	Methodological considerations	101
6.5	Conclusion	101
6.6	Appendix	102
7	Validation of Athlete Body Model and Center of Mass Position	105
7.1	Introduction	106
7.2	Methods	107
7.2.1	Measurement protocol	107
7.2.2	Reference system	108
7.2.3	Wearable system	110
7.2.4	Validation	112
7.3	Results	113
7.4	Discussion	116
7.4.1	Possible joint position error sources	117
7.4.2	CoM position	117
7.4.3	Vertical distance and fore-aft position	118
7.4.4	Methodological limitations	119
7.5	Conclusion	120
8	Combination of Inertial Sensors with Differential GNSS	121
8.1	Introduction	122
8.2	Materials and methods	123
8.2.1	Protocol	123
8.2.2	Wearable system	123
8.2.3	Centre of mass kinematics	124

Contents

8.2.4	Reference system	128
8.2.5	Error analysis	128
8.3	Results	129
8.4	Discussion	133
8.5	Conclusions	136
9	Position drift correction for absolute CoM kinematics	137
9.1	Introduction	138
9.2	Methods	139
9.2.1	Inertial system	139
9.2.2	Reference system	145
9.2.3	Validation	145
9.3	Results	148
9.3.1	CoM kinematics	148
9.3.2	Performance parameter-related findings	149
9.4	Discussion	150
9.4.1	Accuracy and precision of CoM kinematics in GS	151
9.4.2	Expected accuracy and precision in SG and DH	152
9.4.3	Potential benefit of adding a low-cost GNSS	152
9.4.4	Limits of Agreement for CoM-derived performance parameters	153
9.5	Conclusion	153
10	GNSS-free anchor point estimation	155
10.1	Introduction	156
10.2	Methods	156
10.3	Results	158
10.4	Discussion	158
10.5	Conclusion	159
11	Applications to performance analysis and injury prevention	161
11.1	Performance Analysis	162
11.1.1	Performance criterion section time	164
11.1.2	Performance criterion exit speed	166
11.1.3	Comparison of two runs	170
11.2	Injury prevention	171
11.2.1	Joint flexion angles	173
11.2.2	Trunk acceleration	174
11.2.3	Segment vibrations	175
11.3	Conclusion	176

IV	Direct Speed Estimation	179
12	Direct Estimation of Walking Cadence and Speed	181
12.1	Introduction	182
12.2	Methods	183
12.2.1	Measurement Protocol	183
12.2.2	Materials and Setup	184
12.2.3	Wrist algorithm	186
12.2.4	Validation and statistical analysis	189
12.3	Results	190
12.3.1	Overview	190
12.3.2	Error dependencies	191
12.4	Discussion	193
V	Conclusion	199
13	General Discussion and Conclusion	201
13.1	Main contributions	201
13.1.1	Part 1 – Static drift correction	202
13.1.2	Part 2 – Dynamic drift correction	203
13.1.3	Part 3 – Direct speed estimation	204
13.1.4	Current uses of the proposed systems and relevance for industry applications	204
13.2	Limitations	205
13.2.1	Cross-country skiing and ski mountaineering	205
13.2.2	Alpine ski racing	206
13.2.3	Wrist locomotion detection and analysis	208
13.3	Performance analysis and feedback	208
13.4	Future developments	209
13.4.1	Drift correction	209
13.4.2	Soft tissue artefact reduction	210
13.4.3	Functional calibration	211
13.4.4	Integration of other sensor data	211
13.4.5	Extensions to other sports	212
13.4.6	Data visualization and interpretation	212
13.5	The End	213
	Bibliography	215
	Curriculum Vitae	241

List of Figures

1.1	Ski angle drift in cross-country skiing	6
1.2	Ski velocity drift in cross-country skiing	6
1.3	Principle of joint drift correction	8
1.4	Position drift in alpine ski racing	8
1.5	Acceleration feature mapping to estimate walking speed	10
2.1	Spring-mass model of an accelerometer	14
2.2	Tuning fork gyroscope model	15
2.3	Influence of temperature on sensor bias	17
2.4	Gyroscope saturation during running	18
2.5	Pendulum experiment setup and axis definition	19
2.6	Pendulum experiment results	19
2.7	Acceleration and angular velocity of the foot for walking	20
2.8	Acceleration and angular velocity of the shank for walking	20
2.9	Acceleration and angular velocity of the sacrum for skiing	21
2.10	Flowchart for integration of inertial signals	22
2.11	Falling block experiment setup and axis definition	23
2.12	Results from the falling block experiment	24
2.13	Zoom to second shock of the falling block experiment	24
2.14	Results from the guided block experiment	25
2.15	Gravity removal example setup and axis definition	26
2.16	Velocity drift for the falling block experiments	27
2.17	Zoomed view for the velocity drift change at impact	28
2.18	True peak height loss due to sampling	28
2.19	Accelerometer mounting platform from Morris (1973)	30
2.20	Accelerometer and goniometer setup from Willemsen et al. (1990)	31
2.21	Illustration of virtual sensor from Dejnabadi et al. (2006)	32
2.22	Proposed Kalman filter from Luinge and Veltink (2005)	35
2.23	Block diagram for the algorithm of Madgwick et al. (2011)	35
2.24	Arm orientation error from Luinge et al. (2007)	37
2.25	Block diagram from Bonnet et al. (2013)	38
2.26	Drift correction from Mariani et al. (2010)	39

List of Figures

3.1	Temporal phases in diagonal stride	47
3.2	Setup and inertial sensor axes	49
3.3	Temporal event detection	50
3.4	Instantaneous ski speed	54
3.5	Parameter values	55
4.1	Setup	61
4.2	Acceleration and speed plots	63
4.3	Acceleration comparison indoor - outdoor	66
5.1	Materials and setup	73
5.2	Estimated drift magnitude	78
5.3	Errors for the outside leg and trunk	80
5.4	Errors inside leg and trunk	81
5.5	Knee flexion for the Adelboden World Cup giant slalom	82
6.1	Illustration carpet skiing	89
6.2	Sensor and marker placement	90
6.3	Drift magnitude	94
6.4	3D knee angles with and without azimuth drift correction	97
6.5	Typical joint angles	99
7.1	Illustration of the treadmill setup	108
7.2	Sensor and marker setup	109
7.3	Complete and simplified body model	112
7.4	Average hip and knee errors curves	114
7.5	Average hip and knee errors curves	115
7.6	Bland-Altman plots for RoM parameters	116
7.7	Bland-Altman plots for RoM parameters	119
8.1	Materials and setup	123
8.2	Body model and kinematic chain for computing CoM	125
8.3	Estimated and reference position and speed	130
8.4	Speed normalized to a cycle	131
8.5	Joint position errors	132
8.6	CoM position and speed errors	133
9.1	Sensor setup and magnet positioning at gates	140
9.2	Algorithm flow chart	141
9.3	Athlete posture at gate crossing	143
9.4	Definition of the local skiing frame S	146
9.5	Turn speed and distance parameters	147
9.6	CoM speed comparison	149
9.7	Bland-Altman plots for the performance parameters	150

10.1 Local slope deformations	159
11.1 Performance parameters for one segment	163
11.2 Slope angle at every gate	164
11.3 Performance parameter comparison time	165
11.4 CoM trajectory comparison and speed difference	166
11.5 Performance parameter comparison speed	168
11.6 CoM trajectory comparison and speed difference	169
11.7 Pre/post ration in function of slope angle	170
11.8 Gate to gate timing analysis	171
11.9 CoM trajectory comparison and speed difference	172
11.10Knee, hip, trunk flexion for slalom and giant slalom	174
11.11Trunk acceleration for slalom and giant slalom	175
11.12Acceleration frequency spectrum for slalom	176
11.13Acceleration frequency spectrum for giant slalom	177
12.1 Altitude profile Dataset 1	184
12.2 Sensor placement	186
12.3 Cadence estimation flowchart	188
12.4 Typical cadence and speed time series	191
12.5 Error plot for the instantaneous cadence	192
12.6 Error plot for the instantaneous speed estimate	193
12.7 Boxplot for the cadence and speed errors	193

List of Tables

3.1	Event definitions	51
3.2	Event errors	53
3.3	Spatial parameter and phase duration errors	53
3.4	Errors partitioned into conditions	54
4.1	Measured skiing conditions	61
4.2	Validation results	64
5.1	Accuracy, precision, and correlation	79
6.1	Overview of measurement protocol	89
6.2	Functional calibration movements	92
6.3	Dispersion of the calibration quaternions	96
6.4	Joint angle repeatability	97
6.5	3D joint angles range of motion and errors	98
6.6	Appendix - Dispersion of the calibration quaternions	102
6.7	Appendix - Joint angle repeatability	102
6.8	Appendix - 3D joint angles range of motion and errors	103
7.1	Joint position errors	114
7.2	CoM position errors	115
7.3	Vertical distance and fore-aft position errors	115
7.4	Range of motion errors	116
8.1	Median accuracy and precision	131
9.1	Position and velocity errors	148
9.2	Position errors with and without low-cost GNSS	148
9.3	Velocity errors with and without low-cost GNSS	149
9.4	Speed and position parameter LoA	150
11.1	Performance parameter definitions	163
12.1	Trial description Dataset 1	185
12.2	Trial description Dataset 2	186

List of Tables

12.3 Parameter range and cadence and speed errors	192
---	-----

Introduction and Background Part I

1 Introduction

1.1 Measuring Human Motion

In the books *De Motu Animalium I* and *II* Giovanni Alfonso Borelli (1608 – 1679) described the mechanics of animal and human motion for the first time following the mechanics of motion as proposed by Galileo (Pope, 2005). Since then the field of biomechanics has greatly advanced and diversified. In the field of movement analysis researchers mainly want to measure and understand human locomotion: how do we move, which muscles are involved and how do pathologies affect gait (Whittle, 1996; Wren et al., 2011). For sports, human movement analysis is mainly used to determine energy expenditure and cost of locomotion (Barbosa et al., 2008; Dalleau et al., 1998; Hausswirth et al., 1997; Millet et al., 2003; Minetti et al., 2002; Pellegrini et al., 2013; Veicsteinas et al., 1984), to understand and prevent injuries (Bahr and Krosshaug, 2005; Finch, 2006; Gosling et al., 2008; Haaland et al., 2016), or to analyse and understand performance (Bartlett and Bussey, 2013; Federolf, 2012; Hébert-Losier et al., 2014; Reid et al., 2008; Sandbakk et al., 2012; Supej et al., 2011).

The present thesis is mainly concerned with temporal and kinematics analyses in snow sports (e.g. cross-country skiing, alpine ski racing), with one chapter also covering the topic of outdoor walking. Compared to clinical movement analysis, such as for example gait analysis, snow sports movement analysis is confronted with other challenging issues. Athletes might cover long distances and move within uneven, slippery, and irregular terrain (e.g. steep slopes, forests). Movement dynamics may be extremely high with very fast speeds or rapid changes of directions. Movement variability might be very high, and artefacts and noise (e.g. from ski-snow interaction) can degrade signal quality. The harsh outdoor environment (e.g. low temperatures, snow) might also require special protections for electronic devices. Finally, any movement should be captured with a very high precision. Centre of mass trajectory differences of a few centimetres might differentiate the winner of a race from the second place.

In terms of size and robustness, inertial measurement units (IMUs) might be the ideal choice for temporal and kinematics analysis in snow sports. However, IMUs measure only

angular velocity and acceleration. While this might be sufficient for a temporal analysis (e.g. event detection) IMUs cannot directly measure orientation, velocity, and position. Instead, angular velocity needs to be integrated to find orientation; acceleration needs to be integrated to find velocity and velocity needs to be integrated to find position. During the integration, small errors accumulate and result in signal drift – already after a few seconds of integration. Computed orientations, velocities, and positions might not be valid anymore. Techniques have been proposed in the past to correct such sensor drifts, especially for clinical applications such as gait analysis or functional tests (Duc et al., 2014; Favre et al., 2008; Mariani et al., 2010). However, due to technical challenges, these techniques might not work in outdoor settings and for highly dynamic movements: dedicated algorithms need to be designed such that drift can be reduced to a minimum. In snow sports, the doctoral thesis of Julien Chardonnes (Chardonnes, 2012) provided precious insights in the possibilities and limitations of using IMUs for analysing the kinematics and kinetics of ski jumping. Other strategies proposed by the Laboratory of Movement Analysis and Measurement for clinical gait analysis (Dejnabadi et al., 2006; Favre et al., 2009, 2006; Mariani et al., 2010) might also provide interesting solutions for drift reduction but cannot be directly used for sports. Finally, Dadashi et al. (2012) proposed a mapping algorithm for a direct estimation of speed in the case of swimming where drift-correction based on static moments (i.e. instants of time) was not possible. This thesis builds on these findings and proposes dedicated algorithms for drift reduction in the two main snow sport disciplines: cross-country skiing and alpine ski racing. Movements of the two disciplines are very different. For example, leg movement in classical cross-country skiing alternates between sliding and static phases and is similar to over-ground walking. Alpine skiing involves only sliding phases and the athlete is never at a stop. Therefore, for computing movement kinematics, different drift reduction strategies are necessary for each sport.

Drift reduction strategies can be separated into three main groups. In all groups orientation and velocity are obtained through integration and are thus affected by drift. Drift is then reduced with the help of 1) static constraints, 2) dynamic constraints, or 3) periodic reference updates based on information from other sensors such as global navigation satellite systems (GNSS) or magnetometers. In this thesis, contributions were made in each of the three groups:

- Static constraints were used in cross-country skiing similar to Mariani et al. (2010) for 3D foot kinematics analysis in gait. Cycle events, ski speed and cycle distance were computed for the diagonal stride. The algorithm was further adapted to uphill ski-mountaineering in a second study.
- Dynamic constraints were used in alpine ski racing for determining segment and joint orientations. The concept of joint drift correction from Dejnabadi et al. (2006) was extended to 3D and adapted to highly dynamic movements and movements affected by high noise caused by the ski-snow interactions.
- Periodic reference updates were used in alpine ski racing for estimating CoM

kinematics (velocity and position). Reference gate positions were obtained with differential GNSS. Magnetometers were used to detect gate crossings and fuse them with the reference gate positions with an Extended Kalman Smoother. Two case studies are presented where reference gate positions were estimated either with the help of low-cost GNSS or with inertial data only.

Finally, there exist also algorithms where speed and position are estimated without direct signal integration (Dadashi et al., 2012; Marshall, 2015; Sabatini et al., 2015). These methods are well suited for periodic movements and can also work when no motionless instants are present. For example, with the help of machine learning signal features can be related to movement kinematics and used to estimate speed and position. In this thesis, signal feature mapping was used to compute drift-free speed and distance of outdoor walking based on acceleration measured at the wrist. Based on a similar concept presented in Dadashi et al. (2012) for swimming, wrist acceleration features and walking cadence were mapped to walking speed and step length. The algorithm was optimized for low-power systems and real-time feedback.

1.2 Thesis structure

Drift originates in the accumulation of small measurement errors when integrating angular velocity or acceleration to obtain sensor orientation or sensor velocity, respectively. The sources of measurement error are different for angular velocity and acceleration. While measurement errors in angular velocity have four main sources (static bias, sensitivity, movement-dependent bias, and signal losses during analogue-to-digital conversion), the situation is different for acceleration: prior to integration, accelerations have to be expressed in a fixed global frame and its gravity component has to be removed. Therefore, in addition to the same error sources as for the angular velocity (static bias, sensitivity, movement-dependent bias, and signal losses during analogue-to-digital conversion), errors from incorrect orientation estimation lead further to incorrect global frame orientation and incorrect gravity removal. This incorrectly removed gravity mainly contributes to velocity drifts in the horizontal plane due to the properties of the sine and cosine functions. Thus, different drift reduction strategies should be used for orientation and velocity drift reductions.

The main focus on the thesis was drift reduction in alpine ski racing. Multiple strategies were proposed for reducing orientation and position drifts. The work on cross-country skiing and ski mountaineering could be interpreted as an introduction to the drift reduction problem where the simplest case was covered: drift reduction at every movement cycle based on static moments (instants of time). Finally, the work on walking illustrates another, completely different strategy that can be used for cyclic movements where none of the other drift reduction strategies can be applied. In this case, instead of integrating the acceleration, walking speed was estimated based on a mapping between signal features of the wrist acceleration norm and walking speed.

1.2.1 Part I – Drift reduction based on static constraints

In the case of the diagonal stride in classical cross-country skiing, for a ski-fixed sensor, orientation and velocity drift could be both corrected based on the static (motionless) moments (instants of time) present in the ski-push phase during every movement cycle. Since in diagonal stride the skiing movement is constrained to the sagittal plane, the problem could be reduced to the simpler 2D case. Ski orientation was found by trapezoidal integration of the ski's medio-lateral angular velocity and drift was corrected during each ski-push phase by comparing integrated orientation with the slope angle measured with the help of the accelerometer when only the gravity component (inclination) is present (Fig. 1.1). Velocity was obtained by trapezoidal integration of the acceleration measured along the axis of progression (i.e. forward direction of the ski track) and corrected based on the ski's zero-velocity constraint during the push phase (Fig. 1.2).

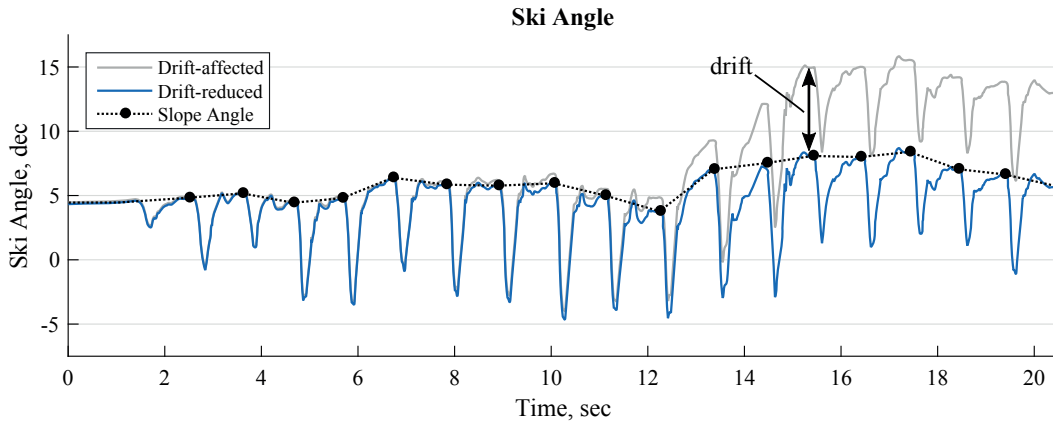


Figure 1.1 – Drift-affected (grey) and drift-reduced (blue) ski angle during cross-country skiing. Slope angle computed based on measured gravity during the static moments (instants of time) is marked in black.

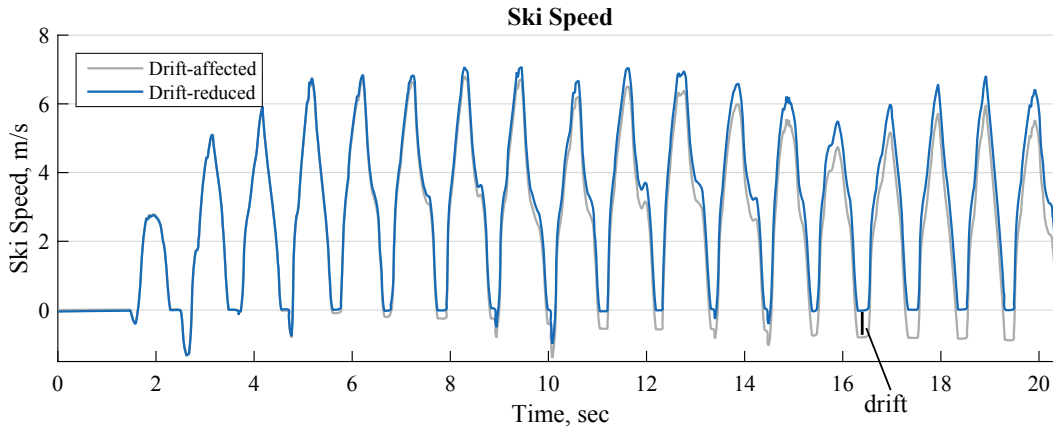


Figure 1.2 – Drift-affected (grey) and drift-reduced (blue) ski velocity during cross-country skiing.

The detailed algorithm description and an in-lab validation has been published in Fasel et al. (2015a) and is presented in Chapter 3 of this thesis. In a side project the algorithm was then adapted to the very similar but slower movement of ski-mountaineering. The work has been published in Fasel et al. (2016c) and is presented in Chapter 4 of this thesis.

1.2.2 Part II – Drift correction based on dynamic constraints and periodic reference updates

In alpine ski racing static moments (instants of time) that could be used for drift reduction only exist at the start and finish of a run. These moments are generally between one and three minutes apart and therefore only provide a very limited drift correction ability. For efficient drift correction complementary methods have to be found such that drift can also be estimated and corrected during moments of motion. The concept of joint drift correction can be used to reduce orientation drift. Suppose that two IMUs are fixed on two segments connected by a joint. If the IMU – joint centre distance vector is known, measured acceleration of each segment can be translated to the joint centre. Since the segments remain connected at the joint, both accelerations expressed in a common frame must be identical. Any disagreement must result from measurement errors. The common frame can be estimated by strap-down integration of the angular velocity. Since drift is accumulating, the frames of both sensors tend to diverge and the accelerations no longer match. Therefore, differences in the accelerations can be related to sensor drift and used to estimate drift of one sensor relative to the other (Fig. 1.3). Position drift can be reduced based on periodic reference position information. Traditionally, reference position is obtained from GNSS and is fused with IMU measurements based on Kalman filters. However, provided that such updates occur sufficiently often, they can also come from a different source. In alpine ski racing, the athlete is constrained to follow a course marked by gates. For maximum performance gates are usually crossed with minimal distance. Therefore, if gate crossings could be detected, gate positions could be used to correct position drifts (Fig. 1.4). Once segment orientations are known a body model can be computed to estimate joint positions and the athlete's CoM. These parameters can then be used for subsequent processing, for performance analysis, and for injury prevention. Examples are presented in Chapter 11.

The joint drift reduction algorithm description and in-field validation has been published in Fasel et al. (2017b) and is presented in Chapter 5. The algorithm was improved in a follow-up study and validated against a 3D camera system for indoor skiing. This work is presented in Chapter 6 and was submitted to the journal PLOS ONE. The validation study for the reconstruction of the joint positions and estimation of the athlete's CoM is presented in Chapter 7.

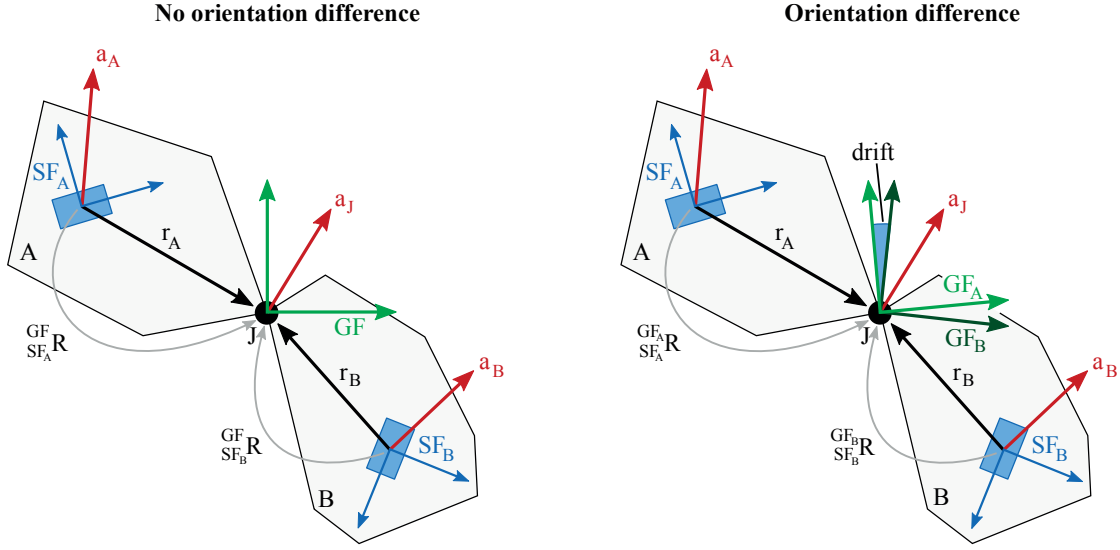


Figure 1.3 – Illustration of the joint drift correction concept. On the left: the case where the global frame (GF) at the joint is identical. On the right: the case where the global frame at the joint is no longer identical due to orientation drifts at both sensors. Thus, the components of the joint acceleration a_J are different in GF_A and GF_B and can be used to deduce the orientation difference.

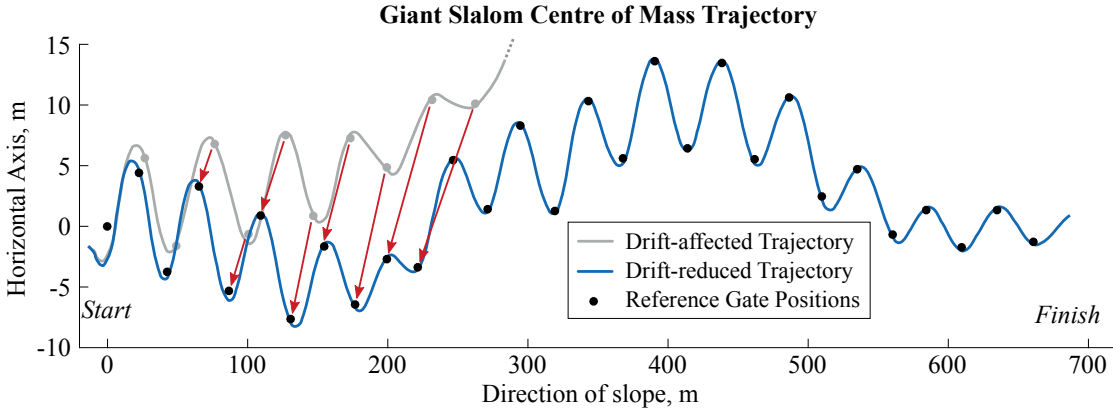


Figure 1.4 – Illustration of the position drift correction method based on reference gate positions during giant slalom skiing.

Next, the body model was combined with differential GNSS measurements to obtain absolute CoM kinematics. This study was published in Fasel et al. (2016e) and is presented in Chapter 8. However, the use of differential GNSS proved rather cumbersome and was complicated since a reference base station was needed and the GNSS antenna and data-logger had to be fixed somehow on the athlete. Therefore, a new system has been designed where position drift was corrected at each gate based on a gate crossing detection and previously obtained reference gate positions. The algorithms are described and validated in Chapter 9. Although the measurement of the athlete's movement did

not require a GNSS, reference gate positions still had to be measured somehow. Terrain surveying with differential GNSS or drones is feasible but requires extra measurements and the availability of GNSS signals which may be limited in certain parts of the slopes. Thus, an approach to estimate gate positions solely on inertial measurements has been proposed and validated. The study was accepted for an oral presentation at the 35th International Conference on Biomechanics in Sports (2017) and is presented in Chapter 10.

Finally, published work and possible performance analysis applications based on the described algorithms are summarized in Chapter 11.

1.2.3 Part III – Movement speed estimation based on signal feature mapping

There exists also the case where none of the presented drift correction methods can be applied: when one single inertial sensor is used and no static moments (instants of time) are present. This is for example the case for the wrist motion during walking: because of arm-swing and the trunk's up/down movement at each step, the wrist is never static during walking. Moreover, it cannot be expected that the person is walking in a predefined path where sporadically available reference positions could be used for position drift reduction. Wrist position is unknown and may vary over time (e.g. free arm swing versus holding a bag). If the orientation cannot be estimated reliably (e.g. in the absence of a gyroscope and orientation drift correction), gravity cannot be removed from the measured acceleration. Finally, the person may walk indoors and outdoors and GNSS cannot be used to obtain reference position or speed. Therefore, an altogether different approach is needed for estimating the walking speed. Since wrist movement is correlated to walking speed, machine learning approaches can be used to map signal features to walking speed (Fig. 1.5). Thus, speed can be estimated directly and no integration and drift reduction methods are required.

This method has been described and validated on a large set of outdoor walking measurements published in Fasel et al. (2017a) and is presented in Chapter 12.

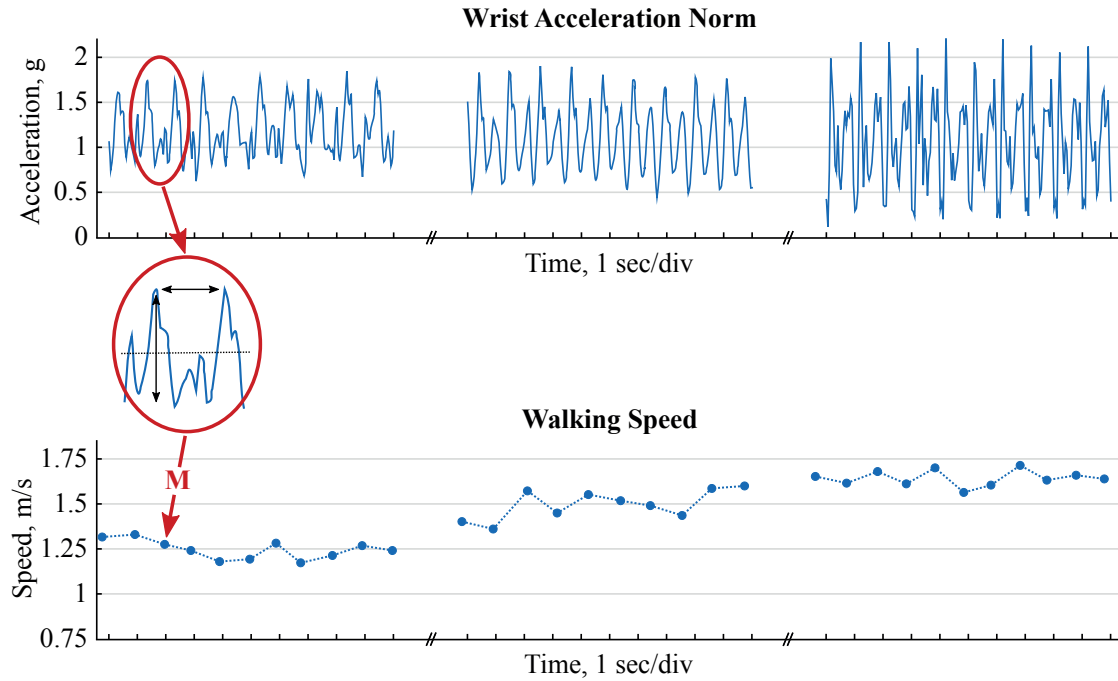
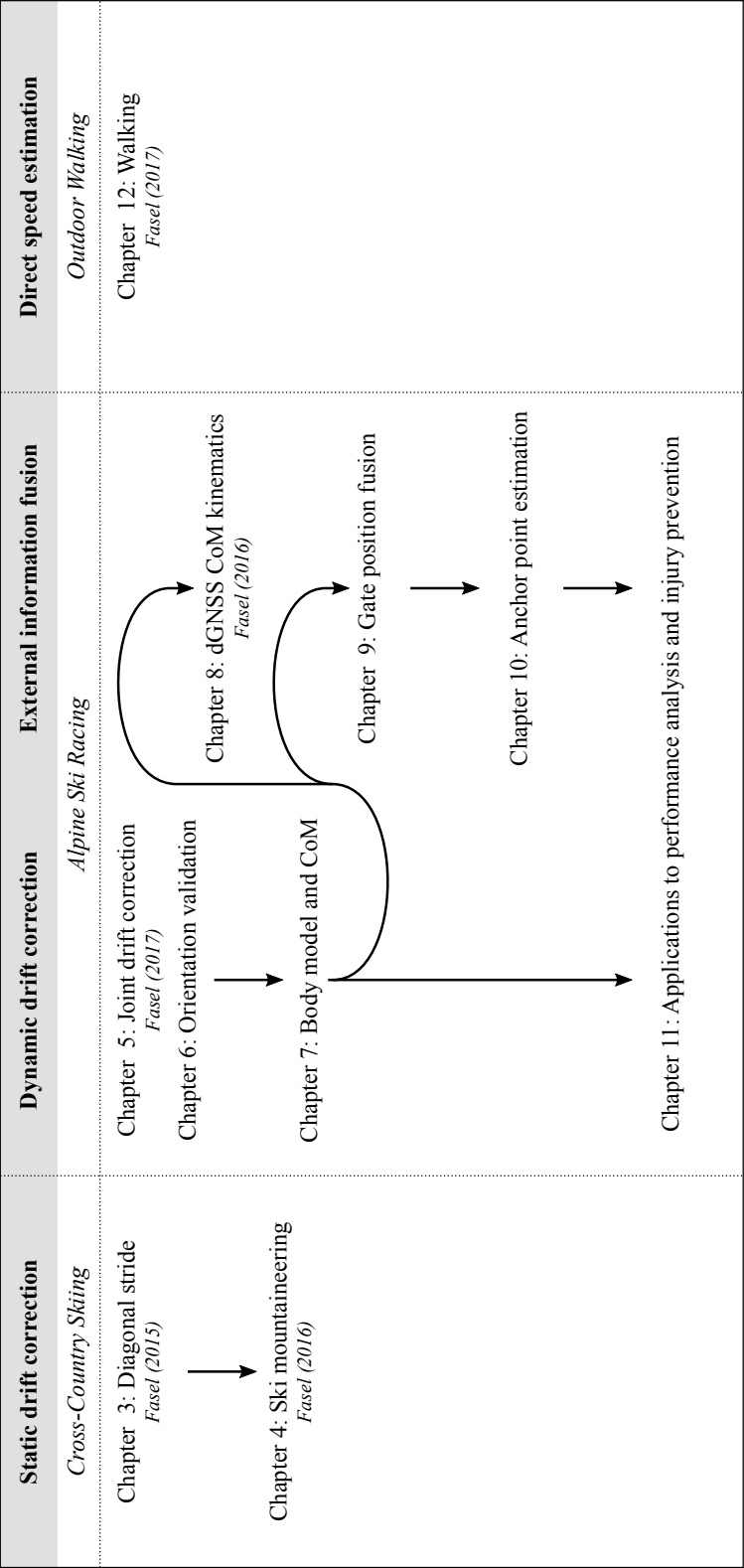


Figure 1.5 – Feature mapping for estimating walking speed without signal integration. Function M estimates the waking speed based on a set of signal features of the acceleration norm.

1.2.4 General discussion and conclusion

Finally, the thesis ends with Chapter 13. That chapter summarizes the main contributions and discusses the thesis' principal results critically. The chapter ends with an outlook on future work and outlines possible applications of the system.

1.3 Graphical summary



2 State of the Art

2.1 Inertial sensors

Inertial sensors, also known as inertial measurement units (IMU), consist of accelerometers and gyroscopes. Their most common implementation contains a 3D accelerometer measuring linear acceleration in all three spatial dimensions and a 3D gyroscope measuring angular velocity among all three spatial dimensions. A few high-grade IMUs contain two 3D accelerometers, one for low acceleration values (e.g. $<2g$) and one for high acceleration values (e.g. $>2g$) (e.g. myoMOTION Research Pro Sensors, Noraxon). In addition, many commercially available IMUs contain also a sensor to measure barometric pressure and a 3D magnetometer to measure the magnetic field. However, strictly speaking, these two sensors are not inertial sensors and will not be covered in this chapter.

This section provides a brief introduction into the measurement principles of inertial sensors. The most relevant error sources for processing inertial sensor data for movement analysis are presented. Finally, examples of measured acceleration and angular velocity are provided for static, slow, and fast movements. They illustrate the diversity of inertial signals and demonstrate that they are highly dependent on activity and sensor location.

2.1.1 Accelerometer measurement principle

A uniaxial accelerometer can be modelled as a spring-mass model (Fig. 2.1), allowed to move only along the spring's axis. Forces from accelerations acting on the mass are elongating or compressing the spring. Hooke's law (Eq. 2.1) states that the force acting on a spring is proportional to its elongation. Thus, by measuring the spring's elongation, the acting force and acceleration can be deduced. In micro-electro-mechanical-system (MEMS) accelerometers, this elongation is usually measured with a change in capacitance of the sensing structure. It is important to note that this system can measure not only dynamic but also static accelerations, such as for example the Earth's gravity. To measure acceleration in all three spatial dimensions three uniaxial accelerometers are mounted

perpendicular to each other to form a 3D (triaxial) accelerometer.

$$ma = F = kX \quad (2.1)$$

where m is the mass, a the acceleration, F the force, k the spring stiffness, and X the spring elongation.

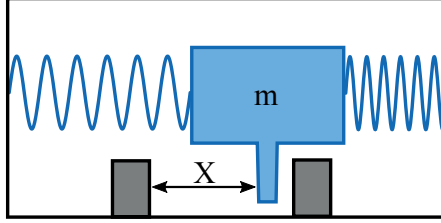


Figure 2.1 – Illustration of the spring-mass model of an accelerometer. A displacement of the mass changes the distance X which can be sensed by a change of capacitance.

During sensor calibration, the relation between the spring's elongation and acting acceleration is determined. For the simplest measurement model a linear relation between spring elongation and acting acceleration is assumed and only two parameters have to be estimated: offset and sensitivity (Eq. 2.2). The sensor can then be calibrated relative to the Earth's gravity. The simplest calibration is based on three measurements which are performed with the accelerometer's sensing axis orientated parallel, anti-parallel, and perpendicular to gravity. Sensor reading should be +1 when the sensor is oriented parallel to the gravity, -1 for anti-parallel orientation, and 0 when the sensing axis is perpendicular to gravity (Ferraris et al., 1995). More advanced calibration techniques take also into account sensor non-linearity (e.g. non-linear relation between modelled spring length and acting acceleration) and temperature (Aggarwal et al., 2008; Wang et al., 1996).

$$a = sX + o + \eta \quad (2.2)$$

where a is the acting acceleration, X the spring elongation, s the sensitivity, o the offset, and η measurement noise.

2.1.2 Gyroscope measurement principle

In modern MEMS gyroscopes, the Coriolis force is used to determine the angular velocity of a rotating sensor unit. The Coriolis force is a force perpendicular to both the angular velocity and linear velocity (Eq. 2.3). Generally, a tuning fork sensor is used where two masses are vibrating with velocities of opposite signs, thus creating a linear velocity v which in terms results in a Coriolis force if the vibrating masses are rotating at the same time (Fig. 2.2 left). Since the two masses are vibrating with opposite velocities the torsion bar will be twisted accordingly, resulting in "torsional vibrations" of the same

frequency. Similar to accelerometers where a change of spring elongation changes the sensing element's capacitance, these "torsional vibrations" change the capacitance of a sensing element at the top of the fork (Fig. 2.2 right) and the acting angular velocity can be deduced (Xia et al., 2014). The sensing element is usually constructed by the same principles than an accelerometer. Thus, a gyroscope can be seen as a combination of accelerometers and a driving unit to vibrate masses.

$$\mathbf{F}_C = -2m\boldsymbol{\omega} \times \mathbf{v} \quad (2.3)$$

where \mathbf{F}_C is the Coriolis force, m the mass, $\boldsymbol{\omega}$ the angular velocity, and \mathbf{v} the linear velocity.

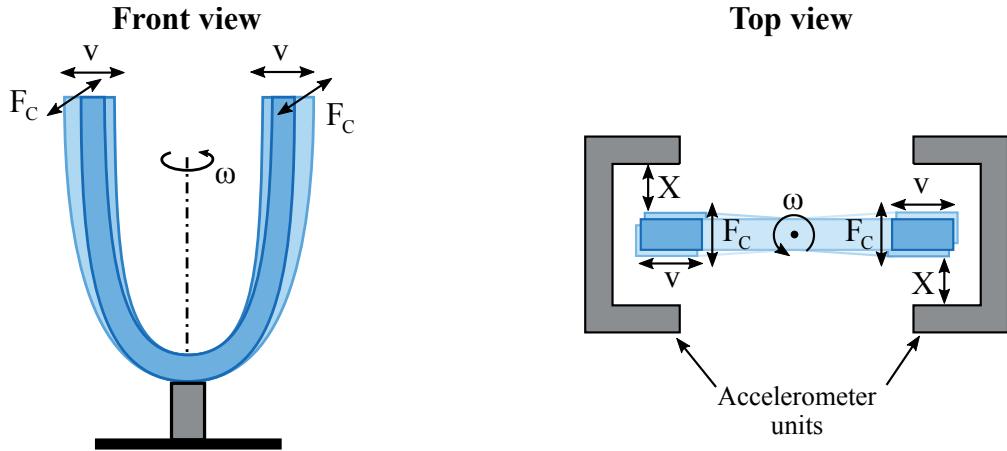


Figure 2.2 – Illustration of the tuning fork sensor for measuring angular velocity based on the Coriolis force. For the front view the accelerometer units are not shown.

Similar to the accelerometers, the gyroscope's most simple measurement model considers a sensor offset, sensitivity, and bias induced by external linear accelerations (Eq. 2.4). While the offset can be easily found by measuring the average value at rest a special rotating table may be required for determining the sensitivity precisely (Ferraris et al., 1995). For calibration the bias ba induced by external linear accelerations a is usually neglected.

$$\omega = sX + o + ba + \eta \quad (2.4)$$

where ω is the acting angular velocity, X the range of the "torsional vibrations", s the sensitivity, o the offset, ba the bias due to external linear acceleration a , and η the measurement noise.

Often, to simplify computation, the acceleration and gyroscope measurement models are written in the more abstract form of Eqs. 2.5 and 2.6.

$$a_{\text{measured}} = s_a a_{\text{true}} + o_a + \eta_a \quad (2.5)$$

$$\omega_{\text{measured}} = s_\omega \omega_{\text{true}} + o_\omega + ba_{\text{true}} + \eta_\omega \quad (2.6)$$

2.1.3 Measurement errors

Despite careful calibration, accelerometer and gyroscope measurements are not completely error-free. Measurements can be affected by errors of different sources and magnitudes (Lambrecht et al., 2016; Martin et al., 2016; Sabatini, 2005). The most important error sources relevant to movement analysis with inertial sensors are briefly explained below. The errors may be non-stationary and movement-dependent. Thus, depending on the performed movement and movement velocity, measurement errors may be different.

Both the accelerometer and gyroscope measurements are affected by the movement dynamics. High rotational speeds affect the mass-spring system and change the relationship between acceleration and spring length. For the gyroscope, linear accelerations acting on the tuning fork are added to the Coriolis acceleration and thus generate an additional moment of force at the torsion bar.

The individual 1D accelerometers and gyroscopes might not have been mounted perfectly perpendicular to each other to obtain the 3D accelerometers and 3D gyroscopes. Thus, the non-orthogonality produces axes cross-talk. Calibration procedures to estimate and cancel the misalignment error have been proposed (Aggarwal et al., 2008; Bonnet et al., 2009; Gietzelt et al., 2012, 2013). However, in contrast to the simple Ferraris calibration (Ferraris et al., 1995), they may require highly precise calibration equipment and are complex to perform. Non-orthogonality was especially present in the past where individual 1D accelerometers and gyroscopes have been mounted manually to form 3D systems. However, in the modern MEMS design sensors are directly produced in 3D, and thus, non-orthogonality has been greatly minimized. Therefore, simple calibration procedures assuming an orthogonal mounting of the individual sensors could be considered sufficient. A change in temperature is also influencing the inertial sensors' offset and sensitivity. For measurements taking place at constant temperature (e.g. indoors) this effect may only add errors if the calibration has not been performed at the same temperature. For example, the sensors were calibrated at 25°C but then fixed on a person's body where sensor temperature might reach 37°C. In outdoor settings with measurements in snow, this temperature difference might be even larger, adding more errors. A lab-experiment where an inertial sensor unit was held in static conditions at room temperature, in a freezer, and again at room temperature was performed. For representative axes the accelerometer bias and sensitivity changed the measured value by 0.1 g and gyroscope bias changed the measured value by 0.75 deg/sec for a temperature change of approximately 30°C (Fig. 2.3). The observed values were in the range specified in the sensor's datasheet (MPU6000, InvenSense, USA).

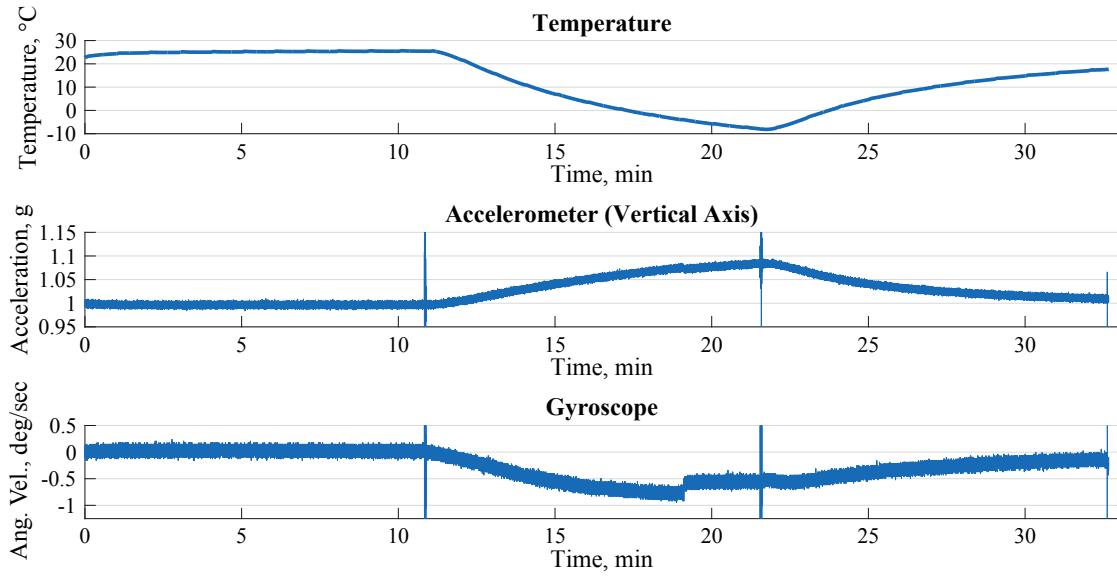


Figure 2.3 – Influence of temperature on the bias of the accelerometers and gyroscopes (MPU6000, InvenSense, USA). At around minute 19 the freezer’s cooling system switched on and induces vibrations that affect both the accelerometer and gyroscope measurements.

Another source of measurement error is sensor saturation. Sensors may saturate during highly dynamic movements or during shocks where the acceleration and angular velocity exceed the sensor’s range. In gait analysis, typically such saturation instants can be observed during initial ground contact of the foot for fast walking or running. Fig. 2.4 shows a four second recording of running at medium to fast speed. The gyroscope was fixed to the foot and was sampling at 500 Hz with a range of ± 1000 deg/sec. It can happen that saturation for a very short duration of a few milliseconds might not be visible since the duration was too short to be accurately measured by the sensor.

Finally, signal sampling and quantification may also be an important error source. While quantification noise impacts the signal less since its noise is comparatively small and zero-mean (Gray and Neuhoﬀ, 1998), errors from the sampling itself might be a larger problem. For signal sampling, two error types may be of relevance: (1) Signal losses due to an insuﬃciently high sampling frequency and inadequate low-pass filter at analogue-to-digital conversion. Signal losses can be observed especially for movements with rapid changes in dynamics such as the foot movement during gait. At each initial contact the foot is abruptly decelerated to zero velocity in a shock-like movement. Thus, at initial contact the acceleration approaches a Dirac delta function with infinite amplitude and zero duration. Thus, the frequency spectrum is approaching infinity and precise representation by a sampled signal is diﬃcult. A real-world example of this phenomenon is presented in the next section. (2) The anti-alias low-pass filter at analogue-to-digital conversion may alter the signal if the filter’s cut-oﬀ frequency is close or below the signal’s maximum frequency. Especially peak heights and rapid changes may be attenuated, resulting in an underestimation of acceleration or angular velocity peaks.

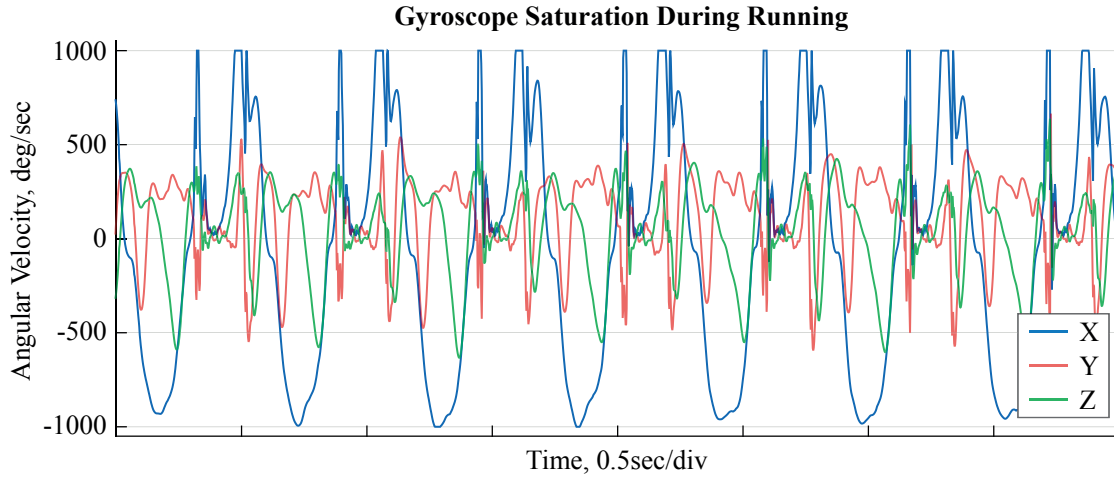


Figure 2.4 – Gyroscope saturation during running. The gyroscope’s range was configured at ± 1000 deg/sec. The data is represented in the sensor frame and was not aligned with the foot anatomical frame since a transformation of the sensing frame towards any other frame could mask such saturations as the new axes are formed by a weighed sum of the old axes.

2.1.4 Example signals

To illustrate measured acceleration, angular velocity, and their interplay, a forced-pendulum movement was performed. An inertial sensor was fixed to the end of a 45 cm long pendulum. At the start, the pendulum was held vertically and was then moved by hand with increasing speeds. The setup and axis definition is shown in Fig. 2.5.

During static periods the accelerometers only measure Earth’s gravity and angular velocity is zero (Fig. 2.6, seconds 0 – 5). Depending how the sensor is oriented with respect to gravity, the gravity is measured on different axes. Since no other accelerations are present, the measured gravity can be used to determine the sensor inclination. For slow pendulum-like movements angular velocity is non-zero and Earth’s gravity is measured on multiple axes depending on the sensor’s orientation (Fig. 2.6, seconds 5 – 15). For faster pendulum-like movements angular velocity increases and the centripetal acceleration can be seen on the sensing axis parallel to the pendulum’s longitudinal Y-axis (Fig. 2.6, seconds 15 – 35). In addition, accelerations and decelerations from the forced pendulum movement become apparent on the axis perpendicular to the pendulum’s longitudinal axis (X-axis).

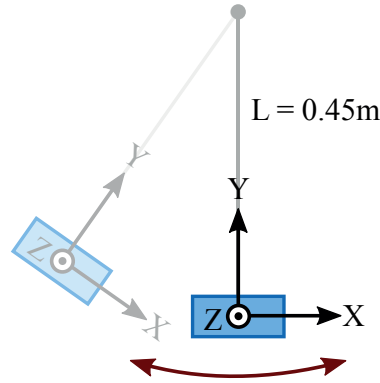


Figure 2.5 – Graphical description of the setup for the forced pendulum movement. X axis was perpendicular to the pendulum’s rotation axis and the pendulum’s longitudinal axis. Y axis was aligned with the pendulum’s longitudinal axis and the Z axis was aligned with the pendulum’s rotation axis. The experiment was started with the pendulum oriented vertically.

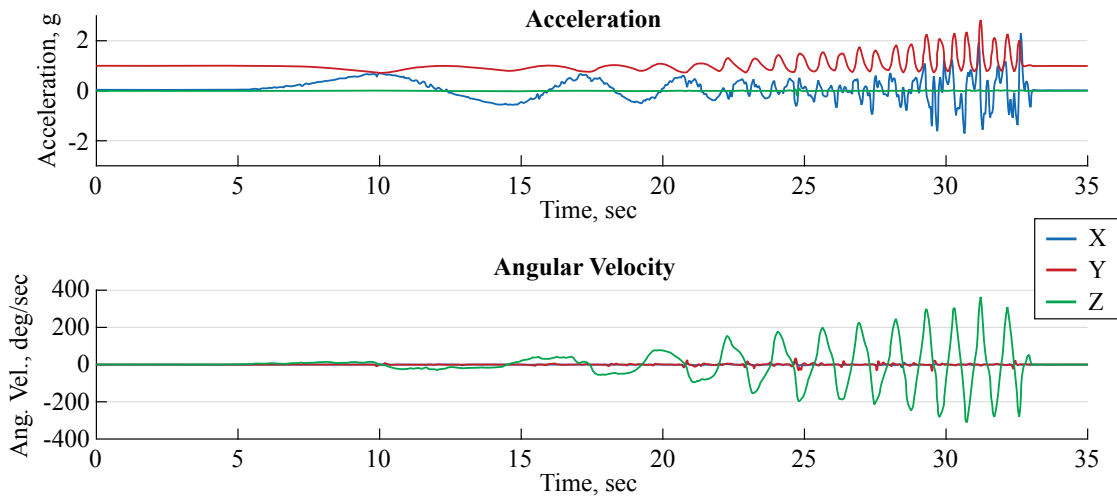


Figure 2.6 – Measured acceleration and angular velocity during the forced pendulum movement. The movement started slowly and was then slowly accelerated. The axes are defined as illustrated in Fig. 2.5.

In contrast to the well-controlled signals illustrating static and pendulum-like movement, signals from body-fixed sensors are generally more variable and noisy. Accelerations are usually present on all three axes and are highly location-dependent. Fig. 2.7 shows the acceleration and angular velocity measured with a sensor fixed to the right foot during normal walking. For the same movement, Fig. 2.8 shows the acceleration and angular velocity measured with a sensor fixed to the shank. Even though the segments are connected by the ankle their movement is very different and is reflected in the signal differences. While the foot-flat phase (marked with FF in Fig. 2.7) is well visible on the foot’s acceleration signal, it is very difficult to identify the same phase on the shank

sensor's signals. On the other hand, the angular velocity along the shank's lateral-medial axis is better suited for detecting the mid-swing since it is less noisy than on the foot.

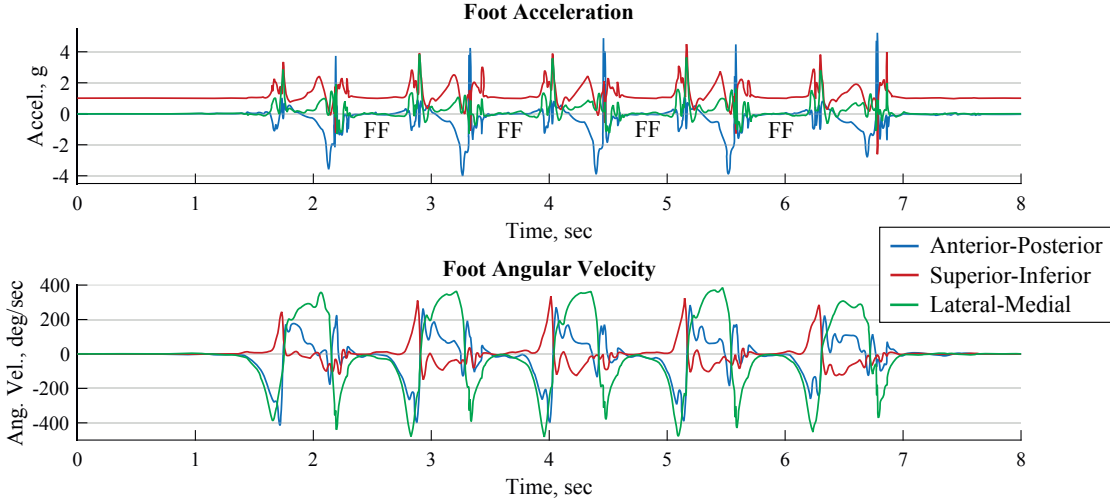


Figure 2.7 – Acceleration and angular velocity measured at the foot for walking five steps. All data is presented in the foot's anatomical frame. The foot flat phases between each step are marked with FF.

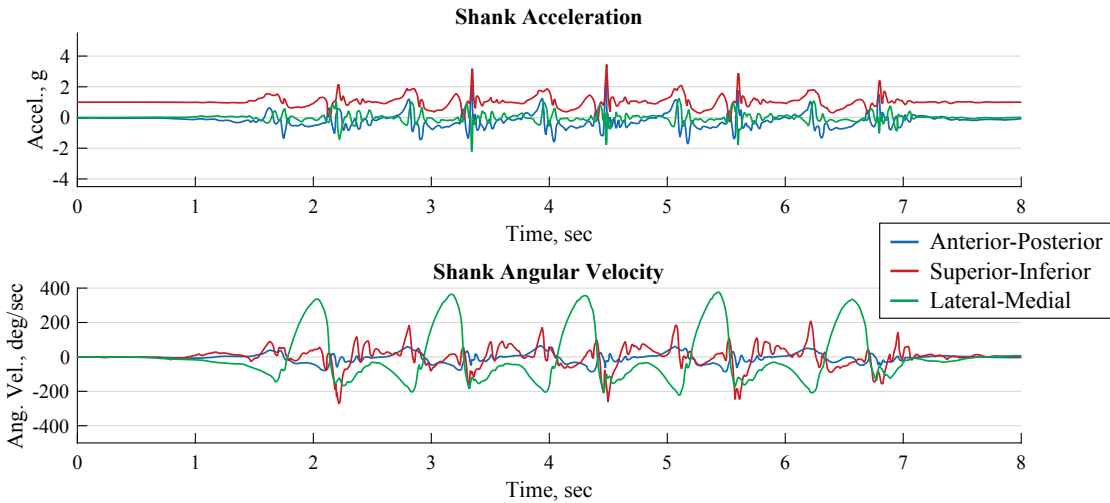


Figure 2.8 – Acceleration and angular velocity measured at the shank for walking the five steps displayed for the foot in Fig. 2.7. All data is presented in the shank's anatomical frame.

Finally, Fig. 2.9 shows the acceleration and angular velocity recorded at the sacrum during a part of a giant slalom skiing. Again, the signal is very different from the previously shown signals. As for walking the signal shows some periodicity which comes from the left and right turns. Since the movement and sensor location is different, the signal shape looks again very different compared to the previous examples from walking.

Moreover, both the acceleration and angular velocity is affected by considerable noise from the ski-snow interaction (i.e. skidding movement of the ski on the snow). Since the athlete is always in motion, no events marking turns and turn phases are apparent. At turn switch the athlete's skis are not in ground-contact and the athlete is in a free-fall movement. During this brief instant, measured acceleration is approaching zero on all axes and vibration is significantly reduced.

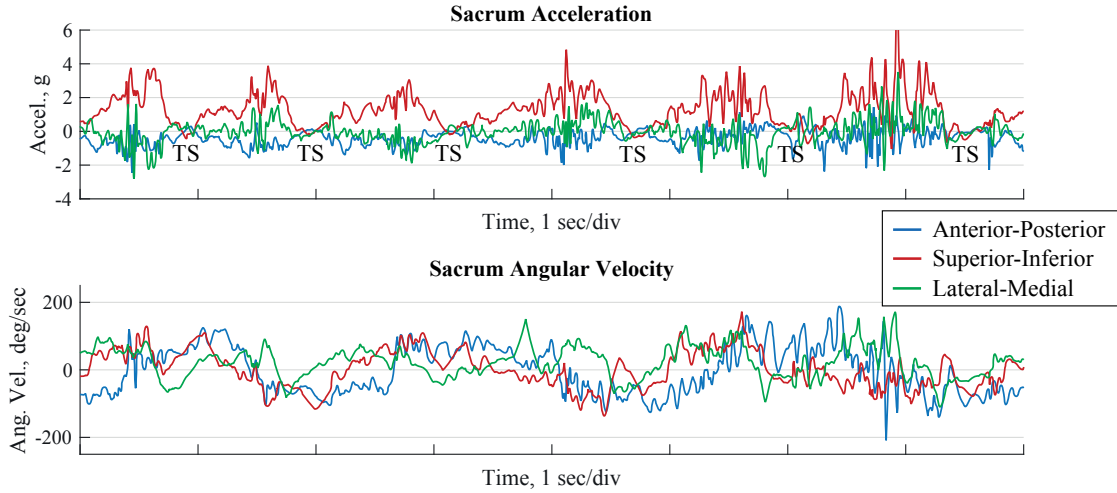


Figure 2.9 – Acceleration and angular velocity measured at the sacrum for six turns of a giant slalom. All data is presented in the sacrum's anatomical frame. The approximate location of the turn switches (i.e. change from left turn to right turn or vice versa) is marked by TS.

These examples show how the signal contents and characteristics change for different activities. Signals are also dependent on the sensor location and can be very different for the same movement measured on different segments. Thus, signal periodicity, time-correlation, frequency content, noise spectrum, etc. are highly activity dependent. Algorithms optimized for recording a given movement might not work for another movement. Prior to applying the algorithms for motion capture, they need to be carefully validated in conditions as close to the target conditions and activities as possible.

2.2 Drift

Inertial sensors measure acceleration and angular velocity. If velocity, position or orientation have to be determined, acceleration and angular velocity need to be integrated. To find velocity, acceleration has to be integrated. However, since measured acceleration is expressed in the sensor's local frame and contains Earth's gravity, it first has to be expressed in a global frame and gravity has to be removed. Thus, sensor orientation needs to be known which can be obtained by integration of the measured angular velocity. Fig. 2.10 provides an overview of these processing steps.

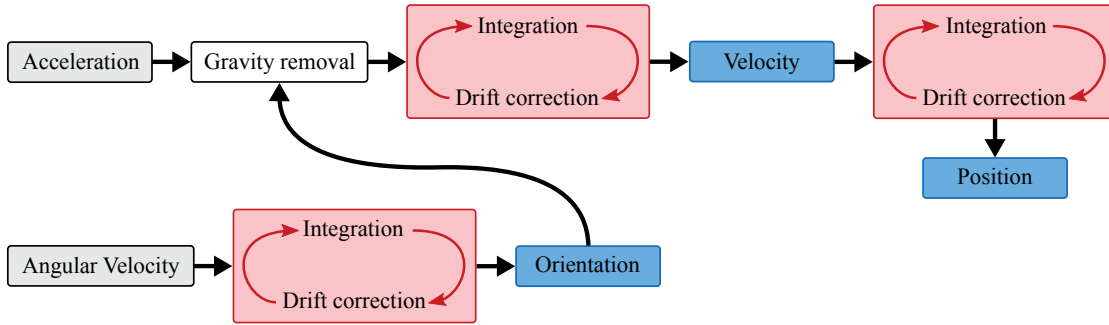


Figure 2.10 – Overview of the computation steps required for tracking the sensor’s position over time. For illustration purposes the drift correction steps have been kept very simple and independent from other steps. More advanced drift correction methods combine the three drift correction steps in order to use signal redundancies and constraints for maximum performance.

During signal integration, the measurement errors accumulate and result in the so-called drift. Drift may be slowly changing over time and and/or have discontinuities. Since measurement errors are dependent on the movement, drift is also movement-dependent. Moreover, drift sources in orientation are different than in velocity. The following section explains the origins of the drift in orientation and in velocity. It concludes by a literature review of methods to estimate, model, and correct drift.

2.2.1 Origins of orientation drift

The origins of orientation drift can be fully attributed to the previously presented measurement errors. Not all measurement errors contribute to significant amounts of drift. The two most important error sources are sensor bias due to temperature changes (see Fig. 2.3 for an illustration) and errors from the sampling (e.g. signal saturation, low-pass filtering). Gyroscope bias from external linear accelerations is oftentimes neglected since it is usually at least one order of magnitude smaller than the other error sources. For example, for the MP6000 gyroscope (InvenSense, USA) the datasheet states a linear acceleration sensitivity of 0.1 deg/sec/g whereas gyroscope bias due to temperature change can be up to 0.32 deg/sec/°C. To illustrate the errors from sampling, the following experiment has been conducted. An IMU was attached to a wooden block which rested on a table (Fig. 2.11). The IMU’s sampling frequency was set to 500 Hz. The low-pass filter at analogue-to-digital conversion was fixed to 94 Hz for the accelerometer and 98 Hz for the gyroscope. Accelerometer range was set to ± 16 g and gyroscope range was set to ± 1000 deg/sec. The right side of the block was lifted to reach an inclination of the block of 45° . Then the block was released and was allowed to fall down on the table. After a short rest it was lifted again to an inclination of 45° . The procedure was repeated eleven times. Gyroscope offset was corrected at the beginning of the experiment and sensor axes were aligned with the blocks axes. Sensor inclination was obtained by trapezoidal

integration of the angular velocity along the axis perpendicular to the block's rotation (Z-axis).

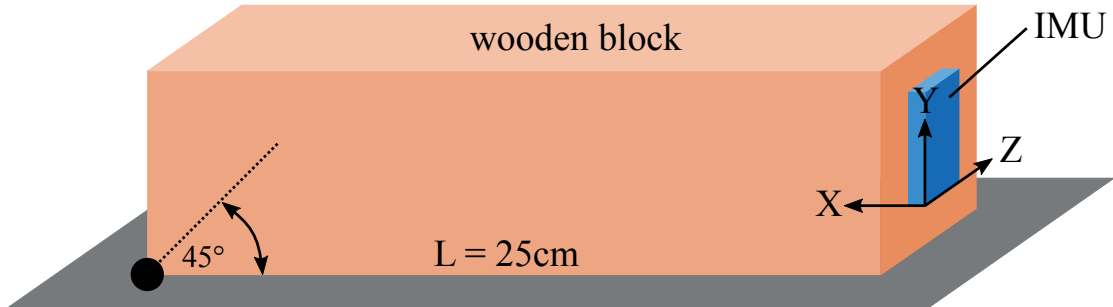


Figure 2.11 – Experimental setup showing the wooden block with the attached inertial sensor resting on the table. The centre of rotation was fixed to the lower left edge, indicated by the black dot.

The impact shocks of the block on the table are clearly visible in the measured acceleration. A peak is especially visible on the vertical Y axis and is reaching over 10 g. Angular velocity peaks from the free-fall rotation movement can also be seen (Fig. 2.12). Inclination shows nearly no drift at the very beginning but increases slowly over time, reaching a value of -5.7° at the end, after the eleventh shock. It can also be observed that even though the same movement was repeated eleven times, drift was not increasing linearly with time. Drift was negative after the first shock, positive after the second shock and again negative after the third shock.

The impact shock was very short and was measurable during approximately 0.01 seconds (Fig. 2.13). Small accelerations and rotations due to the block's and table's shock impulse response can be observed after 0.02 seconds of the end of the measured shock. Due to the small duration of the impact shock, only five samples were taken during this shock. Therefore, especially for the acceleration, it is highly likely that true shock amplitude and impulse response may have been missed. Similarly, the measured decrease in angular velocity at impact may not represent the true change in angular velocity which is likely to occur even faster but has been partly flattened by the low-pass filter during analogue-to-digital conversion.

To illustrate the consequences of shock movements on drift, a second experiment with the same setup has been performed. This time, instead of letting the block fall freely back on the table it was guided down, avoiding any impact shock. Fig. 2.14 shows the measured acceleration and angular velocity and the computed inclination. Since no shocks were present, acceleration was always low and angular velocity did not reach high values. The signal frequency was well below the low-pass filters' cut-off frequencies. Thus, the gyroscopes were able to accurately measure all movements and as consequence almost no drift accumulated (-0.6° after 70 seconds of integration).

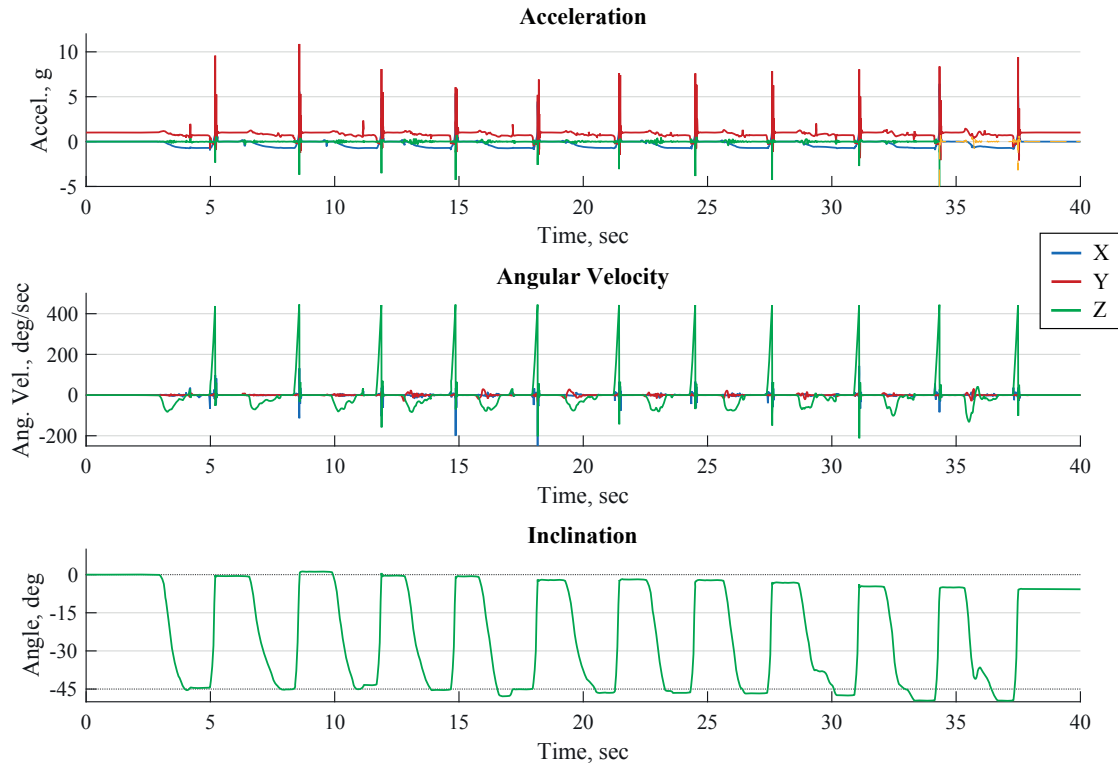


Figure 2.12 – Measured acceleration and angular velocity and computed inclination for the wooden block experiment. Even though the gyroscope bias was removed, the inclination is affected by drift.

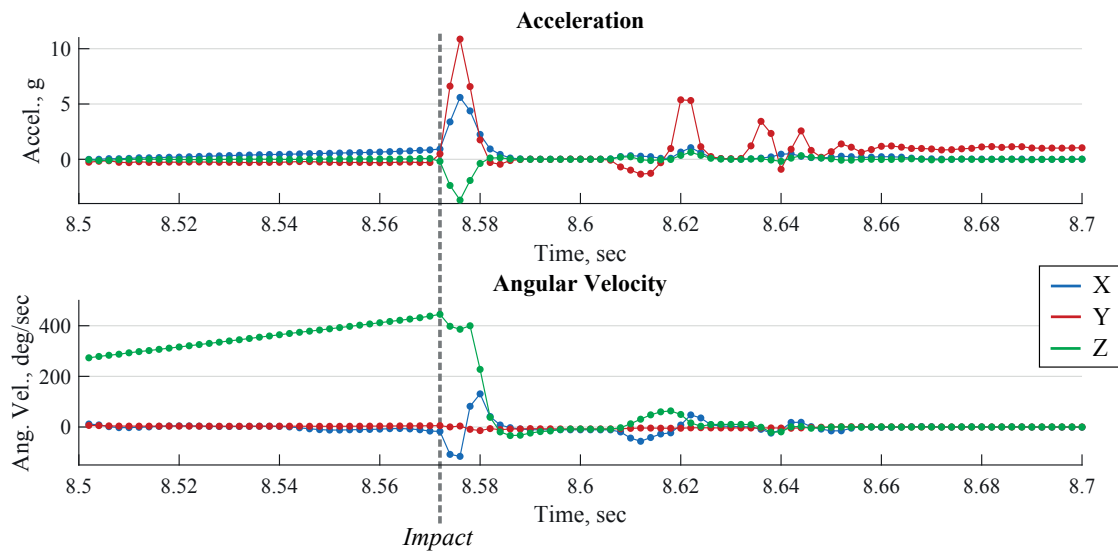


Figure 2.13 – Zoom to the second shock. Each sample is marked by a dot.

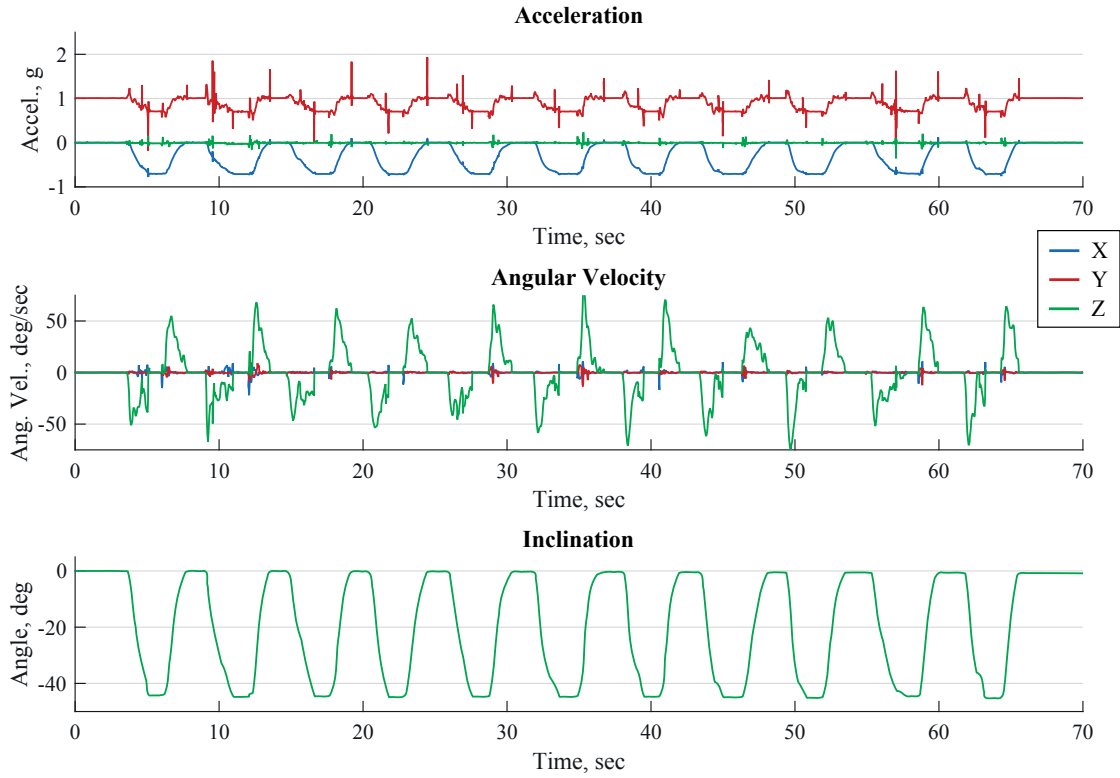


Figure 2.14 – Measured acceleration and angular velocity and computed inclination for the wooden block experiment where the block was not allowed to freely fall back onto the table. No shocks occurred and inclination drift was significantly lower compared to the free-falling block experiment.

2.2.2 Origins of velocity drift

In contrast to orientation drift, velocity drift is of higher magnitude and has an additional error source: incorrect removal of gravity due to errors in estimated orientation. As already mentioned, the gravity component in the measured acceleration has to be removed prior to integration. Therefore, the sensor's orientation in a global frame needs to be known. Since the sensor's orientation has to be estimated by integration of the angular velocity, it is affected by drift. Even if it is well corrected it is likely that some orientation error of 1-2 degrees may be remaining. Thus, gravity removal might be incorrect: on one axis too much gravity is removed while on another axis some gravity is incorrectly added. Consider the following mathematical example as an illustration: Suppose we measure only in two dimensions and that the global frame's x-axis (X_G) is horizontal and y-axis Y_G vertical, parallel to gravity. Suppose further that an accelerometer is inclined by 10° with respect to X_G (Fig. 2.15) and is motionless. Thus, its sensing axes X_S and Y_S are rotated by 10° with respect to the global frame. The measured acceleration a due to Earth's gravity g is therefore $a_x = \sin(10^\circ)g \approx 0.173g$ and $a_y = \cos(10^\circ)g \approx 0.985g$. Now suppose that due to orientation drift we consider that the sensor is inclined 11° (instead

of 10°) and we want to compute the inertial acceleration, i.e. the measured acceleration minus Earth's gravity. Since we are motionless, the inertial acceleration should be 0. However, because of the orientation error, it is:

$$\begin{aligned} a_x &= \sin(10^\circ)g - \sin(11^\circ)g \approx -0.01716g \\ a_y &= \cos(10^\circ)g - \cos(11^\circ)g \approx 0.00318g \end{aligned}$$

Thus, assuming a gravity value of $g = 9.81 \text{ m/s}^2$ we would have an acceleration offset (and thus drift after integration) of -0.1683 m/s^2 along X_S and 0.0312 m/s^2 along Y_S . Thus, after 10 seconds of integration we would obtain a speed of -1.7 m/s along X_S and of 0.3 m/s along Y_S , while in reality the sensor was always motionless.

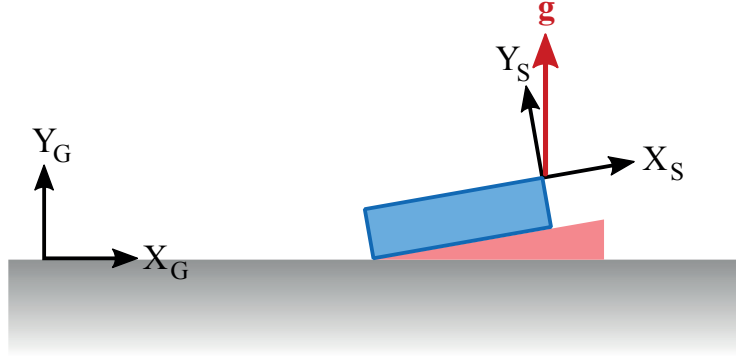


Figure 2.15 – Setup and frame definition for the gravity removal example

For the two wooden block experiments from above (free-falling and guided-movement) sensor velocity has been computed over time, first by removing gravity based on the computed sensor inclination, and second by trapezoidal integration of the inertial acceleration. Initial orientation was set to 0° . The results are shown in Fig. 2.16 (top) for the free-falling, and (bottom) for the guided-movement experiment.

The velocity estimate for the free-falling experiment is affected by drifts from both shocks and inaccurate orientation while the velocity estimate for the guided-movement experiment is only affected by drift from inaccurate orientation. Each shock creates a sudden increase in drift since the acceleration change was too fast to be accurately measured by the accelerometers. The velocity decrease back to zero at the instant of impact on the table is not measured (Fig. 2.17). It is important to note here that it appears that the accelerometer did not saturate at impact (in Fig. 2.13 peak acceleration is around 11 g). However, due to the integrated low-pass filter at analogue-to-digital conversion the true peak height was attenuated and therefore appears to be below 16 g . If we assume a speed of 1.9 m/s at impact and an impact duration of 0.01 seconds, mean acceleration during the impact would be 190 m/s^2 ($\approx 19.4 \text{ g}$). Modelling the acceleration at impact with a squared sine with a frequency of 50 Hz would result in a peak of 380

m/s^2 ($\approx 38.7 \text{ g}$). Under the assumption that impact shock caused an acceleration peak of 50 Hz, the low-pass filter at analogue-to-digital conversion should not have affected the peak. However, sampling of this squared sine almost guarantees that we miss the true peak since no sample has been taken at this instant of time (Fig. 2.18).

The orientation drift creates a slowly increasing or decreasing velocity drift. Well visible are the difference of the influence of small orientation errors on the two axes. Due to the nature of the cosine and sine functions, incorrectly removed gravity has different effects on the horizontal and vertical axes. Observed drift along the vertical axis (Y_G) is mostly linear over time and is less affected by the changing orientation error. Drift along the horizontal axis (X_G) has a more non-linear behaviour – the relation between orientation error and resulting bias in the acceleration is non-linear.

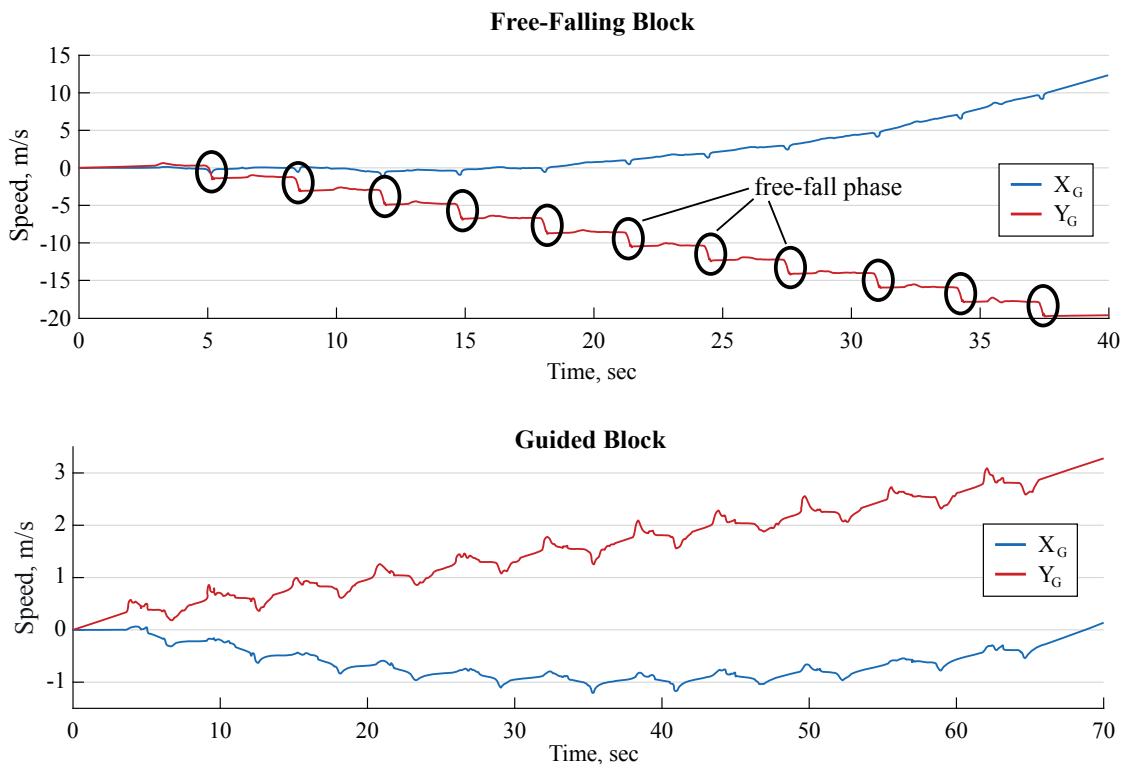


Figure 2.16 – Drift-affected velocity for the free-falling and guided-movement experiments. Less drift has been observed for the guided-movement experiments because the absence of shocks led to reduced orientation drift and more accurately measured acceleration.

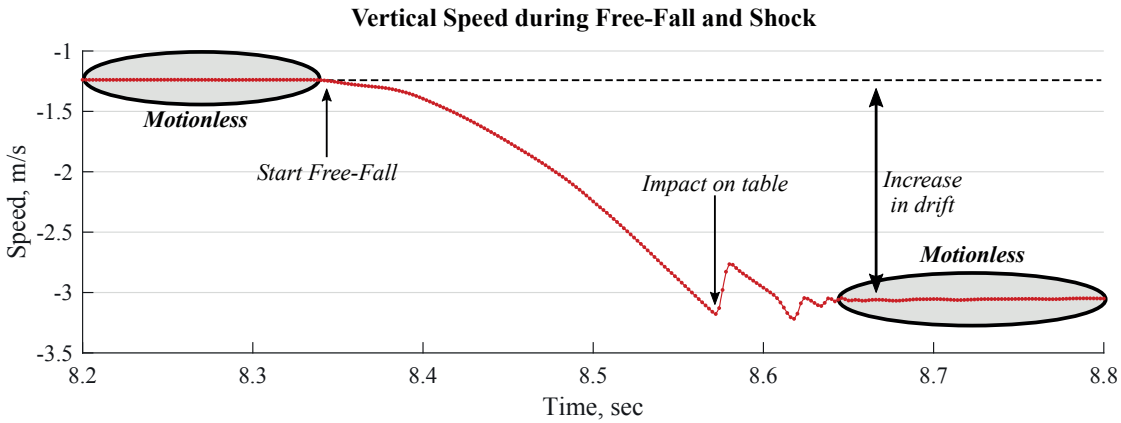


Figure 2.17 – Zoom on the second free-fall and shock phase of the free-falling block experiment. The graph shows the speed along the vertical axis (Y_G). The impact is too short to be accurately measured by the accelerometer. Thus, speed change at this moment (instant of time) cannot be captured and is lost. A zoom of the acceleration and angular velocity measured for the same impact is shown in Fig. 2.13.

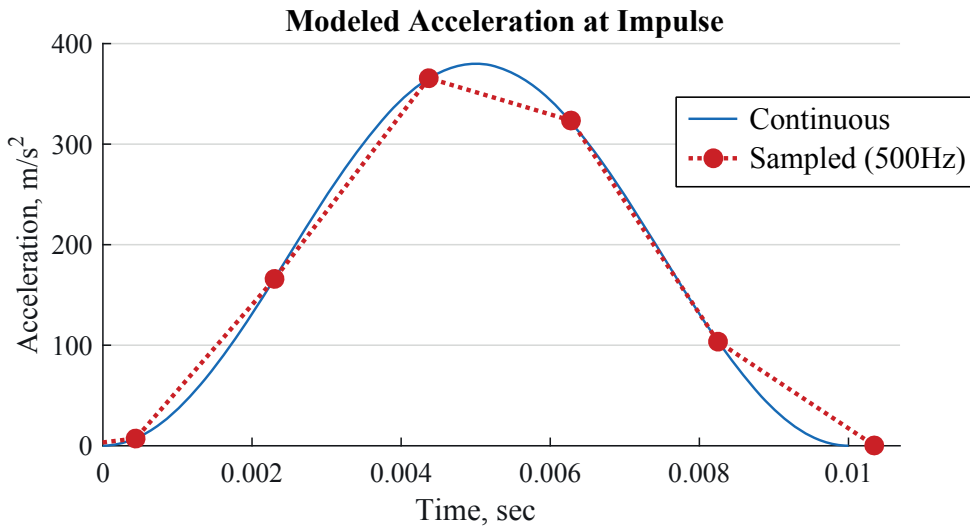


Figure 2.18 – Sampling of a squared sine used to model the measured acceleration at impact.

2.2.3 Summary

Drift for orientation and velocity have different sources. Compared to orientation, velocity drift has additional drift sources from incorrect gravity removal due to wrongly estimated orientation. Drift is highly movement dependent and especially for velocity is also dependent on the axis – velocity drift along the vertical axis is smaller than velocity drift along the horizontal axis. Moreover, drift depends on the movement itself. It is low for smooth movements, and abrupt movement changes (e.g. shocks) cause local

discontinuities. Thus, efficient drift correction methods might be different for different movements and sensor locations.

2.3 Proposed drift correction methods for human movement analysis

Drift was described, quantified and corrected since the very beginning of inertial sensor-based human movement analysis. Considerable effort has been invested in orientation drift correction where multiple approaches for different movements and sensor positions have been proposed. Velocity and position drift was investigated much less frequently.

2.3.1 First studies and drift-free computation of lower limb angles

The origin of using inertial sensors in movement analysis can probably be traced back to gait analysis. Already in the 1970s several studies using accelerometers for gait analysis were published (e.g. Morris (1973); Smidt et al. (1977, 1971)). Smidt et al. (1971) used a 3D accelerometer fixed to the waist and foot-switches for analysing several types of walking. Acceleration was translated to the frequency domain and a harmonic analysis was performed to report walking smoothness and irregularity. This work was extended by Smidt et al. (1977) where the authors described a procedure combining a 3D accelerometer fixed to the sacrum with foot-switches (for determining initial and terminal ground contact times) and video measurements (for obtaining step length and validation of the accelerometer data). Acceleration was integrated once to obtain velocity and a second time to obtain position information. However, no information was provided if and how gravity was corrected and whether any drift was observed. Morris (1973) presented a very nice mathematical theory where five one-dimensional accelerometers fixed to the shank (Fig. 2.19) were used to compute the sagittal plane acceleration and angular velocity of the shank during walking, based on the properties derived from Eqs. 2.7-2.9, projected onto the sagittal plane. Further, they proposed a scheme to estimate the accelerometers' absolute orientation in the sagittal plane, to reduce the gravity component, and to compute velocity and position of the mid-shank origin. The constraint of zero ankle translation (i.e. zero velocity and acceleration) during the stance phase was used to compute the shank's orientation and correct orientation and velocity drift from integration.

$$\alpha_m = \dot{\omega} \times \mathbf{r} + \omega \times (\omega \times \mathbf{r}) + \mathbf{g} + \mathbf{f} \quad (2.7)$$

$$\beta_m = \dot{\omega} \times \mathbf{s} + \omega \times (\omega \times \mathbf{s}) + \mathbf{g} + \mathbf{f} \quad (2.8)$$

$$\alpha_m - \beta_m = \dot{\omega} \times (\mathbf{r} - \mathbf{s}) + \omega \times (\omega \times (\mathbf{r} - \mathbf{s})) \quad (2.9)$$

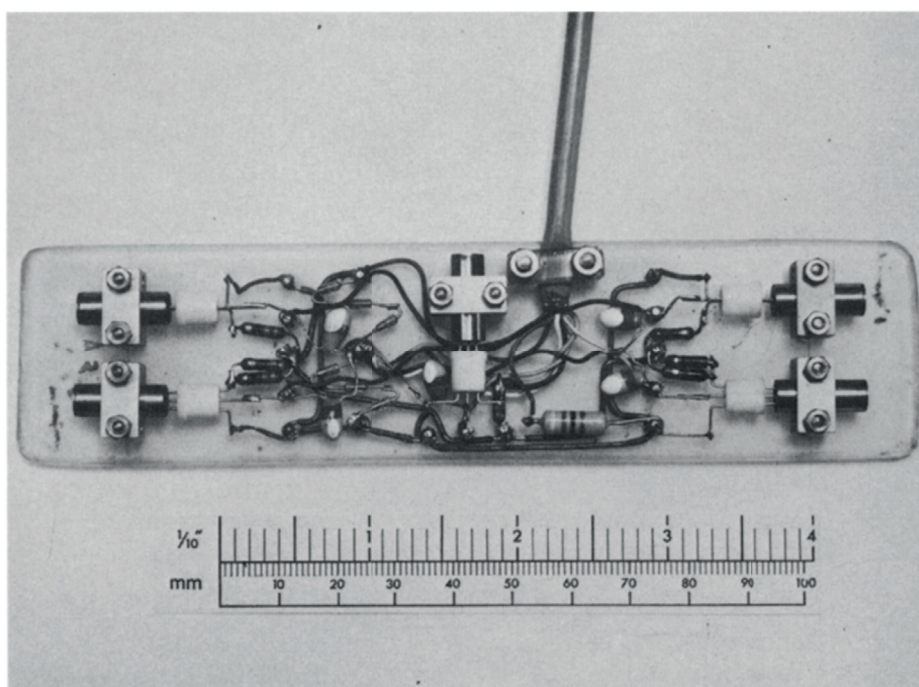


Figure 2.19 – Accelerometer mounting platform used in Morris (1973). The picture shows the five accelerometers and the associated electrical components. Figure taken from Morris (1973).

It took almost 20 years for the next publication on drift-reduction in human movement analysis to appear. Willemsen et al. (1990) used the method from (Morris, 1973) to compute drift-free knee flexion angles for gait. Two pairs of uniaxial accelerometers were fixed to the thigh and two pairs of uniaxial accelerometers were fixed to the shank (Fig. 2.20). The eight accelerometers were used to find the "equivalent accelerations" at the knee joint and to estimate knee flexion without integration. The assumption was that both shank and thigh should generate same "equivalent accelerations" when translated to the joint centre and therefore their angle difference would correspond to the knee angle. In addition, the authors also described how to compute the relative orientation of the shank during stance with respect to the gravity field based on Eq. 2.7. Computed angles were validated against a goniometer. A precision of $<3.5^\circ$ for static and periodic movements in the absence of shocks was reported. Shocks, for example caused by the heel strike during walking, added substantial vibration in the measured acceleration and therefore resulted in inaccurate angle measurements. A low-pass filter with a cut-off frequency of 5 Hz was used to filter the computed knee angles and a precision of $<5.2^\circ$ was reported. In the discussion, the problem of soft tissue artefacts was pointed out as one of the main error sources: muscle contraction could lead to significant orientation offsets and wobbling of the soft tissues adds noise in form of vibrations to the computed angles.

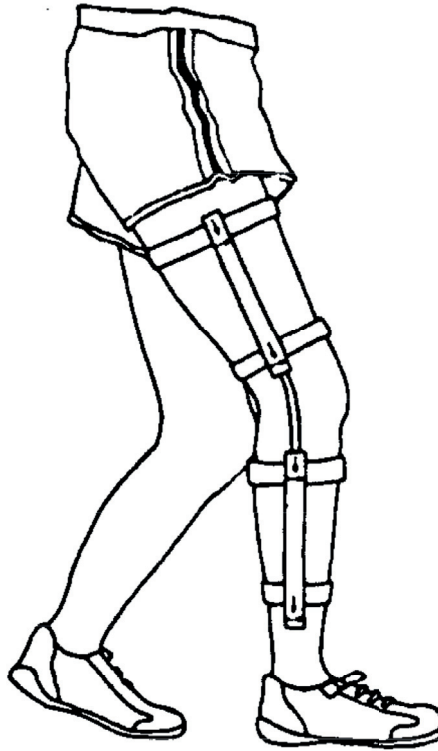


Figure 2.20 – Accelerometer and goniometer setup for the study from Willemsen et al. (1990). The accelerometer pairs were fixed to either end of the plastic plates fixed to the thigh and shank. A goniometer connecting the two plates was used to obtain reference knee angles. Figure taken from Willemsen et al. (1990).

Another 15 years later Dejnabadi et al. (2006) extended the concept and simplified the sensor configuration by using a gyroscope to estimate and correct orientation drift for gait. In their paper the "equivalent accelerations" were called "virtual accelerations" and used to correct orientation drift from gyroscope integration during moments (instants of time) of low acceleration. Fig. 2.21 shows a figure where acceleration measured with a shank-fixed accelerometer is translated to the ankle joint centre. The concept was also used to translate the acceleration to the knee joints, both from a shank- and thigh-fixed sensors. With their method, shank and thigh segment inclination as well as knee flexion angles could be estimated. The obtained segment inclinations were validated for different walking speeds (2 km/h, 3 km/h, 4 km/h). Root mean square errors of 1.0° for the shank and 1.6° for the thigh were reported. As in all the previous studies, the estimated angles were restricted to the sagittal plane. However, it was suggested that 3D segment and joint angles could be obtained with the same method if 3D accelerometers and 3D gyroscopes would be used.

Finally, for gait analysis, Seel et al. (2014) computed the knee flexion angle based on the integral of the difference of the thigh's and shank's angular velocity projected onto the

joint's principal axis of rotation. Drift was corrected with a Kalman filter and drift-free knee angles obtained from the "equivalent accelerations" at the knee joint. In addition to previous methods, although not related to drift, an automatic sensor-to-segment calibration procedure was proposed. As with the other methods, only the joint angle with the highest range of motion (e.g. knee flexion/extension during walking) could be computed due to the optimization used for the sensor-to-segment calibration. They assessed the system based on multiple walking trials over 10 m of a transfemoral amputee. Knee flexion root mean square error was 0.7° for the prosthetic leg and 3.3° for the contralateral leg. The authors state that the difference of errors between prosthetic and contralateral leg were most likely caused by soft tissue artefacts. For the prosthetic leg markers and sensors could be fixed directly to the prosthesis, thus preventing any soft tissue artefacts.

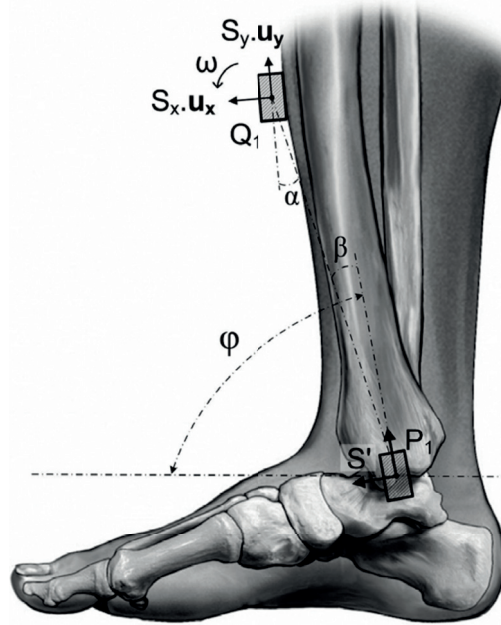


Figure 2.21 – Inertial sensor fixed to the shank and its corresponding virtual sensor at the ankle joint centre. The virtual acceleration at the ankle can be used to estimate the shank's inclination during the stance phase where the ankle joint centre is motionless on the ground. Figure taken from Dejnabadi et al. (2006).

The advantage of this acceleration-based approach is that the relative orientation of one segment with respect to another can be estimated without the need of motionless periods to estimate and correct the drift. Motionless periods are only required if the segment's orientation has to be estimated with respect to a fixed global frame. If for one instant of time a given point on the segment is static (e.g. the angle during the stance phase) then Eq. 2.7 can be used to estimate the segment's inclination directly since the only measured acceleration at this point is gravity and its orientation is known. Next, to compute the orientation in 3D (i.e. find the azimuth angle), one could either

2.3. Proposed drift correction methods for human movement analysis

take biomechanical constraints or use other aiding sensors such as magnetometers, as explained in the next sections. All the methods above were targeted at gait analysis. Even though these algorithms should in theory also work for higher dynamic movements and movements out of the sagittal plane, the algorithms have not been applied to and validated for such movements.

2.3.2 The common approach for orientation drift correction

By far the most common approach for orientation drift correction is closely related to the strap-down integration and is also integrated in most Kalman filters: periodical use of a reference orientation for estimating and correcting the drift. These algorithms were mostly targeted at gait analysis. For example, reference orientation can be obtained during static moments (instants of time) of the stance phase where measured acceleration ${}^S\mathbf{a}_m$ is compared to the known gravity vector. Gravity is expressed in the sensor frame (${}^S\mathbf{g}$) based on the sensor orientation obtained from integration of the angular velocity. Any orientation difference between ${}^S\mathbf{a}_m$ and ${}^S\mathbf{g}$ is attributed to orientation drift (Eq. 2.10-2.11).

$$\delta = \arccos \left(\frac{{}^S\mathbf{a}_m \cdot {}^S\mathbf{g}}{\|{}^S\mathbf{a}_m\| \|{}^S\mathbf{g}\|} \right) \quad (2.10)$$

$$\mathbf{r} = \frac{{}^S\mathbf{a}_m \times {}^S\mathbf{g}}{\|{}^S\mathbf{a}_m \times {}^S\mathbf{g}\|} \quad (2.11)$$

where δ is the drift magnitude and \mathbf{r} the drift axis.

Strap-down integration and deterministic drift correction

In Favre et al. (2006); Sabatini (2005); Sabatini et al. (2005) sensor orientation was computed with the strap-down integration, i.e. 3D integration of the angular velocity. Sensor orientation between time t and $t+dt$ can be expressed by the following relationship (Eq. 2.12):

$$q(t+dt) = dq \otimes q(t) \quad (2.12)$$

where $q(t+dt)$ is the quaternion representation of the orientation at time $t+dt$, $q(t)$ the orientation at time t , dq the change of orientation between time t and $t+dt$, and \otimes the quaternion multiplication operator.

Supposing that the angular velocity ω measured at time t remains constant until time $t+dt$, dq can be found according to Eq. 2.13-2.14 (Favre et al., 2006):

$$\Omega(t) = q(t) \otimes \tilde{\omega}(t) \otimes q^{-1}(t) \quad (2.13)$$

$$dq = \left[1, \frac{[\Omega_X(t), \Omega_Y(t), \Omega_Z(t)]}{2} \right] \quad (2.14)$$

where $\tilde{\omega}(t) = [0, \omega_x(t), \omega_y(t), \omega_z(t)]$ is the quaternion representation of the angular velocity $\omega(t) = [\omega_x(t), \omega_y(t), \omega_z(t)]$ measured at time t , and $\Omega(t)$ its quaternion representation in the global frame.

During each motionless period, the orientation drift was then computed according to Eqs. 2.10-2.11. Orientation drift was supposed to be linearly distributed between two subsequent motionless periods occurring at times u and v and could be corrected in the global frame according to Eq. 2.15 following the works of Favre et al. (2006); Sabatini et al. (2005) or with the so-called SLERP quaternion interpolation (Shoemake, 1985) following the work of Sabatini (2005).

$$\delta_{\text{drift}}(u + w) = \frac{w\delta}{v - u}, \quad w \in [0; v - u] \quad (2.15)$$

where $\delta_{\text{drift}}(u + w)$ is the drift magnitude (i.e. drift angle) at time $u + w$ around rotation axis \mathbf{r} from Eq. 2.11, and δ is the total drift angle from Eq. 2.10.

The problem of using this method is that even if static moments (instants of time) are available sufficiently often, drift can be corrected only along the vertical (gravity) axis. Therefore, azimuth drift (i.e. drift around the vertical (gravity) axis) cannot be corrected.

Kalman filters and statistical drift correction

The deterministic drift correction is advantageous in the sense that drift can be estimated explicitly and in a very intuitive way. However, at the same time this is also a disadvantage: adding more orientation constraints, more realistic drift modeling, or other sensor sources may not be possible. Kalman filters were already used successfully for inertial navigation since the 1960s (Grewal and Andrews, 2010b) and proved therefore to be the ideal candidate for orientation drift correction for human movement analysis. Luinje and Veltink (2005) proposed a Kalman filter which fuses sensor inclination computed from a 3D accelerometer with 3D orientation found by integration of the angular velocity (Fig. 2.22).

A large number of studies (e.g. Lee et al. (2003); Plamondon et al. (2007); Sabatini (2006); Schepers et al. (2010); Yun and Bachmann (2006); Zhu et al. (2007)) used magnetometers as an additional information source. Similar to gravity, the Earth's magnetic field is providing a locally constant vector field and is sufficiently perpendicular to gravity (excluding regions close to the magnetic north and south poles) so that azimuth drift can be estimated. Drift estimation is done similar to the gravity case with the difference that the measured magnetic field is not influenced by the sensor's movement. Therefore, all time samples are available for drift correction. However, the magnetic field is disturbed by ferro-magnetic objects such as steel. In order to obtain reliable and precise azimuth estimates magnetic disturbances should be first detected and corrected (e.g. Lee and Park (2009); Madgwick et al. (2011); Roetenberg et al. (2005)).

2.3. Proposed drift correction methods for human movement analysis

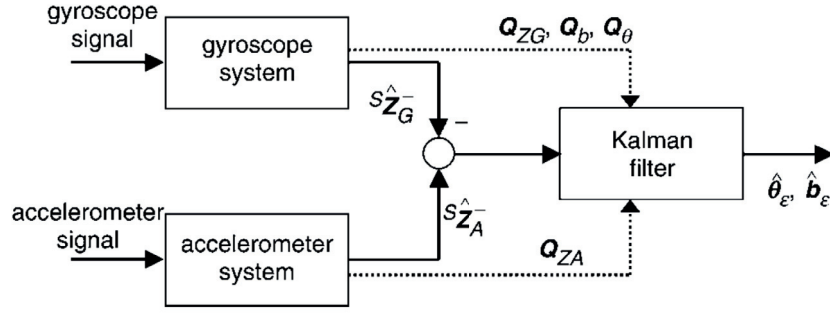


Figure 2.22 – Proposed Kalman filter from Luinge and Veltink (2005) to fuse angular velocity with acceleration to estimate a drift-corrected sensor orientation. Both the accelerometer and gyroscope systems compute a sensor inclination ($\hat{S}\hat{\mathbf{z}}_A^-, \hat{S}\hat{\mathbf{z}}_G^-$) and estimation error covariance matrices ($\mathbf{Q}_{ZA}, \mathbf{Q}_{ZG}, \mathbf{Q}_b, \mathbf{Q}_\theta$) for the fusion in the Kalman filter. Figure taken from Luinge and Veltink (2005)

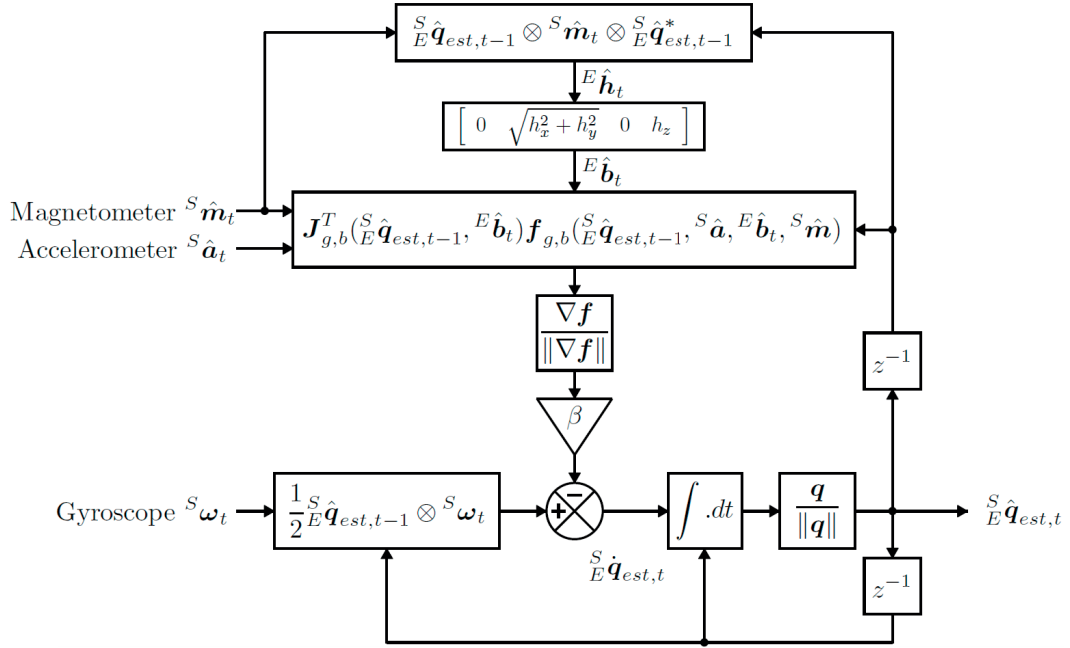


Figure 2.23 – Block diagram of the algorithm from Madgwick et al. (2011) which fuses acceleration, gyroscope and magnetometer measurements and includes a magnetic distortion compensation. Figure taken from Madgwick et al. (2011).

Especially the algorithm by Madgwick et al. (2011) is very popular since its implementation code has been published open source (<http://x-io.co.uk/open-source-imu-and-ahrs-algorithms>, accessed March 29th 2017) and has been downloaded thousands of times. The algorithm is based on a gradient descent search to estimate and track the change of gyroscope measurement error over time. Accelerometer, gyroscope and magnetometer measurements are fused and the algorithm automatically performs a magnetic distortion

compensation. The algorithm's block diagram is depicted in Fig. 2.23. RMS errors of less than 1.1° were reported for simple rotations in 3D and were smaller than a Kalman-based algorithm used as additional comparison.

2.3.3 Kinematic chains for orientation drift correction

The "common approaches" for correcting orientation drift for movement analysis are based on single sensors only. If multiple sensors are placed on the same person, for example to measure joint angles, measurement redundancy can be exploited. This redundancy was already exploited in the very first publications where drift-free joint angles were obtained by comparing the accelerations measured on two adjacent segments. Several studies further developed this idea based on kinematic chains and joint motion constraints.

Luinge et al. (2007) introduced an elbow joint constraint for reducing relative azimuth drift of the elbow joint angle. Two inertial sensors fixed to the upper arm and wrist. For each sensor, orientation was obtained with a Kalman filter according to Luinge and Veltink (2005) where gyroscope drift was corrected based on measured acceleration (Fig. 2.22). The mechanical constraint of minimum elbow abduction-adduction was then used in a least-square optimization procedure. Their approach was able to reduce the relative drift between the two sensors. However, not all drift could be reduced and was still reaching up to 40° for 2 minutes of measurement (Fig. 2.24). In the discussion, the authors speculated that an inaccurate sensor-to-segment calibration (i.e. anatomical or functional calibration) might be responsible for the large errors observed.

The group further refined their approach and extended it to the entire body. In the concept paper (Roetenberg et al., 2013) a full-body IMU system consisting of 17 sensor modules (Xsens MVN) was described. In a first step, sensor orientation was estimated using the "common approaches" (i.e. Kalman filter with single sensor drift correction based on measured gravity during static moments (instants of time) and Earth's magnetic field). In a second step, the estimated sensor orientations were used to obtain segment kinematics and construct a kinematic chain. Third, joint constraints, external contact points (i.e. both feet must touch the ground when still standing or during the double support phase of walking), and aiding sensors (i.e. GNSS) were used to update the kinematics and correct any remaining errors. Lower limb joint angles were validated with an optical camera-based system for level walking, stair ascent and stair descent (Zhang et al., 2013). A precision of $<2^\circ$ and correlation (CMC) >0.96 for flexion/extension angles was reported. Precision of abduction/adduction and internal/external joint angles was significantly worse and reached values of up to 4.2° for knee abduction/adduction during level walking. Angles along these axes also showed a significant offset of up to 6.7° for ankle abduction/adduction during stair descent. For simple tasks of manual materials handling (e.g. lifting or carrying a box) Kim and Nussbaum (2013) validated knee, hip, trunk, and shoulder angles obtained with the Xsens MVN system and reported overall mean absolute errors of up to 3.7° .

Cooper et al. (2009) estimated the knee joint flexion/extension angles where drift was

2.3. Proposed drift correction methods for human movement analysis

corrected in two steps. First, a Kalman filter was used to correct orientation drift on the sensors fixed to the shank and thigh independently. Second, the knee joint angle was computed and drift was further reduced by constraining the knee motion to the sagittal plane (knee joint modelled as hinge joint). The method was validated for different walking and running speeds for five minutes on treadmill. Seven persons were enrolled to the study. Average root mean square errors were lowest for the slowest walking trial (0.7° for walking at 0.45 m/s) and steadily increased for faster speeds reaching 3.4° for slow running at 2.2 m/s.

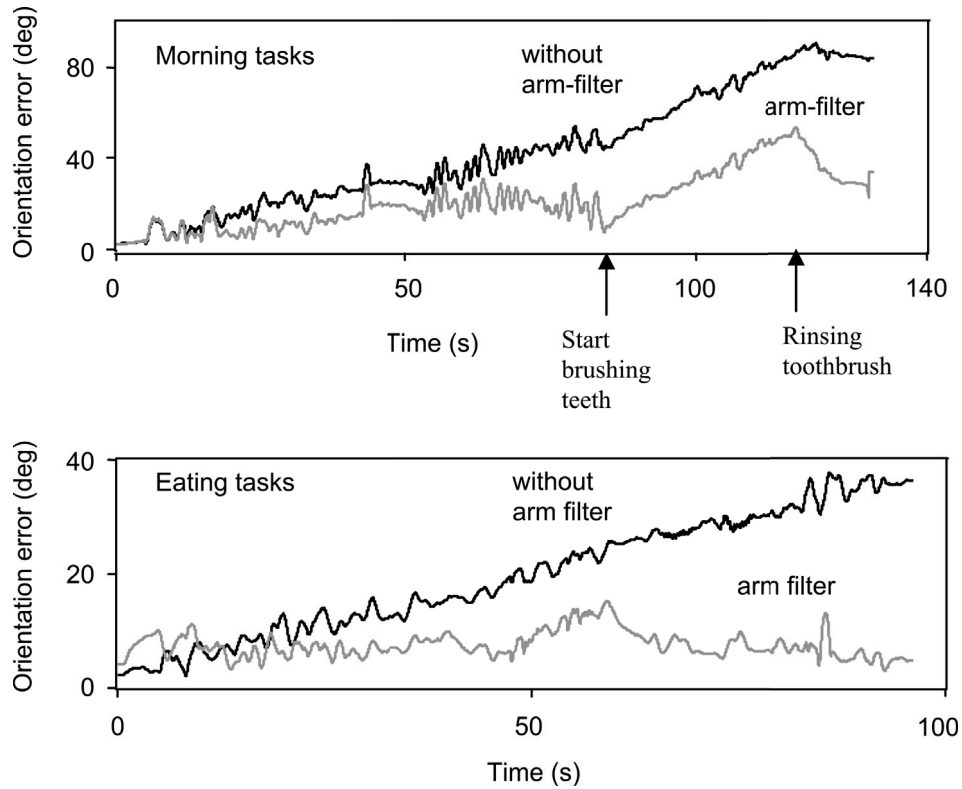


Figure 2.24 – Reduction of orientation error of the upper arm with respect to the forearm for morning and eating tasks from Luinge et al. (2007). The black curves show the orientation error without the proposed arm filter and the grey curves show the orientation error with the proposed arm filter. Figure taken from Luinge et al. (2007).

Young (2010) presented a method to estimate and remove linear accelerations at each sensor and then estimated orientation drift by comparing the resulting acceleration with the gravity vector. A full body model and iterative processing along the body's kinematic chain was used to iteratively estimate the linear acceleration for each segment. The root of the body model was fixed at the pelvis and radial accelerations (i.e. accelerations due to rotations) were estimated and removed based on Eq. 2.7. For simulated walking measurements, mean root mean square error between all trials was found to range between 1.2° and 1.9° for the various body segments.

Another way is to combine the kinematic chains with biomechanical constraints of a known movement. Chardonnnens et al. (2013) proposed and validated this approach on the example of ski jumping. The ski jumping movement can be separated into different phases, and different motion constraints based on biomechanical constraints can be applied during each phase. For example, during the in-run phase the athlete is accelerating in the sagittal plane and the movement of the skis are restricted by the jumping hill. His posture is almost constant – therefore accelerations measured on all segments must be similar and deviations can be used to estimate and correct drift.

2.3.4 Drift-free orientation for periodic signals

Instead of numerically integrating angular velocity to obtain the orientation, it could also be integrated analytically. Bonnet et al. (2013) proposed to use the Weighted Fourier Linear Combiner for this purpose. Sensor orientation was obtained by analytical integration of the Fourier series identified with the Weighed Fourier Linear Combiner (Fig. 2.25). They validated their method on 18 volunteers with an inertial sensor fixed to their lower back. Average root mean square orientation errors below 1.2° were reported for all axes and measurement duration of 80 seconds of treadmill walking with a short break after 40 seconds. However, it was not clear how the initial conditions (i.e. initial angle) were defined.

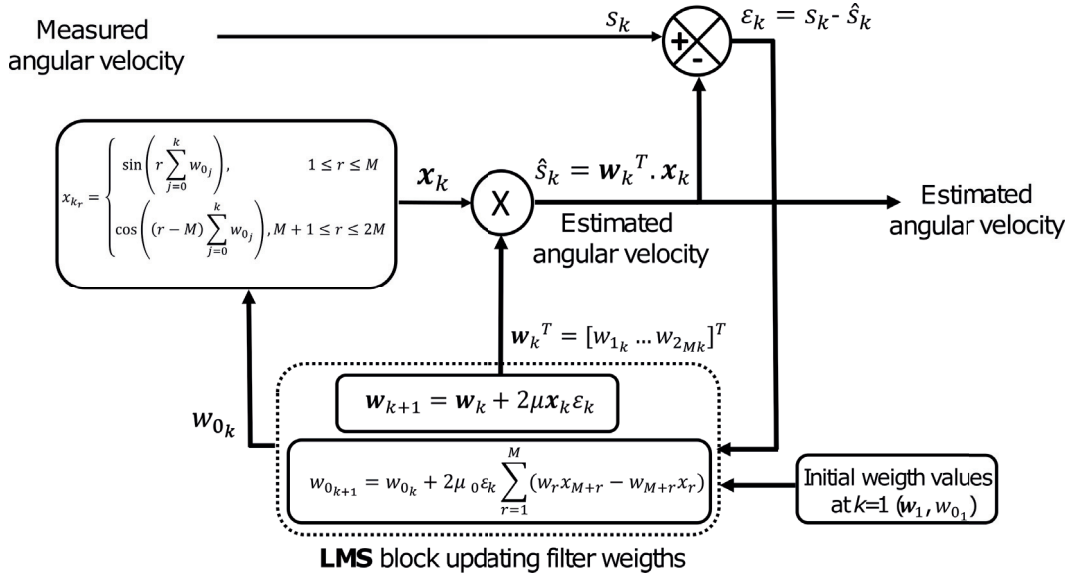


Figure 2.25 – Block diagram of the weighed Fourier linear combiner filter. LMS is the abbreviation for least mean square and M the order of the Fourier series representing the measured signal s. Figure taken from Bonnet et al. (2013).

2.3.5 Velocity and position drift correction

Similar to orientation drift correction, different strategies have been presented for velocity and position drift correction. Again, especially for foot-based gait analysis, motionless constraints can be used to set velocity to zero (i.e. zero-velocity update) (Foxlin, 2005; Sabatini et al., 2005). This very simple resetting procedure has been further refined to linear and non-linear velocity drift estimation over one or multiple gait cycles. For example, Mariani et al. (2010) proposed to fit a sigmoid-like curve to take into account a varying amount of velocity drift for motionless and in-motion instants of time (Fig. 2.26). Velocity was again constrained to zero at each motionless phase. The method was validated during various walking conditions and an average precision of 5.8% for stride velocity and 6.5% for stride length was found.

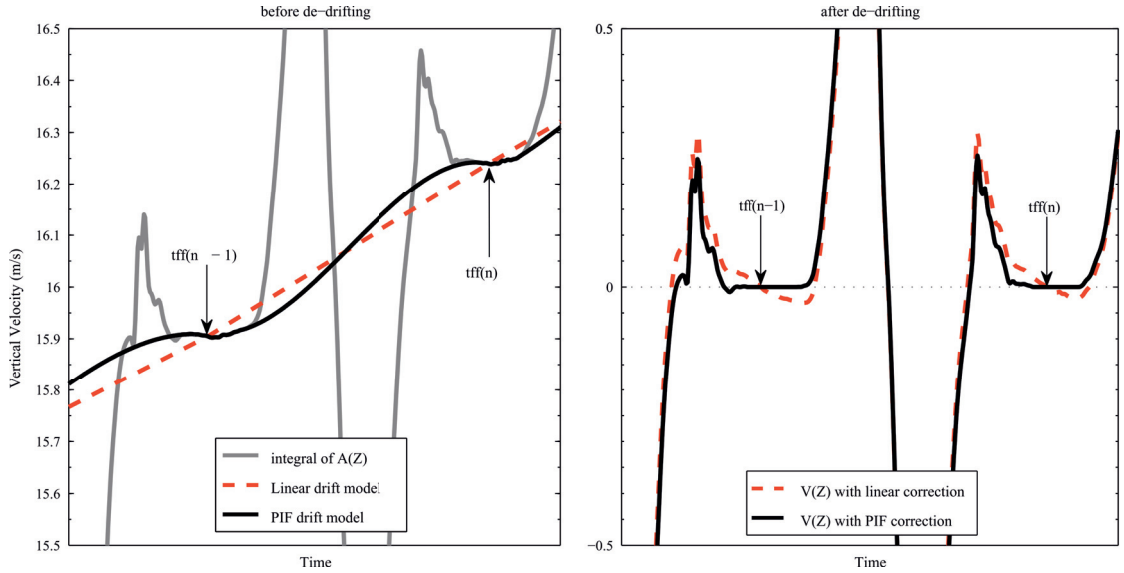


Figure 2.26 – Improved velocity drift model (black line) proposed by Mariani et al. (2010). This model allowed to model velocity drift differently during motionless and in-motion instants of time. Figure taken from Mariani et al. (2010).

Such motionless instants are only present for sensors fixed to a person's feet. Therefore, other procedures have been proposed to estimate velocity and distance for sensors fixed to segments with no motionless phases. Similar to orientation, analytical integration of measured acceleration in the Fourier domain can be used for obtaining a drift-free velocity and position estimation (Sabatini et al., 2015). Initial conditions were defined during a static posture at the beginning of the measurements. Acceleration signals were de-trended (i.e. zero mean acceleration over a gait cycle) prior to computing the Fourier series (Ramsay, 2006). Therefore, only velocity and position variations within a gait cycle (i.e. relative speed and position change) could be determined. They assessed the method based on an inertial sensor fixed to the lower back and treadmill walking at

different speeds. Limits of agreements were below 30 mm for the relative displacement along each axis.

Another method to estimate speed for cyclic movements without integration is to find a mapping between acceleration features and speed during a learning process and then apply this mapping to new data. Dadashi et al. (2013b) used this concept for estimating the cycle speed for front-crawl swimming. Using a Gaussian process regression, five acceleration features for each swimming cycle were mapped to reference cycle speed obtained with a tethered speedometer. Twenty swimmers were recruited for the study and randomly separated into two groups of ten swimmers. The first group was used to train the model, and the second group to test the model. An average cycle speed precision of 0.07 m/s was reported and cycle speed was underestimated on average by 0.01 m/s.

Finally, for outdoor applications global navigation satellite systems (GNSS) were used as aiding sensors for correcting velocity and position drift. Drift was corrected with frequent (at least 1 Hz) updates of velocity and position obtained from low-cost or differential GNSS, usually in a Kalman-filter design (Blumenbach, 2004; Brodie et al., 2008; Foxlin, 2005; Roetenberg et al., 2013; Supej, 2010). Other applications were presented for pedestrian localization but were based on the same fusion principle (Anacleto et al., 2014; Grewal et al., 2013; Godha et al., 2006). In many of these applications, inertial sensors were used as a means to handle GNSS outages rather than using GNSS to correct velocity and position drifts.

2.4 Conclusion

This brief literature overview presented the most common methods for estimating and correcting orientation, velocity, and position drifts for human movement analysis. The presented methods were most of the time designed for analyzing walking movement. There exist systems based on single sensors or based on a combination of multiple sensors fixed to different body segments. The systems were generally validated for slow movements and in laboratory conditions even if the goal of most systems was to use the systems outside the lab, in a partly or fully uncontrolled environment. Under the validated conditions, most systems showed a good precision and accuracy and could be used for biomechanical analyses.

However, little to no work was published for more complex and highly dynamic movements taking place outside the sagittal plane. Some studies even explicitly stated that their method might not provide accurate results for movements with high accelerations or for movements outside the sagittal plane. Except for one study (Jakob et al., 2013), drift correction capabilities for fast movements were not validated.

Thus, up to today, it is not clear whether the existing concepts could also be applied to fast movements and movements with high variability such as present in sports and other outdoor activities (e.g. walking). The following chapters of this thesis will take

these existing drift correction concepts, improve and redesign them so that they can be applied to other activities than gait analysis. Static drift correction constraints have been used to correct orientation and velocity drift during classical cross-country skiing and ski mountaineering based on ski-fixed inertial sensors. Biomechanical constraints and kinematic chains were used to correct orientation and position drift for alpine ski racing based on inertial sensors fixed to the lower limbs, trunk, and head. Finally, drift-free speed estimates were obtained for outdoor walking in various environments based on a single accelerometer worn on the wrist.

Static Drift Correction Part II

3 Spatio-Temporal Analysis of Classical Cross-Country Skiing

Abstract

The present study proposes a method based on ski fixed inertial sensors to automatically compute spatio-temporal parameters (phase durations, cycle speed and cycle length) for the diagonal stride in classical cross-country skiing. The proposed system was validated against a marker-based motion capture system during indoor treadmill skiing. Skiing movement of ten junior to world-cup athletes was measured for four different conditions. The accuracy (i.e. median error) and precision (i.e. interquartile range of error) of the system was below 6 ms for cycle duration and ski thrust duration and below 35 ms for pole push duration. Cycle speed precision (accuracy) was below 0.1 m/s (0.005 m/s) and cycle length precision (accuracy) was below 0.15 m (0.005 m). The system was sensitive to changes of conditions and was accurate enough to detect significant differences reported in previous studies. Since capture volume is not limited and setup is simple, the system would be well suited for outdoor measurements on snow.

Keywords: cross-country skiing, diagonal stride, inertial sensors, phase detection, spatio-temporal parameters

3.1 Introduction

Design of new materials and techniques, as well as the increasing number of persons practicing cross-country (XC) skiing ask for better methods to study the biomechanics of this sport (Bilodeau et al., 1992; Nilsson et al., 2004; Stöggl et al., 2008b, 2011). Easier quantification of the XC skiing movement under various conditions would be helpful in reducing risks for injury and improving training, performance, or materials. Prior research about the diagonal stride, a major technique in classical XC skiing (Lindinger et al., 2009), has shown that spatio-temporal analysis is essential for providing an overall description of the movement and, like for gait analysis (Perry and Burnfield, 2010), it constitutes an essential basis for more complex analyses, such as energy consumption or kinematic determinants (Mognoni et al., 2001; Stöggl and Müller, 2009; Stöggl et al., 2007). While the relevance of spatio-temporal parameters, including speed, cycle length, duration of the gliding, recovery and polling phases, and ratio between phase durations (see Fig. 1 for phase definitions), is admitted (Bilodeau et al., 1992; Lindinger et al., 2009; Nilsson et al., 2004; Stöggl and Müller, 2009; Stöggl et al., 2011; Vähäsöyrinki et al., 2008), these parameters are mainly measured during indoor treadmill skiing using complex instrumentation (e.g., marker-based motion capture system and force sensors). Outdoor skiing was mainly analyzed using video-based systems (Andersson et al., 2014; Bilodeau et al., 1992, 1996; Lindinger et al., 2009; Nilsson et al., 2004) or force measurement systems (Ohtonen et al., 2013; Stöggl et al., 2008a, 2010). These specific setups only available in few research centers worldwide limits the analysis to a small number of athletes, therefore the need for simpler systems allowing XC skiing movement analysis in-field. Such systems would be useful not only for research but also for recreational practitioners with probable benefits for performance and safe training. Easy-to-use sports tracking and training devices could stimulate physical activity and possibly contribute to better general health (Hottenroot and Urban, 2011).

A convenient solution for in-field measurement is the use body worn sensors (Aminian, 2006). Wearable inertial sensor-based systems were first introduced for spatio-temporal gait analysis (Aminian et al., 2002; Sabatini et al., 2005). Inertial measurement units (IMUs) have also been described for spatio-temporal analysis in a variety of sport disciplines, including running (Lee et al., 2010), swimming (Dadashi et al., 2013a, 2012), jumping (Dowling et al., 2011), ski jumping (Chardonens et al., 2012, 2014) and the skating technique for XC skiing (Myklebust et al., 2014). Accelerometer signals were used to classify skating technique based on visual inspection (Marsland et al., 2012) or machine learning techniques (Stöggl et al., 2014). No study proposed and validated an inertial-sensor based system for a spatio-temporal analysis of the skiing movement. This review suggests that it could be possible to design algorithms to quantify the spatio-temporal characteristics of the diagonal stride in classical XC skiing using a combination of inertial sensors distributed on the equipment.

By hypothesizing that diagonal stride involves some temporal events that could be detected using inertial sensors, the objective of this study was to design an easy-to-wear

system and a method to detect key temporal events and compute cycle speed and length for the diagonal stride in XC skiing. The validity of the proposed system and methods has been investigated during skiing on a treadmill by using a standard motion capture system as reference. Measurements were performed at different speeds and slope inclinations to evaluate the sensitivity to changes of the proposed system with skiing conditions.

3.2 Methods

3.2.1 Definition of the diagonal stride events and phases

The diagonal stride is a periodic movement, split into cycles starting and ending with the plant of the left pole (Fig. 3.1) (Bilodeau et al., 1992). During a cycle, the arm movement is further subdivided into poling and swing phases and the leg movement into thrust, recovery and gliding phases. The poling is the period during which the pole is in contact with the ground, whereas the swing corresponds to the period during which the pole performs a swing movement forwards without touching the ground. The leg thrust is defined as the period during which the ski is being pushed on the ground and does not slide forwards or backwards. Still according to Bilodeau et al. (1992), the recovery follows the thrust phase and lasts until the two feet come closest together. Finally, the remaining time between the end of the recovery and the beginning of the next thrust is the gliding phase. Cycle length is defined as the distance travelled during a complete cycle and cycle speed is defined as the cycle length divided by the cycle duration (Bilodeau et al., 1996).

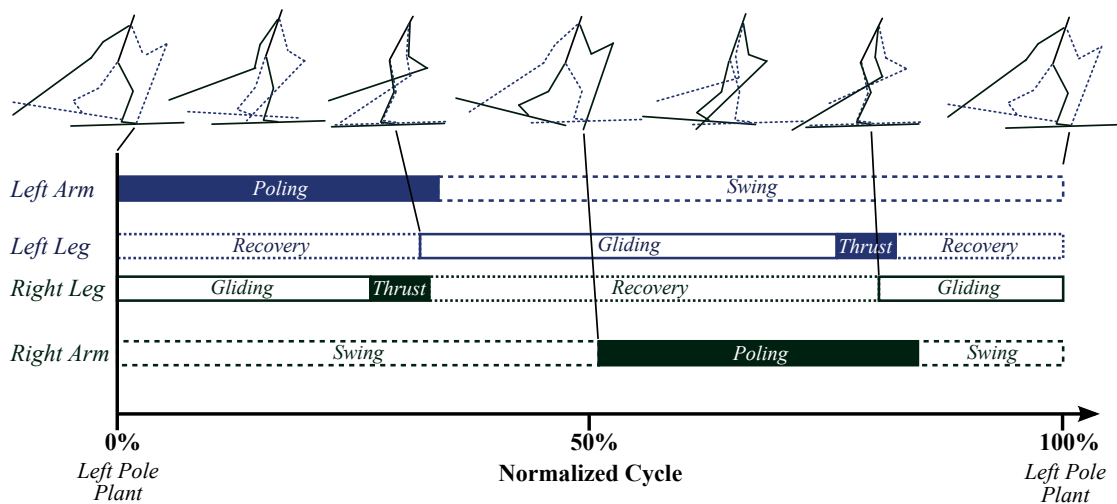


Figure 3.1 – The main temporal phases in diagonal stride. The arm movement is divided into two phases, poling and swing. The leg movement is divided into three phases, thrust, recovery, and gliding. A cycle is defined to start at the left pole plant and to end at the subsequent left pole plant.

3.2.2 Measurement protocol

Ten junior to world cup athletes (4 men and 6 women, 19.6 ± 5.6 years, 170 ± 8 cm, 61 ± 8 kg) were tested after providing IRB-approved written consent to compare the spatio-temporal parameters of the IMU-based system to the reference parameters. They were asked to ski the diagonal stride on treadmill (Saturn 250/100, h/p/cosmos, Germany, belt dimension 250 cm \times 100 cm) with their own classic roller skis. During the entire measurement the athletes were secured with a safety harness connected to the emergency stop. After a warm-up period, four conditions of approximately two minutes each were recorded: flat at low speed (3% inclination, 2.5 m/s), flat at medium speed (3% inclination, 3.1 m/s), uphill at low speed (8% inclination, 1.8 m/s) and uphill at medium speed (8%, 2.6 m/s). The speeds were selected rather low to avoid signal perturbations by athletes struggling to keep up with the speed. Each subject wore two IMUs (Physilog III, Gait Up, Switzerland) fixed to the left roller ski in front of the binding and to the left pole below the hand (Fig. 3.2a). Each IMU was composed of a 3-axial accelerometer (± 11 g), 3-axial gyroscope (± 1200 deg/sec), and a data logger sampling at 500 Hz, for a total weight of 36 grams each. An external trigger was used to start and stop the IMUs, which were synchronized wirelessly. The sensors were calibrated following a standard procedure (Ferraris et al., 1995). Gravity measured during a static recording and the principal component of ski acceleration during skiing was used to align the ski sensor with the ski-embedded frame (Chardonens et al., 2013). The superior axis (y) was perpendicular to the ski outsole. The anterior axis of the ski frame (x) pointed forwards and the medial axis (z) was the cross product of the two other axes (Fig. 3.1b) (Dadashi et al., 2012). No procedure was done to align the pole IMU to a particular frame.

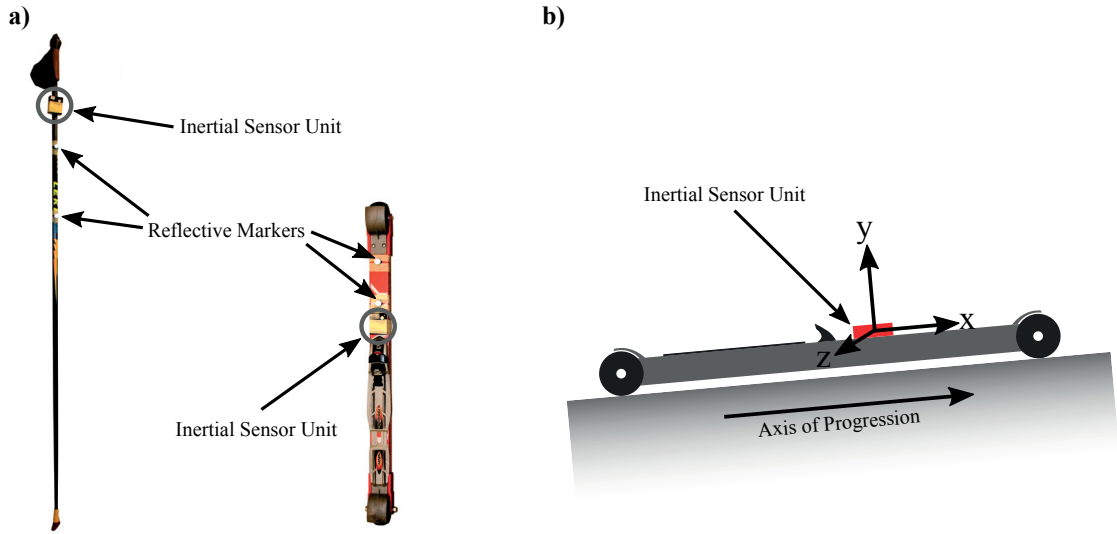


Figure 3.2 – Setup and inertial sensor axes. a) Sensor configuration and marker placement. In total two inertial sensor units and four reflective markers have been fixed to the left pole and left roller ski. Two additional markers were placed on the right roller ski. b) Inertial sensor axes of the ski sensor after functional calibration. The x-axis (anterior-posterior axis) is parallel to the axis of progression.

3.2.3 Reference System

A reference system consisting of a marker-based motion capture system with nine infrared cameras (Vicon Peak, Oxford, United Kingdom) sampling at 200 Hz was used to measure the trajectory of two markers placed along the anterior-posterior axis of both skis and two markers fixed on the top of the left pole (Fig. 3.2a). An electronic circuit was used to synchronize IMUs with the reference system. Prior to the measurements, the distance of the pole markers to the pole tip was measured, allowing the calculation of the trajectory of the pole tip. Three additional markers placed on the left and right anterior-posterior edges of the treadmill belt were used to determine the treadmill plane. Following definitions in prior literature (Bilodeau et al., 1992; Nilsson et al., 2004), Table 1 describes the criteria used for detecting the temporal events based on marker trajectories and Fig. 3.3(a, b) provides an illustration of these definitions. Thresholds for detecting ski thrust start and stop were determined empirically, optimized on visual inspection of a large set of acceleration and velocity curves, and were hard coded in the algorithm. The phase durations were defined as the time difference between the start and end of each phase (Fig. 3.1). The relative instantaneous ski speed and inertial acceleration was obtained by derivation of the position of the roller skis along the progression axis (i.e., the anterior axis parallel to the surface of the treadmill). To be consistent with the speed calculated with the IMU-based system, the treadmill velocity was added to the relative instantaneous ski speed, thus describing the actual speed. The cycle duration

Chapter 3. Spatio-Temporal Analysis of Classical Cross-Country Skiing

was obtained based on the time separating two pole plants (Bilodeau et al., 1996; Nilsson et al., 2004). The cycle speed was obtained by averaging this variable over each cycle, and the cycle length by multiplying the cycle speed with the cycle duration.

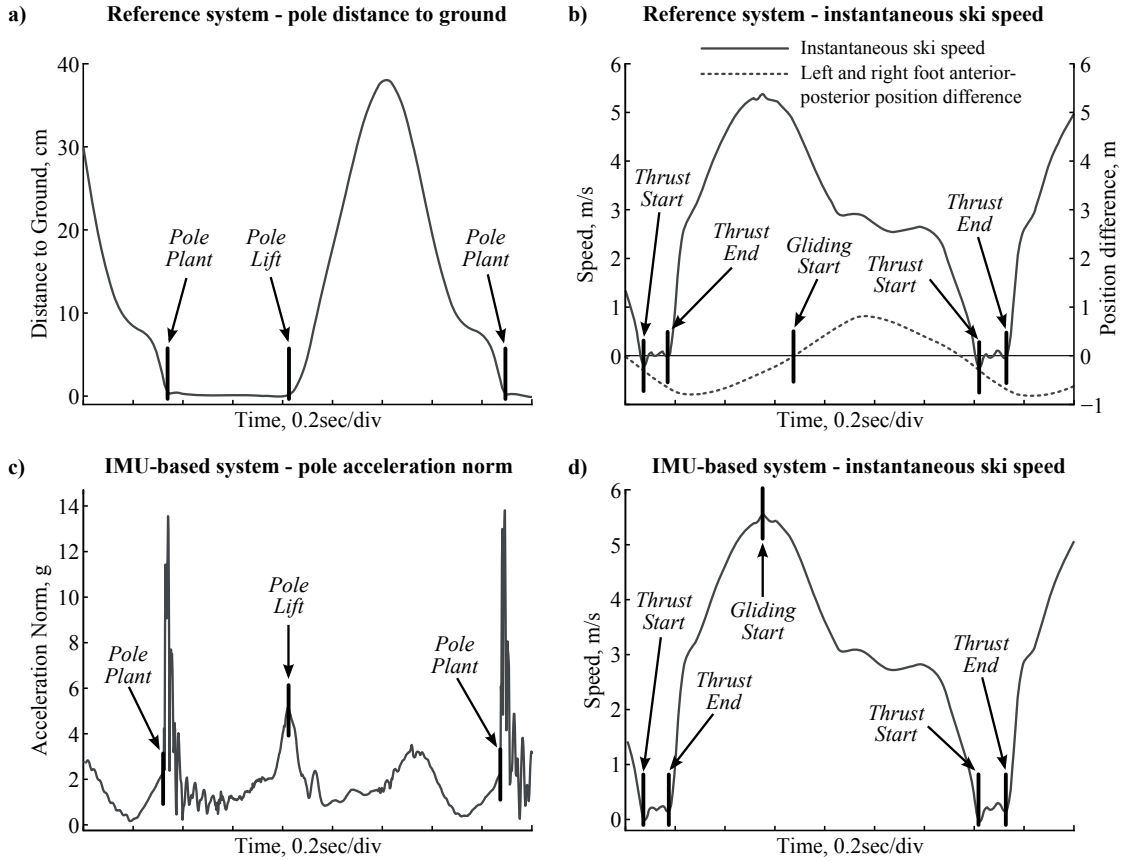


Figure 3.3 – Event detection showed on example curves. a) The pole distance to the ground recorded by the reference system. b) Solid line: the instantaneous ski speed obtained by differentiation of the ski's position measured by the reference system. Dashed line: the anterior-posterior position difference between the two feet computed from the ski positions recorded with the reference system. c) The pole acceleration norm recorded by the IMU-based system. d) The instantaneous ski speed computed using the IMU-based system.

3.2.4 Pole event detections by IMU

The occurrence of the pole events (plant and lift) was detected using the acceleration measured by the IMU fixed to the pole (Fig. 3.3c, Table 3.1): pole plants are characterized by vibrations from the pole's mechanical response of the pole plant; pole lifts are marked by an acceleration peak caused by the sudden velocity increase during pole lift. First, the maxima of the vibration patterns in the acceleration norm were detected using an envelope technique (Shiavi, 2007). Second, the windowing method in Jasiewicz et al.

Event	Biomechanical definition	IMU-based system	Reference system
Pole Plant	First contact of the pole on the ground	Start of shock pattern in the pole acceleration norm	First time the distance between the pole tip and the ground is below a predefined threshold indicating contact with the ground
Pole Lift	Terminal contact of the pole on the ground	Peak in pole acceleration norm between two successive pole plants	Last time the distance between the pole tip and the ground is below a predefined threshold indicating contact with the ground
Thrust Start	Start of the ski being pushed on the ground to thrust the athlete forwards	First time instantaneous ski speed and inertial acceleration are below small predefined thresholds and remain so for several samples	First time instantaneous ski speed and acceleration are below small predefined thresholds and remain so for several samples
Thrust End	Start of the ski being pushed on the ground to thrust the athlete forwards	Last time instantaneous ski speed and inertial acceleration are below small predefined thresholds and have remained so for several samples	Last time instantaneous ski speed and inertial acceleration are below small predefined thresholds and have remained so for several samples
Gliding Start	Switch between passive (recovery) and active leg forward swing and gliding movement	Maximum instantaneous ski speed between two successive thrust phases	Instant of minimum anterior-posterior distance between left and right skis

Table 3.1 – Event definitions for the IMU-based system (based solely on the signals measured by the IMUs) and the reference system (only based on the marker trajectories measured by the camera-based system).

(2006) was used to search for the start of the vibrations in the acceleration norm within search windows limited to 100 ms before each maximum detected in the first step. Third, pole lifts were identified by searching for the local maximum in the pole acceleration norm between two successive pole plant events. Cycle duration was defined as the time between two consecutive pole plants.

3.2.5 Estimation of spatio-temporal parameters for the ski IMU

To determine the instantaneous speed the orientation of the ski IMU was calculated for each cycle by fusing accelerometer and gyroscope signals (Favre et al., 2006; Rouhani et al., 2012). Drift was corrected during thrust phases where the ski IMU's accelerometer served as an inclinometer as the ski is moving at a constant speed, thus only measuring gravity. The ski-inclination was used to remove the gravity and project the measured acceleration onto the progression-axis (x). The instantaneous speed was obtained by trapezoidal integration of the this inertial acceleration followed by a drift correction assuming zero-velocity during the ski thrust phase (Mariani et al., 2010; Sabatini et al., 2005). Once the instantaneous speed calculated, the cycle speed was obtained by averaging this variable over each cycle, and the cycle length by multiplying the cycle speed with the cycle duration.

Thrust phase detection was improved based on the inertial acceleration and instantaneous velocity of the ski (Fig. 3.3d, Table 3.1) obtained by IMUs. The ski gliding starts were defined as the local maxima of the instantaneous skiing velocity between two successive thrust phases. We hypothesized that these maxima mark the start of the ski gliding movement during which the ski is a) passively slowed down due to the friction and b) actively slowed down by the muscles to prepare for the subsequent ski thrust. The phase durations were defined as the time difference between the start and end of each phase.

3.2.6 Data analysis

First, the differences between the occurrence of the temporal events (Table 3.1) detected by the proposed IMU-based system and the reference system were computed. Second, the duration of the five phases as well as the cycle speed and length of both systems was compared. Data was checked for normality using the Lilliefors test at significance level of 1%. Since normality could not always be assumed the differences between IMU-based and reference systems were reported using median and interquartile range. Later, these metrics are referred to as accuracy and precision, respectively, as in Chardonens et al. (2012). Relative errors were computed with respect to the reference values. To assess the sensitivity of the IMU-based system to changes between skiing conditions, the parameters were compared among the four conditions using Kruskal-Wallis and Wilcoxon signed rank tests with significance level set to 1% and Bonferroni correction for multiple comparisons. These comparisons were done separately for both systems and the differences among the

four conditions identified by the IMU-based system were compared to the differences obtained with the reference system using Cohen’s d (Cohen, 1988).

3.3 Results

A total of 1200 cycles (10 athletes \times 4 conditions \times 30 cycles per condition) were obtained for analysis. The IMU-based method described above resulted in robust and automatic (i.e., without operator intervention during data processing) detection of the five events. The ski thrust start and end were detected with accuracies of less than 6 ms and pole plant and lift with accuracies below 15 ms (Table 3.2). Precision was below 6 ms for these four events except pole lift (26 ms). The results were less satisfactory with the ski gliding start, which had both a lower accuracy of -94 ms and a lower precision of 64 ms.

Event	Absolute Error, ms		Relative Error, % cycle duration	
	Accuracy	Precision	Accuracy	Precision
Pole plant	-12	6	-1.8	0.7
Pole lift	14	26	2.0	3.8
Ski gliding start	-94	64	-12.5	9.2
Ski thrust start	2	4	0.3	0.6
Ski thrust end	6	6	0.8	0.9

Table 3.2 – Absolute and relative errors for the detection of the event occurrences. The accuracy (median) and precision (interquartile range) were calculated based on 1200 individual cycles. The relative errors have been computed with respect to the cycle duration obtained with the reference system. The time resolution of the reference system was 5 ms (200 Hz sampling rate).

Parameter	Range	Absolute Error		Relative Error, % of reference parameter value	
		Accuracy	Precision	Accuracy	Precision
Cycle duration, ms	1179 - 1939	-0.26	5.93	-0.02	0.38
Cycle speed, m/s	1.63 - 3.50	0.0048	0.0993	0.21	3.96
Cycle length, m	2.38 - 5.16	0.0048	0.1466	0.16	4.09
Ski thrust duration, ms	60 - 408	2	4	1.39	3.08
Pole push duration, ms	354 - 940	28	32	4.70	5.54
Ski gliding duration, ms	620 - 974	96	65	12.31	8.84
Ski recovery duration, ms	380 - 664	-98	66	-19.19	14.51

Table 3.3 – Parameter range, absolute and relative errors for the spatio-temporal parameters. The accuracy (median) and precision (interquartile range) were calculated based on 1200 individual cycles. The relative errors have been computed with respect to the value obtained with the reference system. The time resolution of the reference system was 5 ms (200 Hz sampling rate).

Chapter 3. Spatio-Temporal Analysis of Classical Cross-Country Skiing

Parameter	flat, slow	flat, medium	uphill, slow	uphill, medium
	Absolute error: accuracy (precision)			
Cycle duration, ms	0.67 (5.09)	-0.36 (4.56)	-0.18 (6.93)	-0.32 (5.99)
Cycle speed, m/s	0.0246 (0.0466)	0.1175 (0.0523)	-0.0306 (0.0667)	-0.0267 (0.0477)
Cycle length, m	0.0336 (0.0744)	0.1572 (0.0779)	-0.0481 (0.1040)	0.0427 (0.0782)
Ski thrust duration, ms	2 (4)	4 (4)	0 (6)	4 (4)
Pole push duration, ms	20 (32)	28 (22)	28 (37)	32 (28)
Ski gliding duration, ms	110 (63)	93 (62)	90 (71)	86 (67)
Ski recovery duration, ms	-110 (64)	-96 (62)	-90 (70)	-93 (68)

Table 3.4 – Absolute errors for all parameters partitioned into conditions. The accuracy (median) and precision (interquartile range) were calculated based on 300 individual cycles per condition. The time resolution of the reference system was 5 ms (200 Hz sampling rate).

Absolute and relative errors of the temporal parameters are given in Table 3.3 and 3.4. The cycle duration and duration of the ski thrust phase were the most accurate ($<1.4\%$) and precise ($<3.1\%$), whereas the duration of the ski gliding and recovery phases were the least accurate ($<19.2\%$) and precise ($<14.5\%$). Accuracy approached zero when positive and negative errors of individual cycles cancelled each other. An example curve comparison between the wearable and reference system is shown in Fig. 3.4. It can further be seen that the drift was well corrected, supported by the cycle speed and length accuracy of 0.005 m/s and 0.005 m ($<1\%$) and precision of 0.099 m/s and 0.147 m (both 4%), respectively. Errors for the ski gliding and recovery phases and for the spatial parameters showed a dependency on the condition: errors on temporal phases decreased and errors on cycle speed and length increased at higher speeds (Table 3.4).

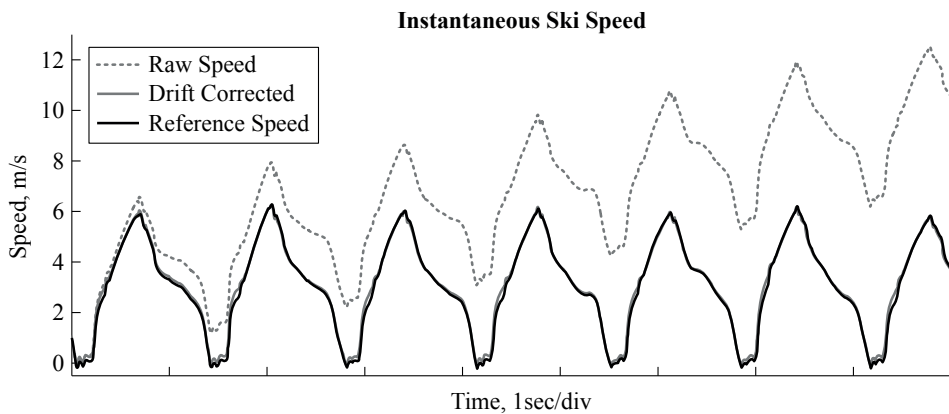


Figure 3.4 – Instantaneous ski speed for the raw speed before (dashed line) and after (gray solid line) drift correction, and for the reference speed (black line).

The values of the seven spatio-temporal parameters measured by both systems are reported for each condition in Fig. 3.5. For all significant differences between conditions reported using the IMU-based system, the reference system showed the same significant differences (same order of magnitude of Cohen's d). However, in three condition comparisons, the IMU-based system was not able to report the significant differences detected by the reference system: ski recovery, cycle speed and pole push (i.e. false negative). On the other hand, the IMU-based system did not detect any differences between conditions that were not present in the reference system (i.e., false positive).

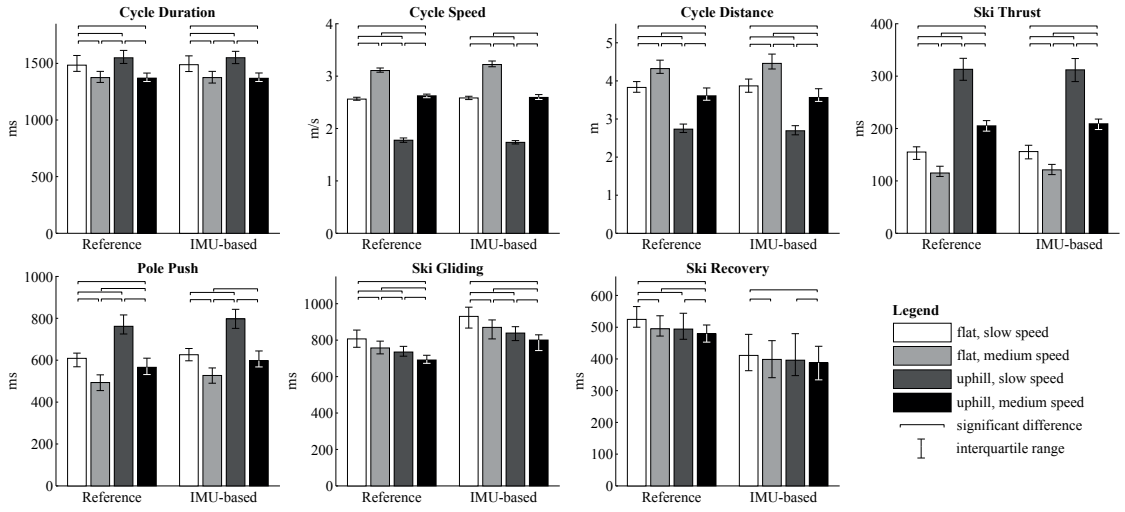


Figure 3.5 – Parameter values of the reference and IMU-based system. The height of the bars is the median parameter value computed based on 300 cycles. The interquartile range is shown with the whiskers and the horizontal lines represent significant differences ($\alpha = 1\%$)

3.4 Discussion

The results obtained in this study confirmed our hypothesis that the IMU-based system was able to successfully detect the different ski and pole events for all conditions. Cycle, ski thrust and pole push durations were measured with a very low error. Similarly, spatial parameters showed very good accuracy and precisions with relative errors below 5%. Vähäsöyrinki et al. (2008) reported group differences in the order of 20 ms between ski thrust, pole push and skiing speed. Nilsson et al. (2004) found even larger differences of approximately 100 ms and 200 ms ski thrust and pole push durations between slow and fast speed, respectively. These differences are of the same order of magnitude or larger than the IMU-based system's precision and accuracy. Therefore, the proposed system is sensitive enough and would be able to detect the same group differences. Stöggl and Müller (2009) measured kinematic parameters across different inclines at constant skiing velocity. For one degree of slope inclination increase they reported a

Chapter 3. Spatio-Temporal Analysis of Classical Cross-Country Skiing

cycle length decrease of about 0.2 m. Similar differences were reported between different skiing speeds (Vähäsöyrinki et al., 2008). They measured skiing speed differences of over 0.5 m/s between different self-selected skiing speeds at 65%, 75%, 90%, and 100% of their maximum performance. The proposed system's accuracy and precision was up to five times better than the above reported differences. Therefore, it is also valid to use for measuring performance or terrain related differences for the spatial parameters.

While having a high sensitivity, accuracy and precision, the proposed system is not only restricted to its use for in-lab conditions. It could be used for both indoor and snow conditions with unlimited capture volume. The proposed system could be used to measure entire runs over several kilometers. It would be an ideal tool to investigate the influence of terrain (e.g. slope angles, snow condition) and fatigue on the skier's movement. As the parameters are recorded cycle-by-cycle it would be possible to use the proposed system to relate inter-cycle variability of spatio-temporal parameters to fatigue as proposed for angular displacements (Cignetti et al., 2009).

Ski gliding and ski recovery durations showed a much higher error, for both accuracy and precision. Especially for the ski recovery duration, the proposed system was not as sensitive to change as the reference system. The main reason for these large errors was a different definition of ski gliding start event: Whereas the reference system used the anterior-posterior position difference of the left and right foot, the IMU-based system considered the instant of maximum instantaneous skiing velocity as the ski gliding start. These two events showed a systematic difference of 0.1 sec on average, which explains the large accuracy of both ski recovery and gliding phases. If the systematic error is confirmed with a larger sample size and higher skiing speeds, the event's accuracy could be improved by shifting each ski gliding start event by this systematic error. The large precision values indicate that the two events were not well correlated. It seems that the time difference between both events was also dependent on skiing speed (better accuracy for ski gliding and recovery duration at higher speeds, Table 3.4). This could be a hint for an altered coordination of the athlete's ski movement depending on the speed. With respect to performance it is believed that a longer recovery phase coupled with short but very intensive thrust durations characterizes a more efficient and less tiring movement (Lindinger et al., 2009; Stöggl et al., 2011). More measurements are needed in order to explain the role of the recovery and gliding phase durations as measured in the present study. It would be interesting to compare the phases of the IMU-based system with the phases defined using force data, as presented in Vähäsöyrinki et al. (2008). Both systems together would allow a comprehensive analysis for both kinematics and kinetics of the diagonal stride.

It has to be emphasized that the skiing speeds in this study were very low compared to other studies on treadmill (Stöggl and Müller, 2009; Stöggl et al., 2007; Vähäsöyrinki et al., 2008) in order to ensure a proper skiing movement for the purpose of a technical validation. Despite the low speeds tested the method provides a powerful way for event detection and measurement of the skiing phases. We do not expect much larger errors for the ski thrust and pole push durations at medium to high speeds (>3.5 m/s) as the

system's accuracy and precision were of the same order of magnitude for different skiing speeds and did not seem to be affected by vibrations of the treadmill. However, for higher speeds the IMU-based system showed an overestimation of the cycle speed and cycle lengths. Further tests should be performed at medium to high speeds in order to obtain a complete system assessment. A differential GNSS (Supej et al., 2013) could be used as reference system for accurate speed and distance measurements during outdoor skiing. Only the left side has been analyzed. The same algorithms could be used to measure the movements of both the left and right sides by placing additional sensors to the right ski and pole. This would allow investigating asymmetries and inter-coordination. The proposed system could be used to detect the pole push phases and cycle durations for the other classic and skating styles as the same pole plant and pole lift events are present. Extending the current algorithm to ski events and computing spatial parameters may be possible but needs new algorithms as the movement of the skis cannot anymore be simplified to a two-dimensional movement with frequent motionless moments (instants of time).

In conclusion, based on adequate signal processing of IMU sensors, this study introduced an easy-to-use system to measure the spatio-temporal parameters in diagonal stride XC skiing. While the system has been validated inside a laboratory it could be used in field to provide an efficient tool to study the biomechanics of XC skiing. Preliminary test measurements on snow showed very similar signals. However, further measurements on snow are necessary to confirm the system's validity. A major advantage is its usability: the athletes themselves can set up the sensors in less than five minutes and data analysis is fully automatic. Moreover, manufacturers could integrate the IMUs in the poles and skis. Considering outdoor usage, this new system could be very useful for a variety of applications ranging from basic research on performance, fatigue, training to personal coaching (Dowling et al., 2012).

Acknowledgements

The authors thank the cross-country skiing athletes and coaches involved in this study and the sports institute of the University of Lausanne, Switzerland, for allowing using their treadmill. The study was supported by the "Département de l'appareil locomoteur" of the University Hospital of Lausanne (CHUV).

4 Spatio-Temporal Analysis of Ski-Mountaineering

Abstract

In this study an algorithm designed for the diagonal stride in classical cross-country skiing was adapted to compute spatio-temporal parameters for uphill ski mountaineering using a ski-fixed inertial sensor. Cycle duration, thrust duration, cycle speed, cycle distance, elevation gain, and slope angle were computed and validated against a marker-based motion capture system during indoor treadmill skiing. Skiing movement of 12 experienced, recreational level athletes was measured for nine different speed and slope angle combinations. The accuracy (i.e. mean error) and precision (i.e. standard deviation of the error) were below 3 ms and 13 ms for the cycle duration and thrust duration, respectively. Accuracy \pm precision for cycle speed, cycle distance and elevation gain were $-0.013 \text{ m/s} \pm 0.032 \text{ m/s}$, $-0.027 \text{ m} \pm 0.018 \text{ m}$, and $0.006 \text{ m} \pm 0.011 \text{ m}$, respectively. Slope angle error was $0.40 \text{ deg} \pm 0.32 \text{ deg}$, respectively. If the cross-country skiing algorithm would be used without adaptations, errors would be up to one order of magnitude larger. The adapted algorithm was shown to be valid for measuring spatio-temporal parameters for ski-mountaineering on a treadmill. It is expected that the algorithm would show similar performance on snow.

Keywords: ski mountaineering, ski touring, inertial sensors, phase detection, spatio-temporal parameters

4.1 Introduction

In contrast to cross-country skiing the slopes in ski-mountaineering are steeper, both uphill and downhill. Therefore, during climbing the skis are equipped with adhesive skins to prevent sliding backwards. Several studies investigated energy expenditure during ski-mountaineering races (Duc et al., 2011; Praz et al., 2014; Tosi et al., 2009, 2010). Energy expenditure was estimated from measured oxygen consumption (Duc et al., 2011; Tosi et al., 2009, 2010) or with a model estimating oxygen consumption from heart rate (Praz et al., 2014). Another study investigated exercise intensity based on heart rate (Schenk et al., 2011). These studies found that age, body mass, gear mass, aerobic capacity and efficiency were significantly correlated with climbing performance. However, it is unknown if certain biomechanical features are associated with performance. The objective of this study was to propose a ski-fixed inertial sensor system to automatically quantify spatio-temporal parameters of ski-mountaineering such as cadence, speed, and slope angle. Ski-mountaineering movement resembles the cross-country diagonal stride skiing movement but is slower, lacks the gliding phase and has a longer ski push duration. Thus, the algorithm designed originally for the diagonal stride of classical cross-country skiing (Chapter 3) was adapted to uphill ski-mountaineering to extract the relevant spatio-temporal parameters. The algorithm was validated against a 3D camera reference system while simulating ski-mountaineering with roller skis on a treadmill.

4.2 Methods

4.2.1 Protocol

The study protocol was approved by the Valais research ethics committee (CCVEM 033/11). Each participant gave informed written consent prior to participating to the study. 12 experienced, recreational level athletes were enrolled to the study. The measurement was performed indoors on a treadmill (Saturn 250/100, h/p/cosmos, Germany, belt dimension 250 cm \times 100 cm) using forward-only cross-country roller skis with bindings adapted for ski-mountaineering boots and normal ski-mountaineering poles fitted with a rubber stop at the extremity. Each athlete used their own, regular ski-mountaineering boots. A familiarization session a few days prior to data recording was organized for each athlete. After an individual warm-up each athlete performed the nine trials listed in Table 4.1 in randomized order. Each trial was performed for 3 minutes. No instructions were given with respect to skiing style.

4.2.2 Materials

A small inertial measurement unit (Physilog III, Gait Up, Switzerland) measuring 3D acceleration and angular velocity at 500 Hz was attached to the left ski, in front of the

Label	Slope	Speed
Flat, slow	5.71°	1.11 m/s
Flat, medium	5.71°	1.39 m/s
Flat, fast	5.71°	1.67 m/s
Medium, slow	9.65°	0.83 m/s
Medium, medium	9.65°	1.11 m/s
Medium, fast	9.65°	1.39 m/s
Steep, slow	13.5°	0.56 m/s
Steep, medium	13.5°	0.83 m/s
Steep, fast	13.5°	1.11 m/s

Table 4.1 – Measured skiing conditions, values as entered in the treadmill control computer. 5.71° corresponds to 10% inclination, 9.65° corresponds to 17% inclination, and 13.5° corresponds to 24% inclination.

binding. Additionally, two reflective markers were placed on the ski aligned with its longitudinal axis (Fig. 4.1). The marker positions were recorded at a sampling rate of 200 Hz with an optical motion capture system consisting of seven infrared cameras positioned around the treadmill (Vicon Peak, Oxford, United Kingdom). The system was first calibrated and then electronically synchronized with the inertial measurement unit (IMU). Electronical synchronization was achieved by recording a synchronization pulse by the Vicon system and the IMU system simultaneously, at the start and end of each trial. The time offset and sampling rate of both systems were then adjusted so that the synchronization pulses recorded on both systems matched perfectly.

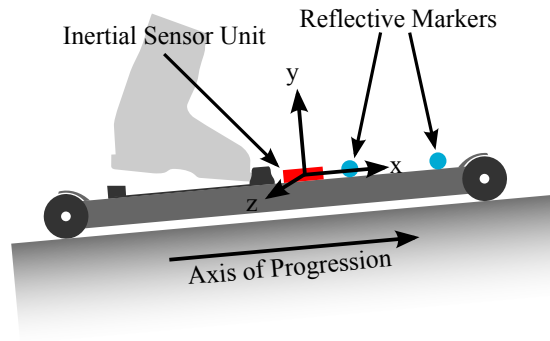


Figure 4.1 – Inertial measurement unit and reflective marker placement on the roller ski.

4.2.3 Definition of the parameters

The ski thrust phase was defined as the phase during which the ski was flat on the treadmill, not moving relative to the belt, as in Chapter 3. The start of the cycle was defined at the beginning of the ski thrust phase of the left leg and end at the beginning of the subsequent left ski thrust phase. Cycle speed was the average ski speed during one cycle. Cycle duration was the time difference between the two beginnings of the ski thrust phase. Cycle distance was the distance covered by the ski in one cycle. Elevation

gain was the vertical elevation gain from one cycle and the slope angle was the inclination of the slope surface.

4.2.4 Parameter computation with the inertial unit

The algorithm described in Chapter 3 was adapted for the movement of ski-mountaineering. The difference with regard to the cross-country skiing algorithm was adapted motionless detection and drift correction, since in ski-mountaineering the thrust phase is considerably longer than in diagonal stride cross-country skiing. The motionless detection in the proposed algorithm was based only on a threshold in skiing velocity (see below), whereas in the cross-country skiing algorithm the acceleration was used for detecting the motionless phase as well. Furthermore, for the current algorithm only the central 50% of the motionless period was used to estimate the drift for both ski orientation and speed.

In short, the adapted algorithm works as follows: after functional calibration, ski inclination with respect to gravity was computed using trapezoidal integration of the ski's medio-lateral angular velocity. The orientation drift was corrected using samples from the central 50% of each motionless ski thrust phase, approximately estimated based on the criterion of locally minimal skiing speed detected in the drift- and gravity-affected speed estimate obtained by integration of ski's forward acceleration. Second, knowing the ski's orientation, the earth's gravity was removed from the measurements and the inertial acceleration along the longitudinal axis of the ski (Fig. 4.2A) was integrated to obtain the instantaneous skiing speed (Fig. 4.2B). Third, speed drift was corrected using the previously estimated motionless phases. Fourth, the ski thrust phases were improved using an empirically selected threshold of 0.1 m/s on the instantaneous ski speed (Fig. 4.2B). All samples below this speed threshold were considered as belonging to the ski thrust phase.

The slope angle was estimated as the average ski inclination during each ski thrust phase. Cycle speed was the average instantaneous ski speed over one cycle. For the purpose of robustness and precision, the start of a cycle was defined as the peak of the forward ski acceleration after each motionless phase (Fig. 4.2A). Cycle duration was the time difference between two consecutive cycle starts. Cycle distance was the product of cycle speed and cycle duration. The elevation gain was computed as the product between the cycle distance and the sine of the slope angle.

For comparison the original cross-country skiing algorithm from Chapter 3 was applied to the ski-mountaineering dataset as well.

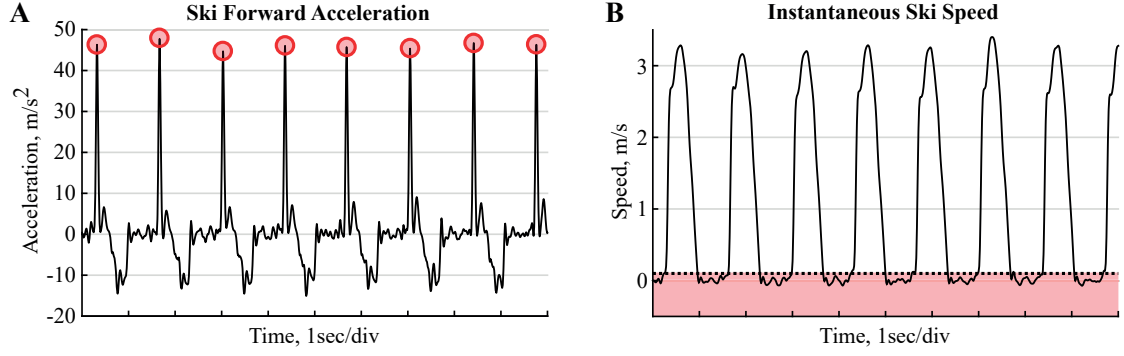


Figure 4.2 – Ski forward acceleration and speed obtained from the inertial sensor. A) Example curve of the unfiltered ski forward acceleration during 10 seconds of ski mountaineering. The cycle starts are marked with the red circles. Phases of zero acceleration correspond to the ski thrust phases. B) Example curve of the ski forward speed (same measurement as in A). The threshold for motionless is marked with the dashed line. The phases where the ski speed is in the red zone correspond to the ski thrust phases.

4.2.5 Reference parameter computation

The reference parameters for cycle duration, thrust duration, cycle speed, cycle distance and elevation gain were computed based on the ski markers' speed as determined with the motion capture system using the same method as for the IMU. The marker speed was obtained through numerical differentiation of the marker positions. Details are provided in Chapter 3. The reference slope angle was directly obtained from the treadmill.

4.2.6 Statistical analysis

For each trial t , the cycle-by-cycle difference between the IMU-based parameters and the reference parameters was computed for all cycles of the trial. Next, the mean difference (μ_t) and standard deviation (std) of the difference (σ_t) was computed for each trial. The algorithm's accuracy was defined as the mean of all μ_t . The algorithm's precision was defined as the mean of all σ_t . Relative accuracy and precision were defined identically where the cycle-by-cycle difference was normalized by the reference parameter value prior to computing any mean or standard deviation. Error dependency on trial condition (speed and slope) was assessed using Pearson's correlation coefficient on the cycle-by-cycle data.

4.3 Results

Valid data were obtained for 11 athletes. For one athlete the IMU did not work properly. Additionally, two trials had to be discarded because of missing synchronization. Thus,

Chapter 4. Spatio-Temporal Analysis of Ski-Mountaineering

Parameter	Reference		IMU mount.		Error mount.		Error cross-country	
	Mean	Std	Mean	Std	Accuracy (relative)	Precision (relative)	Accuracy (relative)	Precision (relative)
Cycle duration, ms	1574	322	1574	322	0.03 ^{aa,bb} (0.00%)	2.84 (0.18%)	0.11 ^{aa,bb} (0.03%)	45.60 (2.94%)
Thrust duration, ms	700	246	711	250	10.36 ^{a,b} (1.29%)	12.83 (2.05%)	-175.93 (19.03%)	35.38 (4.44%)
Cycle speed, m/s	1.15	0.32	1.14	0.33	-0.013 ^{a,bb} (-1.28%)	0.032 (2.75%)	-0.026 ^{a,b} (-2.73%)	0.036 (3.27%)
Cycle distance, m	1.74	0.34	1.72	0.35	-0.027 ^{bb} (-1.64%)	0.018 (1.04%)	-0.050 ^{a,b} (-3.08%)	0.056 (3.24%)
Elevation gain, m	0.28	0.08	0.28	0.07	0.006 ^{aa,bb} (2.82%)	0.011 (5.14%)	0.071 ^{aa,b} (27.35%)	0.034 (12.57%)
Slope angle, deg	9.58	3.20	9.98	3.27	0.40 ^{aa,bb} (4.46%)	0.32 (5.14%)	2.83 ^{aa,bb} (32.14%)	1.34 (14.32%)
Ski thrust start, ms	-	-	-	-	-0.64 ^{a,b}	2.98	15.13 ^{aa,bb}	11.58
Ski thrust stop, ms	-	-	-	-	9.72 ^{a,b}	12.70	-160.80	32.04

Table 4.2 – Reference and IMU average parameter values and errors. The IMU average parameter values were computed with the proposed ski mountaineering algorithm. Errors are provided for the proposed ski mountaineering algorithm (mount.) and with the original cross-country diagonal style algorithm (cross-country). Relative errors (normalized with respect to reference parameter value) are written in parentheses. Pearson’s correlation coefficient between error and slope <0.25 was marked with ^{aa} and with ^a when <0.5 . Similarly, Pearson’s correlation coefficient between error and speed <0.25 was marked with ^{bb} and with ^b when <0.5 .

97 trials were used for the validation. All cycles (N=10699) were successfully detected by the proposed algorithm. Table 4.2 gives an overview of the average parameter values, computed based on the data from the reference system and the IMU system. In addition, Table 4.2 lists the errors for the different parameters and the two events ski thrust start and stop. The cross-country skiing algorithm presented in Chapter 3 could not detect the cycle events for two trials out of the 97 trials. The errors on the remaining 95 trials are reported in Table 4.2. In short, errors were up to one order of magnitude larger compared to the adapted algorithm. In particular, the ski thrust stop event was not accurately detected. For the proposed algorithm Pearson’s correlation coefficient between the errors and conditions was below 0.55 for all errors (Table 4.2).

4.4 Discussion

In comparison to the reference motion capture system all parameters computed with the algorithm showed high accuracy and precision. Cycle duration showed errors below the resolution of the reference system (5 ms). Speed and distance measures showed errors below 0.032 m/s and 0.027 m, respectively. The ski thrust stop event (i.e. the first instant the ski’s forward speed is above the threshold of 0.1 m/s, Fig. 4.2B) was less accurate and precise, and also led to lower accuracy and precision for the thrust duration. The reduced accuracy and precision of the ski thrust stop event could be attributed to measurement noise from vibrations of the ski on the treadmill.

The proposed algorithm clearly outperformed the original cross-country skiing algorithm from Chapter 3. The ski movement in cross-country skiing is too different from the one in ski-mountaineering. In ski-mountaineering the thrust phase is much longer and the overall movement slower and smoother. Thus, the differences in acceleration and speed curves did not allow using the same algorithm. Even though the adaptations were minor, they were tailored to and optimized for the biomechanics of ski-mountaineering, taking into account all available constraints for precise event detection and efficient drift correction.

The slope angle errors had a large effect on the accuracy of the elevation gain. A small over- or underestimation of the slope angle by $0.5^\circ - 1^\circ$ resulted in a bias of the elevation gain of a few centimeters over one cycle. However, similar to the timing parameters the accuracy and precision of the slope angle was within resolution of inclination obtained by the treadmill. In outdoor use, the slope angle accuracy and precision could further be improved by using barometric pressure sensors (el Achkar et al., 2016).

In contrast to cross-country skiing, the ski thrust phase (i.e. ski motionless duration) was considerably longer for ski-mountaineering. Therefore, there were more samples available for estimating the drift which in turn allowed a more precise estimation of the orientation and speed drift. Compared to the results from Chapter 3, the accuracy of the cycle speed and distance was decreased (-0.013 m/s and -0.027 m for ski-mountaineering versus 0.005 m/s and 0.005 m for cross-country skiing) whereas the precision improved (0.032 m/s and 0.018 m for ski-mountaineering versus 0.1 m/s and 0.15 m for cross-country skiing). The slower movements in ski-mountaineering led to a lower accuracy and precision for the detection of the endpoints of the ski thrust phases. In cross-country skiing the end of the motionless phase was indicated by an abrupt change in speed with accelerations reaching over 10g. In ski-mountaineering the slower movement led to a gentler increase in speed, thus adding uncertainty around the exact time point where the ski had sufficient forward speed to be detected as moving.

In conclusion, the algorithm from Chapter 3, adapted for ski-mountaineering, is valid for measuring key spatio-temporal parameters for ski-mountaineering on treadmill. It is expected that the algorithm would perform similarly on snow, as the movement is very similar. Higher movement variability (e.g. snow condition, turns) might deteriorate the system's performance in certain instants but the absence of high frequency noise from the vibrations of the treadmill (Fig. 4.3) should improve the system's overall accuracy and precision.

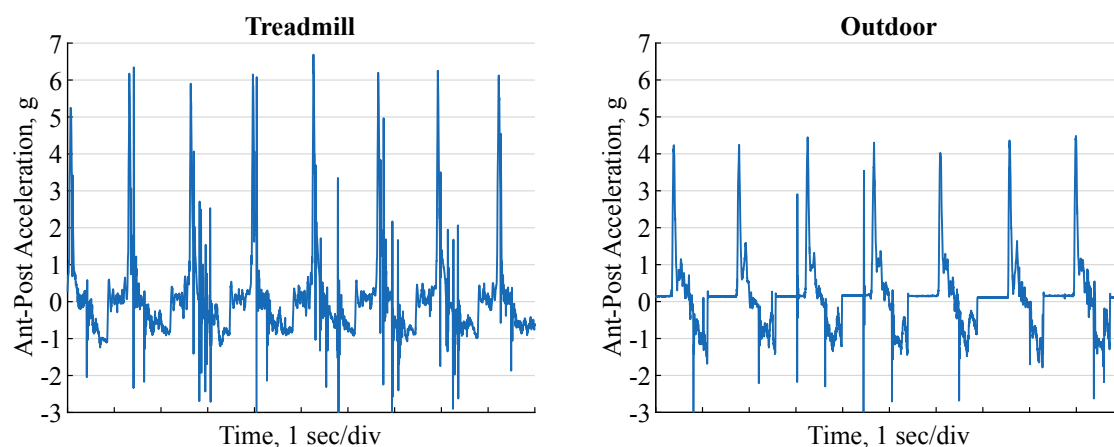


Figure 4.3 – Comparison between the ski’s anterior-posterior acceleration measured for indoor ski-mountaineering on the treadmill and for outdoor ski-mountaineering on snow. Displayed are typical acceleration patterns where in both conditions the slope angle was approximately 6° and skiing speed was approximately 1.7 m/s. The noise caused by the treadmill vibrations was absent in the outdoors data resulting in a very clear signal with the distinct motionless phases of no inertial acceleration.

Acknowledgements

The authors would like to thank the volunteers for their participation and Serge Metrailler for his help in recording the data. This study was in part supported by a grant from the Swiss Federal Office for Sports.

Dynamic Drift Correction **Part III**

5 Joint Drift Reduction for Alpine Ski Racing

Abstract

Inertial sensor drift is usually corrected at a single sensor-unit level. When multiple sensor units are used, mutual information from different units can be exploited for drift correction. This study introduces a method for drift-reduced estimation of three dimensional (3D) segment orientations and joint angles for motion capture of highly dynamic movements frequently encountered in many sports. 3D acceleration measured on two adjacent segments is mapped to the connecting joint. Drift is estimated and reduced based on the mapped accelerations' vector orientation differences in the global frame. Algorithm validity is assessed on the example of alpine ski racing. Shank, thigh and trunk inclination as well as knee and hip flexion were compared to a multi-camera-based reference system. For specific leg angles and trunk segment inclination, mean accuracy and precision were below 3.9° and 6.0° , respectively. The errors were similar to those reported in other studies for lower intensity movements. Drift increased axis misalignment and mainly affected joint and segment angles of highly flexed joints such as the knee or hip during a ski turn.

Keywords: body sensor networks, drift correction, inertial sensors, joint angles, orientation measurement, sensor fusion

5.1 Introduction

While the gold standard for measuring position and orientation of human body segments in space are optical motion capture systems (Cappozzo et al., 2005), such systems are not well suited for large capture volume outdoor applications. Body-worn inertial sensors started being used as an alternative for field measurements (Gouwanda and Senanayake, 2008). Many studies have tried to estimate segment orientations from inertial sensors for low-intensity movements, such as walking or upper limb reaching tasks (Bergamini et al., 2014; Bonnet et al., 2013; Luinge and Veltink, 2005; Mazzà et al., 2012). However, inertial sensors cannot measure segment orientation directly: it is obtained by integrating the acceleration and angular velocity signals. During this process, small errors accumulate over time (drift), thereby adding large errors to the position and orientation estimates (Bergamini et al., 2014).

From these studies, it can be concluded that errors are positively correlated with measurement duration, measurement volume, and range of motion. For the "worst case" in Bergamini et al. (2014), average orientation errors reached up to 45° after 3 minutes of continuous movement. Several studies addressed this drift problem and proposed various methodologies for drift reduction (Bergamini et al., 2014; Sabatini et al., 2015). Three main approaches have generally been used: drift reduction through sensor fusion (e.g. Kalman filters (Bergamini et al., 2014; Jakob et al., 2013; Luinge and Veltink, 2005)), drift reduction based on biomechanical constraints (e.g. static periods (Favre et al., 2006; Mariani et al., 2010; Sabatini, 2005), cyclic motion (Sabatini et al., 2015)), or a combination thereof (Cooper et al., 2009; Miezal et al., 2014). All those studies have in common that they were based on a single inertial measurement unit. The reader is referred to Seel et al. (2014) for a brief review of the most common methods. However, if multiple sensors are used, other strategies could be applied to obtain drift-reduced segment orientations. Dejnabadi et al. (2006) proposed a method to obtain drift-free ankle and knee angles in the sagittal plane without signal integration. They estimated the (virtual) acceleration at ankle and knee joint centres based on acceleration and angular velocity measured with inertial sensors placed on the shank and thigh where the distance between each sensor and the joint centre was known. A comparison of the acceleration vectors at the joint centres allowed estimating the shank and thigh segment orientation in the sagittal plane without integrating the angular velocity. However, their method was designed for only two dimensions and required knowing the distance between the sensor and the joint centre. Seel et al. (2014) presented a similar approach to obtain orientation without signal integration but proposed a method to estimate the sensor-to-joint-centre position vector based on optimization of acceleration norm differences. However, they stated that the angle estimation might be compromised by significant errors for high accelerations in the medio-lateral direction as often present in dynamic sports. Salehi et al. (2015) proposed a method for finding the sensor-to-joint-centre position vector based on a joint optimization method with three inertial sensors fixed to the pelvis, upper leg, and lower leg. However, their work assumed that sensor orientation was already

known. Accordingly, a more recent study by the same group (Taetz et al., 2016) presented an optimization method to find sensor-to-segment orientation and sensor-to-joint-centre position vectors based on squat movements; nevertheless, relatively high maximum angle differences of 8.5° and maximum position differences of 0.07 m were observed. Young (2010) proposed another method for estimating sensor orientation by cancelling the effect of linear accelerations and comparing the residual acceleration vector to gravity. Once again, here the sensor-to-joint-centre position vector was assumed to be known, although the discussion did explain a numerical optimization procedure for finding these vectors automatically. They only tested their algorithm on simulated data and it is unclear whether their approach would be valid for real measurements. Roetenberg et al. (2013) described a Kalman filter-based strategy for full body segment orientation tracking with joint constraints. Anthropometric measurements were required to determine the segment lengths, and kinematic chains were used for optimizing the functional calibration for the alignment of the sensor and anatomical frames.

Alpine ski racing is a highly dynamic sport with ground reaction forces reaching up to 3 times body weight (Kröll et al., 2016a; Spörri et al., 2016a,c, 2015) and centre of mass acceleration reaching up to 4-5g (Gilgien et al., 2015c; Supej et al., 2011, 2015). A typical downhill race is 3.5 km long, has an elevation loss of 860 m with speeds reaching 120 km/h, and lasts up to 2:20 minutes (Gilgien et al., 2015a). Estimating segment orientation with inertial sensors during such highly dynamic movements such as those observed in alpine skiing could be even more challenging. For dynamic sports, few studies have validated segment or joint orientations obtained with inertial sensors. For example, Jakob et al. (2013) implemented a Kalman filter and observed knee flexion root mean square errors of up to 10° for a recording duration of 10 seconds of running. Chardonens et al. (2013) proposed a drift reduction method for ski jumping based on a specific biomechanical constraint, i.e. same acceleration on multiple inertial sensors fixed on different body segments during the flight phase. But this constraint is not always present in other gliding sports and the duration of recording was still very short. Although inertial sensors have been used to quantify skier movement (Brodie et al., 2008; Krüger and Edelmann-Nusser, 2010; Supej, 2010; Zorko et al., 2015), design and validation of a ski-specific algorithm was not the focus. Only Krüger and Edelmann-Nusser (2010) compared their Kalman filter-based system to a three-dimensional (3D) camera system on snow and reported knee flexion angle accuracy and precision of 4.9° and 1.0° , respectively. However, only a fraction of a turn of length 1.5 m (<0.1 sec) for a single run performed by one ski instructor was analysed. It is not clear to what extent the system's performance can be generalised.

To summarize, error evaluation for highly dynamic movements with shocks and large capture volumes as is the case in many sports is still lacking and it is unclear whether common Kalman filters provide a good solution for computing segment and joint orientation for highly dynamic sports. Other approaches for obtaining a drift-free angle without using signal integration still have some limitations such as having to manually measure the sensor-to-joint-centre position vector, restrictive joint motion models (e.g. modelling

the knee as a hinge joint), or applicability limited to relatively low-intensity movements. In this study, we propose a novel drift reduction method based on information fusion from multiple inertial sensors, with a focus on sport applications where high accelerations in all three dimensions are frequently encountered.

The main aim was to obtain a drift-reduced measure of the 3D segment orientations of both shanks and thighs and the lower- and upper-trunk. To this end, the concept of joint-drift reduction was introduced: the position vector of the proximal and distal sensors to the connecting joint was estimated, then the 3D orientation of the difference of the distal and proximal accelerations vector translated to the connecting joint was expressed in a common global frame to estimate orientation drift. Finally, a sequential approach iteratively reduced the drift of the distal segment with respect to its proximal segment where the sacrum was considered as the starting segment. The algorithm was assessed with alpine ski racing measurements and validated in-field against a multi-camera-based reference system.

5.2 Methods

5.2.1 Protocol

Six European Cup level alpine ski racers were selected for the study. A giant slalom slope inclined at 26° , with a constant gate distance of 27 m and offset of 8 m with a total of 11 gates was prepared (Fig. 5.1A). Each athlete skied the run twice, where one left turn was simultaneously measured with the wearable system and the video-based reference system. The protocol was approved by the University Ethics Committee of the Department of Sport Science and Kinesiology at the University of Salzburg (EC_NR. 2010_03). Each athlete gave his written consent prior to participation.

In addition, a case study during the World Cup giant slalom race in Adelboden, Switzerland, was performed to evaluate the efficiency of the wearable system in a real race situation.

5.2.2 Wearable system

Inertial sensors

The wearable system consisted of six wireless inertial measurement units (Physilog III, Gait Up, Switzerland; 36 g per unit). Each unit included a 3D accelerometer, a 3D gyroscope and a data logger sampling at 500 Hz. All data were low-pass filtered with a cut-off frequency of 100 Hz. The accelerometers were calibrated in-lab using the procedure from Ferraris et al. (1995) and gyroscope offset was removed based on a static measurement prior to each run (Bergamini et al., 2014). The units were placed on the left and right shank on the tibial plateau above the ski boots; on the left and right thigh

on the lateral side midway between the knee and hip joint centre; on the sacrum; and on the sternum using a custom made skin-tight underwear suit (Fig. 5.1B).

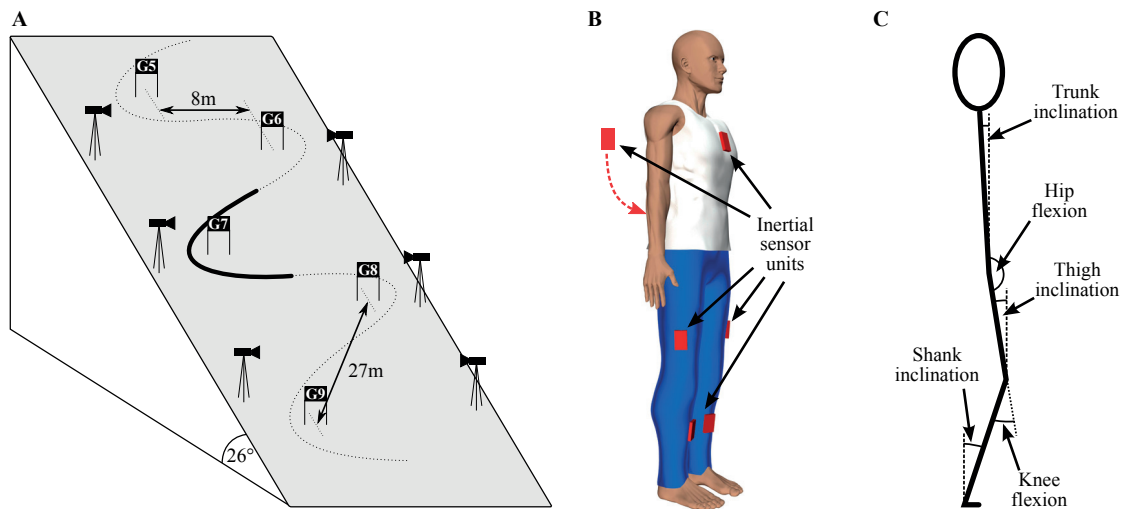


Figure 5.1 – Materials and setup. A) Giant slalom slope with the six cameras. The left turn analysed is marked by the black bold line. B) Inertial sensor setup with sensors on both shanks, thighs, on the sacrum, and on the sternum. C) Angle definitions for the segment inclinations and hip and knee flexion. The vertical axis was parallel to Earth's gravity.

Functional calibration

A functional calibration procedure optimised for in-field measurements was used to align the sensor frames with the anatomical frame of each segment (Chardonnnens et al., 2012). The anatomical frames were chosen according to the recommendations of the International Society of Biomechanics (Wu and Cavanagh, 1995). The vertical axis of each segment was found using an upright standing posture where it was hypothesised that the athlete stands perfectly upright. Squat movements with rolling spine and open ski boots were used to find the medio-lateral axes, where it was hypothesised that the main axis of rotation of each segment corresponds to its medio-lateral axis. In order to reduce the effect of the shank flexion angle offset induced by the ski boot's ankle flexion, the following hypothesis was made for the shank orientation: during turn switches (i.e. the instant of time when the athlete switches from a left to a right turn or vice versa), the shank's main rotation occurs along the anterior-posterior axis. Therefore, the recorded angular velocity during turn switches was used to optimise the shank segment calibration by maximising rotational movement along the anterior-posterior axis using principal component analysis.

Drift-reduced computation of the segments' 3D orientation

Three dimensional strap-down integration according to Favre et al. (2006) was performed for each sensor independently to find $R_{segment}^G(t)$, i.e. the segment's orientation expressed in the global frame at time t . The X-axis was pointing forwards, the Y-axis vertically upwards, and the Z-axis to the right. A still-standing upright posture before the start of the race was used to initialise the integration (Bergamini et al., 2014).

The main source of error when estimating 3D orientation from strap-down integration of the angular velocity is known to be the drift accumulated during the integration procedure (Bergamini et al., 2014). While this drift could be reduced by assuming quasi-static periods in the movement such as the stance period in walking (Favre et al., 2006), one cannot assume this hypothesis in sports where body segments are always in a sliding motion (e.g. alpine ski racing). Therefore, a new method for drift removal was designed, which included three steps: drift modelling, drift estimation, and drift reduction, as described in the following sections.

Drift modelling

A new model was devised to estimate the 3D orientation drift between two adjacent segments (e.g. left shank and left thigh) with no restrictions on joint movement and well suited for highly dynamic movements. The main idea was to calculate for each segment (distal and proximal) the expected acceleration vectors ($\tilde{\mathbf{a}}_{distal}$, $\tilde{\mathbf{a}}_{proximal}$) of a virtual sensor module placed at a virtual joint (ball joint, no joint translation allowed) connecting the two adjacent segments. Since one point should have a unique acceleration, the two virtual sensors must give identical distal ($\tilde{\mathbf{a}}_{distal}^G(t)$) and proximal ($\tilde{\mathbf{a}}_{proximal}^G(t)$) accelerations in the global frame (Eqs. 5.1 - 5.2).

$$\tilde{\mathbf{a}}_{distal}^G(t) = R_{distal}^G(t) \tilde{\mathbf{a}}_{distal}(t) \quad (5.1)$$

$$\tilde{\mathbf{a}}_{proximal}^G(t) = R_{proximal}^G(t) \tilde{\mathbf{a}}_{proximal}(t) \quad (5.2)$$

$R_{distal}^G(t)$ and $R_{proximal}^G(t)$ are the drift-affected orientations at time t of the distal and proximal segment estimated by the strap-down integration and expressed in the global frame as described earlier. $\tilde{\mathbf{a}}_{distal}(t)$ and $\tilde{\mathbf{a}}_{proximal}(t)$ were estimated from (Eqs. 5.3 - 5.4):

$$\tilde{\mathbf{a}}_{distal}(t) = \mathbf{a}_{distal}(t) + \dot{\omega}_{distal}(t) \times \mathbf{r}_d + \omega_{distal}(t) \times (\omega_{distal}(t) \times \mathbf{r}_d) \quad (5.3)$$

$$\begin{aligned} \tilde{\mathbf{a}}_{proximal}(t) &= \mathbf{a}_{proximal}(t) + \dot{\omega}_{proximal}(t) \times \mathbf{r}_p \\ &+ \omega_{proximal}(t) \times (\omega_{proximal}(t) \times \mathbf{r}_p) \end{aligned} \quad (5.4)$$

where $\mathbf{a}_{distal}(t)$ and $\mathbf{a}_{proximal}(t)$ are the accelerations measured at the distal and proximal sensors. $\omega_{distal}(t)$ and $\omega_{proximal}(t)$ are the low-pass filtered angular velocities (second order Butterworth filter with cut-off frequency of 6 Hz (Mester, 1992)) of the distal

and proximal sensors. \mathbf{r}_d and \mathbf{r}_p are the position vectors connecting the distal and proximal sensor positions with the virtual joint, respectively, all expressed in the local segment's anatomical frame. \mathbf{r}_d and \mathbf{r}_p were obtained through numerical optimisation (Lagarias et al., 1998) by minimising the error function of Eq. 5.5 and using the initial, drift-affected $\tilde{\mathbf{a}}_{distal}^G(t)$ and $\tilde{\mathbf{a}}_{proximal}^G(t)$.

$$E = \sum_{t \in C} \left| \tilde{\mathbf{a}}_{distal}^G(t) - \tilde{\mathbf{a}}_{proximal}^G(t) \right| \quad (5.5)$$

where C is the set of all samples satisfying $|\omega_{proximal}(t)| > 40^\circ/s$ during the entire downhill run. E is the residual error caused by drift and sensor noise.

Drift estimation

Once \mathbf{r}_d and \mathbf{r}_p were estimated, the virtual accelerations ($\tilde{\mathbf{a}}_{distal}(t)$, $\tilde{\mathbf{a}}_{proximal}(t)$) were re-computed for estimating the drift. Drift introduces a slowly increasing time-dependent orientation difference between $\tilde{\mathbf{a}}_{distal}^G(t)$ and $\tilde{\mathbf{a}}_{proximal}^G(t)$, and noise alters their norms. The higher the accelerations (dynamic movement), the higher the signal-to-noise ratio, and the more reliable the computation of the orientation difference is. In alpine ski racing, high accelerations are not only present in the sagittal plane but also along the medio-lateral axis (centripetal acceleration). Therefore, the drift $\delta(t)$ corresponding to the 3D orientation difference between $\tilde{\mathbf{a}}_{distal}^G(t)$ and $\tilde{\mathbf{a}}_{proximal}^G(t)$ was estimated for samples of high signal-to-noise ratio satisfying Eqs. 5.6 - 5.8.

$$\left| \left| \tilde{\mathbf{a}}_{distal}^G(t) \right| - \left| \tilde{\mathbf{a}}_{proximal}^G(t) \right| \right| < 2.5 \text{ m/s}^2 \quad (5.6)$$

$$\left| \tilde{\mathbf{a}}_{distal}^G(t) \right| > 8 \text{ m/s}^2 \quad (5.7)$$

$$\left| \tilde{\mathbf{a}}_{proximal}^G(t) \right| > 8 \text{ m/s}^2 \quad (5.8)$$

The thresholds used in Eqs. 5.5-5.8 were found upon inspection of a large set of skiing data from the same measurements. $\delta(t)$ was computed using the quaternion notation (Eq. 5.9). Quaternion notation was used instead of orientation matrices since the average orientation needed to be computed for the final drift estimation (see below).

$$\delta(t) = \left[\cos \left(\frac{\beta(t)}{2} \right), \sin \left(\frac{\beta(t)}{2} \right) \cdot U(t) \right] \quad (5.9)$$

where $\beta(t)$ and $U(t)$ are the axis-angle representation of $\delta(t)$ (Eqs. 5.10 - 5.11):

$$\beta(t) = \arccos \left(\frac{\tilde{\mathbf{a}}_{distal}^G(t) \cdot \tilde{\mathbf{a}}_{proximal}^G(t)}{|\tilde{\mathbf{a}}_{distal}^G(t)| \cdot |\tilde{\mathbf{a}}_{proximal}^G(t)|} \right) \quad (5.10)$$

$$U(t) = \frac{\tilde{\mathbf{a}}_{distal}^G(t) \times \tilde{\mathbf{a}}_{proximal}^G(t)}{|\tilde{\mathbf{a}}_{distal}^G(t) \times \tilde{\mathbf{a}}_{proximal}^G(t)|} \quad (5.11)$$

The final drift estimate $\tilde{\delta}(t)$ for each time sample t was defined as the average quaternion (i.e. average orientation) (Markley et al., 2007) of all available drift estimates in the interval $[t - 1.25s; t + 1.25s]$ where this interval duration was chosen so as to include at least one full turn cycle.

Drift reduction

First, the drift of the sacrum sensor was reduced based on the average relative drift between the sacrum sensor and its neighbouring sensors at the sternum and left and right thighs, similar to Chardonens et al. (2013) (Eqs. 5.12 - 5.13).

$$\tilde{\delta}_{sacr}(t) = \Pi(\tilde{\delta}_{st}(t), \tilde{\delta}_{lt}(t), \tilde{\delta}_{rt}(t)) \quad (5.12)$$

$$\hat{R}_{sacr}^G(t) = \text{q2m}(\tilde{\delta}_{sacr}(t)) * R_{sacr}^G(t) \quad (5.13)$$

where $\tilde{\delta}_{st}(t)$, $\tilde{\delta}_{lt}(t)$, $\tilde{\delta}_{rt}(t)$ are the final joint-drifts between the sacrum and, respectively, the sternum, left and right thigh. Π denotes the average quaternion operator (Markley et al., 2007), and $\tilde{\delta}_{sacr}(t)$ is the final drift of the sacrum orientation. q2m denotes the quaternion to matrix conversion, $R_{sacr}^G(t)$ is the initial drift-affected sacrum orientation, and $\hat{R}_{sacr}^G(t)$ is the drift-reduced sacrum orientation.

In the second step, assuming the sacrum sensor orientation is now drift-free, the sensors' drifts were reduced from proximal to distal sensors, e.g. the relative drift between the sacrum and left thigh was equal to the drift of the left thigh sensor (Eq. 5.14). Thus, in the end, all drifts were reduced relative to the sacrum. Even if the sacrum drift is not completely removed, the relative joint-drift between each proximal and distal segment reduces, allowing the computation of more accurate joint orientations.

$$\hat{R}_{distal}^G(t) = \text{q2m}(\hat{\delta}_{distal}(t)) * R_{distal}^G(t) \quad (5.14)$$

where $\hat{\delta}_{distal}(t)$ is the final joint-drift between proximal and distal segments (e.g. sacrum and left thigh), $R_{distal}^G(t)$ the drift-affected orientation of the distal segment (e.g. left thigh), and $\hat{R}_{distal}^G(t)$ the drift-reduced orientation of the distal segment.

Computation of the parameters

Based on the segment's 3D orientation, the following angles were computed and validated with the reference system (Fig. 5.1C): (1) shank, thigh inclination α_s and α_t : the angle between each segment's longitudinal axis $R_{s/t,y}^G$ and the Earth's gravity \mathbf{g} (Borghese et al., 1996) (Eq. 5.15); (2) trunk inclination: mean of the sacrum and sternum segment inclinations, both calculated as in (1)), (3) knee flexion, α_k : the angle between the longitudinal axes of the shank and thigh segments (Eq. 5.16); (4) hip flexion, α_h : the angle between the longitudinal axis of the thigh and the vector given by the mean of the

longitudinal axes of the sacrum and sternum segments (Eq. 5.17). The flexion angles were chosen in this way in order to be consistent with the multi-camera-based reference system.

$$\alpha_{s/t}(t) = \arccos \left(R_{s/t,y}^G(t) \cdot \mathbf{g} \right) \quad (5.15)$$

$$\alpha_k(t) = \arccos \left(R_{s,y}^G(t) \cdot R_{t,y}^G(t) \right) \quad (5.16)$$

$$\alpha_h(t) = \arccos \left(R_{t,y}^G(t) \cdot \frac{0.5 \left(R_{sacr,y}^G(t) + R_{st,y}^G(t) \right)}{\left| 0.5 \left(R_{sacr,y}^G(t) + R_{st,y}^G(t) \right) \right|} \right) \quad (5.17)$$

5.2.3 Reference system

Six panned, tilted and zoomed high definition video cameras (PMW-EX3, Sony, Tokyo, Japan) with a frame rate of 50 Hz and synchronised by a gen-lock signal were used to assess the athlete's body kinematics over one left turn cycle (Fig. 5.1A). Using a direct linear transform-based panning algorithm developed by Drenk (1994), the trajectories of a manually digitised 22-point body segment model were reconstructed in 3D, as done in earlier studies (Gilgien et al., 2015c, 2013; Spörri et al., 2016c, 2012a,b). In order to synchronise the reference system with the inertial measurement units an external trigger was used. The segment inclination, as described in Borghese et al. (1996); Soechting and Ross (1984), was defined as the angle between the segment vector and the vertical gravity axis. The knee and hip flexion angles were computed using the same definition as the one used with the wearable system (Fig. 5.1C). It is important to note that the reference system did not allow measuring joint angles in three dimensions as only the longitudinal axis for each limb segment was known. The reference system's vertical axis was aligned with the wearable system's vertical axis to avoid axis-crosstalk. The resultant photogrammetric error of the reference system used to collect kinematic data on ski tracks has been reported to be 23 ± 10 mm, which is comparable to the accuracy achieved with similar methods under laboratory conditions (Klous et al., 2010). Furthermore, it is known from laboratory studies that the joint angle precision of systems with similar point determination accuracy is of the order of 1-3.9° for knee and hip flexion (Della Croce et al., 1999).

5.2.4 Error analysis

For the purpose of validation the angles obtained from the wearable system were low pass filtered (linear-phase FIR filter, 25 Hz cut-off frequency) and down-sampled to 50 Hz to match the sampling frequency of the video-based reference system. For each of the twelve turns analysed the error was defined as the curve difference $d_i(t)$ between the

angles obtained with the reference and wearable systems (Eq. 5.18).

$$d_i(t) = c_{wearable}(t) - c_{ref}(t) \quad i \in \{1, 2, \dots, 12\} \quad (5.18)$$

where $c_{wearable}$ and c_{ref} are the angle curves (i.e. segment inclination or joint angle) of the reference system and wearable system, respectively. i is the turn number.

The mean and standard deviation (SD) of $d_i(t)$ were computed for each run. The system's accuracy was defined as the mean \pm SD of the mean errors and the precision as the mean \pm SD of the standard deviation errors over all turns. Pearson's linear correlation coefficient r was used to quantify the correlation between the angle curves of the reference and wearable systems.

5.3 Results

The proposed method allowed to estimate the drift in all three dimensions. Fig. 5.2 shows the drift magnitude over time, where the left turn covered by the reference system was around second 25. The estimated drift was approximately $0.15^\circ/s$. Table 5.1 compares the errors for the drift-affected (angles after strap-down integration) and drift-reduced angles. Drift reduction improved the mean accuracy averaged over all parameters by 1.0° and improved the standard deviation of the accuracy averaged over all parameters by 1.7° , with the greatest improvement being observed for the knee flexion of the outside leg (i.e. outside knee). The precision did not change and the correlation coefficient increased on average by 0.04 for the outside leg.

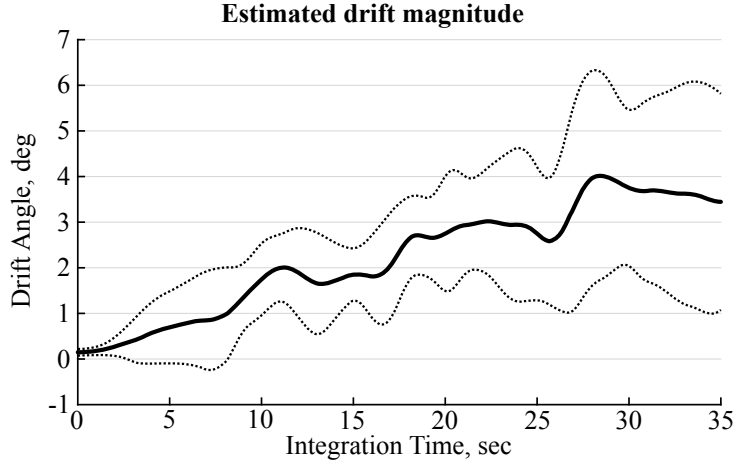


Figure 5.2 – The estimated drift magnitude (in degrees). Shown are the mean (solid line) and standard deviation (dotted line) of the estimated drift magnitudes for all twelve left turns.

The accuracy and precision of the wearable system for the outside (right) leg was below 3.9° and 6.0° , respectively (Table 5.1). For the inside (left) leg, the algorithm was less

Angle	Accuracy, deg		Precision, deg		Correlation	
	drift-affected	drift-reduced	drift-affected	drift-reduced	drift-affected	drift-reduced
Inside shank inclination	1.0 ± 3.7	1.1 ± 3.6	2.6 ± 1.1	2.6 ± 1.0	0.97 ± 0.02	0.97 ± 0.02
Inside thigh inclination	15.3 ± 7.7	13.2 ± 4.5	3.1 ± 0.9	3.8 ± 1.3	0.99 ± 0.00	0.99 ± 0.01
Inside knee flexion	16.9 ± 6.3	13.2 ± 4.7	4.0 ± 2.0	3.1 ± 1.4	0.98 ± 0.02	0.98 ± 0.02
Inside hip flexion	13.1 ± 14.9	11.4 ± 10.0	4.4 ± 1.7	4.5 ± 1.7	0.97 ± 0.02	0.97 ± 0.02
Outside shank inclination	-0.1 ± 4.0	-1.8 ± 3.5	2.9 ± 1.0	2.9 ± 1.2	0.98 ± 0.02	0.98 ± 0.02
Outside thigh inclination	-4.1 ± 3.7	-3.9 ± 5.2	5.9 ± 1.5	5.3 ± 1.1	0.65 ± 0.24	0.75 ± 0.14
Outside knee flexion	7.6 ± 8.4	1.7 ± 7.9	4.3 ± 1.5	4.8 ± 1.7	0.90 ± 0.05	0.90 ± 0.06
Outside hip flexion	-0.3 ± 15.4	-3.8 ± 13.2	6.2 ± 1.5	6.0 ± 1.5	0.76 ± 0.18	0.80 ± 0.18
Trunk inclination	-3.4 ± 11.6	-3.1 ± 8.0	2.3 ± 1.9	2.1 ± 0.8	0.93 ± 0.09	0.94 ± 0.08

Table 5.1 – Accuracy and precision of the algorithm proposed for the wearable system and correlation of the angles with the reference system.

accurate (mean accuracy of 11-13°) but more precise (mean precision below 4.5°) (Table 5.1). The correlation coefficient between the angles computed with the wearable and reference systems were all above 0.9 except for the outside thigh inclination (0.75) and outside hip flexion (0.80) (Table 5.1).

The wearable system was robust against inaccuracies in the estimation of the position vectors between the sensors and virtual joints (\mathbf{r}_d and \mathbf{r}_p): increasing and decreasing their norm by 20% or changing their direction by 10° affected the system’s accuracy and precision by less than 0.6°. Moreover, the wearable system was insensitive to changes by $\pm 20\%$ of the acceleration and angular velocity thresholds chosen in Eqs. 5.5-5.8 for the sensor-to-joint-centre position vector estimation and for the drift estimation. With the proposed thresholds, approximately 2/3 of all samples were used for drift estimation. To highlight the enhancements added by the proposed drift reduction algorithm, Figs. 5.3 and 5.4 compare the errors for the drift-affected and drift-reduced angles. Drift reduction mainly improved joint angles and less segment inclinations. The process of drift reduction from proximal to distal segments worked well: the most distal segment (shank) inclination showed similar accuracy and precision to that of the most proximal segment (trunk) (Table 5.1).

The wearable system was also used during the World Cup giant slalom race in Adelboden, Switzerland. Fig. 5.5 illustrates the efficiency of the drift reduction algorithm for a typical race. As expected, the drift increased over time and especially affected the results for high knee flexion angles (i.e. knee flexion for inside leg).

5.4 Discussion

In addition to traditional single-sensor orientation drift correction, in the current study an algorithm was designed for joint inertial sensor orientation drift reduction. Information from multiple inertial sensors connected by a joint was used for drift modelling, estimation, and correction. First, unlike other studies (Dejnabadi et al., 2006; Young, 2010) which assumed the sensor-to-joint-centre position vector to be known or required specific calibration movements (Taetz et al., 2016), we devised a scheme to automatically

estimate this vector. Second, we overcome the 2D limitation of the method proposed in Dejnabadi et al. (2006) by proposing a 3D estimation of orientation drift by sequentially removing drift starting from the most proximal segment (sacrum) and then reducing that of distal segments relative to their respective proximal segments. Third, joint angles were computed for anatomically relevant angles and unlike existing methods (Seel et al., 2014) the algorithm took advantage of high movement dynamics present in many sports. Finally, the system was tested for a giant slalom course where one left turn was covered by a multi-camera-based reference system. Twelve runs were simultaneously recorded with the wearable and reference systems, and segment inclinations and joint angles were compared. The proposed drift reduction model was able to reduce the drift and improve the accuracy of the orientation estimation. Overall, accuracy was better for the outside leg ($<3.9^\circ$) than for the inside leg ($<13.2^\circ$). Drift reduction improved the accuracy by up to 5.9° , as observed for the outside knee flexion. Precision was better for the inside leg ($<4.5^\circ$) than for the outside leg ($<6.0^\circ$).

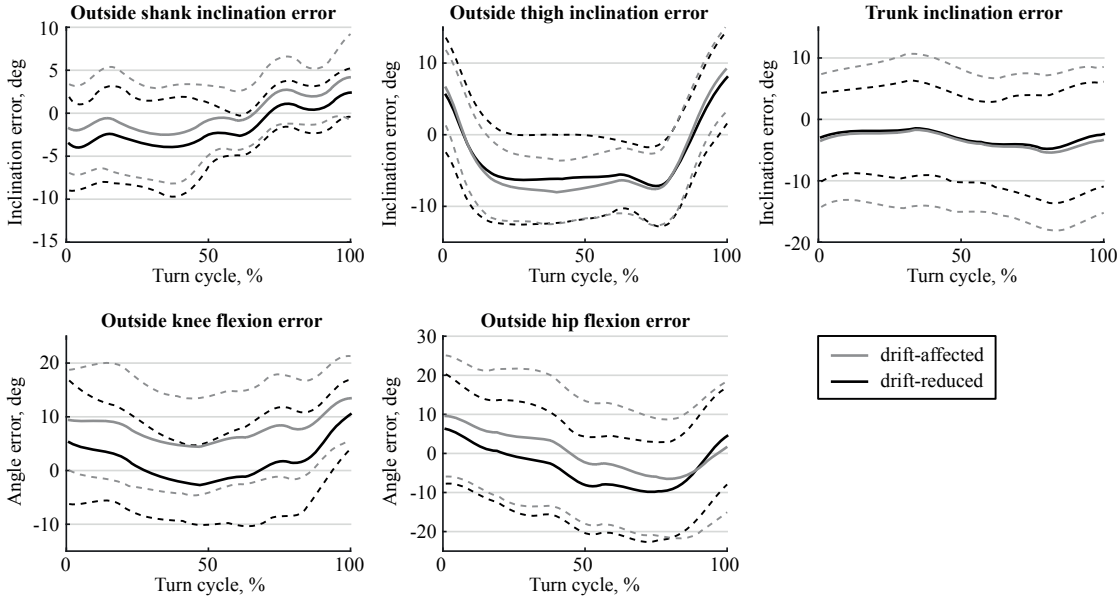


Figure 5.3 – Errors outside leg and trunk. Error curves (mean: solid line, standard deviation: dotted line) for the outside leg and trunk inclination for drift-affected (grey) and drift-reduced (black) angles are shown.

Drift is known to originate from stationary and non-stationary gyroscope bias, which is influenced by inaccuracies in sensor calibration, the environment (e.g. changing temperature), and the movement itself (Bergamini et al., 2014; Grewal and Andrews, 2010a). Estimating gyroscope bias during a motionless phase immediately prior to each run allowed reduction of the stationary bias. Joint-drift correction allowed estimation of the non-stationary bias. The remaining drift was considered to be independent between measurements. It tended to add a slowly increasing or decreasing offset to the sensor ori-

entation estimate. Therefore, when considering validation time windows of a few seconds, drift was found to affect orientation accuracy (mean error) but not precision (standard deviation of the error): accuracy improved with drift reduction whereas the precision did not change (Table 5.1). Moreover, since the analysed turn occurred approximately 25 seconds after the start, the amount of accumulated drift was quite small. For longer time periods, drift is known to become more prominent (Bergamini et al., 2014): for the long-duration measurement in Fig. 5.5, e.g. 90 sec, the drift-reduced knee angle towards the end of the race was more plausible than the drift-affected knee angle, which reached up to 170° during maximum flexion. The drift reduction decreased axis cross-talk, thus improving the system's accuracy (Table 5.1).

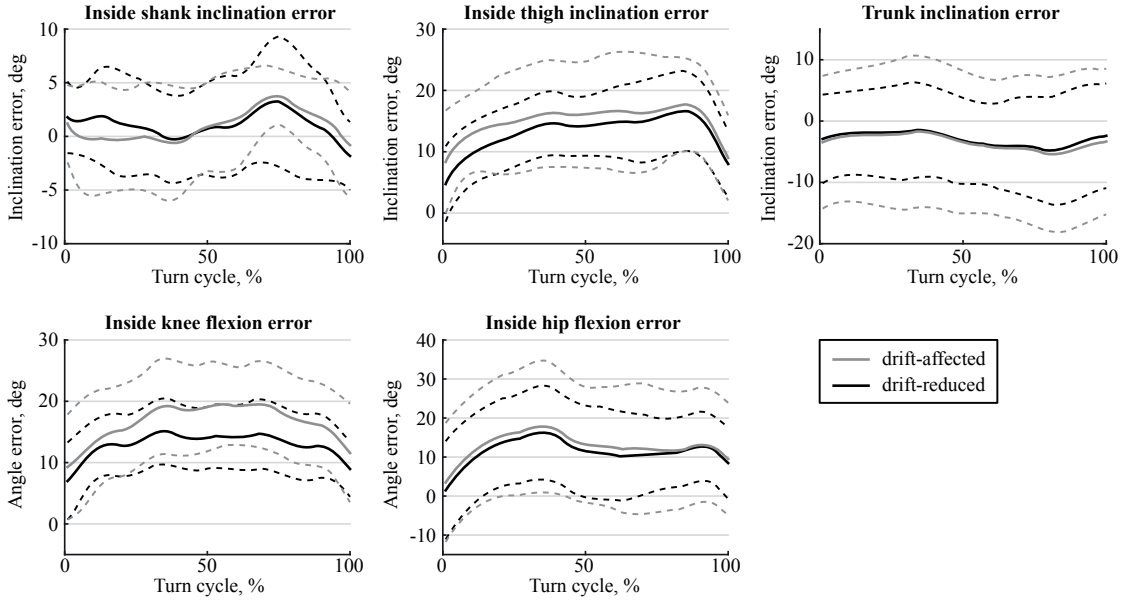


Figure 5.4 – Errors for the inside leg and trunk. Error curves (mean: solid line, standard deviation: dotted line) for the outside leg and the trunk inclination for drift-affected (grey) and drift-reduced (black) angles are shown.

The proposed algorithm succeeded in leveraging highly dynamic movement patterns, traditionally seen as rendering orientation estimation problems intractable when small errors are desired, to model drifts observed during alpine ski racing. It also made use of the centripetal acceleration present during such movements, and was independent of the athlete's posture. Standard approaches such as Kalman filters perform well for slow and smooth movements: root-mean-square (RMS) sensor orientation errors of 2.7° were reported by Roetenberg et al. (2005) and knee angle RMS errors of 3.4° for walking and running (Cooper et al., 2009; Favre et al., 2008). However, attempts to adapt such filters to highly dynamic movements gave poor results: RMS knee flexion errors of 10° for running and jumping were reported by Jakob et al. (2013). Bergamini et al. (2014) reported heading errors of over 20° after 3 min of continuous walking. No study reported

errors for in-field alpine ski racing movements, except Krüger and Edelmann-Nusser (2010) who reported a better accuracy and precision but only analysed a fraction of a turn for a single skier and, therefore, cannot be compared to our results. Thus, on the one hand, for the highly dynamic movements present in alpine ski racing, the proposed method seemed to perform at least as well or better than the above cited studies. On the other hand, it is expected that the proposed method might not perform well for low-intensity movements as the signal-to-noise ratio of joint accelerations might be too low to provide reliable drift estimates. However, a direct comparison of different methods on the same set of measurements would be needed in order to draw a final conclusion (Bergamini et al., 2014).

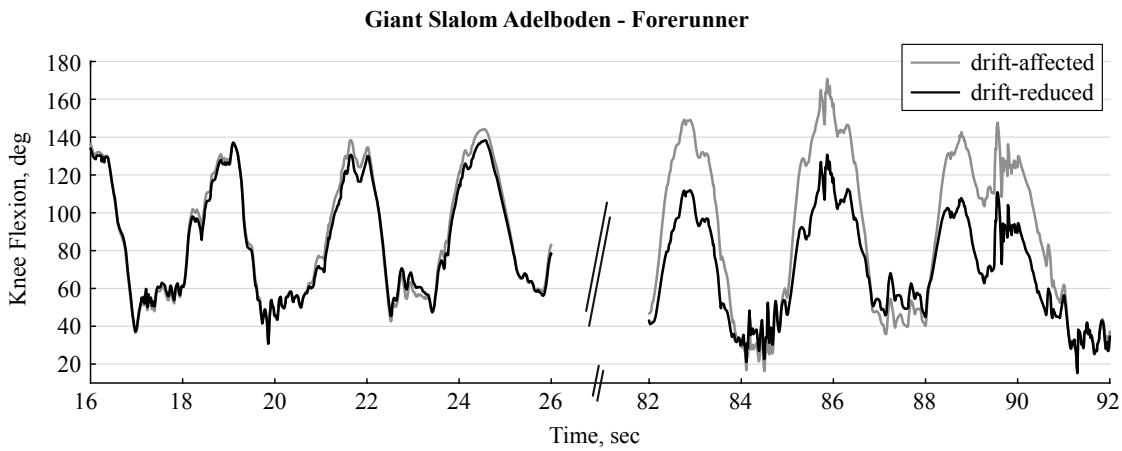


Figure 5.5 – Knee flexion angles obtained using the wearable system of a forerunner during the Adelboden World Cup giant slalom race. The figure shows the knee flexion angles for 10 seconds at the beginning and end of the race. The grey line depicts the raw angles after strap-down integration, without any drift reduction (drift-affected angles). The black line shows the same angles after applying the drift reduction. Drift did accumulate towards the end of the race and especially influenced the results for highly flexed knee angles (i.e. inside leg during a turn). For example, knee flexion reached 170° during the turn at second 86 which, from a biomechanical point of view, would be unlikely to occur. It is to be noted that knee flexion angle minima and maxima towards the end of the run were lower compared to the beginning because of the different turn types (e.g. steeper terrain, different speed).

A considerably poorer accuracy was observed for the inside leg than for the outside leg. In skiing, knee flexion is typically higher for the inside leg (Berg et al., 1995; Kröll et al., 2010); at these higher flexion angles, axis cross-talk due to sensor misalignment is known to be higher (Brennan et al., 2011; Kadaba et al., 1990). Pearson's linear correlation coefficients between the angle parameter and its error were 0.64 for the knee angle, 0.71 for the thigh inclination, and -0.15 for the shank inclination ($p < 0.001$). Thus, the errors were significantly correlated with the angle values. The main source of error for the knee angle was found to be an inaccurate thigh orientation (i.e. inclination-dependent sensor

misalignment). Other potential reasons for inaccurate knee angles might have been: first, the inertial sensors were covered by an elastic racing suit resulting in higher tension for higher knee flexion, potentially altering the sensor position and orientation of the thigh sensor in particular. Second, soft tissue artefacts and substantial muscle wobbling could temporarily alter the sensor orientation. Third, errors from the functional calibration movements could add constant orientation bias, thus increasing errors from cross-talk for higher knee angles. Fourth, in some parts of the turn, the visibility of the hip, knee or ankle joint centres, and therefore the accuracy of the reference system, might have been limited by extreme body inclinations or snow spraying while skidding. Based on the current study design, these explanations remain purely speculative and should be addressed by further studies. However, it is worth noting that in the field of alpine ski racing, the limited accuracy of the inside leg kinematics will be problematic only occasionally, as most studies focus on the functionally more important outside leg (Spörri et al., 2012b; Turnbull et al., 2009).

In alpine ski racing, there are only a handful of studies where joint kinematics were compared between different skiing styles, equipment, and/or course setting. For recreational skiing, Scheiber et al. (2012) reported turn-average knee flexion angle differences of 5° to be meaningful when comparing different skiing techniques. The wearable system's precision could allow the detection of such angle differences, particularly when assessing the outside leg. It could be used, for instance, to analyse left/right symmetry or the effects of an external intervention (e.g. equipment, course setting) as long as the expected difference is higher than the wearable system's precision.

Calibration movements were adapted and simplified for the purpose of in-field measurements in alpine ski racing. Nevertheless, the calibration movements turned out to be challenging in ski boots. Flexion offsets during the upright posture introduced offsets in the estimation of the segment's longitudinal axis which could explain the high standard deviation for the reported accuracy of trunk and thigh inclination, which may be a limiting factor of the proposed algorithm. For future measurements, different functional calibration movements (e.g. hip abduction (Favre et al., 2008)) could be considered in order to reduce potential axis-misalignments.

In order to estimate the sensor-to-joint-centre position vectors (\mathbf{r}_p and \mathbf{r}_d), an initial drift-affected segment orientation was used. Theoretically, orientation drift may increase the error in Eq. 5.5 and may lead to an orientation bias in \mathbf{r}_p and \mathbf{r}_d . However, tests showed that direction errors of 10° in \mathbf{r}_p and \mathbf{r}_d affected segment inclination and joint angle accuracy and precision by less than 0.6° . This observation could point to the conclusion that in order to obtain sufficiently accurate estimates of \mathbf{r}_p and \mathbf{r}_d , sensor orientation drift should remain below 10° . This could, for example, be achieved by limiting the samples taken for the optimization to the first 30 seconds of measurement. A limitation of the current study might be the fact that only segment inclination, knee and hip flexion angles were compared to the reference system even though the proposed algorithm computed all segment and joint orientations in 3D. The experimental setup of the camera-based system did not allow the measurement of the 3D orientation of

the segments since the labelled joint centres allowed for the computation of only the lower limbs' longitudinal axes. However, since a segment's inclination is a projection of 3D orientation onto two dimensions, the initial 3D segment orientation is expected to have a similar accuracy and precision. This expectation is further supported by the fact that an entire turn was recorded: the segments' 3D orientations changed substantially during the turn, yet the errors remained more or less constant (refer to Figs. 5.3 and 5.4 for shank and trunk inclination). Nevertheless, knee and hip abduction/adduction and internal/external rotation need further validation, since the inaccuracies of the thigh segment orientation may have an impact on these angles (Brennan et al., 2011; Kadaba et al., 1990; Piazza and Cavanagh, 2000).

The thresholds for including samples for drift estimation were chosen empirically. However, changing the thresholds by up to $\pm 20\%$ of their initial values did not affect the results. We therefore hypothesize that these thresholds would also be applicable for data collected during other measurements.

In conclusion, the proposed method was found to be successful for reducing 3D segment- and joint-orientation drift for highly dynamic movements. Even though it was specially tailored to measure segment orientations in alpine ski racing, it could be adapted to other highly dynamic sports such as running or cross-country skiing. In future studies, the functional calibration movements could be optimised, and the impact of motion artefacts of suit-based sensor fixation and soft tissue artefacts should be assessed. The system could be used to gain further insights into the kinematics involved in the sport of alpine ski racing. In particular, the unlimited capture volume, the easy setup (less than 15 minutes) and the fully automatized data analysis are major strengths of the proposed method.

6 Joint Drift Correction Improvements and Indoor Validation

Abstract

To obtain valid 3D joint angles with inertial sensors careful sensor-to-segment calibration (i.e. functional or anatomical calibration) is required and measured angular velocity at each sensor needs to be integrated to obtain segment and joint orientation (i.e. joint angles). During the integration of the angular velocity small errors accumulate and result in orientation drift. Functional and anatomical calibration procedures as well as methods to reduce orientation drift have been proposed in the past. However, these methods were optimized for gait analysis and calibration movements were impractical to perform in outdoor settings. The aims of this study were 1) to propose and validate a set of calibration movements that were optimized for alpine skiing and could be performed outdoors and 2) validate the 3D joint angles of the knee, hip, and trunk during alpine skiing. The proposed functional calibration movements consisted of squats, trunk rotations, hip ad/abductions, and upright standing. The joint drift correction previously proposed for alpine ski racing was improved by adding a second step to reduce separately azimuth drift. Calibration repeatability was on average $<2.7^\circ$ (i.e. 3D joint angles changed on average $<2.7^\circ$ for two repeated sets of calibration movements) and all movements could be executed wearing ski-boots. Joint angle precision was $<4.9^\circ$ for all angles and accuracy ranged from -10.7° to 4.2° where the presence of an athlete-specific bias was observed especially for the flexion angle. Errors were similar to the values reported in other studies for gait. The system may be well suited for within-athlete analysis but care should be taken for between-athlete analysis because of a possible athlete-specific joint angle bias.

Keywords: inertial sensors, functional calibration, drift correction, joint angles, knee angles, hip angles, trunk angles, alpine skiing, movement analysis, biomechanics, sports

Chapter submitted to the journal PLOS ONE: B. Fasel, J. Spörri, P. Schütz, S. Lorenzetti and K. Aminian. "Validation of functional calibration and strap-down joint drift correction for computing 3D joint angles of knee, hip, and trunk in alpine skiing".

6.1 Introduction

Tracking of body segments and joints is traditionally performed with stereo-photogrammetric marker-based motion capture systems. Excluding errors from soft tissue artefacts (STA) such systems can measure three-dimensional (3D) positions and orientations of segments with an accuracy of <0.2 mm and $<0.6^\circ$, respectively (Windolf et al., 2008; Kedgley et al., 2009). Joint orientations can be computed by calculating the relative orientation between two adjacent segments following ISB recommendations (Wu et al., 2002, 2005). While such systems are well suited for in-lab measurements with relatively small capture volumes of a few cubic meters, they become unsuitable for larger volumes, such as often present in outdoor sports. For such sport applications inertial sensors have been proposed instead; e.g. to measure the kinematics of ski jumping (Chardonens et al., 2013), to estimate the instantaneous velocity for front-crawl swimming (Dadashi et al., 2012), to estimate spatio-temporal parameters in cross-country skiing (Chapter 3), or to estimate temporal parameters during sprint running (Bergamini et al., 2012). They are especially well suited for sports movement analysis because of their small size, possibility of being integrated into sports equipment or clothing, low dependence on environmental conditions (e.g. weather), and autonomy offering a pervasive monitoring. However, inertial sensors cannot measure segment orientations directly. In order to obtain segment orientations with inertial sensors, several steps are required: 1) functional or anatomical calibration to align the sensor frame with the segment frame, 2) estimation of an initial segment orientation, and 3) mathematical procedure for tracking the change in segment orientation over time. Generally, this procedure is based on strap-down integration of angular velocity (Sabatini, 2005) combined with a drift reduction method (Miezal et al., 2016; Won et al., 2010; Mazzà et al., 2012; Cooper et al., 2009; Bergamini et al., 2014; Lunge and Veltink, 2005; Jakob et al., 2013; Favre et al., 2006; Madgwick et al., 2011; Sabatini, 2006; Fasel et al., 2017b). Each step adds its own errors to the final segment orientation estimate: 1) misalignment from the anatomical or functional calibration, 2) inaccuracy of the initial segment orientation, and 3) lack of drift reduction. In the past, different anatomical and functional calibrations were proposed mainly for gait analysis. Favre et al. (2009) proposed and validated a functional calibration procedure for measuring knee joint angles during walking. The calibration was based on active hip ab/adduction and passive shank movements in the sagittal and frontal planes performed by the examiner while the subject was sitting on a chair. A repeatability (i.e. dispersion, defined as the spread of orientation differences in the calibration quaternions obtained with different movement repetitions) of 2.4° for thigh and 2.0° for shank segment orientations was reported. Picerno et al. (2008) proposed an anatomical calibration method based on palpation of anatomical landmarks for measuring hip, knee, and ankle joint angles. They evaluated inter-rater and intra-rater repeatability based on the root mean square deviation (RMSD) from the mean joint angles estimated during the upright posture. Inter-rater RMSD was up to 6.6° and 7.3° for hip and knee internal/external rotation, but was $<2.4^\circ$ for the other angles. Similarly, inter-rater RMSD was up to 3.5°

and 4.9° for hip and knee internal/external rotation and was $<2.9^\circ$ for the other angles. Finally, Palermo et al. (2014) used two static postures (standing and lying on a bed) to functionally calibrate lower trunk and lower limb inertial sensors. They defined the repeatability as the standard deviation of the mean absolute variability computed on a set of two times three repeated trials. They reported a repeatability $<4^\circ$ for all angles except ankle internal/external rotation (7.2°). The calibration movements proposed in these studies have been proposed for gait analysis in clinical settings where the time limitation constraint and context are totally different than for in-field sport applications. In sport situations, e.g. alpine skiing, calibration should take minimal time and should be performed without external equipment such as a chair or bed. In addition, calibration movements could involve more complex movements and benefit from the athlete's high movement control abilities.

Although rarely specified, a wrong choice of initial segment orientation can noticeably affect the performance of the subsequent orientation tracking by adding orientation offsets. It is generally assumed that an initial posture is known (Sabatini, 2006) or can be measured (Miezel et al., 2016). Fusion schemes have also been proposed where wrong initial conditions have only minimal impact on orientation tracking; however, at the cost of having wrong orientation estimates during the first few seconds of tracking (Madgwick et al., 2011). Movement constraints and hypotheses for initialization were rarely stated explicitly. For the subsequent orientation tracking, the above cited methods were able to reduce drift sufficiently and to obtain accurate and precise estimates of segment orientations and joint angles for gait analysis. However, as mentioned before, these algorithms were designed for gait, indoor measurements, relatively slow movements, and movements mostly constrained to the sagittal plane. It remains unknown whether the results could be generalized to faster movements and movements taking place out of the sagittal plane such as present in sports. For example, it could be expected that fast movements diminish the performance of such algorithms: for slow movements, measured acceleration mainly reflects Earth's gravity. Sensor drift can be estimated by comparing measured gravity and true gravity (Favre et al., 2006). In fast movements, measured acceleration also contains acceleration from the movement itself (linear and rotational), thus masking Earth's gravity. As a consequence, the measured acceleration can no longer be compared to true gravity in order to have an estimate of inclination and, therefore, not being used to correct the drift (Seel et al., 2014). Nevertheless, the higher accelerations due to fast movements have the advantage to give high signal to noise ratio and could be exploited differently for drift estimation. For example, suppose acceleration is measured at known locations on two segments connected by a common joint. If the measured accelerations are high enough in all directions when being translated to this joint, the accelerations must be equal in both magnitude and direction. Any deviation could then be attributed to measurement errors, for example induced by drift. This concept using the joint acceleration constraint was successfully exploited in Chapter 5 and validated for the case of a single turn of alpine ski racing. Accuracy and precision of the outside leg's knee flexion were 1.7° and 4.3° , respectively. However, the observed accuracy greatly

varied between runs (standard deviation of 7.9°). Poorly performed calibration movements might be one plausible explanation for this observation. Accordingly, optimized calibration movements might help to improve the accuracy being achieved. Moreover, since the study was limited to flexion angles, it is still unclear how well the proposed joint drift reduction approach performs regarding the other two 3D angle components (i.e. ad/abduction and inter-external rotation angles).

Therefore, the aim of this study was (1) to propose and validate an improved functional calibration which is fast and usable in-field, and uses available sports equipment components (e.g. ski boots, poles) only; (2) to validate the 3D joint angles of the knee, hip, and trunk obtained by the use of this functional calibration for relatively long measurement durations (>30 seconds) in order to evaluate the impact of drift reduction.

6.2 Methods

6.2.1 Measurement Protocol

Eleven male competitive alpine skiing athletes (20.9 ± 5.2 years, 176.1 ± 6.7 cm, 74.0 ± 10.9 kg) were enrolled in the study. The study was approved by the university's local ethics committee (Study Number: HREC 006-2016) and athletes gave written informed consent prior to the measurements. The measurement protocol consisted of skiing on a specially designed indoor skiing carpet (Maxxtracks Indoor Skislopes, The Netherlands) with dimensions 6 m \times 11 m and 12° inclination (Fig. 6.1). After warming up and familiarization, athletes skied a total of four trials at 21 km/h. Each trial lasted 120 seconds and was divided in two parts during which wide (entire carpet width) and narrow (half carpet width, marked with cones) turns were skied respectively. This within-trial protocol was applied to long radii turns (140 cm long skis with a sidecut radius of 11 m) and short radii turns (110 cm long skis with a sidecut radius of 8 m), for which two trials were performed each (Table 6.1). A custom made belt exerted a variable backwards force to ensure that the athlete remained in the central part of the carpet (Fig. 6.1). Basic motion tasks (BMT, (List et al., 2013)) for the reference system were performed once at the beginning. The calibration movements (FC1-FC5) for the wearable system were performed once before each trial and once after the last trial (Table 6.1).

6.2.2 Reference System

The reference system consisted of ten infrared cameras (Vicon Peak, United Kingdom) covering the volume spanned by the skiing carpet. Sampling frequency was set at 100 Hz. Athletes were equipped with the IfB marker set (List et al., 2013; Husa-Russell et al., 2011; Wolf et al., 2009) (Fig. 6.2). Joint centres were determined functionally based on the data collected during the basic motion tasks. This setup allowed measuring 3D joint angles of ankle, knee, hip, and trunk (List et al., 2013) following the recommendations of

Trial code	Ski length	Speed	Turn types
BMT	-	-	-
FC1	-	-	Functional calibration 1
140A (test)	140 cm	21 km/h	45 sec wide / 45 sec narrow
FC2	-	-	Functional calibration 2
140B (retest)	140 cm	21 km/h	45 sec wide / 45 sec narrow
FC3	-	-	Functional calibration 3
110A (test)	110 cm	21 km/h	45 sec wide / 45 sec narrow
FC4	-	-	Functional calibration 4
110B (retest)	110 cm	21 km/h	45 sec wide / 45 sec narrow
FC5	-	-	Functional calibration 5

Table 6.1 – Order of tested skiing conditions, measured basic motion tasks (BMT) to calibrate the reference system and functional calibrations (FC1 – FC5) for the wearable system.

Grood and Suntay (1983). Joint angles were set to zero during a barefoot standing trial. Then, the feet markers were put on the ski shoes and a static trial was used to define the functionally determined ankle joint centre with respect to the four shank markers (without the malleoli markers). The assumption was made that the foot was parallel to the sole of the ski boot. Therefore, ankle angles represent the angle between the shank segment and the rigid foot segment of the ski boot.

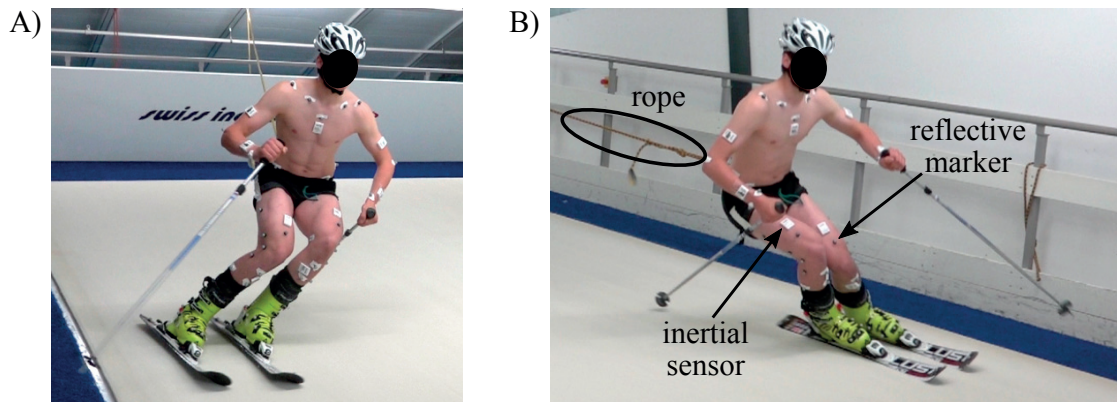


Figure 6.1 – Illustration of skiing on the indoor skiing carpet for trial condition 110A, wide turns. A) left turn, B) right turn. The rope was connecting an external weight with the athlete's belt for keeping him centred on the carpet. The inertial sensors can be identified as the small white boxes and the reflective markers as the small grey dots. The carpet surface was designed such that ski gliding friction is minimized.

6.2.3 Wearable system

Nine inertial sensors (Physilog 4, Gait Up, Switzerland) were attached with adhesive tape to the shanks, thighs, lower back (L5-L4 transition), sternum, upper back (T2-C7 transition), and head (Figs. 6.1, 6.2). Additional sensors not used in the present study

Chapter 6. Joint Drift Correction Improvements and Indoor Validation

were fixed slightly below T11 and to the upper limbs. The inertial sensors measured acceleration and angular velocity at 500Hz. Accelerometer offset and sensitivity were corrected according to Ferraris et al. (1995). Gyroscope offset was estimated during the upright posture of the functional calibration. The wearable system was synchronized with the reference system by an electronic trigger.

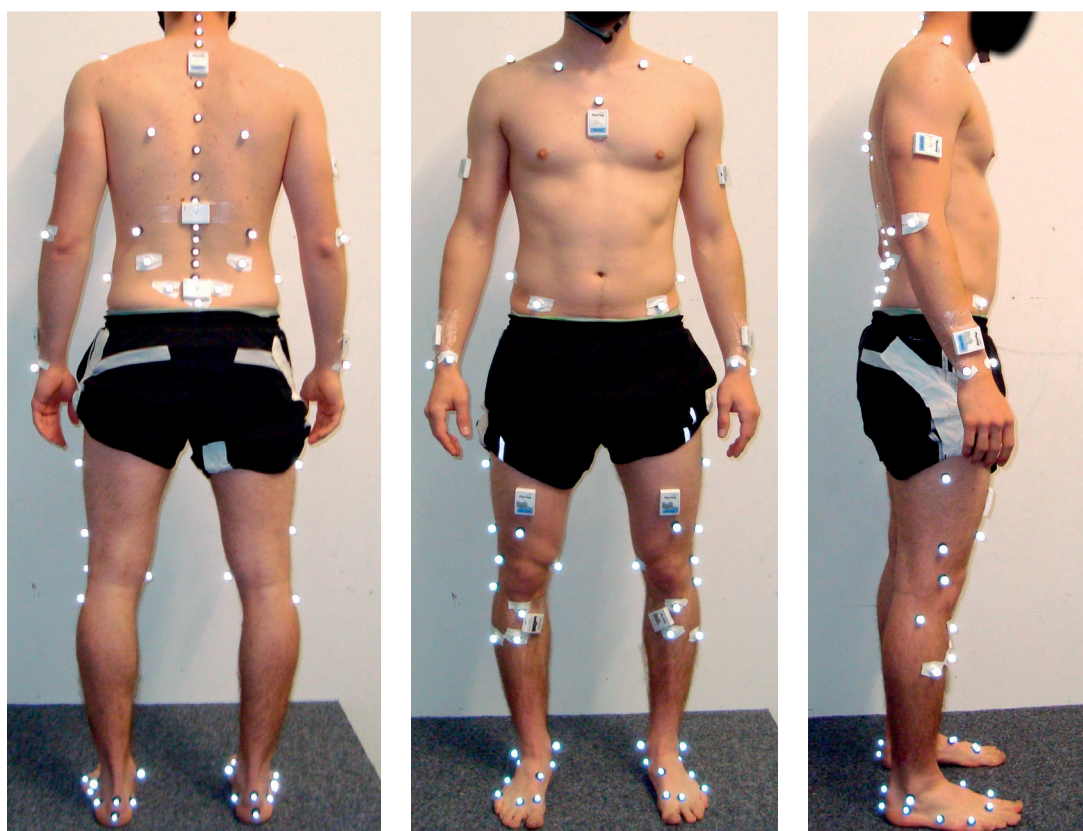


Figure 6.2 – Sensor and marker placement from the back, front and side view. One additional inertial sensor was fixed to the athlete's helmet (not shown).

Functional Calibration

In this study it is assumed that the functional calibration is a procedure to estimate the calibration quaternion which rotates the sensor frame to their corresponding segment anatomic frame. It was achieved based on the following movements: squats, trunk rotation, hip ad/abduction, and upright standing. The movements have been optimized to be performed in a minimum time while wearing ski boots and on-snow, requiring

no special equipment such as a scale or chair. Instructions on how to perform these movements and which movement was used to calibrate which sensor are provided in Table 6.2. Segment and joint coordinate systems were defined according to the ISB recommendations (Wu et al., 2002, 2005).

Since the movements were performed in ski boots they might not be executed properly, potentially leading to misalignment of the estimated anatomical frames. In order to counteract this problem, the segment's functional axes and "zero" joint angles were approximated by combining different calibration movements and biomechanical constraints according to the following hypotheses. The trunk and head sensors were calibrated based on the following hypotheses: 1) squat movements occur around the medio-lateral axis, 2) trunk rotations are performed along the vertical axis, 3) during upright posture the trunk segment is perfectly vertical (i.e. no flexion and lateral bending). The thigh sensors were calibrated based on the following hypotheses: 1) squat movements occur around the medio-lateral axis, 2) orientation differences of measured lower back and thigh acceleration translated to the hip joint centre are minimal, where acceleration was translated according to Eqs. 6.3-6.4. For the optimization procedure it was sufficient to fix the sensor-to-hip-joint-centre distance for the lower back sensor to (0.05 m, -0.10 m, 0.00 m) along the anterior-posterior, superior-inferior, lateral-medial anatomical axes. For the thigh it was sufficient to fix the sensor-to-hip-joint-centre distance at (-0.05 m, 0.30 m, 0.00 m). Shank sensors were calibrated according to the following hypotheses: 1) ad/abduction occurred around the anterior-posterior axis, 2) at the beginning of the ad/abduction movement the medio-lateral axis is perpendicular to gravity. Finally, the lower limb calibration was optimized according to the following hypotheses: 1) average knee flexion during the hip ad/abduction is zero, 2) medio-lateral axis of shank and thigh is perpendicular to gravity during upright standing, 3) left and right shanks and thighs have the same segment orientation at the beginning of the squat movement.

Estimating initial orientation

The segment orientations were estimated using the strap-down integration and joint drift correction presented in Chapter 5. The global frame was defined as follows: the Y-axis was aligned with gravity, pointing upwards. X-axis was perpendicular to gravity and pointing forwards in the direction of the fall-line. The Z-axis was the cross-product between the X- and Y-axis, pointing to the right. For determining the initial conditions of the strap-down integration, it was assumed that all trunk and lower limb segments had the same azimuth (i.e. were heading the same direction). The segments' inclinations were determined using gravity.

Chapter 6. Joint Drift Correction Improvements and Indoor Validation

Movement	Instruction	Calibrated segments	Calibrated axes
Squats	Slow squats with knee, hip, trunk, head flexion. Arms are parallel to leg, flex until fingers reach the ankles. Perform the movement three times.	Shank, thigh, lower back, upper back, sternum, head	Medio-lateral
Trunk rotations	Slow trunk rotations around the vertical axis with hips fixed. Arms hold a ski pole lying horizontally behind the neck. Head turns with the trunk. Perform the movement three times where rotation starts by looking to the right.	Lower back, upper back, sternum	Inferior-superior
Hip ad/abductions	Slow hip ad/abductions of the right leg. Control balance using the ski poles. Right heel is positioned in-line with left toe. Keep knee straight through the entire movement. Perform the movement of slow hip abduction and adduction three times. Then perform the same for left leg.	Shank, thigh	Anterior-posterior
Upright	Stand upright with knees slightly flexed. Keep equal weight on both feet. Look straight to the front. Stand still for 10 seconds.	Shank, thigh, lower back, upper back, sternum, head, head	Inferior-superior

Table 6.2 – Description of the functional calibration movements used to align the sensor axes to the segment axes.

Improved drift correction

Let's consider $\mathbf{a}_{distal}(t)$ and $\mathbf{a}_{proximal}(t)$ as the accelerations measured by the distal and proximal sensors placed at a certain distance \mathbf{r}_d and \mathbf{r}_p from the connecting joint, and $\tilde{\mathbf{a}}_{distal}^G(t)$ and $\tilde{\mathbf{a}}_{proximal}^G(t)$ as the distal and proximal accelerations translated to the connecting joint (Eqs. 6.1-6.4). As proposed in Chapter 5, theoretically there should not be any difference in orientation between $\tilde{\mathbf{a}}_{distal}^G(t)$ and $\tilde{\mathbf{a}}_{proximal}^G(t)$. Therefore, any orientation difference should express only error. In Chapter 5 this error was considered as drift and was expressed by the quaternion $\delta(t)$ (Eqs. 6.5-6.7).

$$\tilde{\mathbf{a}}_{distal}^G(t) = R_{distal}^G(t) \tilde{\mathbf{a}}_{distal}(t) \quad (6.1)$$

$$\tilde{\mathbf{a}}_{proximal}^G(t) = R_{proximal}^G(t) \tilde{\mathbf{a}}_{proximal}(t) \quad (6.2)$$

$$\tilde{\mathbf{a}}_{distal}(t) = \mathbf{a}_{distal}(t) + \dot{\omega}_{distal}(t) \times \mathbf{r}_d + \omega_{distal}(t) \times (\omega_{distal}(t) \times \mathbf{r}_d) \quad (6.3)$$

$$\begin{aligned} \tilde{\mathbf{a}}_{proximal}(t) &= \mathbf{a}_{proximal}(t) + \dot{\omega}_{proximal}(t) \times \mathbf{r}_p \\ &\quad + \omega_{proximal}(t) \times (\omega_{proximal}(t) \times \mathbf{r}_p) \end{aligned} \quad (6.4)$$

$$\delta(t) = \left[\cos\left(\frac{\beta(t)}{2}\right), \sin\left(\frac{\beta(t)}{2}\right) U(t) \right] \quad (6.5)$$

$$\beta(t) = \arccos\left(\frac{\tilde{\mathbf{a}}_{distal}^G(t) \cdot \tilde{\mathbf{a}}_{proximal}^G(t)}{|\tilde{\mathbf{a}}_{distal}^G(t)| \cdot |\tilde{\mathbf{a}}_{proximal}^G(t)|}\right) \quad (6.6)$$

$$U(t) = \frac{\tilde{\mathbf{a}}_{distal}^G(t) \times \tilde{\mathbf{a}}_{proximal}^G(t)}{|\tilde{\mathbf{a}}_{distal}^G(t) \times \tilde{\mathbf{a}}_{proximal}^G(t)|} \quad (6.7)$$

where $R_{distal}^G(t)$ and $R_{proximal}^G(t)$ are the drift-affected orientations at time t of the distal and proximal segment estimated by the strap-down integration expressed in the global frame and $\omega_{distal}(t)$ and $\omega_{proximal}(t)$ are the angular velocities of the distal and proximal segments. $\beta(t)$ and $U(t)$ is the axis-angle representation of the quaternion $\delta(t)$. Drift was estimated for all time instants t satisfying Eqs. 6.8-6.10, by considering high signal to noise ratio:

$$\left| |\tilde{\mathbf{a}}_{distal}^G(t)| - |\tilde{\mathbf{a}}_{proximal}^G(t)| \right| < th_{min} \quad (6.8)$$

$$|\tilde{\mathbf{a}}_{distal}^G(t)| > th_{max} \quad (6.9)$$

$$|\tilde{\mathbf{a}}_{proximal}^G(t)| > th_{max} \quad (6.10)$$

In our previous study, th_{min} and th_{max} were selected to $2.5m/s^2$ and $8m/s^2$ to include only samples with high signal to noise ratio. However, these thresholds were good for on-snow skiing with relatively high accelerations. Since skiing speed for indoor carpet skiing was substantially lower, th_{max} was fixed to $6m/s^2$ and the constraint on th_{min} was adapted to include all samples with less than 20% acceleration magnitude difference (Eq. 6.11):

$$\frac{\left| |\tilde{\mathbf{a}}_{distal}^G(t)| - |\tilde{\mathbf{a}}_{proximal}^G(t)| \right|}{0.5 \left(|\tilde{\mathbf{a}}_{distal}^G(t)| + |\tilde{\mathbf{a}}_{proximal}^G(t)| \right)} < 0.2 \quad (6.11)$$

Not all orientation misalignments between $\tilde{\mathbf{a}}_{distal}^G(t)$ and $\tilde{\mathbf{a}}_{proximal}^G(t)$ could be explained by drift. In addition to drift, other estimation error sources might be present: inaccurately estimated \mathbf{r}_d and \mathbf{r}_p or different kinematics for the distal and proximal segments (e.g. different soft tissue artefact in the proximal segment compared to the distal segment). As can be noticed in Fig. 6.3, in addition to a potentially linear drift, the instantaneous drift magnitude $\delta(t)$ is correlated to the changing knee angle between left and right turns. Therefore, to minimize the movement's influence on the estimated drift, $\delta(t)$ should be averaged over at least one movement cycle. For this study, we chose to average over two movement cycles. A movement cycle was determined to include a left and a right turn. It was assumed that a movement cycle starts at a local maximum of the segment's angular velocity in the global frame's X-axis. For estimating the drift, axes with larger accelerations are weighed more. Due to Earth's gravity there is always considerable acceleration along the vertical axis. Thus, the proposed joint drift method may miss drift along the azimuth axis since accelerations in the horizontal plane are too small compared to the acceleration along the vertical axis. Therefore, joint drift was corrected a second time by setting all acceleration along the vertical axis in the global frame to zero (Eqs. 6.12-6.13).

$$\hat{\mathbf{a}}_{distal}^G(t) = [\tilde{\mathbf{a}}_{distal,X}^G(t), 0, \tilde{\mathbf{a}}_{distal,Y}^G(t)] \quad (6.12)$$

$$\hat{\mathbf{a}}_{proximal}^G(t) = [\tilde{\mathbf{a}}_{proximal,X}^G(t), 0, \tilde{\mathbf{a}}_{proximal,Y}^G(t)] \quad (6.13)$$

Since the vertical axis has been set to zero, the threshold th_{max} (Eqs. 6.9 - 6.10) for valid drift estimation samples had to be adapted and was set to $th_{min} = 0.6m/s^2$ where a trade-off between strict conditions and enough available valid samples had to be found. The drift was averaged over the same time windows as for the initial estimation.

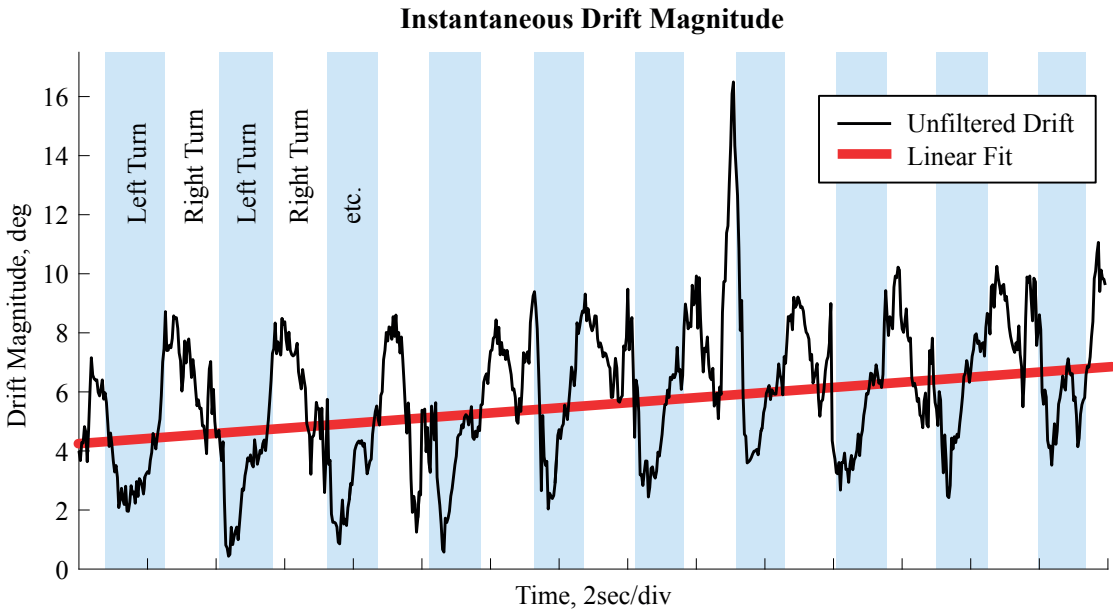


Figure 6.3 – Estimated drift magnitude for the left thigh for 30 seconds of a typical trial showing the existence of noise due to kinematic components of the movement. Left turns are marked in light blue. The red line shows a linear fit to the drift magnitude for illustration purpose only.

Computing the joint angles

The 3D joint angles of the knee and hip were computed following the ISB recommendations (Wu et al., 2002) and Grood and Suntay (1983). Knee angles $\alpha_{[left/right]knee}(t)$ were computed based on the shank and thigh orientations. Hip angles $\alpha_{[left/right]hip}(t)$ were computed based on the thigh and lower back orientations. The 3D joint angles for the trunk were computed using a slightly adapted version of Grood and Suntay as done in earlier studies (Spörri et al., 2016a, 2015). The trunk angles were computed in two ways: $\alpha_{l.back-stern}(t)$ used the lower back and sternum orientation, as in Spörri et al. (2016a) and Chapter 5. $\alpha_{l.back-u.back}(t)$ (t) used the lower back and upper back orientation.

6.2.4 Validation

Functional Calibration

The proposed functional calibration procedure was validated based on the repeatability of the calibration quaternions (i.e. influence of the movements on the calibration quaternion) and on the repeatability of the 3D knee, hip, and trunk angles (i.e. error propagation from calibration quaternion to joint angles). Both quantities were defined as proposed by Favre et al. (2009) where the repeatability of the calibration quaternion was defined as the dispersion χ of the five calibration quaternions $q_{A,F}$ (for each athlete A and each functional calibration F) around their mean q_A for all athletes (Eq. 6.14-6.15).

$$\chi = \sqrt{\frac{1}{A F - 1} \sum_{A,F} \Delta_{A,F}^2} \quad (6.14)$$

$$\Delta_{A,F} = 2 \cos \left(\left| q_A \otimes q_{A,F}^{-1} \right|_{real} \right) \quad (6.15)$$

where $\Delta_{A,F}$ corresponds to the orientation angle difference between q_A and $q_{A,F}$. A denotes the athletes $\{1, \dots, 10\}$, F the functional calibrations $\{1, \dots, 5\}$, and \otimes the quaternion multiplication. The repeatability of the 3D joint angles was obtained by computing first an average joint angle $\bar{\alpha}_{A,J}(t)$ for each angle J and athlete A based the mean of the five functional calibrations applied to the same trial (Eq. 6.16).

$$\bar{\alpha}_{A,J}(t) = \frac{1}{5} \sum_{F=1}^5 \alpha_{A,J,F}(t) \quad (6.16)$$

Trial 110A has been chosen for this purpose. Then, the difference between the five angles $\alpha_{A,J,F}(t)$ and $\bar{\alpha}_{A,J}(t)$ was computed for each athlete and their mean $\Lambda_{A,J,F}^{mean}$ and standard deviation $\Lambda_{A,J,F}^{std}$ was computed over time. Next, the mean absolute deviation of $\Lambda_{A,J,F}^{mean}$ and the mean of $\Lambda_{A,J,F}^{std}$ was computed by averaging over the five functional calibrations for each athlete. Finally, these values were averaged over all athletes to obtain the offset Λ_J^{mean} and precision Λ_J^{std} for each joint angle. The coefficient of multiple correlation $CMC_{J,A}$ was computed between $\alpha_{A,J,F}(t)$ of the five functional calibrations and then averaged over all athletes to obtain CMC_J (Favre et al., 2009; Kadaba et al., 1989).

Joint Angles

The 3D joint angles computed with the wearable system were down-sampled to 100 Hz to match the sampling frequency of the reference system. For each of the four trials per athlete the functional calibration immediately preceding the trial was taken. The joint angle error $\epsilon_{A,T,J}(t)$ was defined as the sample-by-sample difference between the

wearable and the reference system for trial T (Eq. 6.17).

$$\epsilon_{A,T,J}(t) = \alpha_{A,T,J}^{wearable}(t) - \alpha_{A,T,J}^{reference}(t) \quad (6.17)$$

Per-Trial accuracy and precision were then defined as the mean $\mu_{A,T,J}$ and standard deviation $\sigma_{A,T,J}$ of $\epsilon_{A,T,J}(t)$ over time. The relationship between the joint angles obtained with the wearable and reference systems was assessed by Pearson's correlation coefficient $c_{A,T,J}$. Overall accuracy and precision were then defined as the average and standard deviation of $\mu_{A,T,J}$, respectively $\sigma_{A,T,J}$, computed over all trials and athletes. Overall correlation was obtained the same way.

6.3 Results

Functional calibration and joint angle validity could be assessed for all 11 athletes and trials, resulting in a total of 44 trials. Results for left and right side were similar. Thus, in the following only the results for the left side are presented. Similarly, no differences between upper trunk orientation computed from the sternum or upper trunk sensors were found. Thus, the results for trunk segment and joint orientation are only shown with respect to the lower trunk – sternum sensors. The appendix provides an exhaustive presentation of the results for both left and right sides and for the trunk angles computed based on the upper trunk sensor.

6.3.1 Functional Calibration

Dispersion (χ) of the calibration quaternion ranged from 5.5° for the shank to 1.6° for the sternum (Table 6.3). Joint angle repeatability offset (Λ_J^{mean}) was $<2.7^\circ$ for all angles. Generally, offsets for the flexion axis were 1° larger than for the other axes. Repeatability standard deviation (Λ_J^{std}) ranged between 0.5° and 1.5° . Average CMC was >0.87 for the lower limbs and >0.81 for the neck but lower for the trunk with a minimum CMC of 0.5 for trunk flexion (Table 6.4).

Segment	Dispersion χ
Left Shank	5.50°
Left Thigh	2.94°
Lower back	4.11°
Sternum	1.57°
Head	3.13°

Table 6.3 – Dispersion of the calibration quaternions

		Repeatability Offset	Repeatability Standard Deviation	CMC
Left Knee	Flexion, deg	2.0 (0.7)	1.4 (0.6)	0.934 (0.021)
	Abduction, deg	1.0 (0.4)	0.5 (0.2)	0.941 (0.055)
	Rotation, deg	0.8 (0.3)	0.7 (0.2)	0.932 (0.059)
Left Hip	Flexion, deg	2.7 (1.1)	0.5 (0.2)	0.957 (0.031)
	Abduction, deg	1.2 (1.0)	0.7 (0.2)	0.866 (0.287)
	Rotation, deg	1.3 (0.9)	0.7 (0.3)	0.970 (0.043)
Trunk	Flexion, deg	2.1 (1.2)	0.3 (0.3)	0.490 (0.335)
	Abduction, deg	1.5 (1.4)	0.3 (0.3)	0.741 (0.402)
	Rotation, deg	0.7 (0.8)	0.4 (0.3)	0.883 (0.271)
Neck	Flexion, deg	2.2 (1.1)	0.4 (0.3)	0.835 (0.162)
	Abduction, deg	1.1 (1.4)	0.6 (0.4)	0.864 (0.229)
	Rotation, deg	1.8 (2.3)	0.8 (0.6)	0.808 (0.301)

Table 6.4 – Joint angle repeatability and CMC. Reported are mean values (standard deviation) for the calibration repeatability of all eleven athletes.

6.3.2 3D Joint Angles

Reference angle minima and maxima were largest for knee and hip flexion with $36.3^\circ - 74.7^\circ$ and $-67.2^\circ - -24.8^\circ$, respectively. They were smallest for trunk abduction with $\pm 6.3^\circ$ (Table 6.5). Accuracy ranged from -10.7° for the left hip flexion to 4.2° for the left knee abduction. Precision ranged from 2.2° for the trunk flexion up to 4.9° for the left hip internal rotation (Table 6.5). Correlation between the wearable and reference system was above 0.9 except for the left knee internal/external rotation and for all three trunk angles (Table 6.5). The adapted joint drift correction proposed in this study allowed to reduce the azimuth drift. For a typical trial 3D knee joint angles obtained with and without the proposed azimuth drift correction are compared in Fig. 6.4. Azimuth drift correction allowed to reduce azimuth drift and also decreased axis cross-talk for the flexion and ad/abduction angles. For illustration purposes, joint angles for a typical trial of condition 110B were segmented into double turns (left and right turn), time-normalized and averaged for thirteen wide turns (Fig. 6.5).

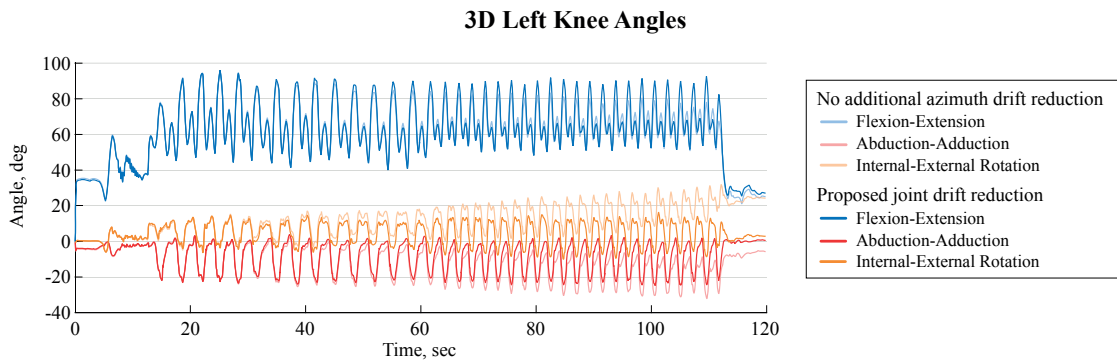


Figure 6.4 – Comparison of the 3D knee angles for the joint drift reduction without the proposed azimuth drift correction (light colours) and with the additional azimuth drift correction (dark colours).

Chapter 6. Joint Drift Correction Improvements and Indoor Validation

		Reference		Wearable		Error		
		Min.	Max.	Min.	Max.	Accuracy	Precision	Correlation
Left Knee	Flexion, deg	36.3 (5.6)	74.7 (8.4)	33.9 (6.5)	77.1 (12.2)	-0.1 (7.4)	3.4 (1.4)	0.955 (0.043)
	Abduction, deg	-11.6 (4.1)	2.3 (2.9)	-11.5 (6.3)	11.9 (4.9)	4.2 (5.5)	3.6 (0.9)	0.919 (0.094)
	Rotation, deg	-9.4 (3.7)	10.2 (3.4)	-11.4 (4.4)	11.2 (4.8)	0.0 (4.4)	3.8 (1.2)	0.781 (0.172)
Left Hip	Flexion, deg	-67.2 (11.0)	-24.8 (7.9)	-82.7 (10.5)	-32.6 (8.8)	-10.7 (4.3)	3.6 (1.3)	0.974 (0.016)
	Abduction, deg	-10.5 (5.6)	16.5 (6.2)	-14.7 (5.7)	14.0 (7.6)	-3.3 (4.1)	3.1 (1.4)	0.896 (0.135)
	Rotation, deg	-30.5 (5.9)	23.6 (5.7)	-24.0 (5.4)	21.1 (7.0)	0.5 (4.8)	4.9 (1.5)	0.977 (0.013)
Trunk	Flexion, deg	3.7 (5.6)	16.6 (5.6)	5.8 (5.5)	16.6 (4.9)	1.1 (6.4)	2.2 (0.9)	0.711 (0.208)
	Abduction, deg	-6.3 (3.2)	6.3 (3.8)	-8.7 (3.7)	8.5 (3.6)	0.1 (3.6)	2.6 (0.9)	0.790 (0.199)
	Rotation, deg	-6.7 (4.4)	7.0 (3.5)	-10.2 (7.0)	9.4 (4.0)	-0.6 (2.5)	3.6 (1.5)	0.669 (0.309)

Table 6.5 – Reference and wearable minimum and maximum angles and accuracy (error mean), precision (error standard deviation), and correlation. Values are given as mean (standard deviation) of all trials.

6.4 Discussion

In this study a new functional calibration that can easily be used in-field was proposed and validated. The calibration movements were designed such they could be performed wearing ski boots and using ski poles. In addition, the previously presented joint drift correction method from Chapter 5 was improved (Fig. 6.4). 3D joint angles of the knee, hip and trunk estimated with the inertial sensors (wearable system) were validated against reference angles obtained with a marker-based stereo-photogrammetric system during indoor carpet skiing.

6.4.1 Functional Calibration

Functional calibration movements proposed in the past required either active or passive movements of the lower limbs (Favre et al., 2009) or standing and lying postures (Palermo et al., 2014). Since these movements were not dedicated to outdoor movements and cannot be performed reliably by athletes wearing ski boots, new and adapted functional calibration movements have been proposed. The main difficulty comes from aligning the inertial sensors to the body segments in the sagittal plane. The ski boots imposed an ankle flexion of approximately 17° in standing posture, making impossible the acquisition of a neutral pose required to initialize joint angles to 0° (Favre et al., 2009; Leardini et al., 1999; Della Croce et al., 1999). Thus, in the proposed scenario, the "zero" joint angle was approximated by combining the different calibration movements and biomechanical

constraints. In addition to that, the proposed approach was sufficiently repeatable: joint angle offsets between different repetitions of functional calibrations were below 2.7° and their impact on joint angle precision was below 1.4° (Table 6.4). CMC for trunk angles was low, probably due to the small angle ranges (Table 6.5). The results are comparable to previous studies which also reported repeatability ranging between 2° and 4° for most joint angles (Favre et al., 2009; Picerno et al., 2008; Palermo et al., 2014). Despite this high repeatability, a comparatively high standard deviation of joint flexion angle offsets (up to 7.4° for the knee, Table 6.4) was observed. Post-hoc one-way ANOVA for the knee flexion offset showed that 86.5% of its total variance was explained by the between-athlete variance and only 13.5% was explained by the within-athlete variance. Thus, the functional calibration provided highly repeatable results within athletes, but not between athletes. The computed joint angles contained an athlete-specific bias. While this could easily be corrected with a neutral posture without ski boots, further work may be required to remove the athlete-specific bias when wearing ski boots.

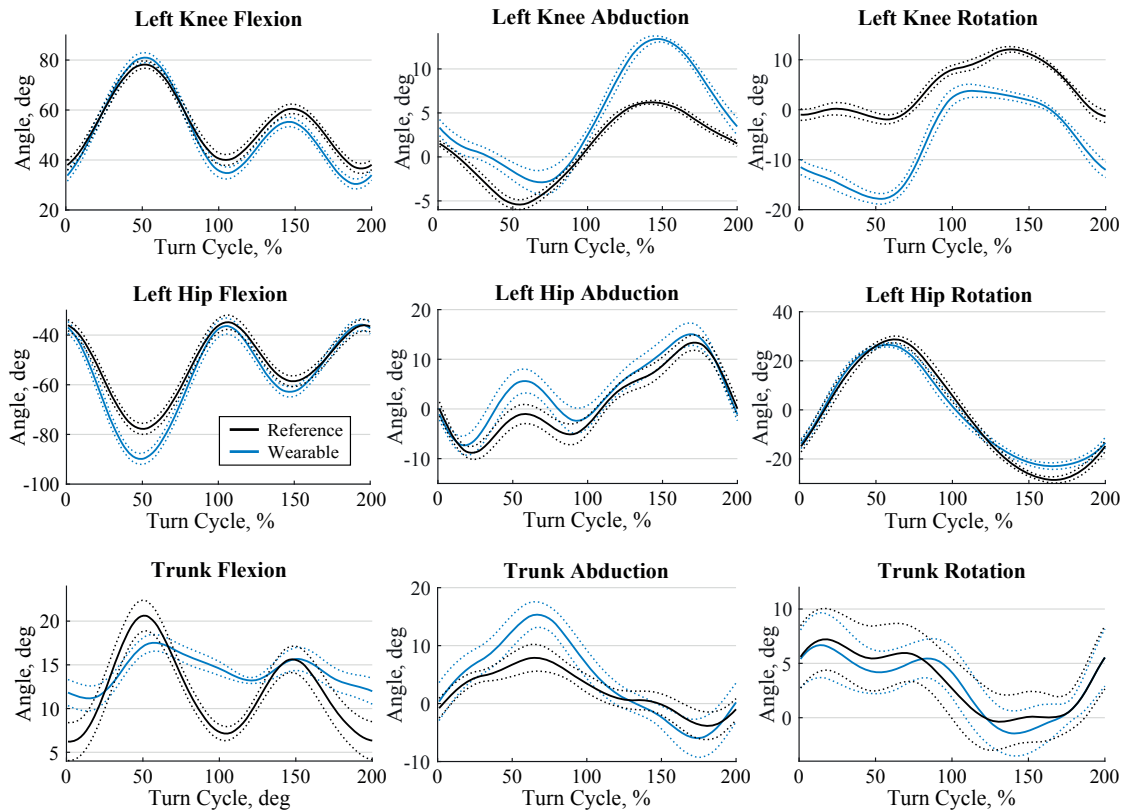


Figure 6.5 – Time normalized joint angles for the knee, hip and trunk of a typical athlete for 13 wide double turns (left and right turn) of trial 110B. The first 100% of the turn cycle is a left turn where the left leg is the inside leg. The second 100% of the turn cycle is a right turn where the left leg is the outside leg. Solid line is the average and dotted the standard deviation. Black is the reference system and blue the wearable system.

6.4.2 3D Joint Angles

The 3D joint angles estimated with the wearable system showed a good agreement to the reference system (precision of $2.2^\circ - 4.9^\circ$, correlation >0.9 for most joint angles). In a similar validation study focusing on sports movements and using a Kalman filter to estimate orientations Jakob et al. (2013) reported knee flexion root mean square error (RMSE) between 7.0° for walking to 10.2° for running with correlation values >0.95 . However, they partly removed systematic offsets between wearable and reference system for each trial prior to computing the RMSE, making a comparison to our results difficult. We chose not to align the anatomical and functional frames of both systems, since we wanted to assess how well the proposed functional calibration is able to approximate the joint kinematics in the anatomical frame. Compared to Favre et al. (2009) accuracy of the proposed system (mean absolute difference (standard deviation) of 5.7° (4.7°), 6.0° (3.4°), 3.2° (3.0°) for left knee flexion, abduction, and rotation, respectively) was better, but precision was worse. Improved accuracy could be explained by the different functional calibration procedure. The worse precision could be explained by the higher joint range of motion and movement dynamic, and, therefore, a different (potentially increased) amount of soft tissue artefact (Leardini et al., 2005). However, even though marker setup was chosen such as to minimize influence of soft tissue artefacts and joint angle estimation errors due to small errors in marker placement (List et al., 2013), knee ad/abduction and internal/external angles should be interpreted with care; both for the reference system and for the wearable system. Precision was best for the trunk angles, however the correlation between the wearable and reference system was below 0.8. On the one hand, these small correlation values could originate in the small range of motion of only $15^\circ - 20^\circ$ for all axes. On the other hand, the different definition of trunk angles between the two systems could also explain the reduced correlation: while for the reference system the trunk angles were defined as the orientation difference between the pelvis and cervical spine segments, for the wearable system the trunk angles were defined as the orientation difference between the lower back and sternum. Since precision (but not accuracy) of all axes was good, the angle curves could be well suited for comparing differences in shape, but not absolute values. For example, the system would be suitable to detect angle pattern differences caused by a change of condition, such as the difference between different turn techniques or equipment used.

In this study, the long acquisition duration with both the reference and the wearable system allowed to validate the drift reduction algorithm for periods of up to two minutes. The improved joint drift reduction did allow a better drift reduction along the vertical axis (azimuth drift). The azimuth drift reduction did not only improve the joint's internal-external angles, but also reduced axis-cross talk, improving the angles along all three axes (Fig. 6.4). Moreover, since only acceleration and angular velocity were used, the system was independent from magnetic distortions as present indoors due to metallic structures. Therefore, in contrast to other drift reduction methods using magnetometer measurements, the system would be an ideal choice for indoor measurements on the

skiing carpet and could also be used for other sports such as treadmill cross-country skiing.

6.4.3 Methodological considerations

A limitation of the current study might have been the limited speed when skiing on the indoor carpet (21 km/h). As a consequence, joint accelerations were smaller and the thresholds for including valid samples for joint drift correction that were proposed in Chapter 5 had to be adapted. Since the proposed thresholds are dependent on the measured acceleration, they can also be used for on-snow measurements where higher accelerations are present. Thus, the validity of joint angles for on-snow measurements can be considered guaranteed as well. Potential joint angle errors for on-snow measurements might be higher due to the ski chattering-induced vibration noise from the ski-snow interaction. This noise might reduce the observed systems precision by a few degrees but should be still smaller than the precision of 6° reported for the hip flexion in Chapter 5.

6.5 Conclusion

An optimized functional calibration movement was proposed and validated. The wearable system was able to estimate the 3D joint angles for hip and trunk, as well as the knee flexion angle. The knee ad/abduction and internal/external rotation should be interpreted with care as the estimated angles may include axis-cross talk and soft tissue artefacts. The accuracy might not be sufficient for absolute angle comparisons across different athletes. However, the system should be sufficiently sensitive for within-athlete comparisons assessing the influence of certain conditions or interventions on joint kinematics. Further investigation should be targeted on reducing soft tissue artefacts of the thigh.

Acknowledgements

The authors would like to thank Swiss Indoor Skiing for providing us access to their indoor skiing carpet.

6.6 Appendix

Segment	Dispersion χ
Left Shank	5.50°
Right Shank	4.43°
Left Thigh	2.94°
Right Thigh	3.08°
Lower back	4.11°
Upper back	2.85°
Sternum	1.57°
Head	3.13°

Table 6.6 – Dispersion of the calibration quaternions

		Repeatability Offset	Repeatability Standard Deviation	CMC
Left Knee	Flexion, deg	2.0 (0.7)	1.4 (0.6)	0.934 (0.021)
	Abduction, deg	1.0 (0.4)	0.5 (0.2)	0.941 (0.055)
	Rotation, deg	0.8 (0.3)	0.7 (0.2)	0.932 (0.059)
Right Knee	Flexion, deg	1.9 (0.5)	1.3 (0.4)	0.944 (0.032)
	Abduction, deg	1.2 (0.5)	0.6 (0.2)	0.895 (0.113)
	Rotation, deg	1.2 (0.6)	0.7 (0.3)	0.846 (0.149)
Left Hip	Flexion, deg	2.7 (1.1)	0.5 (0.2)	0.957 (0.031)
	Abduction, deg	1.2 (1.0)	0.7 (0.2)	0.866 (0.287)
	Rotation, deg	1.3 (0.9)	0.7 (0.3)	0.970 (0.043)
Right Hip	Flexion, deg	2.7 (1.0)	0.5 (0.3)	0.958 (0.034)
	Abduction, deg	1.2 (0.7)	0.8 (0.2)	0.870 (0.262)
	Rotation, deg	1.4 (1.0)	0.7 (0.3)	0.966 (0.040)
Trunk	Flexion, deg	2.1 (1.2)	0.3 (0.3)	0.490 (0.335)
<i>lower trunk - sternum</i>	Abduction, deg	1.5 (1.4)	0.3 (0.3)	0.741 (0.402)
	Rotation, deg	0.7 (0.8)	0.4 (0.3)	0.883 (0.271)
Trunk	Flexion, deg	2.2 (1.3)	0.4 (0.3)	0.519 (0.357)
<i>lower trunk - upper trunk</i>	Abduction, deg	1.6 (1.3)	0.4 (0.3)	0.715 (0.370)
	Rotation, deg	1.0 (0.8)	0.7 (0.6)	0.840 (0.302)
Neck	Flexion, deg	2.2 (1.1)	0.4 (0.3)	0.835 (0.162)
	Abduction, deg	1.1 (1.4)	0.6 (0.4)	0.864 (0.229)
	Rotation, deg	1.8 (2.3)	0.8 (0.6)	0.808 (0.301)

Table 6.7 – Joint angle repeatability and CMC. Reported are mean values (standard deviation) for the calibration repeatability of all eleven athletes.

6.6. Appendix

		Reference		Wearable		Accuracy	Error	
		Min.	Max.	Min.	Max.		Precision	Correlation
Left Knee	Flexion, deg	36.3 (5.6)	74.7 (8.4)	33.9 (6.5)	77.1 (12.2)	-0.1 (7.4)	3.4 (1.4)	0.955 (0.043)
	Abduction, deg	-11.6 (4.1)	2.3 (2.9)	-11.5 (6.3)	11.9 (4.9)	4.2 (5.5)	3.6 (0.9)	0.919 (0.094)
	Rotation, deg	-9.4 (3.7)	10.2 (3.4)	-11.4 (4.4)	11.2 (4.8)	0.0 (4.4)	3.8 (1.2)	0.781 (0.172)
Right Knee	Flexion, deg	36.3 (5.7)	71.1 (6.8)	32.4 (6.4)	76.9 (9.6)	-1.3 (8.0)	4.1 (2.7)	0.926 (0.131)
	Abduction, deg	-10.8 (2.8)	2.9 (2.5)	-10.6 (6.5)	13.0 (4.0)	4.8 (3.7)	3.8 (1.2)	0.922 (0.085)
	Rotation, deg	-8.6 (3.7)	8.1 (4.9)	-9.8 (6.2)	10.8 (5.8)	0.8 (5.7)	3.4 (1.2)	0.796 (0.154)
Left Hip	Flexion, deg	-67.2 (11.0)	-24.8 (7.9)	-82.7 (10.5)	-32.6 (8.8)	-10.7 (4.3)	3.6 (1.3)	0.974 (0.016)
	Abduction, deg	-10.5 (5.6)	16.5 (6.2)	-14.7 (5.7)	14.0 (7.6)	-3.3 (4.1)	3.1 (1.4)	0.896 (0.135)
	Rotation, deg	-30.5 (5.9)	23.6 (5.7)	-24.0 (5.4)	21.1 (7.0)	0.5 (4.8)	4.) (1.5)	0.977 (0.013)
Right Hip	Flexion, deg	-68.1 (10.5)	-25.8 (8.1)	-83.1 (9.6)	-31.0 (8.4)	-9.1 (4.9)	4.1 (1.2)	0.966 (0.026)
	Abduction, deg	-11.6 (4.3)	15.5 (7.1)	-13.1 (5.4)	14.6 (8.1)	-1.4 (3.5)	3.2 (1.4)	0.882 (0.173)
	Rotation, deg	-22.4 (5.5)	31.7 (4.9)	-20.7 (8.5)	22.9 (5.1)	-2.8 (3.6)	5.2 (2.1)	0.980 (0.011)
Trunk <i>lower trunk - sternum</i>	Flexion, deg	3.7 (5.6)	16.6 (5.6)	5.8 (5.5)	16.6 (4.9)	1.1 (6.4)	2.2 (0.9)	0.711 (0.208)
	Abduction, deg	-6.3 (3.2)	6.3 (3.8)	-8.7 (3.7)	8.5 (3.6)	0.1 (3.6)	2.6 (0.9)	0.790 (0.199)
	Rotation, deg	-6.7 (4.4)	7.0 (3.5)	-10.2 (7.0)	9.4 (4.0)	-0.6 (2.5)	3.6 (1.5)	0.669 (0.309)
Trunk <i>lower trunk - upper trunk</i>	Flexion, deg	3.7 (5.6)	16.6 (5.6)	6.6 (6.2)	17.9 (5.9)	2.4 (6.0)	2.0 (0.8)	0.754 (0.164)
	Abduction, deg	-6.3 (3.2)	6.3 (3.8)	-8.7 (4.1)	8.5 (4.3)	0.1 (3.7)	2.7 (1.0)	0.762 (0.254)
	Rotation, deg	-6.7 (4.4)	7.0 (3.5)	-10.4 (6.5)	11.4 (4.0)	0.3 (4.0)	4.2 (1.4)	0.635 (0.369)

Table 6.8 – Reference and wearable minimum and maximum angles and accuracy (error mean), precision (error standard deviation), and correlation. Values are given as mean (standard deviation) of all trials.

7 Validation of Athlete Body Model and Center of Mass Position

Abstract

This study proposes a method to use inertial sensors to estimate the athlete's posture and center of mass (CoM) position with respect to the lumbar joint center for alpine skiing. Inertial sensors fixed to the lower and upper limbs, trunk, and head allowed to estimate the ankle, knee, hip, shoulder, elbow, and wrist joint positions as well as the athlete's CoM. The relative joint and CoM positions were validated against a marker-based optoelectronic motion capture system during indoor carpet skiing. For all joints analyzed position accuracy (mean error) was below 110 mm and precision (error standard deviation) was below 30 mm. CoM accuracy and precision were 25.7 mm and 6.7 mm. For the purpose of performance feedback, the proposed method allowed to obtain the distance between the outside leg's ankle and CoM (representing the skier's overall vertical motion) with an accuracy and precision of below 11 mm and was sensitive to changes in equipment and turn type (wide / narrow). The fore/aft position could not be estimated with sufficient accuracy and precision for performance feedback. Thus, the proposed method could provide sufficient precision for computing the relative CoM and conducting performance analysis in-field and during regular on-snow training. In order to better track the absolute CoM position, the proposed system could be combined with a global navigation satellite system.

Keywords: body sensor networks, inertial sensors, joint positions, center of mass, body model, movement analysis

Chapter to be submitted as B. Fasel, J. Spörri, P. Schütz, S. Lorenzetti and K. Aminian. "Estimation and validation of relative joint positions and athlete's center of mass for skiing movements", to the Special Issue "Wearable Sensor Technology for Monitoring Training Load and Health in the Athletic Population" in *Frontiers in Physiology*

7.1 Introduction

Measuring the athlete's center of mass (CoM) kinematics plays a central role for analyzing performance in alpine ski racing (Federolf et al., 2008; Federolf, 2012; Hébert-Losier et al., 2014; Kipp et al., 2008; Reid, 2010; Schieffermüller et al., 2005; Spörri et al., 2012a; Supej et al., 2011, 2003). Earlier studies primarily used video-based stereo-photogrammetric systems to determine athletes' CoM kinematics on a ski track (Federolf, 2012; Hébert-Losier et al., 2014; Spörri et al., 2012a; Supej et al., 2003). Under such in-field conditions, photogrammetric errors of <1.5 cm were reported (Klous et al., 2010; Spörri et al., 2016d). However, measurement setup is complex, capture volume is limited to a few turns only and post-processing is very time consuming. For those reasons, in recent years, differential navigation satellite systems (GNSS) have gained attention as being a valuable alternative for estimating absolute CoM kinematics in-field (Brodie et al., 2008; Fasel et al., 2016e; Gilgien et al., 2015c,a, 2013, 2016, 2014a,b; Kröll et al., 2016b; Lachapelle et al., 2009; Supej et al., 2013; Supej, 2010; Waegli and Skaloud, 2009). However, because the GNSS antenna cannot be placed on the CoM directly, the relative position of the GNSS antenna with respect to the CoM needs to be estimated. For that purpose the most simple method is a pendulum model suggested by Gilgien et al. (2015c); Supej et al. (2013). An alternative might also be the fusion or combination of GNSS with body worn inertial sensor systems (Brodie et al., 2008; Fasel et al., 2016e). Accelerated by the recent advantages in measurement technology, several experimental field studies considered these systems to estimate the athlete's posture and the relative CoM (Brodie et al., 2008; Fasel et al., 2016e; Supej, 2010). However, only Fasel et al. (2016e) validated the CoM and joint center trajectories that were obtained by the use of a body model with eight segments (left/right shank, left/right thigh, lower trunk, upper trunk, head, upper limbs) and reported an accuracy and precision of 0.08 m and 0.06 m, respectively. Moreover, in the same study joint positions were found to be estimated with accuracy and precision of <0.17 m and <0.09 m, with the highest errors reported for the knee and ankle joint centers.

For the purpose of performance analysis, CoM kinematics need to be measured with high precisions. Position differences of less than 1 m and speed differences of less than 0.5 m/s can be considered to be performance relevant in alpine ski racing (Reid, 2010; Spörri et al., 2016c, 2012a; Supej et al., 2011). For giant slalom skiing Spörri et al. (2012a) compared CoM kinematics of twelve runs performed by the same athlete on two course settings (10 m vs 12 m gate offset). For the course with 12 m gate offset, the fastest turn was initiated 1.6 m higher on the slope compared to the slowest run. Total path length of the CoM trajectory was 0.33 m longer for the fastest run with an entrance speed difference of 0.3 m/s compared to the slowest run. Reid (2010) analyzed slalom ski racing and reported center of mass speed changes in the order of 0.5 m/s during a turn. He also reported that the outside ski speed was on average around 0.9 m/s faster than the CoM speed. Furthermore, besides the absolute CoM kinematics, also the relative CoM position is of certain interest, e.g. for turn segmentation (Supej et al., 2003) or improving

skiing technique (Läuppi and Spörri, 2014). For example, for slalom skiing Kipp et al. (2008) reported that skiing performance was dependent on fore-aft position (i.e. the relative position of the CoM with respect to the outside leg’s ankle joint center) where faster skiers stood more central on the skis. Moreover, vertical motion is considered a performance-relevant factor in coaching practice (Läuppi and Spörri, 2014).

Several studies tried to approximate CoM movement with a single inertial sensor placed to the trunk for both human (e.g. (Esser et al., 2009; Myklebust et al., 2015; Peyrot et al., 2009)) and animal (e.g. (Pfau et al., 2005; Warner et al., 2010)) locomotion analysis. The main aims of these studies was to approximate energy expenditure and cost of locomotion based on the cyclical relative movement of the inertial sensor. Although guaranteeing a very simple setup, these methods are limited in accuracy and precision. Usually, the CoM does not exactly match the sensor location and may have considerable relative displacement with respect to the sensor location due to limb movements. Moreover, these methods do not allow a 3D reconstruction of the athlete’s (or animal’s) posture. Fasel et al. (2016e) proposed to use an inertial sensor-based body model for estimating joint and CoM positions in alpine ski racing. However, the experimental setup used in that study did not allow a thorough analysis of the validity for CoM estimation based on multiple inertial sensors. Moreover, the body model used in that study relied on precise segment lengths obtained with 3D video analysis and, thus, its generalizability to other athletes might not be guaranteed.

Therefore, the first objective of this study was to expand the body model suggested by Fasel et al. (2016e) for the estimation of CoM to a more comprehensive and scalable model and including the upper limbs. The second objective was to validate the relative positions for the upper and lower limb joint centers and the athlete’s CoM obtained from the inertial sensors against a video-based stereo-photogrammetric reference system. The third objective was to evaluate the benefits of adding the upper limbs to the CoM estimation.

7.2 Methods

7.2.1 Measurement protocol

The measurements were conducted indoors on an indoor skiing carpet (Maxxtracks Indoor Skislopes, The Netherlands) with belt dimensions $6\text{m} \times 11\text{m}$ and 12° inclination (Fig. 7.1). Eleven male competitive alpine skiers (20.9 ± 5.2 years, 176.1 ± 6.7 cm, 74.0 ± 10.9 kg) participated in the study. Written informed consent was obtained from all athletes prior to the measurements and the study was approved by the ethics committee of Ecole Polytechnique Fédérale de Lausanne (Study Number: HREC 006-2016). Each athlete skied two trials with 140 cm skis and two trials with 110 cm skis at maximum belt speed of 21 km/h. Each trial lasted approximately 120 seconds and during the first half the athlete skied wide turns taking up the entire carpet width while for the second

Chapter 7. Validation of Athlete Body Model and Center of Mass Position

half the athlete skied narrow turns taking up half the carpet width. Cones placed in front of the treadmill where used to indicate the turn width. To ensure that the athletes stayed in the measurement volume, a spring system attached to a custom made belt pulled the athlete backwards (Fig. 7.1).

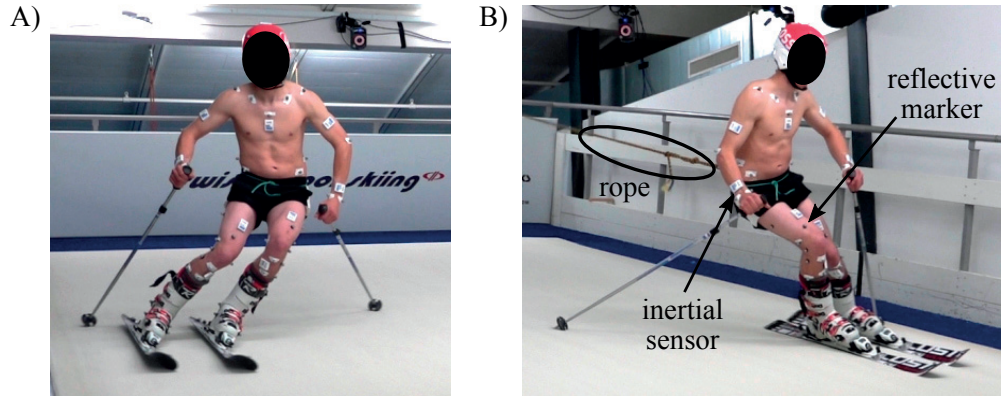


Figure 7.1 – Illustration of the treadmill skiing setup. A) Left turn, B) right turn. To ensure that the athlete stayed in the capture volume, a rope connected a spring system with the athlete. The small white boxes are the inertial sensors and the grey dots the reflective markers.

7.2.2 Reference system

Ten infrared cameras (Vicon Peak, UK) sampling at 100 Hz surrounded the carpet and covered the entire volume spanned by the carpet. The IfB marker set (Husa-Russell et al., 2011; List et al., 2013; Wolf et al., 2009) (Fig. 7.2) was used to obtain functionally determined ankle, knee, and hip joint centers and the 3D orientation of the shanks, thighs, pelvis, and lumbar, thoracic, and cervical trunk segments. Basic motion tasks as described in List et al. (2013) were performed to define the functional joint centers. Since the IfB marker set could not directly measure upper limb joint centers, markers have been placed in addition on the lateral humeral epicondyle, ulnar styloid, and radial styloid of both the left and right upper limbs. The shoulder joint center was defined to lie 3 cm below the acromion marker in the direction of the marker placed on the scapula inferior angle. The wrist joint center was defined to lie in the middle between the markers placed on the ulnar and radial styloids. The elbow joint center was defined to lie 3 cm to the medial direction with respect to the marker placed on the lateral humeral epicondyle. The medial direction has been defined to be normal to the plane spanned by the shoulder, wrist and lateral humeral epicondyle. In addition, to allow comparison to the wearable model, the cervical joint center (CJC) and lumbar joint center (LJC) were estimated based on the anatomical tables from Dumas et al. (2007) scaled to the athlete height. CJC was estimated with respect to the marker placed on C7. LJC was estimated based on the average estimated LJC position with respect to the left and right hip joint centers. Four markers were placed on the athlete's helmet. Their mean position was

used to approximate the position of the head vertex. Two markers were placed on each ski's tip and tail and allowed defining the skis' longitudinal axis. The segments' CoM were computed according to Dumas et al. (2007). Since the upper limbs' and head's 3D orientation was not known, their CoM position was simplified as follows: the upper limb CoM were restricted to lie on the respective segment's longitudinal axes where the hand's longitudinal axis was the same as the forearm's longitudinal axis. The head's CoM was defined to lie in the mid-point between the marker placed on C7 and the average position of the two markers fixed at the front of the helmet.

In order to allow a comparison to the inertial system, the joint and CoM positions were expressed relative to the LJC. The coordinate system was defined as follows: the Y-axis was vertical, pointing upwards; Z-axis was horizontal and parallel to the treadmill-plane pointing to the right; the X-axis was the cross-product of the Z- and Y-axis and was pointing forwards.

The coaching-relevant performance parameters vertical distance and fore-aft position were computed according to Spörri et al. (2012b). For each leg (left and right) the vector $v_{\text{CoM, ankle}}(t)$ connecting the CoM with the ankle joint center was computed. The vertical distance was the norm of $v_{\text{CoM, ankle}}(t)$. The fore-aft position was obtained by the projection of $v_{\text{CoM, ankle}}(t)$ onto the line corresponding to the projection of ski's longitudinal axis on the snow surface.

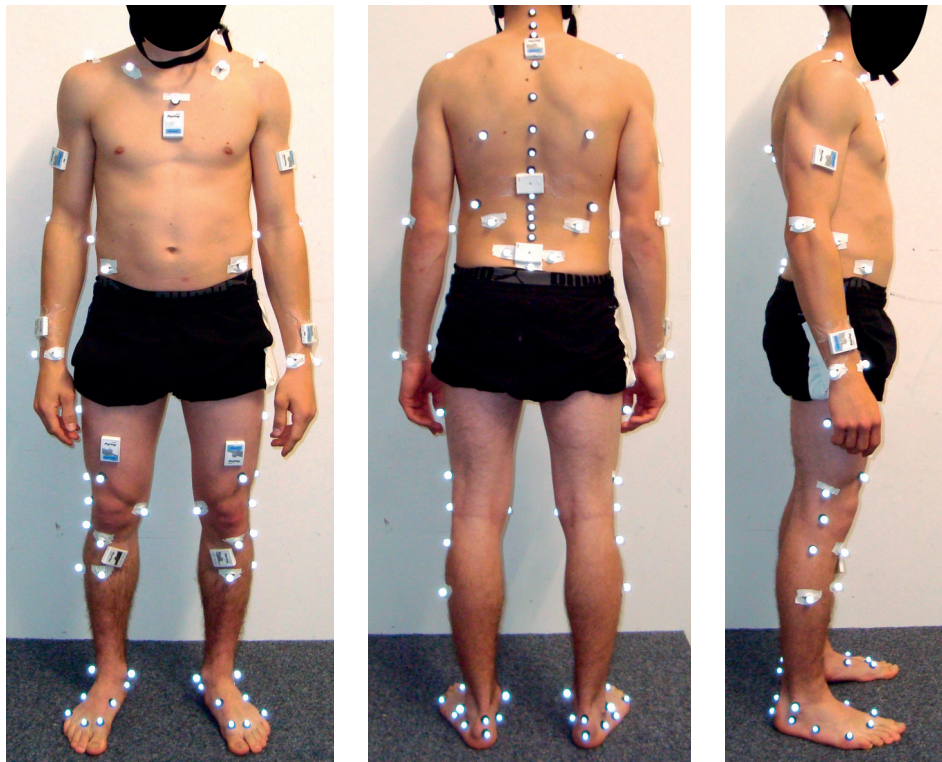


Figure 7.2 – Sensor and marker setup from the front, back and side view. The four markers fixed to the helmet are not shown here. The inertial sensors placed in the middle and upper back were not used for this study.

7.2.3 Wearable system

Eleven inertial sensors (Physilog 4, Gait Up, Switzerland) were attached with adhesive tape to the shanks, thighs, sacrum, sternum, head, arms and wrists (Fig. 7.1). Acceleration and angular velocity were measured at 500 Hz. Offset and sensitivity of the accelerometers were corrected according to Ferraris et al. (1995). Offset of the gyroscopes was estimated during the standing still posture before each trial. The wearable system was synchronized with the reference system by an electronic trigger. The sensors' local frames were aligned with the segments' anatomical frames based on the functional calibration (squats, trunk rotation, hip abduction, upright standing) described in Chapter 6. In addition, the functional calibration of the arm sensors consisted of two movements: 1) slow arm swing where the hands hold a pole horizontally with both thumbs pointing medially. The hands were spaced approximately equal to the shoulder width and elbows were kept straight during the entire movement. Three movement cycles of up/down arm movement in the sagittal plane were performed. 2) Upright posture where the arms and wrists were kept vertically with straight elbows. The hands were oriented such that the palms were barely touching the thighs on their lateral side. For the functional calibration the following constraints were assumed: i) the main rotation during the arm swing was supposed to occur along the medio-lateral axis of the arm and along the anterior-posterior axis of the wrist (e.g. forearm); ii) the longitudinal axes of the arms and wrists were presumed to pass parallel to gravity during the upright posture.

Estimating segment orientation

Segment orientation was obtained based on the strap-down and joint drift correction from Chapters 5, 6. For initializing segment orientation, the athletes were standing straight looking into the slope direction for 5 seconds before the treadmill was switched on. The global frame was identical to the frame of the reference system and defined as follows: the Y-axis was aligned with gravity, pointing upwards. X-axis was perpendicular to gravity and pointing in the direction of the slope, facing downwards. The Z-axis was the cross-product between the X- and Y-axis, pointing to the right. It was observed that, despite a standardized posture, the upper limbs' azimuths (i.e. direction of the segments' anterior-posterior axes) were not aligned. In order to find the segment's azimuths the same principle as for the joint drift correction presented in Chapters 5, 6 was used: after initial strap-down integration the segments' azimuths were assumed to be equal to the average joint acceleration orientation difference over the entire trial. Based on this principle, first the initial orientations of the arms were found with respect to the sternum. Second, the initial orientations of the wrists were found with respect to the arms. After this procedure orientation drift was corrected normally as in Chapters 5, 6. As no inertial sensors were placed on the skis, for computing the fore-aft position the ski orientations were estimated based on the shank orientations. To this end, it was assumed that the ankle was held in a constant position by the ski boot with a flexion of

17° without ankle abduction or internal rotation. In other words, the rotation between the ski's longitudinal axis and the shank's anterior-posterior axis was 17° around the shank's medio-lateral axis. As for the reference system, for each leg (left and right) the vector $v_{\text{CoM, ankle}}(t)$ connecting the CoM with the ankle joint center was computed. Vertical distance was the norm of $v_{\text{CoM, ankle}}(t)$ and the fore-aft position was obtained by the projection of $v_{\text{CoM, ankle}}(t)$ onto the line corresponding to the projection of ski's longitudinal axis on the snow surface.

Body model

The body model was estimated based on a kinematic chain similarly to Chapter 8. However, since the main aim of the body model was estimating the athlete's CoM, the origin of the kinematic chain was chosen as the LJC (Fig. 7.3A). All segment dimensions were then defined according to Dumas et al. (2007), scaled for athlete height. It was assumed that the segment orientations obtained by the inertial sensors were identical to the anatomical frames of the corresponding segments. The trunk was modelled as two independent segments: pelvis and trunk. It was assumed that the pelvis orientation was equal to the sacrum orientation, and that the trunk orientation was equal to the sternum orientation. Thus, for example, the left hip joint position $p_{\text{left hip}}(t)$ was determined based on Eq. 7.1 and the left knee position $p_{\text{left knee}}(t)$ based on Eq. 7.2. All other joint positions were obtained with the same iterative way. Once the joint positions were known, the segment CoMs were estimated according to Dumas et al. (2007). In order to estimate the CoM of the hand, the hand was assumed to have the same orientation as the wrist. To estimate the foot CoM, it was assumed that the foot had the same orientation as the ski (i.e. 17° ankle flexion). A weight of 2 kg was added to each foot to take into account the weight of the ski boot. The skis were ignored for computing the CoM. The athlete's CoM was then the weighted average of all segment CoMs. In a simplified model, without the arm and wrist sensors, the upper limbs' combined CoM was approximated at the relative position of (0.15m, 0.10 m, 0.00 m) with respect to LJC expressed in the trunk's (i.e. sternum) anatomical frame (Fig. 7.3B). The upper limbs' relative CoM position was determined from average values of the full model and was scaled for athlete height with the same scaling factor as for the other segments.

$$p_{\text{left hip}}(t) = {}^{\text{sacrum}}R(t) v_{\text{left hip}} \quad (7.1)$$

$$p_{\text{left knee}}(t) = p_{\text{left hip}}(t) + {}^{\text{left thigh}}R(t) v_{\text{left knee}} \quad (7.2)$$

where t is the time, ${}^{\text{sacrum}}R(t)$ the orientation matrix of the sacrum at time t , ${}^{\text{left thigh}}R(t)$ the orientation matrix of the left thigh at time t , $v_{\text{left hip}}$ the vector connecting the LJC to the left hip in the sacrum's anatomical frame, and $v_{\text{left knee}}$ the vector connecting the left hip to the left knee in the left thigh's anatomical frame.

7.2.4 Validation

Error curves were computed by subtracting, for each time sample, the 3D position of the joint centers and CoM expressed relative to the LJC obtained with the reference system from the wearable system. For each trial, each individual axis and the total distance (i.e. the error norm), mean and standard deviation of the error were computed. Accuracy was defined as the group average of all trial mean errors and precision was defined as the group average of all trial standard deviations of the error.

The same error analysis was performed for the fore-aft parameters, whereas in addition Pearson's correlation coefficient was computed. For each trial fourteen wide and fourteen narrow turns were automatically segmented based on the crossing points of left and right vertical distance (i.e. norm of $v_{\text{CoM, ankle}}$) (Fasel et al., 2016f). For each turn the range of motion (RoM) of the vertical distance and the fore-aft position was computed and compared to the reference system with a Bland-Altman plot (Bland and Altman, 2007). Since the data points for the same trial were correlated, we propose to compute the limits of agreements (LoA) as explained in the following section. To assess whether the wearable system was sensitive to changes, Cohen's d was computed between trials (140 cm vs 110 cm skis) and turn types (wide vs narrow).

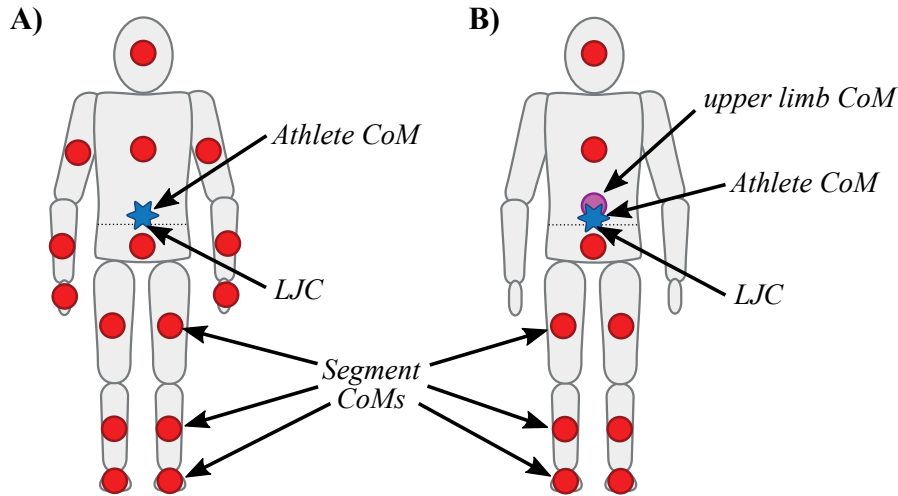


Figure 7.3 – A) body model including the upper limbs. Each red circle represents a segment's CoM. The athlete's CoM is highlighted by the blue star. The LJC is indicated by an arrow and lies on the dotted line. B) Simplified body model without the upper limbs. The approximated location of the upper limb's combined CoM is illustrated by the purple circle.

Computing limits of agreements for dependent observations

To compute the LoA for trials with repeated dependent observations the following reflection can be made: at the cost of reducing the number of observations, the condition of repeated independent observations can be obtained if for each trial all turns except one

would be discarded. However, with this procedure the obtained LoA highly depend on the selected turns and may not be representative of the true LoA. To eliminate this issue, the concept from the Monte Carlo method (Kroese et al., 2014) was used: randomly subsample the dataset and compute the statistics of this subset. Then repeat the random sampling multiple times to obtain multiple estimates of the statistics. By the law of large numbers, the "true" statistics can then be approximated by the average of the multiple subset-estimates. Therefore, for this study, the dataset was subsampled by randomly selecting one cycle per trial. Then the LoA were computed for this subset as described by Bland and Altman (2007). The final LoA were computed on the average LoAs for 50 randomly sampled subsets.

7.3 Results

A total of 44 trials (11 athletes, 4 trials per athlete) were analyzed. Errors for the left and right side were similar, thus, for the sake of clarity, only the results for the left side are presented here. Both accuracy and precision worsen for the more distal joint centers, and were worst for the ankles (total distance accuracy and precision of 109 mm and 30 mm) and wrists (total distance accuracy and precision of 97 mm and 16 mm) (Table 7.1). Standard deviation of the joint center accuracy was found to be between 6.3 mm and 57.6 mm. CoM accuracy and precision for the total distance were 26 mm and 7 mm, respectively.

Especially knee and ankle joint position errors were dependent on turn-cycle. Fig. 7.4 shows time-normalized errors for the knee and ankle joints for a typical athlete and nine wide left/right turns of the trial with 140 cm skis. While the hip's vertical position error (Y-axis) remained below 10 mm throughout the turn cycle, the knee joint position had large errors during left turns (i.e. for inside leg).

Simplifying the model did not impact the CoM precision, but added a bias in the accuracy in the forwards and vertical direction, in which CoM was estimated 8.5 mm too low and 13.5 mm too posterior (Table 7.2).

Correlation was >0.98 for the vertical distance but only around 0.90 for fore-aft position (Table 7.3). Fore-aft position was constantly underestimated by 74 mm on average and its average precision was 34 mm. Vertical distance was on average overestimated by 3 mm with a precision of 11 mm (Table 7.3). Fig. 7.5 shows the average \pm standard deviation curves for 14 wide double turns of two representative athletes.

Chapter 7. Validation of Athlete Body Model and Center of Mass Position

Joint	X-Axis		Y-Axis		Z-Axis		Total distance	
	Accuracy	Precision	Accuracy	Precision	Accuracy	Precision	Accuracy	Precision
Ankle	56.7 (57.6)	35.5 (14.5)	-16.3 (24.5)	20.8 (11.7)	23.1 (46.7)	48.4 (14.6)	109.1 (43.2)	29.7 (12.9)
Knee	26.2 (32.9)	25.3 (6.4)	21.8 (21.2)	20.8 (7.8)	40.0 (33.3)	34.6 (10.4)	79.7 (33.0)	18.9 (6.4)
Hip	-10.0 (10.1)	5.9 (1.6)	-3.8 (6.5)	4.7 (2.4)	21.4 (6.7)	5.1 (2.0)	28.1 (6.3)	4.7 (1.9)
CJC	-22.9 (28.1)	11.9 (3.4)	-5.9 (28.0)	9.1 (3.0)	-1.7 (35.9)	18.5 (5.1)	56.5 (24.7)	12.7 (4.7)
Head Vertex	-58.7 (39.2)	17.2 (6.1)	92.8 (56.6)	10.3 (3.4)	-3.3 (44.8)	25.5 (8.0)	127.3 (57.8)	16.9 (7.3)
Shoulder	-7.7 (31.9)	17.9 (4.8)	-69.0 (26.5)	14.0 (3.3)	-49.5 (28.8)	18.4 (5.7)	99.4 (24.3)	14.3 (4.6)
Elbow	14.0 (28.4)	17.3 (4.9)	-6.1 (30.5)	15.3 (4.6)	-9.4 (27.4)	17.5 (5.3)	55.1 (20.3)	14.7 (3.4)
Wrist	-50.8 (39.3)	20.4 (6.9)	-49.7 (35.7)	21.4 (7.2)	-14.4 (32.37)	21.4 (7.2)	97.0 (29.4)	16.3 (4.8)

Table 7.1 – Average (standard deviation) accuracy and precision of the relative joint positions of the left side limbs and trunk along the X-axis (forwards slope direction), Y-axis (vertical direction), Z-axis (lateral direction), and total distance (norm of 3D difference). All units are mm.

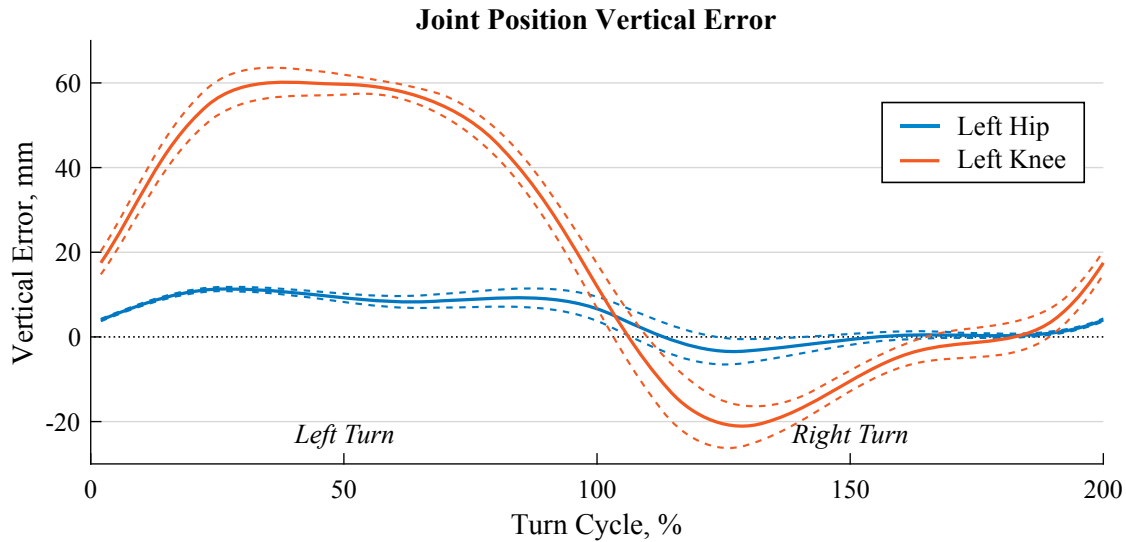


Figure 7.4 – Average (solid lines) ± 1 standard deviation (dashed lines) of time-normalized hip (blue) and knee (orange) joint position errors along the vertical Y-axis for 9 left and right turns of a representative trial. The first 100% of the turn cycle is a left turn and the second 100% is a right turn.

7.3. Results

Joint	X-Axis		Y-Axis		Z-Axis		Total distance	
	Accuracy	Precision	Accuracy	Precision	Accuracy	Precision	Accuracy	Precision
With arms	-8.6 (13.8)	6.4 (1.7)	0.6 (14.2)	4.5 (1.7)	-0.5 (13.1)	11.2 (3.3)	25.7 (10.9)	6.7 (2.2)
Without arms	-13.5 (12.2)	6.6 (1.6)	-8.5 (14.4)	4.5 (1.7)	-0.1 (12.5)	11.5 (3.5)	28.6 (9.6)	7.2 (2.6)

Table 7.2 – Average (standard deviation) accuracy and precision of the relative CoM positions for the full model with arms and the simplified model without arms. All units are mm.

Parameter	Body Model	Accuracy	Precision	Correlation
Vertical distance	with arms	3.3 (19.8)	10.6 (5.4)	0.990 (0.010)
	without arms	-5.5 (19.7)	10.9 (5.7)	0.989 (0.010)
Fore-aft position	with arms	-73.9 (47.0)	34.0 (11.0)	0.896 (0.087)
	without arms	-76.7 (49.1)	33.8 (10.9)	0.897 (0.087)

Table 7.3 – Average (standard deviation) accuracy and precision of the fore-aft parameters and their correlation to the reference system for the full model with arms and the simplified model without arms. Units for accuracy and precision are mm.

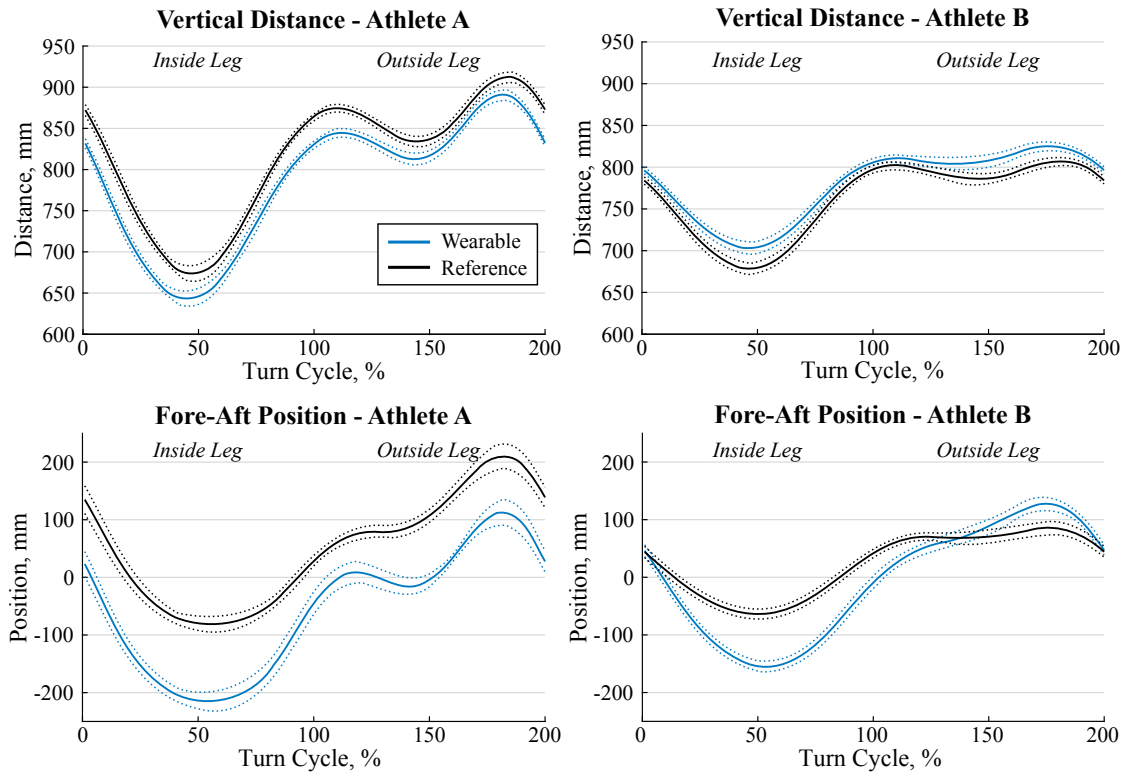


Figure 7.5 – Average (solid lines) ± 1 standard deviation (dotted lines) of vertical distance (top) and fore-aft position (bottom) of the left leg for the same condition for two athletes A and B (left versus right) and 14 wide double turns. The wearable system is shown in blue and the reference system in black. The first 100% of the turn were a left turn, thus the left leg was the inside leg. The second 100% of the turn were a right turn, thus the left leg was the outside leg.

Chapter 7. Validation of Athlete Body Model and Center of Mass Position

Parameter	Body Model	Errors Outside Leg			Errors Inside Leg		
		Lower LoA	Mean	Upper LoA	Lower LoA	Mean	Upper LoA
RoM Vertical distance	with arms	-18.6	8.4	32.4	-49.1	-5.2	40.1
	without arms	-17.8	8.4	30.9	-50.0	-5.8	37.8
RoM Fore-aft position	with arms	-26.8	48.9	117.6	-30.5	29.0	91.9
	without arms	-29.4	47.9	117.3	-25.5	37.0	92.5

Table 7.4 – Limits of agreements (LoA) for the range of motion (RoM) of the vertical distance and fore-aft positions. All units are in mm.

LoA for the RoM of the vertical distance and fore-aft position were considerably lower for the outside leg than the inside leg (Table 7.4, Fig. 7.6). Average (standard deviation) of vertical distance RoM was 53.8 mm (23.5 mm) for the outside leg and 168.9 mm (45.0 mm) for the inside leg. Average (standard deviation) of the fore-aft position RoM were 92.7 mm (40.1 mm) for the outside leg and 136.7 mm (47.2 mm) for the inside leg. Cohen’s d for the RoM were similar for both systems. Simplifying the model by removing the arms did only slightly change the fore-aft parameters’ accuracy and precision. As for the full system, Cohen’s d were similar for both systems.

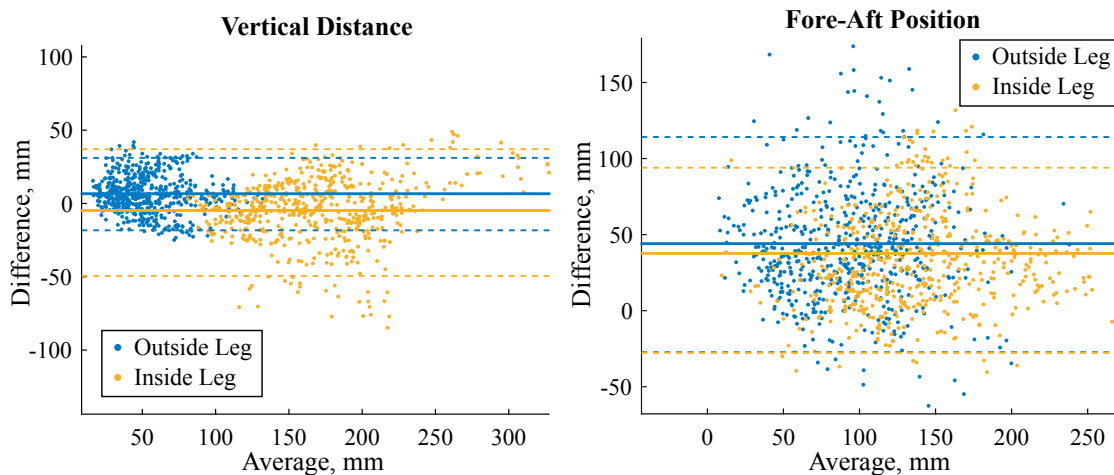


Figure 7.6 – Bland-Altman plots for the range of motion of the vertical distance (left) and fore-aft position (right). The model without arms was used to generate the figures and compute the LoA (dashed lines). Mean error is shown with the solid lines. Blue marks the outside leg and yellow the inside leg. LoA for both models and outside and inside legs are reported in Table 7.4.

7.4 Discussion

A method has been proposed and validated to estimate the athlete’s posture during skiing. Joint positions were expressed relative to the lumbar joint center (LJC) and were validated against an optoelectronic stereo-photogrammetric reference system. Based on the joint positions and segment orientations, the athlete’s relative CoM was estimated

and vertical distance and fore-aft position were computed. Accuracy (precision) for the CoM, vertical distance and fore-aft position were 25.7 mm (6.7 mm), 3.3 mm (10.6 mm), and -73.9 mm (34.0 mm), respectively. Excluding upper limbs decreased the accuracy and performance of all curves by less than 3 mm except for the vertical distance where the offset changed from 3.3 mm to -5.5 mm. The proposed procedure for estimating relative segment azimuth during posture initialization seemed to work well: accuracy and precision for the wrist joint position were similar as for the shoulder joint position. Interestingly, elbow joint position was estimated with better accuracy than shoulder joint accuracy. However, before analyzing movements for which arm motion is key, the proposed orientation initialization should be validated more specifically.

7.4.1 Possible joint position error sources

Errors of the relative joint positions increased along the kinematic chain, as expected. Two factors might have contributed to these errors: incorrect segment dimensions and inaccurate segment orientation estimations. Segment dimensions were taken from Dumas et al. (2007) and were scaled only for athlete height. Therefore, athlete-individual deviations from the model were not considered and led to a potential bias in the estimation of the segment length. As an example, our athletes had on average a 40 mm wider pelvis and 69 mm shorter trunk. Subject-specific anthropometric measurements could reduce this error; however, at the costs of a more complicated measurement procedure. Furthermore, segment orientation estimation errors did directly affect joint estimation errors. For example, knee joint position errors were by a factor of 3-4 higher than for the hip joint. The large precision decrease observed could be attributed to soft tissue artefacts of the thigh. Actually, high muscle activation levels during the turns could change temporarily the sensor's alignment with respect to the underlying bone. In this context, it is known that during a turn, the inside leg has higher hip and knee flexion angles but has to support less force (Klous et al., 2012; Kröll et al., 2015). Thus, it is reasonable that the muscle activation at the inside leg is different compared to the outside leg (Kröll et al., 2011). What, while turning, might have led to a different amount of soft tissue artefact and, therefore, different errors in the estimation of the thigh segment orientation (Fig. 7.4). Soft tissue artefacts could be modelled for example with a double static calibration as proposed by Cappello et al. (1997) and by measuring different static postures (i.e. upright standing, sitting on a chair) with and without muscle pre-activation.

7.4.2 CoM position

CoM position was estimated with very good precision despite the worse performance of joint position estimation. One explanation could be that errors from individual joint positions were averaged out when computing the athlete's CoM. Surprisingly, removing

the upper limbs from the model did not decrease CoM accuracy and precision significantly, in contrast to the findings from Eames et al. (1999); Whittle (1997) for walking. One potential explanation for this observation might be the fact that during alpine skiing arm movement is mostly symmetrical and that for the present indoor setup the arms were almost held in a constant position. This is usually not true for on-snow slalom skiing, where the athlete uses his arms for gate clearance at each turn. On the other hand, upper limbs contribute on average 10% to total body mass (Dumas et al., 2007). Thus, even if arm movement may not have been estimated correctly, its impact on total CoM might be negligible for alpine ski racing.

7.4.3 Vertical distance and fore-aft position

Both vertical distance and fore-aft position were estimated with higher precision than Fasel et al. (2015b), suggesting that the new body model was more appropriate. Accuracy was slightly improved for the vertical distance, however, was worse for the fore-aft position. Compared to vertical distance the fore-aft position is more sensitive to ankle position errors. Under the hypothesis that the largest error source could be attributed to incorrectly estimated thigh orientation due to soft tissue artefacts a change in thigh orientation would essentially affect the direction of the vector relying the ankle to the CoM, but not its length. Fore-aft position is obtained by projecting this vector onto the fore-aft axis. Thus, soft tissue artefacts only marginally alter the vertical distance but not the fore-aft position (Figs. 7.6, 7.7). Thus, even though on average a correlation to the reference values of 0.9 was found for the fore-aft position its precision is not sufficient and the parameter should not be used to analyze the skiing movement. The future developments for reducing soft tissue artefacts suggested above might help to decrease ankle joint position errors to acceptable levels to allow an accurate and precise estimation of the fore-aft position.

In view of the average vertical distance differences of 20 mm and the RoM differences of 80 mm that were reported for two course settings in slalom (Reid, 2010), it can be concluded that the proposed system was able to estimate the vertical distance with sufficient accuracy and precision for applied research questions in the context of alpine ski racing. In addition, the comparison of Cohen's d computed with both the reference and wearable system showed that the proposed system was as sensitive to changes as the reference system and was able to measure the same differences. However, absolute vertical distance should not be compared between athletes: even though average accuracy was 11 mm, significant offsets between the wearable and reference system were observed (Fig. 7.5). These offsets most likely originate from the use of the standardized body model segment lengths and might be reduced by including subject-specific anthropometric measurements.

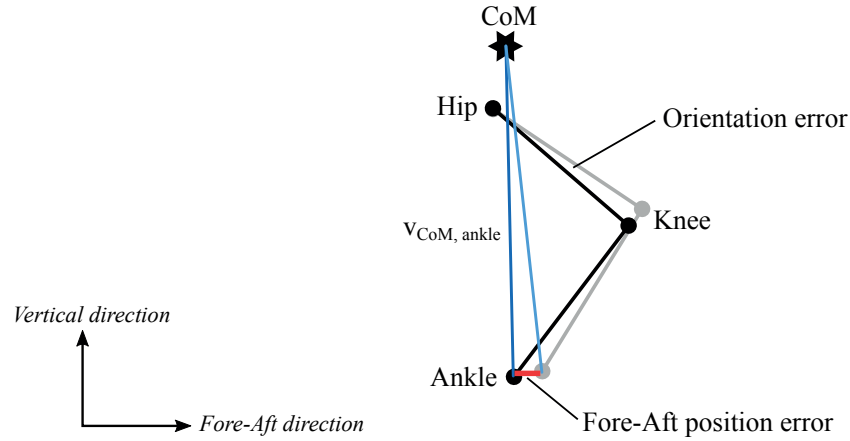


Figure 7.7 – Influence of thigh orientation estimation error on ankle position. Black shows the original leg position and gray the leg position with a thigh and shank orientation error. The blue lines show $v_{\text{CoM, ankle}}(t)$ for each position. The fore-aft position (projection of $v_{\text{CoM, ankle}}(t)$ onto the fore-aft axis) is more affected by this orientation error (difference shown in red) than the vertical distance (norm of $v_{\text{CoM, ankle}}(t)$).

7.4.4 Methodological limitations

Despite the carefully chosen reference system and setup, the study had some limitations: the model was specifically designed for lower limb and trunk motion capture. Accordingly, upper limb joints (shoulders, elbows, wrists) and head vertex were only approximately tracked. Especially for the shoulder joint and head vertex reference positions might have been estimated with errors of up to a few centimeters. This inaccuracy was judged to be acceptable, since a validation of the upper limb position and orientation was not the main aim of this study. For the estimation of CoM, segment inertial parameters were taken from Dumas et al. (2007) and were only scaled to athlete's height. The body model could be individualized by taking into account the athlete's segment lengths and an estimation of their muscle masses. As inertial sensors cannot provide absolute position measurements, only the relative joint and CoM positions were validated. For reasons of convenience, the lumbar joint center (LJC) has been defined as the origin for both systems, even though it could not be measured directly by the reference system. However, by averaging the LJC estimated from the left and right hip joint center measurement errors were aimed to be minimized. The movement patterns on the treadmill corresponded well to the real on-snow skiing situation (Spörri et al., 2016b). However, the reduced speed led to a less dynamic movement and less arm motion. Vibration from skidding on the snow did not exist either. Therefore, it is expected that errors for on-snow skiing might be larger than presented here.

7.5 Conclusion

The proposed system allowed computing the relative CoM with sufficient precision for further use in-field and during regular training. Only the accuracy and precision of the most distal joints (e.g. ankle) are on the limit of an acceptable range. The accuracy and precision of the ankle positions can be considered acceptable for computing the vertical distance, but not for calculating the fore-aft position. Future developments should aim at reducing soft tissue artefacts such that knee and ankle positions could be estimated with better precision. To compute the absolute CoM position with respect to a fixed global frame, the obtained relative CoM position and body model could be combined with an absolute position of a body part (e.g. head), for example measured with differential GNSS.

Acknowledgements

The study was funded by the Swiss Federal Office of Sport (FOSPO), grant 15-01; VM10052. The authors would like to thank Swiss Indoor Skiing for providing us access to their ski treadmill.

8 Combination of Inertial Sensors with Differential GNSS

Abstract

A key point in human movement analysis is measuring the trajectory of a person's center of mass (CoM). For outdoor applications differential Global Navigation Satellite Systems (GNSS) can be used for tracking persons since they allow measuring the trajectory and speed of the GNSS antenna with centimetre accuracy. However, the antenna cannot be placed exactly at the person's CoM but rather on the head or upper back. Thus, a model is needed to relate the measured antenna trajectory to the CoM trajectory. In this paper we propose to estimate the person's posture based on measurements obtained from inertial sensors. From this estimated posture the CoM is computed relative to the antenna position and finally fused with the GNSS trajectory information to obtain the absolute CoM trajectory. In a biomechanical field experiment, the method has been applied to alpine ski racing and validated against a camera-based stereo photogrammetric system. CoM position accuracy and precision was found to be 0.08 m and 0.04 m, respectively. CoM speed accuracy and precision was 0.04 m/s and 0.14 m/s, respectively. The observed accuracy and precision might be sufficient for measuring performance- or equipment-related trajectory differences in alpine ski racing. Moreover, the CoM estimation was not based on a movement-specific model and could be used for other skiing disciplines or sports as well.

Keywords: inertial sensors, GNSS, sensor fusion, wearable system, skiing, centre of mass, biomechanics

8.1 Introduction

In the sport of alpine ski racing, precise data of the centre of mass (CoM) position, speed and acceleration are indispensable for the purposes of performance analysis and injury prevention (Hébert-Losier et al., 2014; Kröll et al., 2013, 2016a,b; Reid, 2010; Spörri et al., 2016c, 2012a,b; Supej et al., 2011). Early studies mainly used camera-based stereo photogrammetry to collect kinematic data on a ski-slope and to reconstruct the CoM kinematics (Federolf, 2012; Gilgien et al., 2013; Klous et al., 2010; Reid, 2010; Spörri et al., 2016c, 2012a; Supej et al., 2003). However, despite advantages in measurement accuracy, these systems are complex to set up and need for time consuming post processing due to manual digitization. Moreover, they are limited in capture volume, allowing the analysis of a short turn sequence only. With the ongoing miniaturization of electronics, it became possible to use global navigation satellite systems (GNSS) in alpine skiing research (Adelsberger et al., 2014; Brodie et al., 2008; Gilgien et al., 2015a,b,c, 2013, 2016, 2014b,a; Kröll et al., 2016b; Lachapelle et al., 2009; Supej, 2010; Waegli and Skalous, 2009). However, one disadvantage of these systems is that the exact CoM position in space and time cannot be measured directly as the GNSS antenna is mounted on the head or neck. Thus, modelling methods are needed to estimate the CoM position relative to the GNSS antenna and to find the absolute position of the CoM, as previously suggested by Gilgien et al. (2015c, 2013); Supej et al. (2013). In these studies, the models were based on inverse pendulum using precise surveying of the snow surface. However, for abnormal skiing movements violating the model hypotheses (e.g. during moments of loss of balance) the estimated CoM kinematics may be wrong. Moreover, surveying the snow surface is time consuming and is only feasible for research applications, but not within regular training sessions. Alternatively, inertial sensors could be used to estimate the athlete's body segment orientations and posture over time (Chardonnnens et al., 2013). In alpine skiing research, such an approach was already used to estimate the relative CoM kinematics (e.g. the athlete's CoM kinematics with respect to the athlete's head), and fused with a GNSS, to estimate the CoM kinematics with respect to a fixed global frame (Brodie et al., 2008; Krüger and Edelmann-Nusser, 2009; Supej, 2010). Although these studies specified the errors of each system independently, they did not validate their final results on snow using the gold standard camera-based stereo photogrammetry. Fasel et al. (2015b) used seven inertial sensors to estimate a relative CoM based on a seven segment body model. Relative distances between the CoM and ankle position were estimated and validated. However, they did not compute the absolute joint and CoM positions in space.

Therefore, the aims of this study were threefold: (1) to design a novel algorithm to estimate the CoM kinematics based on the trajectory and the speed data obtained from a differential GNSS (dGNSS) and body segment orientations obtained from seven inertial sensors; (2) to reduce the number of sensors and to design an alternative algorithm that bases on the dGNSS data and the orientation of the athlete's head and sternum only; (3) to validate these algorithms against a camera-based stereo photogrammetric system.

8.2 Materials and methods

8.2.1 Protocol

The measurements took place on a giant slalom slope of 26° inclination. 11 gates were positioned at a constant distance of 27 m with 8 m offset (Figure 8.1A). The left turn around gate 7 was covered with the video-based reference system. Six European Cup level alpine ski athletes participated in the study. Each athlete skied the course two times. Informed written consent was obtained from each athlete. The protocol was approved by the University Ethics Committee of the Department of Sport Science and Kinesiology at the University of Salzburg.

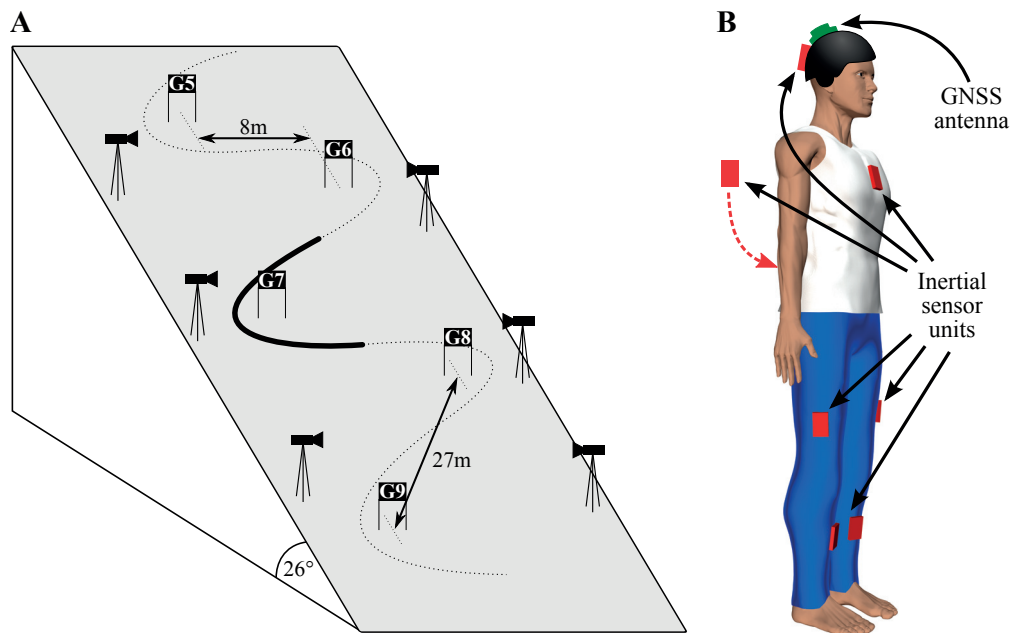


Figure 8.1 – A) Illustration of the giant slalom slope. The left turn marked with the solid line was covered by the six cameras and analysed in this study. B) Inertial sensors placed on both shanks and thighs, on the sacrum, sternum, and head. The GNSS antenna was fixed to the athlete's helmet.

8.2.2 Wearable system

Inertial sensors

Six inertial sensor units (Physilog III, Gait Up, Switzerland) were placed on the left and right shank on the tibial plateau above the ski boots, on the left and right thigh on the lateral side, mid-distance between the knee and hip joint centre, on the sacrum and on the sternum using a custom made skin-tight underwear suit. A seventh inertial sensor unit was fixed to the athlete's helmet (Figure 8.1B). 3D acceleration and angular velocity

were recorded on each sensor unit at 500 Hz. The sensors were wirelessly synchronized via radio (RF) synchronization pulses. Accelerometer offset and sensitivity was corrected as described in Ferraris et al. (1995). Gyroscope offset was removed based on a static measurement before each run (Bergamini et al., 2014). After functional calibration, initial sensor orientation was estimated based on the strapdown and drift-correction algorithm of Favre et al. (2006). In a second step drift was further reduced by applying the method of Dejnabadi et al. (2006) extended to 3D (Chapter 5). The ISB standard convention (Wu and Cavanagh, 1995) was used for the orientation of the segments' anatomical axes. Orientation accuracy and precision for alpine skiing was found to be in the order of 4° and 6°, respectively (Fasel et al., 2013) and Chapter 5.

Differential global navigation satellite system

Position and speed of the skiers head were tracked using dGNSS technology (Gilgien et al., 2014b). The GNSS antenna (G5Ant-2AT1, Antcom, Canada) was fixed to the helmet to ensure optimal satellite visibility (Figure 8.1B) and the receiver (Alpha-G3T, Javad, USA) weighing 430 g was placed in a backpack logging GPS and GLONASS signals using L1 and L2 frequency. Two reference stations equipped with antenna (GrAnt-G3T, Javad) and receiver (Alpha-G3T, Javad, USA) logging GPS and GLONASS signals using frequency L1 and L2 were mounted on a tripod and placed close to the beginning of the race track (short baseline measurement). The reference base station's location was selected to reach the maximal number of satellites possible. The unit on the skier and base station recorded at a sampling frequency of 50 Hz. The antenna position and velocity were computed in post processing applying kinematic carrier phase methods using geodetic software (Justin, Javad, USA) as described in Gilgien et al. (2015c, 2013). The obtained position and velocity were interpolated to 500 Hz using a spline filter to match the sampling frequency of the inertial sensors. The inertial sensors were electronically synchronized with the GNSS receiver using an electronic trigger.

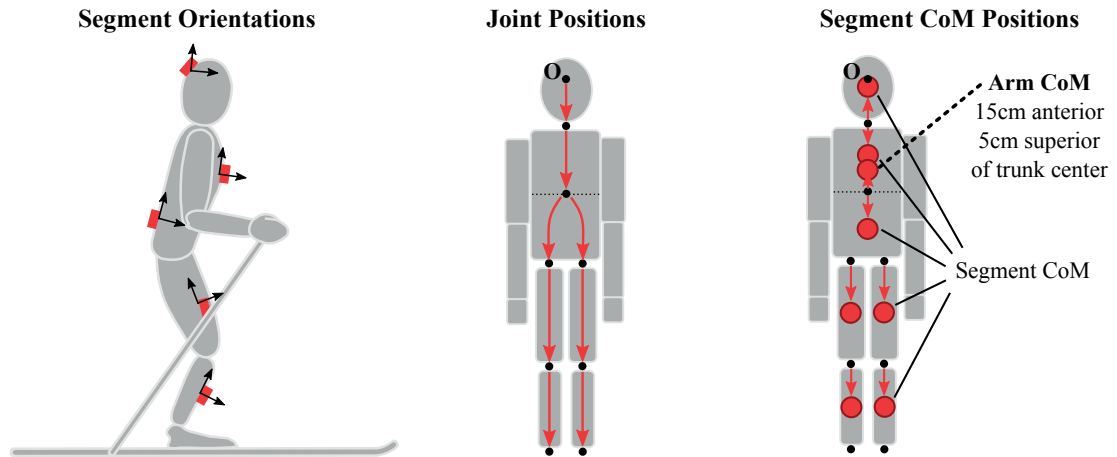
The vertical axis of the dGNSS system and the inertial sensors was aligned using Earth's gravity. The azimuth was aligned using the hypothesis that, on average, the left and right shanks' anterior-posterior anatomical axes were aligned with the skier's velocity direction.

8.2.3 Centre of mass kinematics

The forward kinematic model proposed in Chardonnens et al. (2014) was adapted to compute the CoM kinematics (i.e. position and velocity) based on the GNSS antenna position and body segment orientations obtained with the inertial sensors. Two different models are proposed: the first model is based on a full 3D body model (Figure 8.2A), whereas the second model (Figure 8.2B) only used the orientations of the head and upper body to estimate the CoM kinematics. In both cases, first the relative position and

velocity of the CoM with respect to the GNSS antenna was estimated and then added to the GNSS antenna position and velocity to obtain the final, absolute estimate of CoM position and velocity.

A) Full model



B) Simplified model

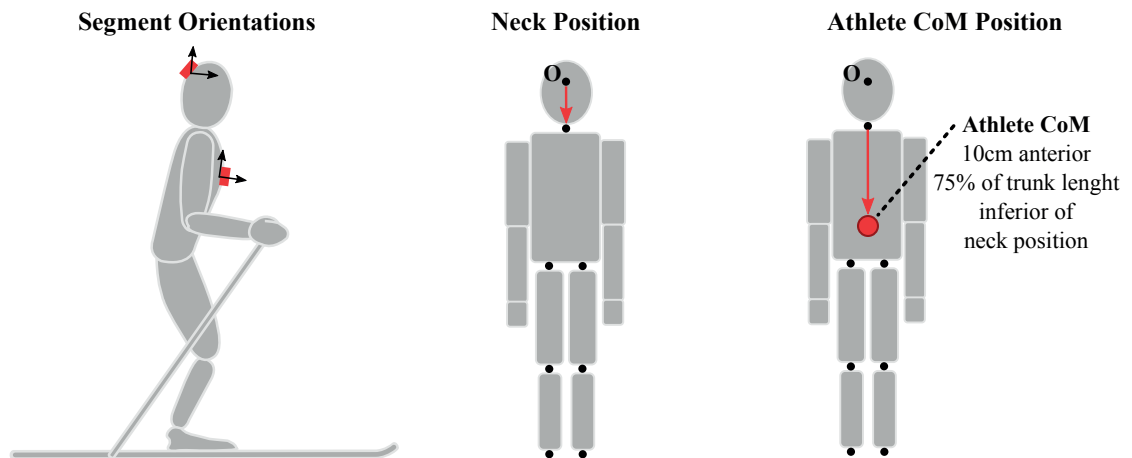


Figure 8.2 – Kinematic chain used to compute the joint and segment CoM positions based on the segment orientations in the anatomical frame. A) Full 3D body model based on all available inertial sensors, B) simplified model based only on head and sternum inertial sensors.

Full 3D body model

The full 3D body model was composed of the following segments: head, upper trunk, lower trunk, left and right thigh, left and right shank, and arms. The weights of feet, boots, and skis were ignored. The weight of the GNSS system and clothing was assumed to be 1 kg, uniformly distributed on the trunk. The weight of the helmet was assumed

constant at 0.5 kg. Segment inertial parameters were taken in accordance to de Leva (1996); Dumas et al. (2007) scaled for athletes' weights. It was assumed that the upper and lower trunk's weight was 40% and 60%, respectively, of the total weight of trunk and pelvis. All segment lengths were obtained from joint centre position measurements from the reference system described in Gilgien et al. (2015c). Trunk joint centre was defined to lie 0.05 m anterior and inferior of the middle of the trunk (i.e. the middle of the left/right hip and shoulder joints). Combining the segment lengths with their orientations allowed computing their 3D orientations and reconstructing the skier's posture (Eq. 8.1). The CoMs for the upper and lower trunk were supposed to be midway between trunk joint centre and neck or hips, respectively. Since the arms' orientations were unknown, it was assumed that the CoM of both left and right arms combined was fixed with respect to the sternum and located 0.15 m anterior and 0.05 m superior to the trunk centre (i.e. $d_{\text{trunk joint centre} \rightarrow \text{arms CoM}} = [0.15 \ 0.05 \ 0]^T$, Figure 8.2A).

In a first step, the joint positions for the neck, trunk centre, left and right hip, left and right knee, and left and right ankle were computed based on Eq. 8.1 (Figure 8.2A). The origin was defined to be at the GNSS antenna. In a second step, the positions for all segment COMs were computed based on Eq. 8.2 (Figure 8.2A). Based on all segments' COMs the CoM of the athlete was estimated using a weighted sum (Eq. 8.3).

$$\begin{aligned}
 \mathbf{p}_{\text{neck}} &= R_{\text{head}} \mathbf{d}_{\text{GNSS} \rightarrow \text{neck}} \\
 \mathbf{p}_{\text{trunk joint centre}} &= \mathbf{p}_{\text{neck}} + R_{\text{sternum}} \mathbf{d}_{\text{neck} \rightarrow \text{trunk joint centre}} \\
 \mathbf{p}_{\text{left hip}} &= \mathbf{p}_{\text{trunk joint centre}} + R_{\text{sacrum}} \mathbf{d}_{\text{trunk joint centre} \rightarrow \text{left hip}} \\
 \mathbf{p}_{\text{right hip}} &= \mathbf{p}_{\text{trunk joint centre}} + R_{\text{sacrum}} \mathbf{d}_{\text{trunk joint centre} \rightarrow \text{right hip}} \\
 \mathbf{p}_{\text{left knee}} &= \mathbf{p}_{\text{left hip}} + R_{\text{left thigh}} \mathbf{d}_{\text{left hip} \rightarrow \text{left knee}} \\
 \mathbf{p}_{\text{right knee}} &= \mathbf{p}_{\text{right hip}} + R_{\text{right thigh}} \mathbf{d}_{\text{right hip} \rightarrow \text{right knee}} \\
 \mathbf{p}_{\text{left ankle}} &= \mathbf{p}_{\text{left knee}} + R_{\text{left shank}} \mathbf{d}_{\text{left knee} \rightarrow \text{left ankle}} \\
 \mathbf{p}_{\text{right ankle}} &= \mathbf{p}_{\text{right knee}} + R_{\text{right shank}} \mathbf{d}_{\text{right knee} \rightarrow \text{right ankle}}
 \end{aligned} \tag{8.1}$$

where \mathbf{p}_j is the position of the joint centre of joint j . R_s the orientation matrix representing the orientation of segment s in the global frame, and $d_{A \rightarrow B}$ the vector connecting the joint A with B , expressed in the anatomical frame of segment connecting joint A with B .

$$\begin{aligned}
 \mathbf{p}_{\text{head}}^{\text{CoM}} &= R_{\text{head}} \mathbf{d}_{\text{neck} \rightarrow \text{head CoM}} \\
 \mathbf{p}_{\text{upper trunk}}^{\text{CoM}} &= \mathbf{p}_{\text{neck}} + R_{\text{sternum}} \mathbf{d}_{\text{neck} \rightarrow \text{upper trunk CoM}} \\
 \mathbf{p}_{\text{lower trunk}}^{\text{CoM}} &= \mathbf{p}_{\text{trunk joint centre}} + R_{\text{sacrum}} \mathbf{d}_{\text{trunk joint centre} \rightarrow \text{lower trunk CoM}} \\
 \mathbf{p}_{\text{arms}}^{\text{CoM}} &= \mathbf{p}_{\text{trunk joint centre}} + R_{\text{sacrum}} \mathbf{d}_{\text{trunk joint centre} \rightarrow \text{arms CoM}} \\
 \mathbf{p}_{\text{left thigh}}^{\text{CoM}} &= \mathbf{p}_{\text{left hip}} + R_{\text{left thigh}} \mathbf{d}_{\text{left hip} \rightarrow \text{left thigh CoM}} \\
 \mathbf{p}_{\text{right thigh}}^{\text{CoM}} &= \mathbf{p}_{\text{right hip}} + R_{\text{right thigh}} \mathbf{d}_{\text{right hip} \rightarrow \text{right thigh CoM}} \\
 \mathbf{p}_{\text{left shank}}^{\text{CoM}} &= \mathbf{p}_{\text{left knee}} + R_{\text{left shank}} \mathbf{d}_{\text{left knee} \rightarrow \text{left shank CoM}} \\
 \mathbf{p}_{\text{right shank}}^{\text{CoM}} &= \mathbf{p}_{\text{right knee}} + R_{\text{right shank}} \mathbf{d}_{\text{right knee} \rightarrow \text{right shank CoM}}
 \end{aligned} \tag{8.2}$$

where \mathbf{p}_s^{CoM} is the position of the CoM for segment s , p_j the position of the joint centre j , R_s the orientation matrix representing the orientation of segment s in the global frame, and $d_{A \rightarrow B}$ the vector connecting the joint A with the CoM of the segment B , expressed in the anatomical frame of segment B .

$$\mathbf{p}_{\text{athlete}}^{CoM} = \frac{\sum_s m_s \mathbf{p}_s^{CoM}}{\sum_s m_s} \quad (8.3)$$

where m_s is the mass of segment s and the sum is computed over the eight segments defined in Eq. 8.2.

The velocity of the athlete's CoM is computed analogous to the position (Eqs. 8.4-8.6).

$$\begin{aligned} \mathbf{v}_{\text{neck}} &= \mathbf{v}_{\text{GNSS}} + (R_{\text{head}} \omega_{\text{head}}) \times (R_{\text{head}} \mathbf{d}_{\text{GNSS} \rightarrow \text{neck}}) \\ \mathbf{v}_{\text{trunk joint centre}} &= \mathbf{v}_{\text{neck}} + (R_{\text{sternum}} \omega_{\text{sternum}}) \\ &\quad \times (R_{\text{sternum}} \mathbf{d}_{\text{neck} \rightarrow \text{trunk joint centre}}) \\ \mathbf{v}_{\text{left hip}} &= \mathbf{v}_{\text{trunk joint centre}} + (R_{\text{sacrum}} \omega_{\text{sacrum}}) \\ &\quad \times (R_{\text{sacrum}} \mathbf{d}_{\text{trunk joint centre} \rightarrow \text{left hip}}) \\ \mathbf{v}_{\text{right hip}} &= \mathbf{v}_{\text{trunk joint centre}} + (R_{\text{sacrum}} \omega_{\text{sacrum}}) \\ &\quad \times (R_{\text{sacrum}} \mathbf{d}_{\text{trunk joint centre} \rightarrow \text{right hip}}) \\ \mathbf{v}_{\text{left knee}} &= \mathbf{v}_{\text{left hip}} + (R_{\text{left thigh}} \omega_{\text{left thigh}}) \\ &\quad \times (R_{\text{left thigh}} \mathbf{d}_{\text{left hip} \rightarrow \text{left knee}}) \\ \mathbf{v}_{\text{right knee}} &= \mathbf{v}_{\text{right hip}} + (R_{\text{right thigh}} \omega_{\text{right thigh}}) \\ &\quad \times (R_{\text{right thigh}} \mathbf{d}_{\text{right hip} \rightarrow \text{right knee}}) \\ \mathbf{v}_{\text{head}}^{CoM} &= \mathbf{v}_{\text{neck}} + (R_{\text{head}} \omega_{\text{head}}) \times (R_{\text{head}} \mathbf{d}_{\text{neck} \rightarrow \text{head CoM}}) \\ \mathbf{v}_{\text{upper trunk}}^{CoM} &= \mathbf{v}_{\text{neck}} + (R_{\text{sternum}} \omega_{\text{sternum}}) \\ &\quad \times (R_{\text{sternum}} \mathbf{d}_{\text{neck} \rightarrow \text{upper trunk CoM}}) \\ \mathbf{v}_{\text{lower trunk}}^{CoM} &= \mathbf{v}_{\text{trunk joint centre}} + (R_{\text{sacrum}} \omega_{\text{sacrum}}) \\ &\quad \times (R_{\text{sacrum}} \mathbf{d}_{\text{trunk joint centre} \rightarrow \text{lower trunk CoM}}) \\ \mathbf{v}_{\text{arms}}^{CoM} &= \mathbf{v}_{\text{trunk joint centre}} + (R_{\text{sacrum}} \omega_{\text{sacrum}}) \\ &\quad \times (R_{\text{sacrum}} \mathbf{d}_{\text{trunk joint centre} \rightarrow \text{arms CoM}}) \\ \mathbf{v}_{\text{left thigh}}^{CoM} &= \mathbf{v}_{\text{left hip}} + (R_{\text{left thigh}} \omega_{\text{left thigh}}) \\ &\quad \times (R_{\text{left thigh}} \mathbf{d}_{\text{left hip} \rightarrow \text{left thigh CoM}}) \\ \mathbf{v}_{\text{right thigh}}^{CoM} &= \mathbf{v}_{\text{right hip}} + (R_{\text{right thigh}} \omega_{\text{right thigh}}) \\ &\quad \times (R_{\text{right thigh}} \mathbf{d}_{\text{right hip} \rightarrow \text{right thigh CoM}}) \\ \mathbf{v}_{\text{left shank}}^{CoM} &= \mathbf{v}_{\text{left knee}} + (R_{\text{left shank}} \omega_{\text{left shank}}) \\ &\quad \times (R_{\text{left shank}} \mathbf{d}_{\text{left knee} \rightarrow \text{left shank CoM}}) \\ \mathbf{v}_{\text{right shank}}^{CoM} &= \mathbf{v}_{\text{right knee}} + (R_{\text{right shank}} \omega_{\text{right shank}}) \\ &\quad \times (R_{\text{right shank}} \mathbf{d}_{\text{right knee} \rightarrow \text{right shank CoM}}) \end{aligned} \quad (8.5)$$

$$\mathbf{v}_{\text{athlete}}^{CoM} = \frac{\sum_s m_s \mathbf{v}_s^{CoM}}{\sum_s m_s} \quad (8.6)$$

where \mathbf{v}_j is the velocity at joint centre of joint j , \mathbf{v}_{GNSS} the velocity measured at the GNSS antenna, \mathbf{v}_s^{CoM} the velocity of the CoM of segment s , ω_s the measured angular velocity in the segment s 's anatomical frame, and $\mathbf{v}_{\text{athlete}}^{CoM}$ the velocity of the athlete's CoM.

Simplified model

The above model was simplified to use only two sensors: head and sternum. Thus, the body model consisted of one joint, the neck, connecting the two segments head and sternum. The athlete's CoM was fixed 0.1 m anterior and 75% of the trunk length (d_{trunk} , measured distance between shoulders and hips) inferior to the neck joint, i.e. $d_{\text{neck} \rightarrow \text{athlete CoM}} = [0.1 \quad -0.75d_{\text{trunk}} \quad 0]^T$. The position and velocity of the athlete's CoM were, therefore, computed according to Eqs. 8.7 and 8.8 (Figure 8.2B).

$$\hat{\mathbf{p}}_{\text{athlete}}^{CoM} = \mathbf{p}_{\text{GNSS}} + R_{\text{head}} \mathbf{d}_{\text{GNSS} \rightarrow \text{neck}} + R_{\text{sternum}} \mathbf{d}_{\text{neck} \rightarrow \text{athlete CoM}} \quad (8.7)$$

$$\begin{aligned} \hat{\mathbf{v}}_{\text{athlete}}^{CoM} = & \mathbf{v}_{\text{GNSS}} + (R_{\text{head}} \omega_{\text{head}}) \times (R_{\text{head}} \mathbf{d}_{\text{GNSS} \rightarrow \text{neck}}) \\ & + (R_{\text{sternum}} \omega_{\text{sternum}}) \times (R_{\text{sternum}} \mathbf{d}_{\text{neck} \rightarrow \text{athlete CoM}}) \end{aligned} \quad (8.8)$$

where $\mathbf{d}_{\text{GNSS} \rightarrow \text{neck}}$ and $\mathbf{d}_{\text{neck} \rightarrow \text{athlete CoM}}$ are the vectors connecting the GNSS antenna position to the neck and the neck to the athlete's CoM, respectively.

8.2.4 Reference system

The reference system consisted of six gen-locked panned, tilted and zoomed HDV cameras (PMW-EX3, Sony, Tokyo, Japan) recording at 50 Hz, explained in detail in Spörri et al. (2016c). Twenty-two joint centres and subject ambient reference points were manually digitized and reconstructed in 3D, as described in detail in Gilgien et al. (2015c); Spörri et al. (2016c). The mean resultant photogrammetric error of this methodology was reported to be 23 mm with a standard deviation of 10 mm (Klous et al., 2010). The reconstructed joint centre positions were then used to compute the athlete's CoM based on the body segment model of de Leva (1996). The reference system was synchronized with the inertial sensors using an electronic trigger. The reference system covered one entire left turn (Gate 7, solid black line Figure 8.1A).

8.2.5 Error analysis

Each left turn at gate 7 was time normalized to 100 samples for both the wearable and reference system. Then, for each normalized turn and parameter, position error curves

were defined as vector norm of the sample-by-sample difference between the wearable and reference system. Position error curves were computed for each joint centre, the GNSS antenna position and the two CoM models. Speed error curves were defined as the difference of the velocity norm between the wearable and reference system. Speed error curves were computed for the GNSS antenna and the two CoM models. For each run, median error and interquartile range were computed by averaging over time. The accuracy was computed as the median of all median errors and the precision as the median of the interquartile range.

8.3 Results

The proposed wearable system fused the data from the dGNSS with the inertial sensor-based system to obtain as accurate and precise position and speed estimates of the CoM as possible. Figure 8.3 shows the antenna position, reference CoM position, and $\mathbf{p}_{\text{athlete}}^{CoM}$ (top) and antenna speed, reference speed, and $\mathbf{v}_{\text{athlete}}^{CoM}$ (bottom) projected onto the horizontal plane (i.e. perpendicular to gravity) for three consecutive turns of a typical run. Figure 8.4 shows the average speed curves for the reference, full model and simplified model over the left turn at gate 7.

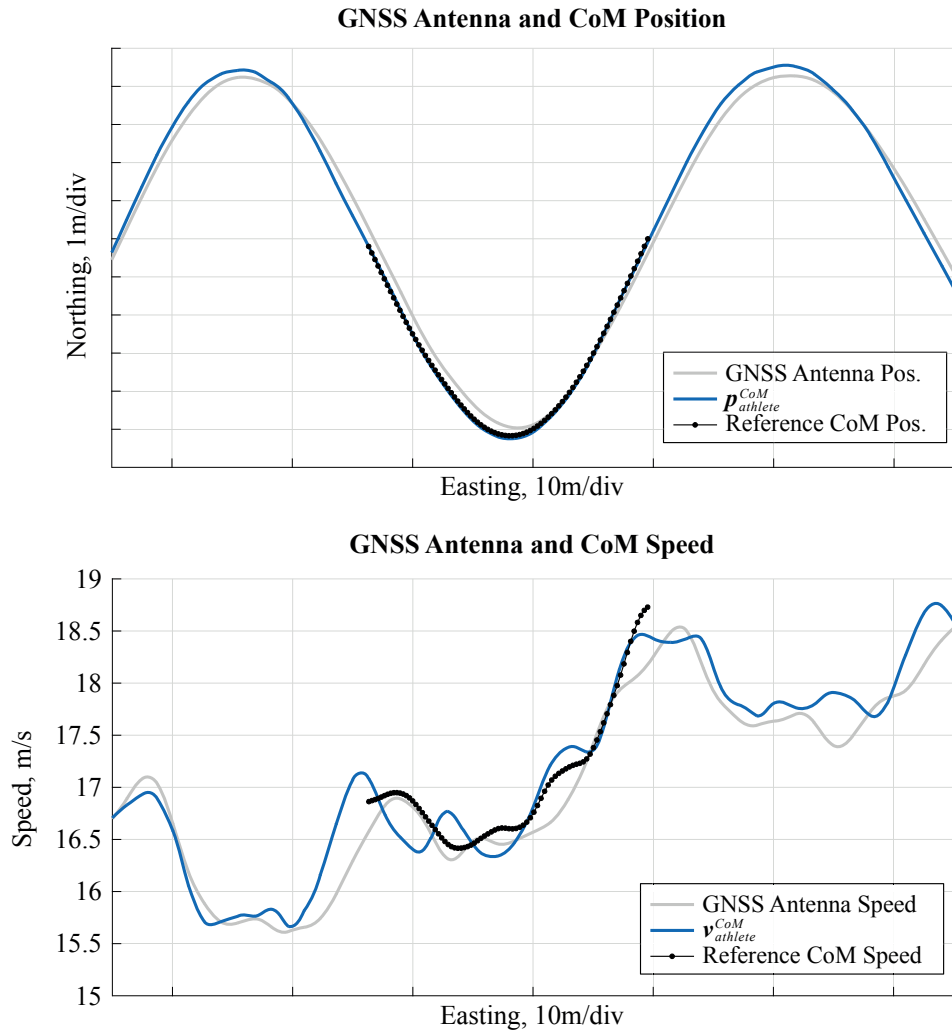


Figure 8.3 – Position and speed curves for three consecutive turns (gates 6-8, Figure 8.1A) of a typical run. The central turn (gate 7) has been covered by the reference system. The athlete skied from left to right. Top) GNSS antenna position (light grey), $p_{athlete}^{CoM}$ (blue), and reference CoM position (dotted black) during the same turn. Bottom) GNSS antenna speed (light grey), $v_{athlete}^{CoM}$ (blue), and reference CoM speed (dotted black) during the same turn. Both figures are aligned such that their Easting axes are identical.

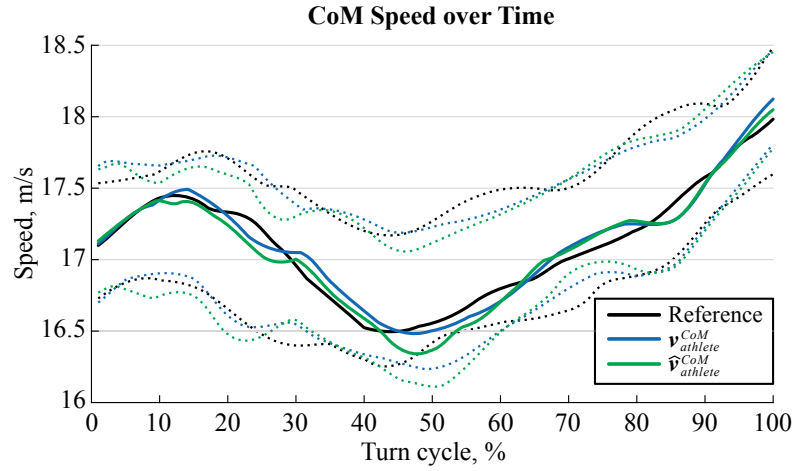


Figure 8.4 – Reference speed (black) and estimated speed (blue and green) for the CoM. Solid lines are the median speed for all twelve turns at gate 7 analysed and the dotted lines the 25th and 75th percentiles.

Parameter	Accuracy ($median(median(E))$)	Precision ($median(iqr(E))$)
Speed		
GNSS antenna speed error, m/s	-0.03	0.15
GNSS antenna - CoM speed difference, m/s	-0.15	0.20
$\mathbf{v}_{athlete}^{CoM}$, m/s	0.04	0.14
$\hat{\mathbf{v}}_{athlete}^{CoM}$, m/s	-0.01	0.14
Position		
GNSS antenna position error, m	0.04	0.03
GNSS antenna - CoM position difference, m	0.62	0.05
$\mathbf{p}_{athlete}^{CoM}$, m	0.08	0.06
$\hat{\mathbf{p}}_{athlete}^{CoM}$, m	0.12	0.06
Neck position error, m	0.06	0.03
Left hip position error, m	0.10	0.07
Right hip position error, m	0.10	0.07
Left knee position error, m	0.16	0.06
Right knee position error, m	0.14	0.08
Left ankle position error, m	0.17	0.07
Right ankle position error, m	0.15	0.09

Table 8.1 – Median accuracy and precision for all errors and differences between GNSS antenna and CoM speed and position.

The GNSS antenna position error was on average (accuracy) 0.04 m with a standard deviation (precision) of 0.03 m (Table 8.1). The position difference between GNSS antenna and reference CoM was on average 0.62 m with a standard deviation of 0.05 m. The CoM model including the data obtained by inertial sensors allowed estimating this distance and correcting for it. After these corrections, the accuracy was found to be 0.08 m for $\mathbf{p}_{athlete}^{CoM}$ and 0.12 m for $\hat{\mathbf{p}}_{athlete}^{CoM}$, with a precision of 0.06 m (Table 8.1).

With respect to the joint centre positions of the full 3D body model, it can be observed that both accuracy and precision worsen the farther away the joint is from the GNSS antenna (Table 8.1). For $\mathbf{v}_{\text{athlete}}^{\text{CoM}}$ accuracy was found to be 0.04 m/s (0.24%) and precision 0.14 m/s (0.83%), respectively. $\hat{\mathbf{v}}_{\text{athlete}}^{\text{CoM}}$ had a similar accuracy (-0.01 m/s) and precision (0.14 m/s). Joint position errors, as well as the CoM position and CoM speed errors of the full 3D body and simplified model remained approximately constant over time (Figures 8.5-8.6).

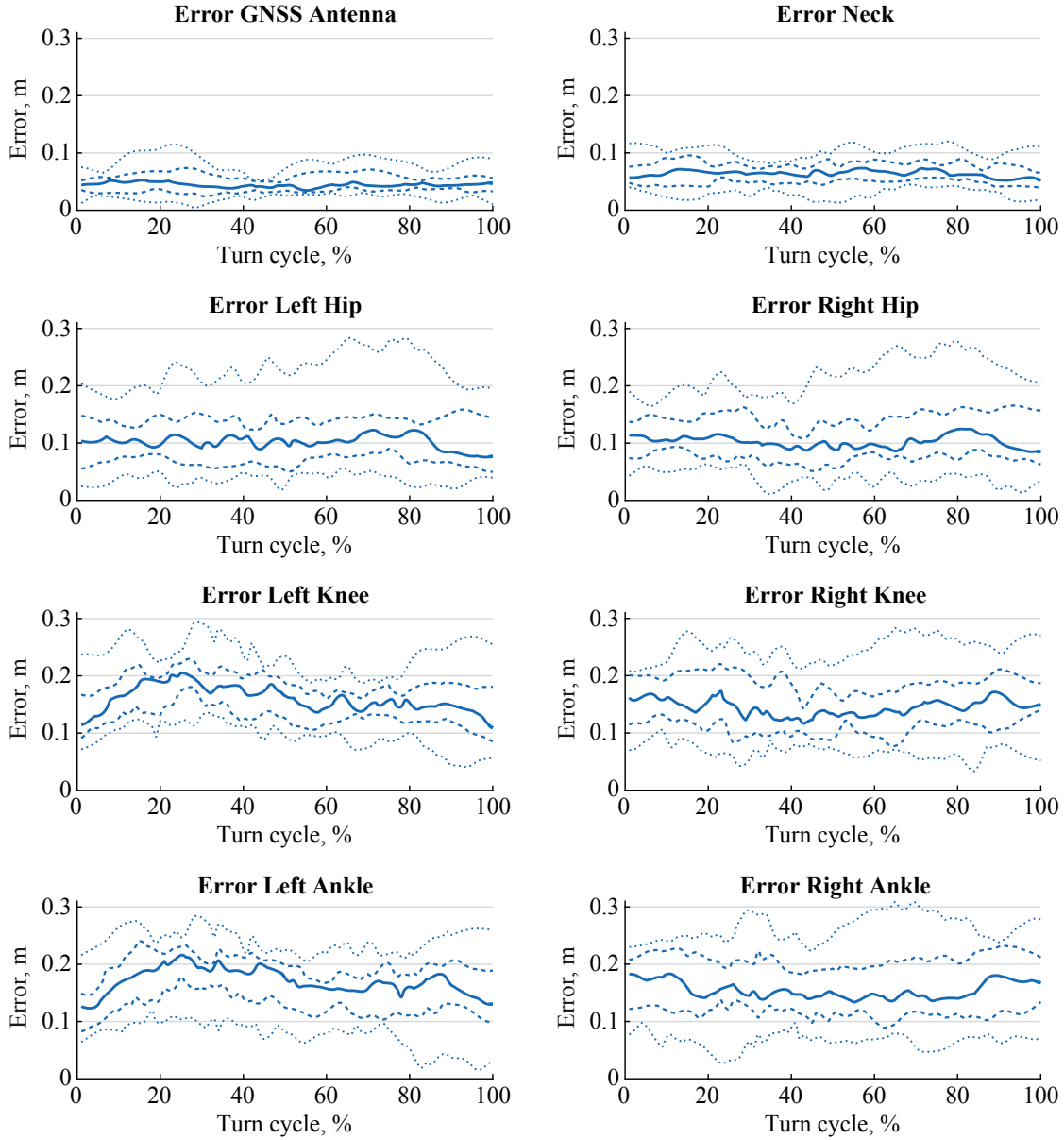


Figure 8.5 – Position error of the GNSS antenna and the joint centres. In each graph the lines are, from bottom to top, the 5th (dotted), 25th (dashed), 50th (solid), 75th (dashed), and 95th (dotted) percentiles.

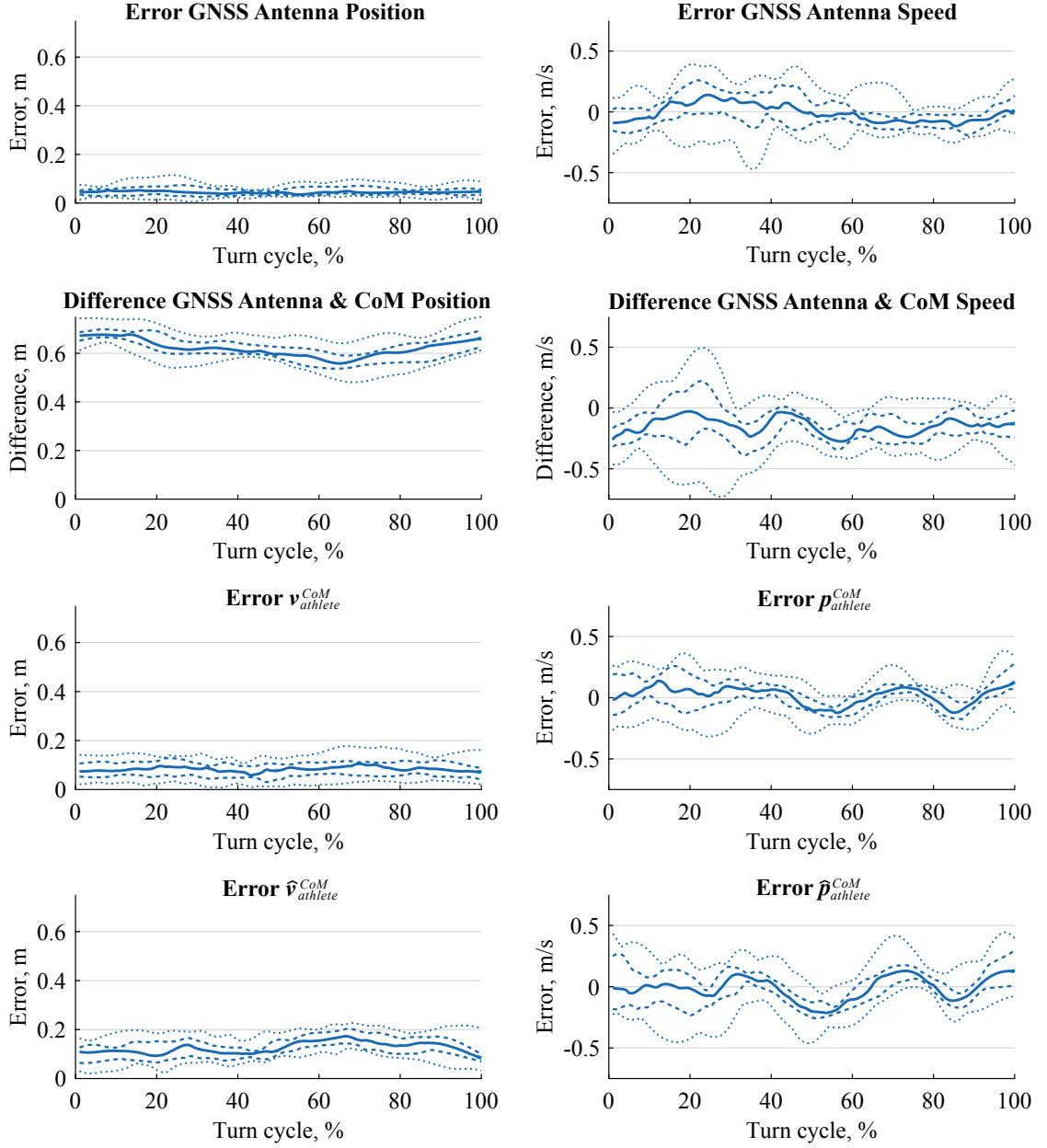


Figure 8.6 – GNSS antenna position, speed and athlete CoM position, speed differences and errors. In each graph the lines are, from bottom to top, the 5th (dotted), 25th (dashed), 50th (solid), 75th (dashed), and 95th (dotted) percentiles.

8.4 Discussion

In the current study, dGNSS and inertial sensors have been combined for obtaining an estimate of the centre of mass kinematics for alpine ski racing. In a first step, inertial sensors were used to compute a full 3D body model of the skier. In the second step,

this model was fused with the position and velocity data obtained from dGNSS and the skier's CoM kinematics were calculated. For an easy application in daily training, a simplified model using only two inertial sensors – fixed to the head and sternum – was proposed. Position errors were on average 0.08 m for the full 3D body model and 0.12 m for the simplified model. On average speed errors were found to be of the same order of magnitude for both models.

The proposed system's performance for measuring the CoM position showed a similar accuracy (0.08 m compared to 0.09 m), but had a better precision (0.06 m compared to 0.12 m) than the inverted pendulum model proposed and validated by Gilgien et al. (2015c). The advantage of the system proposed in the current study compared to the latter, was that no 3D terrain model was needed. However, instead, inertial sensors must be added to the dGNSS system. Medio-lateral motion (i.e. leaning inward)) was better measured by using inertial sensors (Figure 8.3), which may explain the better precision of the system proposed in the current study. This approach was based on a direct measurement of skiing movements and could also estimate speed and position during out-of-balance situations or jumps. When comparing the two systems, the system introduced by Gilgien et al. (2015c) was able to measure the overall CoM position with similar accuracy, but might have missed the full amplitude of the medio-lateral motion (inward leaning). By using a combination of both methods even better accuracy and precision values might be achieved for the CoM position.

Interestingly, for the estimation of the CoM speed, both the full 3D body and the simplified model had a similar accuracy and precision. This similarity in performance could be explained by the fact that the lower limbs have similar speed as the head and trunk segments and therefore have a low impact on overall CoM speed. As for the estimation of the CoM position, the models were able to well measure the medio-lateral movements. Therefore, the system's speed accuracy and precision increased considerably compared to the case where the speed measured at the GNSS antenna would have been used as the CoM speed. In Figures 8.3 and 8.4 it can be observed that the wearable speed estimation is oscillating around the reference speed (for both the average speed between all turns and the individual speed). One potential explanation of this measurement error might be that the wearable system is lacking information about the arm movements, which, perhaps, are used by the athlete to counterbalance small velocity changes. When comparing individual runs instantaneous speed differences below 0.5 m/s, the approximate amplitude of the oscillations, might be caused by measurement errors. Comparing average speeds or accelerations over certain sections (e.g. turn phases) might therefore be advisable to reliably detect small speed changes below 0.5 m/s.

The individual joint position errors showed the typical error propagation characteristic of forward kinematic chains: the further the joint was along the chain the larger grew the errors, both for accuracy and precision (Figure 8.5 and Table 8.1). The accuracy decreased approximately 3-5 cm per joint except between the knee and ankle joints. Especially for the larger segment's orientation (as observed for the trunk or thigh segment), estimation errors of 2-3 degrees could cause errors of 2-3 cm in the estimation of the

distal joint (e.g. hip and knee) position. These errors were then accumulated through the entire chain and did negatively affect the computation of the CoM position. This error accumulation might also explain why the simple model reached almost the same accuracy and precision as the full 3D body model. On the other hand, this relatively small increase in joint position error towards more distal joints could also be an indication of accurate orientation estimate confirming the previously reported accuracy and precision in segment orientation estimation in the order of 2° and 6° , respectively (Fasel et al., 2013).

Comparing the full 3D body with the simplified model it can be observed that the simplified model had a similar performance for both CoM position and speed. Thus, especially from a coaching perspective, the simplified system may be used. However, the full body 3D model has also its advantages: in addition to CoM position and speed the system could also deliver information about the athlete's posture and joint kinematics, which then could be related to skiing performance. For instance, the full body 3D model would allow computing the distance between the ankle joint centre and the athlete's CoM (Fasel et al., 2015b), an important performance-related parameter (Reid, 2010).

Earlier studies reported meaningful CoM speed differences of 0.5 m/s to 1 m/s within a slalom (Reid, 2010) and giant slalom (Spörri et al., 2012b) turn. Differences in the order of 0.5 m/s were also reported between turns of different course settings (Spörri et al., 2012b) or between the fastest and slowest trial of the same athlete and turn (Spörri et al., 2012a). The accuracy and precision of the system proposed in this study was found to be approximately five times lower than the above differences between conditions. Consequently, the proposed systems' performance (both the full 3D body model and the simplified model) can be considered to be well suited for measuring such speed differences, although small meaningful differences might not always be detectable.

With regard to CoM line characteristics, Spörri et al. (2012a) reported differences in the order of 0.1 m to 0.5 m between fast and slow trials of the same athlete at the same course setting or between two different course settings. The proposed system's accuracy and precision of 0.08 m and 0.06 m might probably be just enough to detect larger differences in the skiers' CoM lines, as they can occur within the competition disciplines giant slalom, super-G, and downhill.

One limitation of the system proposed in this study is the fact that even the simplified system might be too complex to be used for performance analysis during everyday training. The handling of the dGNSS system with its reference base stations needs the presence of at least one additional person. Different approaches could be tried in order to increase the system's accuracy and reduce at the same time its complexity. In the current study the inertial data was processed entirely independent from the dGNSS data. In a future development sensor fusion approaches such as Kalman and Particle filtering (Won et al., 2010) could be applied to improve the GNSS trajectory information. In the same time, such a fusion method could also be used to further reduce drift in the estimation of the segment's orientation, increasing the body model's accuracy. To reduce the complexity the dGNSS system could also be replaced by a standard GNSS system not requiring any base stations. Further studies should address whether the loss of accuracy

of standard GNSS compared to dGNSS could be compensated with the fusion of inertial sensor data.

8.5 Conclusions

This study provided the fundamental concepts for an accurate and precise estimation of a skier's CoM trajectory and speed based on the fusion of dGNSS and inertial sensors. Inertial sensor information was used to construct a body model to estimate relative CoM kinematics and was added to the absolute antenna kinematics obtained from a dGNSS. The proposed system was simpler to use than existing systems based on cameras or terrain models. Aiming an even simpler system, the reduction of sensors from a full 3D body model to a simplified trunk model lead to almost no decrease in accuracy and precision. The model's independency should allow to apply the algorithm without adaptations to the different skiing disciplines such as slalom or downhill. Future developments should aim at improving the accuracy and precision through better sensor fusion and at further simplifying the system.

Acknowledgements

This work was supported by the "Fondation de soutien à la recherche en orthopédie et traumatologie" and the Swiss Federal Office of Sport (FOSPO).

9 Position drift correction for absolute CoM kinematics

Abstract

In this study we present and validate a method to correct velocity and position drift for inertial sensor-based measurements of alpine ski racing. Gate positions were surveyed and magnets placed at each gate. Gate crossings were then detected with a magnetometer attached to the athlete's lower back. A full body inertial sensor setup allowed to track the athlete's posture and the magnet positions were used as anchor points to correct position and velocity drift from the integration of the acceleration. Centre of mass (CoM) position errors were $0.24 \text{ m} \pm 0.10 \text{ m}$ and CoM velocity errors were $0.00 \text{ m/s} \pm 0.20 \text{ m/s}$. For extracted turn entrance and exit speeds the 95% limits of agreements were between -0.3 m/s and 0.4 m/s . Limits of agreement for the total path length of a turn were between 0.05 m and 0.17 m . The proposed setup and processing allowed to measure the CoM kinematics with similar errors than with differential global navigation systems (GNSS) even though the athlete's movement was only measured with inertial and magnetic sensors. Assuming that gate positions could also be obtained without (differential) GNSS, the CoM kinematics could also be obtained in areas with reduced or no GNSS signal reception, such as in forests or indoors.

Keywords: drift correction, inertial sensors, position, center of mass, skiing speed, trajectory, fusion, magnet, gate crossing, magnetometer

9.1 Introduction

To measure human body displacement in outdoor settings differential global navigation satellite system (GNSS) is recognised to be well suited. It allows to obtain the antenna trajectory at a reasonably high sampling frequency and with a sub-decimetre accuracy (Gilgien et al., 2014b). For applications where overall body posture remains relatively constant, it can be assumed that centre of mass (CoM) kinematics can be approximated by the GNSS antenna kinematics with sufficient precision (Scott et al., 2016; Terrier and Schutz, 2005; Townshend et al., 2008; Waldron et al., 2011). However, when the body postures are changing significantly during motion cycles, and if instantaneous CoM kinematics are the variables of interest, an approximation of the CoM kinematics by the GNSS antenna kinematics cannot be considered as sufficiently valid. Thus, an alternative solution needs to be found to track the athlete's CoM relative to the GNSS antenna. The determination of the athlete's absolute CoM position consists of two aspects: 1) the global GNSS antenna position and 2) the relative position of the CoM with respect to the GNSS antenna position. To this end, for alpine ski racing, two solutions were proposed: either a modelling approach (Gilgien et al., 2015c; Nemec et al., 2014; Supej et al., 2013) or, more commonly, a combination or fusion of GNSS with inertial sensors (Brodie et al., 2008; Fasel et al., 2016e; Supej, 2010). Generally, both solutions allow the estimation of absolute CoM trajectory with an accuracy and precision of <0.1 m, provided differential GNSS is used. However, the use of differential GNSS has also three major drawbacks: (1) a terrestrial GNSS reference base station and good satellite coverage are needed, while the hardware is very costly; (2) signal shading by forest or topography; and (3) the data-logger has to be carried on the athlete and is usually fixed onto his back. Thus, for routine measurements (e.g. during training sessions) this setup might have the disadvantage of being cumbersome. Therefore, alternatives to measure CoM kinematics should be found.

As already mentioned, inertial sensors can be used to estimate the athlete's relative CoM kinematics (i.e. relative CoM position with respect to a point on the athlete such as the head). For example, for indoor carpet skiing, an accuracy and precision of 29 mm and 7 mm was found for the CoM position relative to the lumbar joint centre (Chapter 7). Considering the above mentioned drawbacks, finding new solutions to estimate not only the relative but also the absolute CoM position would render the use of differential GNSS obsolete. However, the problem of inertial sensors is that they cannot measure the position directly. Instead, measured acceleration in the sensor frame has to be transformed into a global frame, Earth's gravity removed, and then integrated twice to finally obtain position. Measurement errors from the first two steps accumulate during the integration, resulting in large position drifts. Biomechanical movement constraints can help to correct this drift. For example, in gait analysis where inertial sensors are fixed to the feet, drift can be reduced by setting velocity to zero at each stance phase (Mariani et al., 2010). However, for activities without motionless periods, e.g. skiing, this procedure cannot be applied. When combining inertial sensors and GNSS, velocity

and position obtained with inertial sensors can be corrected each time a new GNSS reference sample is available (Grewal et al., 2013). Alternatively, position reference samples (i.e. anchor points) could be obtained independently from GNSS. Provided that each time an athlete crosses a priori known locations corresponding time information is recorded, and as long as such passages occur sufficiently often, the position drift resulting from integrating the acceleration can be corrected. In alpine ski racing the athlete is constrained to follow a predefined path marked by gates. Therefore, these gates could be considered as potential anchor points. If the gate locations and the corresponding time of crossing the gates are known, position drift could be corrected. Hence, it might be possible to measure an athlete's CoM trajectory by the sole use of inertial sensors (i.e. without any GNSS data being required). Gate locations could be measured using land surveying techniques (Gilgien et al., 2015a). Gate crossing times could be obtained by a magnetometer-based method (Fasel et al., 2016d,g).

Accordingly, the aim of this study was to design and validate a system to estimate absolute CoM kinematics during alpine giant slalom (GS) skiing without the use of GNSS (i.e. by the sole use of inertial sensor measurements fused with gate timing and gate position information as anchor points). The decrease in system accuracy and precision for super-G (SG) and downhill (DH) conditions compared to the GS condition was assessed by reducing the anchor points to include only every second or third GS gate, respectively.

9.2 Methods

9.2.1 Inertial system

Experimental setup

Seven inertial sensors (Physilog 4, Gait Up, Switzerland) recording acceleration and angular velocity at 500 Hz were fixed to the left and right shanks and thighs, to the sacrum, to the sternum, and to the helmet using medical tape (Fig. 9.1). Additionally, the sacrum sensor contained a magnetometer sampling at 125 Hz. Accelerometer offset and sensitivity were corrected according to Ferraris et al. (1995). Gyroscope offset was corrected during a static phase before each run. Magnetometer offset, sensitivity and axis-misalignment were corrected according to Bonnet et al. (2009). A low-cost GNSS receiver (CAM-M8, u-blox, Switzerland) was placed in the athlete's back protector together with a GNSS antenna (TW2710, Tallysman, Canada) placed approximately at shoulder height. All inertial sensors and the GNSS receiver were wirelessly synchronized. Prior to each run, athletes performed functional calibration movements as described in Chapter 6. An additional static upright posture with slightly flexed knees and parallel skis was performed at the start and finish. Each gate of a giant slalom course served as an anchor point and was equipped with a magnet. The magnet was constructed by vertically stacking 10 small neodymium magnets (S-20-10-N, Supermagnete, Switzerland) spaced by 5 mm to a 15 cm long stick (Fig. 9.1). Magnet position at each gate was

obtained using differential GNSS. Thus, each anchor point corresponds to a gate position, which was assumed to be identical to the magnet position.

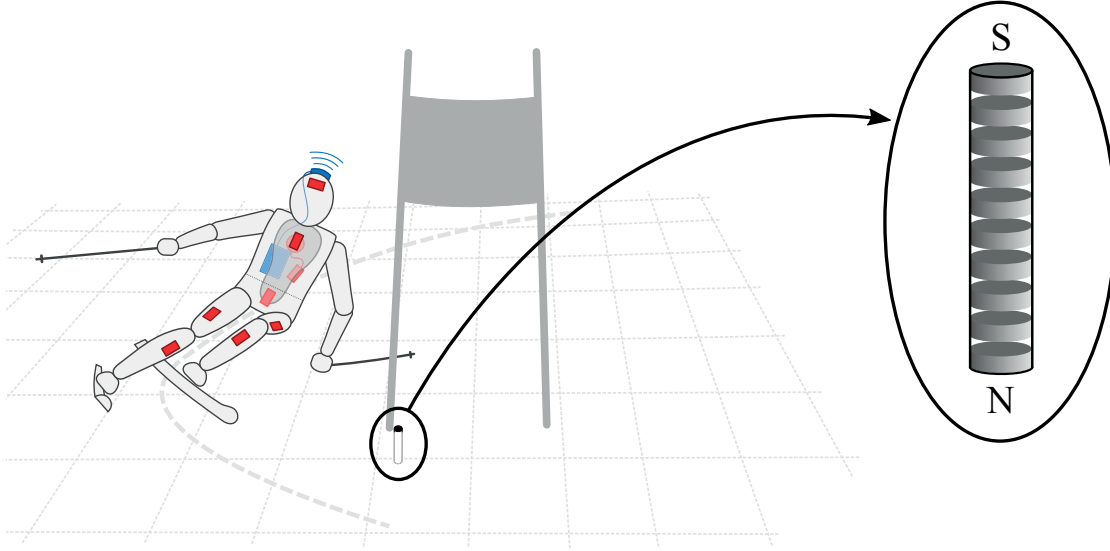


Figure 9.1 – Illustration of the experimental setup during a left turn. The inertial sensors are represented by the red boxes. The reference differential GNSS system is illustrated in blue with the antenna fixed to the helmet and the data logger worn on the back. The back protector contained the low-cost GNSS system with the antenna located approximately between the shoulder blades, as well as the data logger integrated in the inertial sensor fixed to the protector’s left side. The magnets were buried into the snow, close to the pole. A zoomed view of the buried magnet is provided on the right side of the illustration.

Measurement protocol

Eleven European Cup level athletes performed a total of 17 runs on a typical GS course with varying gate distances (21.8 m – 27.8 m). All athletes gave written informed consent prior to the measurements and the study was approved by the Ethical committee of the Ecole Polytechnique Fédérale de Lausanne (Study Number: HREC 006-2016).

Data processing

After functional calibration, segment orientation was found with strap-down integration and joint orientation drift correction as described in Chapters 5 and 6. To fuse the anchor points with acceleration data from the inertial sensor at the sacrum, two separate Extended Kalman Smoothers (EKS) (Hartikainen et al., 2011) were used. The first smoother was used to obtain an initial sacrum trajectory based on the inertial data only (Fig. 9.2). Since the sacrum sensor would not pass the anchor points (i.e. gates) with zero distance, the position offsets between the sacrum sensor position and each anchor point at gate crossing had to be estimated. Next, the anchor points estimated with the inertial

data were matched to the surveyed anchor points. Then, the second smoother fused the anchor points with the inertial data for obtaining a refined sacrum trajectory. Relative anchor points were re-estimated and matched again to the surveyed anchor points and the EKS was run a second time. Finally, the athlete's absolute CoM kinematics were determined by combining the sacrum's refined trajectory with the relative CoM position (Fig. 9.2).

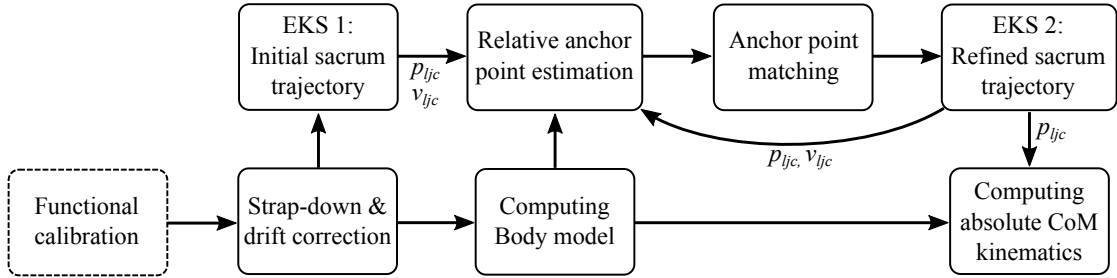


Figure 9.2 – Flow chart of the proposed algorithm for data processing. The outputs of **functional calibration** were the rotation matrices for the sensor-to-segment alignments. **Strap-down & drift correction** provided the segment orientations in a common global frame. During **EKS 1** the initial sacrum (i.e. LJC) position and velocity were obtained. **Computing body model** provided the athlete's joint and CoM positions relative to his LJC. **Relative anchor point estimation** provided the absolute gate positions in the inertial sensor frame and the relative gate positions at gate crossing with respect to the athlete's LJC. **Anchor point matching** computed the transformation between the estimated gate positions expressed in the inertial sensor frame and the global Earth frame. Additionally, all estimated gate positions were matched to the surveyed gate positions. The output of **EKS 2** was a refined sacrum trajectory and velocity. The output of **computing absolute CoM kinematics** was the final estimate of the position and velocity of the CoM.

Extended Kalman Smoother 1: initial sacrum trajectory

The sacrum sensor's acceleration was expressed in the global frame (X-axis: forwards with respect to the athlete's still posture at start; Y-axis: vertical, along Earth's gravity; Z-axis: cross-product between X- and Y-axis; origin: sacrum position at start) and gravity was removed. To estimate the sacrum trajectory $\mathbf{p}_{\text{sacr}}(t)$ an EKS with 16 states (3D position, 3D velocity, 3D acceleration, 3D position offset, 3D acceleration offset, azimuth offset) integrated the gravity-corrected acceleration twice. A zero-velocity constraint during the static instants of time at start and finish was used to reduce the position drift. A constant-acceleration model was used for the state transitions. To take into account the rapidly changing acceleration during each turn, the process noise was designed to be dependent on the measured acceleration with larger noise during phases with high acceleration variations (e.g. turns).

Body model and relative anchor point estimation

The athlete's body model was obtained as described in Chapter 7 with the lumbar joint centre (LJC) as the origin of the athlete's local coordinate system. Lower limb joint positions and athlete's CoM were estimated relative to the LJC. As for the sacrum's initial trajectory, azimuth was set to 0° at the static posture at start. Gate crossings were detected based on the peaks in the recorded magnetic field intensity at the sacrum sensor (see appendix for details). For all further processing, it was assumed that the sacrum sensor position was at the same position as LJC (i.e. $\mathbf{p}_{\text{sacr}}(t) = \mathbf{p}_{\text{ljc}}(t)$) and in consequence $\mathbf{v}_{\text{sacr}}(t) = \mathbf{v}_{\text{ljc}}(t)$.

Suppose the skiing course consisted of N gates equipped with magnets and M gate crossings were detected (where M may be different from N due to missed gates (i.e. distance to magnet too large) or wrong detections due to noise). The N gates' magnet positions (i.e. anchor points) are denoted by $\{\mathbf{g}_n\}$, $n \in [1; N]$. The M "hypothetical" anchor points are denoted by $\{\mathbf{g}_m\}$, $m \in [1; M]$. Suppose further that the LJC trajectory is denoted by $\mathbf{p}_{\text{ljc}}(t)$ with t being time, and that LJC velocity is denoted by $\mathbf{v}_{\text{ljc}}(t)$. For a given gate crossing m , detected at time t_m , the vector \mathbf{r}_m is relying $\mathbf{p}_{\text{ljc}}(t_m)$ to \mathbf{g}_m and $\hat{\mathbf{p}}_m$ is the projection of $\mathbf{p}_{\text{ljc}}(t_m)$ onto the snow surface S_m at gate m . \mathbf{x}_m is the vector connecting $\hat{\mathbf{p}}_m$ to \mathbf{g}_m and is assumed to lie on S_m and perpendicular to $\mathbf{v}_{\text{ljc}}(t_m)$ (Fig. 9.3). $\|\mathbf{r}_m\|$ can be estimated based on the magnetic field intensity at gate crossing, $\|\mathbf{B}(t_m)\|$. For a magnetic point source, its magnetic field intensity $\|\mathbf{B}\|$ decays exponentially to the third power of the distance $\|\mathbf{r}\|$ (Furlani, 2001). For the magnets used in this study, based on in-lab measurements with constant ambient magnetic field, the relation of $\|\mathbf{B}\|$ to $\|\mathbf{r}\|$ was approximated with Eq. 9.1.

$$\|\mathbf{r}\| = \begin{cases} -0.4 \|\mathbf{B}\| + 1.0 & \text{if } \|\mathbf{B}\| < 1.62 \\ -0.062 \|\mathbf{B}\| + 0.452 & \text{else} \end{cases} \quad (9.1)$$

where the magnetometer was calibrated such that $\|\mathbf{B}\| = 1$ for $\|\mathbf{r}\| \gg 0$.

However, $\mathbf{B}(t_m)$ did not allow a precise estimate of the xyz-components of \mathbf{r}_m . Instead it was computed following Eqs. 9.2-9.4 for right turns and Eqs. 9.2-9.3 and 9.5 for left turns, using the trigonometric relations as illustrated in Fig. 9.3. A turn was labelled as "right" if the sacrum's angular velocity along the trunk's longitudinal axis was negative at gate crossing.

$$\mathbf{r}_m = \mathbf{d}_m + \mathbf{x}_m \quad (9.2)$$

$$\mathbf{d}_m = \hat{\mathbf{p}}_m - \mathbf{p}_{\text{ljc}}(t_m) \quad (9.3)$$

$$\mathbf{x}_m = \sqrt{\|\mathbf{r}_m\|^2 - \|\mathbf{d}_m\|^2} \frac{\mathbf{d}_m \times \mathbf{v}_{\text{ljc}}(t_m)}{\|\mathbf{d}_m \times \mathbf{v}_{\text{ljc}}(t_m)\|} \quad (9.4)$$

$$\mathbf{x}_m = \sqrt{\|\mathbf{r}_m\|^2 - \|\mathbf{d}_m\|^2} \frac{\mathbf{v}_{\text{ljc}}(t_m) \times \mathbf{d}_m}{\|\mathbf{v}_{\text{ljc}}(t_m) \times \mathbf{d}_m\|} \quad (9.5)$$

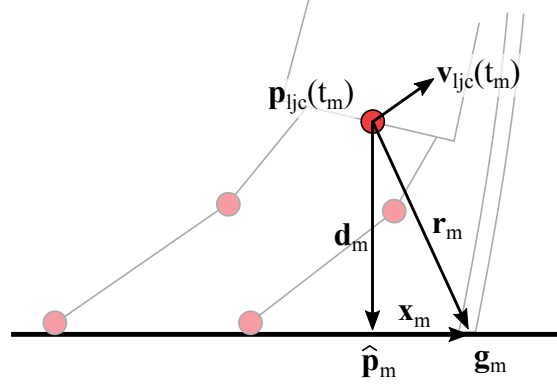


Figure 9.3 – Athlete posture relative to the gate seen from the back at gate crossing illustrated for a right turn. To simplify computation it was assumed that the inertial sensor fixed to the sacrum would measure the acceleration, angular velocity, and magnetic field at the position of the LJC.

To estimate S_m , first, snow contact points of the left and right feet were obtained by combining $\mathbf{p}_{ljc}(t_m)$ with the athlete's body model. It was supposed that the contact point of each leg was located 0.15 m distally from its ankle joint centre, along the shank's longitudinal axis. Second, the ski line $\mathbf{l}(t)$ was computed by averaging between the left and right contact points. Finally, S_m was obtained by fitting a plane to $\mathbf{l}(t)$, $t \in [t_m - 0.4 \text{ sec}; t_m + 0.4 \text{ sec}]$. Thus, $\hat{\mathbf{p}}_m$ could be computed according to Eq. 9.6.

$$\hat{\mathbf{p}}_m = \mathbf{p}_{ljc}(t_m) + \left((\bar{\mathbf{l}}_m - \mathbf{p}_{ljc}(t_m)) \cdot \mathbf{n}_m \right) \mathbf{n}_m \quad (9.6)$$

where $\bar{\mathbf{l}}_m$ is a random point on S_m (e.g. average of $\mathbf{l}(t)$, $t \in [t_m - 0.4 \text{ sec}; t_m + 0.4 \text{ sec}]$), \mathbf{n}_m the normal vector of S_m , and \cdot the dot product.

Anchor point matching

The matching of $\{\mathbf{g}_n\}$, $n \in [1; N]$ with $\{\mathbf{g}_m\}$, $m \in [1; M]$ was conducted under the hypothesis that not all N anchor points may have been detected and that additional anchor points may have been wrongly found due to noise in the recorded magnetic field. Since $\{\mathbf{g}_m\}$ are expressed in the inertial sensor's global frame \mathcal{S} where both the position and azimuth were initialized to zero during the static posture performed at start, the transformation from \mathcal{S} to the global Earth frame \mathcal{G} had to be found first. Note that the vertical axes of \mathcal{S} and \mathcal{G} were already aligned and that only an azimuth rotation angle α and translation \mathbf{o} had to be found. To this end, both $\{\mathbf{g}_n\}$ and $\{\mathbf{g}_m\}$ were interpreted as point clouds. The azimuth rotation angle was defined as the angle between the first principal components of $\{\mathbf{g}_n\}$ and $\{\mathbf{g}_m\}$ projected onto the horizontal plane. To find \mathbf{o} , $\{\mathbf{g}_n\}$ needed to be matched to $\{\hat{\mathbf{g}}_m\}$, the azimuth aligned point cloud of $\{\mathbf{g}_m\}$. To find the best matching solution, a feature vector f_n and f_m was constructed for each

point in $\{\mathbf{g}_n\}$ and $\{\hat{\mathbf{g}}_m\}$, respectively. To construct the features, each anchor point was described relative to its preceding and following anchor point. In addition, each turn was labelled as left / right and was assigned a turn number (Eqs. 9.7-9.8). To assign turn numbers it was assumed that the first detected anchor point was turn number one and that no two consecutive left or right turns could occur. For each point in $\{\hat{\mathbf{g}}_m\}$, the closest matching point k_m in $\{\mathbf{g}_n\}$ was then found by the minimization of Eq. 9.9. Matchings were removed if two or more points of $\{\hat{\mathbf{g}}_m\}$ were matched to the same point in $\{\mathbf{g}_n\}$. \mathbf{o} was then defined as the median position difference of all matched pairs.

$$f_n = [\mathbf{g}_{n+1} - \mathbf{g}_n, \mathbf{g}_n - \mathbf{g}_{n-1}, [l/r], n]^T \quad (9.7)$$

$$f_m = [\mathbf{g}_{m+1} - \mathbf{g}_m, \mathbf{g}_m - \mathbf{g}_{m-1}, [l/r], m]^T \quad (9.8)$$

$$k_m = \arg \min_{n \in [1;N]} \|f_n - f_m\| \quad (9.9)$$

Subsequently, $\{\mathbf{g}_m\}$ was corrected for azimuth and position offset and expressed in frame \mathcal{G} . Denote these points as $\{\mathcal{G}\hat{\mathbf{g}}_m\}$. To find the final matching between the estimated anchor points $\{\hat{\mathbf{g}}_m\}$ and the surveyed anchor points $\{\mathbf{g}_n\}$ the same minimization as described above was used a second time. However, since offset was corrected, feature vectors finally consisted of the absolute position, the left/right turn, and the turn number (Eqs. 9.10, 9.11).

$$f_n = [\mathbf{g}_n, [l/r], n]^T \quad (9.10)$$

$$f_m = [\mathcal{G}\mathbf{g}_m, [l/r], m]^T \quad (9.11)$$

$$(9.12)$$

Extended Kalman Smoother 2: refined sacrum trajectory

As expected, the sacrum trajectory $\mathbf{p}_{\text{jc}}(t)$ which was solely obtained by integration of the sacrum acceleration and by zero-velocity drift correction was not very accurate and position drifts of up to 20 m were observed. Therefore, an accurate estimation of $\{\mathbf{g}_m\}$ could not be guaranteed and not all matching pairs k_m were identifiable. Thus, after a first passage through the EKS, the estimation of $\{\mathbf{g}_m\}$ and the anchor point matching were performed a second time. But this time it was based on the updated sacrum trajectory. Finally, the EKS was run a second time to obtain an improved estimation of the sacrum's trajectory. To account for the improved accuracy of $\{\mathbf{g}_m\}$ the position accuracy of $\{\mathbf{g}_m\}$ in the EKS was reduced from 1 m for the first iteration to 0.2 m for the second iteration.

Absolute CoM kinematics estimation

Finally, the absolute CoM trajectory $\mathbf{p}_{\text{CoM, inertial}}(t)$ was obtained by adding the relative CoM position obtained from the body model of Chapter 7 to the refined sacrum trajectory. The athlete's CoM velocity $\mathbf{v}_{\text{CoM, inertial}}(t)$ was obtained by three-point derivation of $\mathbf{p}_{\text{CoM, inertial}}(t)$. Both $\mathbf{p}_{\text{CoM, inertial}}(t)$ and $\mathbf{v}_{\text{CoM, inertial}}(t)$ were low-pass filtered with a 2nd order Butterworth filter with cut-off frequency of 5 Hz.

9.2.2 Reference system

The reference system consisted of a differential GNSS with the GNSS antenna (G5Ant-2AT1, Antcom, Canada) fixed to the athlete's helmet. The receiver (Alpha-G3T, Javad, USA) was placed in a backpack and logged GPS and GLONASS signals using the L1 and L2 frequencies. A reference base station (receiver: Alpha-G3T, Javad, USA; antenna: GrAnt, Javad, USA) was placed at the end of the ski course. Antenna positions were sampled at 50 Hz and obtained in post processing as described in Gilgien et al. (2015c, 2013). Ambiguities were fixed for the entire run for all runs. Synchronization with the inertial sensor-based system was performed with the GPS timestamp. To obtain antenna trajectory at 500 Hz the antenna position samples were fused with the head's inertial sensor data using an EKS with twelve states (3D position, 3D velocity, 3D acceleration, 3D acceleration offsets). This trajectory was then combined with the athlete's body model derived from the inertial sensors described and validated in Chapters 7 and 8 to obtain the reference CoM trajectory $\mathbf{p}_{\text{CoM, ref}}(t)$. The indoor validation from Chapter 7 showed that the CoM could be estimated relative to the athlete's lumbar joint centre with an accuracy and precision of 29 mm and 7 mm, respectively. The relative position of the athlete's head with respect to the lumbar joint centre could be estimated with an accuracy and precision of 127 mm and 17 mm, respectively. CoM velocity $\mathbf{v}_{\text{CoM, ref}}(t)$ was obtained by three-point derivation of $\mathbf{p}_{\text{CoM, ref}}(t)$. In the end, both $\mathbf{p}_{\text{CoM, ref}}(t)$ and $\mathbf{v}_{\text{CoM, ref}}(t)$ were low-pass filtered with a 2nd order Butterworth filter with cut-off frequency of 5 Hz.

9.2.3 Validation

CoM kinematics

For each run the 3D trajectory error $\mathbf{d}(t)$ was obtained by $\mathbf{d}(t) = \mathbf{p}_{\text{CoM, inertial}}(t) - \mathbf{p}_{\text{CoM, ref}}(t)$. The norm of the trajectory difference, i.e. $d_{\text{tot}}(t) = \|\mathbf{d}(t)\|$, was used to evaluate the error with respect to the reference system. To allow a better error description, $\mathbf{d}(t)$ was also expressed in the local skiing frame S ($^S\mathbf{d}(t)$) which was defined as follows: the x-axis was pointing along the reference CoM velocity vector, the z-axis was the cross-product of the x-axis and the gravity vector, and the y-axis was the cross product of the z- and x-axes (Fig. 9.4). Next, per run-accuracy and precision were calculated with

the average and standard deviation of $d_{\text{tot}}(t)$ and ${}^S\mathbf{d}(t)$, respectively. Overall accuracy was then defined as the average of all per-run accuracies and overall precision was defined as the average of all per-run precisions. The total speed error $s_{\text{tot}}(t)$ was defined as the difference of the velocity norms: $s_{\text{tot}}(t) = \|\mathbf{v}_{\text{CoM, inertial}}(t)\| - \|\mathbf{v}_{\text{CoM, ref}}(t)\|$. ${}^S\mathbf{s}(t)$ was obtained the same way as ${}^S\mathbf{d}(t)$.

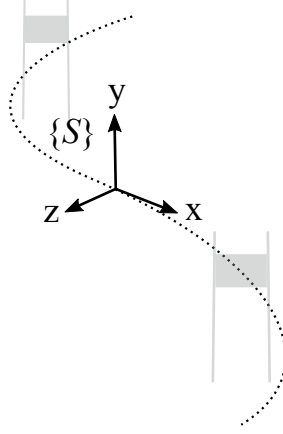


Figure 9.4 – Definition of the local skiing frame S . The x-axis is parallel to the CoM velocity vector, the z-axis is the cross-product of the x-axis and the gravity (i.e. vertical axis), and the y-axis is the cross product of the z- and x-axes.

Simulating SG and DH conditions

In SG and DH, gate distances are roughly two and three times larger compared to giant slalom, respectively (Gilgien et al., 2015a). Hence, distances between anchor points for the trajectory drift correction are larger and a decreased drift correction performance is expected. SG and DH were simulated by considering only anchor points at every second and third giant slalom gate, respectively. To take into account the loss of anchor points the EKS noise parameters were adapted. Acceleration accuracy was increased from 1.5 m/s² to 1 m/s² and the process noise covariance was reduced.

Added benefit of low-cost GNSS

Position information sampled at 10 Hz from the low-cost GNSS were obtained from three runs which were recorded on the same day. To obtain the initial sacrum position and velocity ($\mathbf{p}_{\text{sacr}}(t)$ and $\mathbf{v}_{\text{sacr}}(t)$) the EKS was adapted to also take into account the measured position information from the low-cost GNSS. Prior to the fusion with the position data, the inertial sensors' azimuth was aligned to the GNSS frame. Under the assumption that GNSS accuracy was randomly distributed between each run with zero mean, anchor points were now obtained based on the average gate positions estimated from $\mathbf{p}_{\text{sacr}}(t)$ and $\mathbf{v}_{\text{sacr}}(t)$ for all runs at gate crossings. The EKS fusing the inertial data

with the anchor points was adapted to include also all position samples obtained from the low-cost GNSS. To guarantee numerical stability the azimuth state was removed. CoM kinematics obtained with this method were validated as with the inertial sensor-based system.

Performance parameters derived from CoM kinematics

In order to validate whether the proposed system was sensitive enough to detect changes in performance, for one representative turn, five performance parameters were computed with both the reference and the inertial sensor-based system and for all runs. In analogy to a previous study by Spörri et al. (2012a) the performance parameters compared were: d_{in} distance from turn switch marking the beginning of the turn to the gate position, d_{out} distance from turn switch marking the end of the turn to the gate position (Fig. 9.5). For these two events the instantaneous CoM velocity norm (v_{in} , v_{out}) were extracted. For the same turn, the total 3D CoM trajectory length l_{tot} was computed. In addition the CoM distance to the gate at gate crossing (d_{cross}) was extracted to evaluate the relative anchor point estimation. The beginning of a turn (i.e. turn switch) was detected based on the criterion of equal left/right ankle distance to the athlete's CoM (Fasel et al., 2016f). The parameter results were then compared based on Bland-Altman plots and limits of agreements (LoA) were computed (Bland and Altman, 1999).

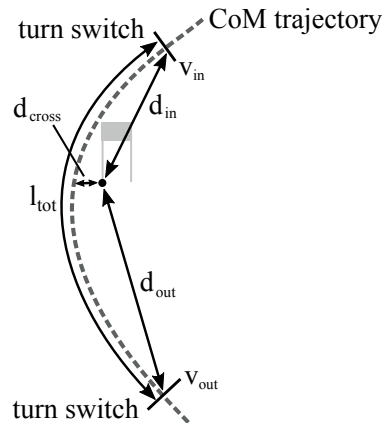


Figure 9.5 – Illustration of a turn's distance and speed performance parameters. A turn starts and stops at a turn switch and speed and position at these instants of time as well as at gate crossing are then expressed in relation to the gate position.

9.3 Results

9.3.1 CoM kinematics

The CoM kinematics' overall accuracy and precision were 0.24 m and 0.10 m for position, and 0.00 m/s and 0.20 m/s for velocity (Table 9.1). Errors were similar along each axis in the local skiing frame S . On average, less than one gate per run could not be detected by the magnetometers because the athlete passed too far from a gate: it was observed that the magnetic field created by the magnets could be always detected up to a distance of approximately 0.8 m. Increasing the distance between available anchor points for trajectory drift correction decreased the accuracy and precision but with similar results for simulated SG (every second anchor point was removed) and DH (two out of three anchor points were removed) (Table 9.1, Fig. 9.6). The use of a low-cost GNSS to first compute the anchor points and second CoM kinematics did affect the accuracy and precision for position, but not for velocity (Tables 9.2 and 9.3).

		All gates Accuracy	Precision	Simulated SG Accuracy Precision		Simulated DH Accuracy Precision	
Position, m	Total error	0.238 (0.076)	0.099 (0.060)	0.397 (0.128)	0.194 (0.101)	0.356 (0.088)	0.218 (0.160)
	X-Axis	-0.018 (0.149)	0.110 (0.057)	-0.107 (0.260)	0.232 (0.108)	-0.023 (0.144)	0.275 (0.174)
	Y-Axis	0.047 (0.051)	0.122 (0.028)	0.001 (0.125)	0.168 (0.053)	0.065 (0.072)	0.186 (0.055)
	Z-Axis	-0.027 (0.088)	0.102 (0.021)	-0.027 (0.121)	0.141 (0.022)	-0.035 (0.102)	0.150 (0.034)
Speed, m/s	Total error	-0.004 (0.021)	0.204 (0.045)	0.031 (0.028)	0.378 (0.176)	0.029 (0.038)	0.371 (0.129)
	X-Axis	-0.007 (0.021)	0.204 (0.045)	0.026 (0.027)	0.378 (0.176)	0.024 (0.037)	0.370 (0.130)
	Y-Axis	0.009 (0.021)	0.260 (0.054)	-0.029 (0.044)	0.310 (0.073)	-0.035 (0.042)	0.314 (0.068)
	Z-Axis	0.003 (0.026)	0.240 (0.049)	0.016 (0.045)	0.272 (0.056)	0.021 (0.042)	0.279 (0.065)

Table 9.1 – Average (standard deviation) accuracy and precision for the total error and the error along each local skiing axis for velocity and position. All values were obtained with the inertial sensor-based system only with surveyed anchor points. For the simulated super-G (SG) only every second anchor point was used for the fusion while for the simulated downhill (DH) every third anchor point was used for the fusion.

	Inertial sensors only		Including low-cost GNSS	
	Accuracy	Precision	Accuracy	Precision
Total error, m	0.242 (0.101)	0.087 (0.027)	45.488 (0.008)	0.144 (0.013)

Table 9.2 – Comparison of the position accuracy and precision between the inertial sensor-based system and the low-cost GNSS-based processing. Provided are mean accuracy and precision. Their standard deviation is given in parentheses.

	Inertial sensors only		Including low-cost GNSS	
	Accuracy	Precision	Accuracy	Precision
Total error, m/s	-0.010 (0.002)	0.182 (0.018)	-0.016 (0.006)	0.173 (0.018)
X-Axis	-0.013 (0.002)	0.181 (0.018)	-0.018 (0.006)	0.173 (0.018)
Y-Axis	0.009 (0.019)	0.268 (0.012)	0.015 (0.010)	0.234 (0.009)
Z-Axis	-0.008 (0.017)	0.225 (0.015)	-0.012 (0.012)	0.200 (0.019)

Table 9.3 – Comparison of speed and 3D velocity direction’s accuracy and precision between the original system and the low-cost GNSS-based processing. Provided are mean accuracy and precision. Their standard deviation is given in parentheses.

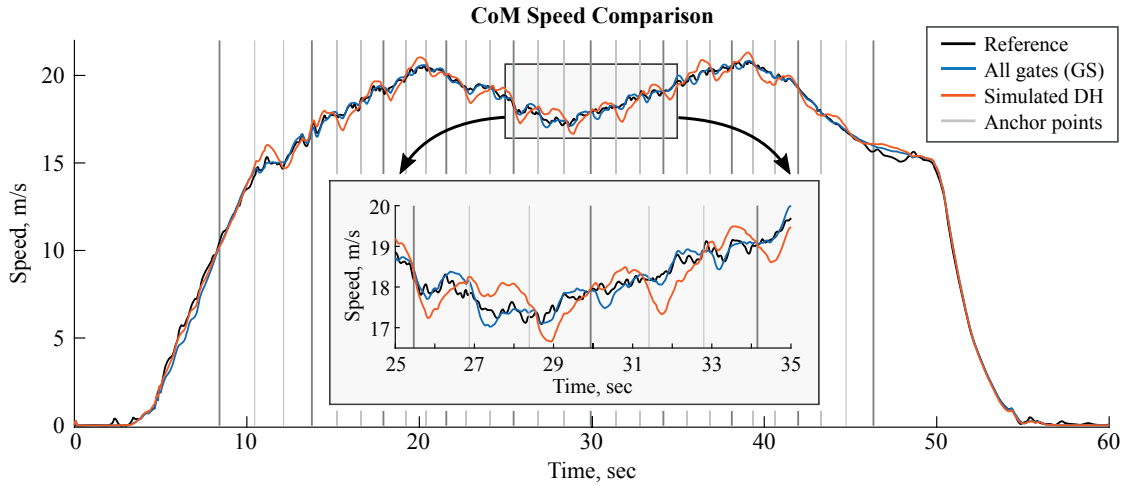


Figure 9.6 – CoM speed comparison for a typical run. Reference CoM speed is shown in black, inertial sensor-based CoM speed with all anchor points (GS) is shown in blue and the simulated DH is shown in orange. Anchor points are marked with the vertical grey lines. For GS all anchor points were considered whereas for simulated DH only the anchor points marked in bold were considered. Especially for the simulated DH, speed errors were largest around the turn switches.

9.3.2 Performance parameter-related findings

Limits of agreement (LoA) were between -0.3 m and 0.35 m for position, between -0.3 m/s and 0.4 m/s for speed, and were -0.05 m and 0.17 m for path length (Table 9.4). With the exception of gate distance at gate crossing, LoAs were up to five times smaller than the performance parameter’s standard deviation (Table 9.4). Gate distance error seemed to depend on the distance: small gate distances were overestimated and large gate distances were underestimated (Fig. 9.7).

	Parameter value		Error		Upper LoA
	Average	Std	Lower LoA	Mean	
v_{in} , m/s	19.94	1.032	-0.224	0.093	0.41
v_{out} , m/s	20.291	0.821	-0.293	-0.044	0.206
d_{in} , m	12.609	1.364	-0.289	0.028	0.345
d_{out} , m	13.249	1.640	-0.250	0.025	0.301
d_{cross} , m	0.684	0.079	-0.160	0.031	0.223
l_{tot} , m	26.212	1.752	-0.053	0.057	0.166

Table 9.4 – Average and standard deviation (std) of the parameter values and the error mean with LoA for the extracted performance parameters.

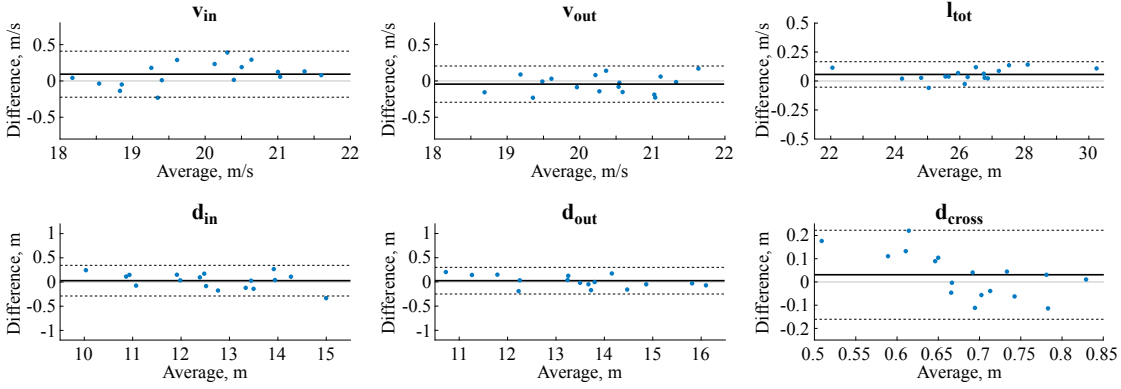


Figure 9.7 – Bland-Altman plots for the performance parameter validation. The solid black lines mark the mean error and the dashed black lines the limits of agreements.

9.4 Discussion

In this study, gates in alpine ski racing were equipped with magnets, and their positions were fused with magnetic and inertial sensor measurements to obtain drift-free absolute CoM kinematics (trajectory and velocity) of the skier. Gate positions were found through surveyed anchor points or low-cost GNSS measurements. Considering that the sacrum would not pass the anchor points with zero distance, difference between the athlete's sacrum and anchor points was estimated based on the athlete's posture and the peak magnitude of the magnetic field. Absolute CoM kinematics were obtained by adding the estimated CoM relative to the lumbar joint centre to the estimated absolute lumbar joint centre trajectory. The measurement performances of the system to estimate CoM trajectory and velocity as well as ski performance parameters were estimated against a differential GNSS as reference with 17 runs on giant slalom courses and simulated super-G and downhill courses.

9.4.1 Accuracy and precision of CoM kinematics in GS

We found a good accuracy and precision for both CoM position (0.238 m and 0.099 m) and velocity (-0.004 m/s and 0.204 m/s) (Table 9.1). In alpine skiing, no other study proposed to compute CoM kinematics based on inertial sensors and surveyed anchor points. Brodie et al. (2008) used a low-cost global positioning system (GPS) sampling at 1 Hz and fused position and velocity data with acceleration obtained from inertial sensors. In addition, the start and finish points were used as anchor points for removing position offsets of the GPS. Nevertheless, over a 300 m run errors of up to ± 1.5 m were reported. For differential GNSS Gilgien et al. (2014b) reported antenna position error standard deviations of 0.15 m. Using the same system but for CoM trajectories, Gilgien et al. (2015c) reported error standard deviations of 0.12 m for position and 0.19 m/s for speed. Thus, even though the proposed system did not use differential GNSS the observed errors were comparable to the above systems.

Even though the fusion of anchor points with inertial sensors allowed correcting velocity and position drift, such performance would probably not have been possible without a considerable pre-processing effort. The sensors' offsets and sensitivities were carefully calibrated prior to the measurements. Moreover, sensor orientation drift was reduced prior to the EKS with the joint drift reduction procedure explained in Chapters 5 and 6. This allowed to estimate orientation with dedicated, non-linear and precise methods, instead of directly including orientation estimation and drift reduction by means of a general model in the EKS. Thus, the EKS could be kept as simple as possible (i.e. with a minimum number of states and only few filter parameters needed to be tuned). The employed EKS was considered as a means to an end instead of forming the core of the study. The system's performance could further be improved by a better estimation of the relative position of the anchor points with respect to the sacrum. Estimating the total distance between sacrum and anchor point (i.e. magnet) based on the measured magnetic peak intensity could involve some errors: it was highly probable that magnetic peak intensity was underestimated because of the magnetometer's low sampling rate of 125 Hz. At 70 km/h the athlete covers 15.5 cm per sample. Therefore, it is likely that the magnetic intensity was not sampled exactly at its peak. Peak intensity could be measured more reliably by increasing the sampling rate and designing an advanced curve fitting and peak identification algorithm. Moreover, the magnetic field intensity created by the magnet decreases with the third power of the distance. Therefore, small measurement errors for low intensities can lead to large errors for the distance estimation. Stronger magnets would increase the generated magnetic field and lead to a more reliable distance estimation. At the same time, fewer gates would be missed since the magnetic disturbance could also be measured for gate distances larger than 0.8 m.

9.4.2 Expected accuracy and precision in SG and DH

When removing anchor points to simulate a SG or DH race, accuracy and precision decreased. Interestingly, errors increased significantly between the normal condition and simulated SG, but not between simulated SG and simulated DH. Fig. 9.6 shows the speed precision loss for a representative run. While no deviation between reference speed and inertial sensor-based speed was visible for the normal condition, deviations were found for the simulated SG, but did not further increase for the simulated DH. This indicates that the acceleration measurement error leading to velocity drift might be composed of two independent elements: a movement-independent bias and a movement-dependent bias. The movement-independent bias was assumed to change slowly over time. Thus, the EKS was able to estimate this bias for all conditions, even if a reference position measurement was available on average only every 4.5 seconds (simulated DH). The EKS was able to partially estimate the movement-dependent bias when anchor points were available for each gate (i.e. each turn). Most likely, the movement-dependent bias had its origins in the incorrect gravity cancelling due to errors in the orientation estimation. While a small orientation error has only a small effect on the vertical axis, its effect is larger on the horizontal plane due to the law of the cosine in the projection of the gravity on the vertical axis and horizontal plane: $1 - \cos(\epsilon) \ll \sin(\epsilon)$ for small inclination errors ϵ . Average per-turn orientation is different for left and right turns because of the pendulum-like movement of the trunk. Thus, gravity projection error changes from turn to turn and causes a turn-dependent error. The reference position at each turn allowed to estimate the average bias per turn. Every second or third gate was taken as a reference for the simulated conditions (SG and DH) and the average bias per turn could not be estimated correctly, leading to a decreased precision especially along the X and Y axes. Thus, precision for a non-simulated measurement of SG or DH might be slightly higher than found with the simulation.

9.4.3 Potential benefit of adding a low-cost GNSS

Including a low-cost GNSS did slightly worsen the velocity accuracy, but improved the precision. For the position, accuracy was poor (45.5 m), but precision could be acceptable (0.14 m). The accuracy was poor, because the low-cost GNSS had a large offset with respect to the differential GNSS frame, especially along the vertical axis (-45.5 m, versus 0.2 m and 1.5 m along the horizontal axes). However, the presented method allowed eliminating the slowly changing GNSS drift due to changing satellite constellations and atmospheric conditions. Thus, even though a low-cost GNSS was used (expected position error standard deviation of around 3.7m for single frequency receiver (Groves, 2008)) and measurements were spread over more than one hour, it was possible to remove GNSS bias and obtain a precision close to differential GNSS. The decrease in position accuracy could also be attributed to the low number of runs (N=3) that was used to estimate the anchor points. Accordingly, we hypothesize that a larger number of runs would further

cancel GNSS drift and a higher precision might be obtained.

The most important advantage of the inclusion of a low-cost GNSS was that anchor points did no longer need to be surveyed with a differential GNSS. Thus, no terrain surveying and no extra hardware except the inertial sensors and low-cost GNSS would be needed. In case of GNSS outages of less than 4.5 seconds due to GNSS signal shading, accurate and precise trajectory kinematics could still be found since the EKS automatically corrected any velocity and position drifts in order to match the positions at each gate crossing.

9.4.4 Limits of Agreement for CoM-derived performance parameters

Spörri et al. (2012a) observed turn entrance and exit speed and distance differences of at least 0.3 m/s and 0.3 m, respectively, for comparisons between the fastest and slowest runs of the same athlete. The LoA found in this study are of the same magnitude (Table 9.4). However, for total turn COM trajectory length LoA were below the reported difference of 0.3 m between the fastest and slowest trial reported in Spörri et al. (2012a). Therefore, the system's resolution might be at the limit for detecting instantaneous performance-related differences such as speed and position at a certain point, but may be well suited for "averaged" performance-related differences such as trajectory lengths.

9.5 Conclusion

The proposed inertial sensor-based system with a fusion with surveyed anchor points did allow to obtain CoM kinematics with a higher accuracy and precision than with a system solely based on a low-cost GNSS (Brodie et al., 2008; Gilgien et al., 2014b). Moreover, the proposed system's performance came surprisingly close to that of the reference system (i.e. differential GNSS). Coordinates of the anchor points had to be measured using land surveying techniques, such as for example differential GNSS. However, the case study showed that such a surveying could be replaced with only little loss in position accuracy by adding a low-cost GNSS to the inertial sensor-based system. Moreover, under the condition that anchor points would be obtained, the independence from GNSS for the inertial system would also allow to use such a system in indoor situations, for example in skiing halls.

Acknowledgements

The study was funded by the Swiss Federal Office of Sport (FOSPO), grant 15-01; VM10052 VM10052 and was partly supported by the "Fondation de soutien à la recherche dans le domaine de l'orthopédie et traumatologie". The authors would like to thank Swiss-Ski and the participating athletes.

10 GNSS-free anchor point estimation

Abstract

For performance analysis in alpine ski racing, an accurate and precise estimation of the centre of mass (CoM) kinematics is indispensable. Currently available systems satisfying this need are video-based stereo-photogrammetry or differential global navigation satellite systems (GNSS). However, both approaches have some practical limitations in regular training settings. The ideal system should be easy to use with minimal hardware carried by the athlete. Inertial sensors would satisfy both requirements; however, they suffer from significant drifts in velocity and position estimation due to the integration of acceleration and angular velocity data. In order to reduce such drifts, the aim of the present study was to propose and validate an inertial and magnetometer sensor-based algorithm that provides an estimate of gate positions based on multiple runs recorded on the same course and, subsequently, re-computes CoM kinematics of each run by matching the individual gate positions to the mean gate positions. Using this algorithm, relative CoM position and speed between-run comparisons were found to be highly accurate and precise with mean absolute deviations <0.15 m and <0.28 m/s. Moreover, the system was easy to use and therefore could be used in regular training settings indoor and outdoor. In particular, the system does not require terrain surveying and GNSS on the athlete, which is a major advantage, particularly when no technical expert is assisting the team during training.

Keywords: body sensor networks, drift correction, inertial sensors, position, centre of mass, kinematics, anchor points

Chapter accepted as B. Fasel, M. Gilgien, J. Spörri and K. Aminian. "Estimation of the centre of mass kinematics in alpine ski racing using inertial and magnetic sensors", 35th International Conference on Biomechanics in Sports, Cologne, ISBS 2017.

10.1 Introduction

Obtaining precise centre of mass (CoM) kinematics is of key interest in alpine skiing research. CoM kinematics is relevant for performance analysis (Hébert-Losier et al., 2014; Spörri et al., 2012a; Supej et al., 2011) or injury risk evaluation (Gilgien et al., 2014a; Spörri et al., 2012b). In previous studies, CoM kinematics was most commonly obtained by video-based stereo-photogrammetry or with differential global navigation satellite systems (GNSS). Both systems require a complex and time-consuming setup and technical experts for data processing. While the capture volumes of video-based systems are usually only a few turns long, differential GNSS can record longer sections up to the entire race course. However, satellite signal quality can degrade due to shading effects typically from terrain and forest along the course and therefore position and velocity accuracy can be degraded severely. When being applied in training settings, these systems are limited in usability, and coaches would prefer a transportable, light-weight system without complex setup and post-processing. Nevertheless, for the purpose of performance analysis, accuracy and precision must be high. For example, CoM trajectory differences between skiers in the order of magnitude of 0.2m can be considered relevant to explain performance (Spörri et al., 2012a). However, as the skiers have to follow a pre-defined course marked by gates, CoM positions are not required to be known in an absolute frame. For most performance applications it would be sufficient to express CoM kinematics relative to gate positions. In a recent study, we have shown that magnets could be used for detecting gate crossings (Fasel et al., 2016g) and that reference gate positions can be used in a fusion scheme to remove inertial sensor drift from integration and GNSS drift from changing satellite constellations and atmospheric conditions (Chapter 9). However, in this approach, gate positions had still to be obtained with land surveying techniques. While reference positions could be obtained quickly (<30 minutes) in the field using land surveying technologies, such surveying could be a constraint in regular training sessions. Under the assumption that inertial sensor drift is independent between different runs and with zero mean, it should be possible to cancel it out when averaging multiple runs. Thus, in a first step gate positions could be estimated by averaging the drift-affected gate positions of individual runs. Having enough runs collected, such estimates of gate positions should converge to the true gate position. In a second step, CoM kinematics could then be computed relative to the gate positions estimated in step 1. The aim of this project was therefore to propose and validate an easy-to-use system which allows to accurately and precisely measure CoM kinematics in alpine ski racing without the need to survey terrain or to use a differential GNSS.

10.2 Methods

The proposed system comprised seven inertial sensors (Physilog IV, Gait Up, Switzerland) attached to the left and right shanks, left and right thighs, sacrum, sternum, and head.

Acceleration and angular velocity was sampled at 500 Hz and the sensors were wirelessly synchronized. In addition, the sacrum sensor contained a magnetometer sampling at 125 Hz. Strong bar magnets (18 cm long, 2 cm diameter) were placed at each gate of a skiing course. Segment orientation was obtained with strap-down integration followed by joint drift correction as described in Chapters 5 and 6. Based on the segment orientations and body segment inertia parameters the athlete's posture and relative CoM was computed as described in Chapter 7. Gate passages were detected based on peak detection of the magnetic field intensity recorded by the magnetometer (Fasel et al., 2016g).

Finally, CoM trajectory was obtained in five steps. First, the drift-affected position of the sacrum trajectory was computed from the inertial sensor fixed on the sacrum. An Extended Kalman Smoother (EKS) with twelve states (position, velocity, acceleration, acceleration offset) was designed. Gravity corrected acceleration in the global frame was integrated to find velocity and position, and velocity drift was corrected based on a zero-velocity constraint at race start and finish. Second, relative gate position with respect to the sacrum was estimated for each gate passage. In an additional lab assessment, magnetic field intensity was related to the sensor – magnet distance and, subsequently, was used to estimate the distance between the sacrum and the gate in-field. To find the components of the distance vector, a trigonometric model using a triangle with vertices sacrum, the sacrum projected onto the snow surface, and the gate position was constructed. The triangle surface was constrained to be normal to the sacrum velocity vector at gate crossing. Third, absolute gate position was computed by adding the sacrum's position at gate crossing to the relative gate position. Fourth, an estimate of gate positions was defined as the mean gate positions recorded for all runs on the same course. Prior to averaging, each run's trajectory was aligned and scaled such that the positions of the first and last gates would match between all runs. Fifth, sacrum trajectory was improved with a second EKS where the estimated gate positions were used in addition to the zero-velocity constraint. Final CoM trajectory was then the sum of the improved sacrum trajectory and relative CoM obtained from the body model.

To validate the system, nine European-cup level athletes were enrolled to the study (written informed consent was obtained from each athlete and the study was approved by EPFL's Ethical committee (HREC 006-2016)). Each athlete skied two runs on a giant slalom course consisting of 28 gates spaced with varying gate distances and a total of ten runs were measured simultaneously with the reference system. Measurements took place during two days on a glacier with good GNSS conditions. All gate locations were surveyed with a differential GNSS. The reference system to assess skier kinematics consisted of a differential GNSS which was integrated with the inertial sensor-based body model as described in Chapter 8. Accuracy (precision) for CoM position of this system was 0.04 m/s (0.14 m/s), and 0.08 m (0.06 m).

For validation purposes, the IMU global frame was matched to the GNSS frame. Azimuth difference was corrected and the IMU frame was shifted in order to match the position of the first gate in both global frames. Position errors were computed for each gate. Accuracy (mean error) and precision (error standard deviation) were computed for CoM

speed and position differences between the second and second last gates of each run. For selected turn performance parameters (i.e. the distance to gate, as well as speed at turn start, gate crossing, and turn end) were computed and compared relative to each day's fastest turn (defined as shortest time between the turn start and end). Mean absolute difference (MAD) between the two systems was computed for the relative performance parameters. In order to test system differences regarding the aforementioned performance parameters, a paired sample t-test was used. Level of statistical significance was set at $p < 0.05$.

10.3 Results

CoM kinematics were successfully obtained for nine runs from day one and eight from day two. Gate position errors increased during the run reaching up to 9.3 m and 18.1 m at the last gate for the first and second day, respectively. Mean absolute CoM speed accuracy (precision) was 0.25 m/s (0.46 m/s). Mean CoM position accuracy (precision) was 7.42 m (4.06 m). Mean relative differences were < 0.15 m for the distance parameters and < 0.28 m/s for the speed parameters. No statistical differences were found between the two systems.

10.4 Discussion

An inertial and magnetometer sensor-based system was proposed and validated to obtain alpine ski racing CoM kinematics which can be expressed in a global frame but without the requirement to capture terrain geomorphology using advanced surveying techniques nor the necessity to use GNSS on the athlete. Magnets placed at gates allowed to detect gate crossings. An estimate of gate positions was found by averaging the gate positions recorded from multiple runs. With the help of an Extended Kalman Smoother (EKS) each run's trajectory was then matched to the estimated gate positions.

The proposed approach allowed to partially cancel out velocity and position drift from integrating the acceleration signal. However, the number of recorded runs per day was not sufficient to cancel out the drift completely. The remaining drift led to inaccuracy in the estimated gate positions where relative position error changed in extreme cases by up to 1.5 m between two subsequent gates. The system's main advantage was that once the estimated gate positions were known all runs could be expressed in the exact same coordinate system. Thus, even though drift was not completely removed, it became identical for all runs of the same day. The remaining drift was interpreted as slowly changing spatial distortions, as illustrated in Figure 10.1. Thus, absolute CoM kinematics were distorted with respect to the GNSS velocity, resulting in the observed absolute position and speed errors; however, for a direct relative comparison between several runs measured on the same course this seems not to be a problematic issue. For example, the mean absolute difference of the relative performance parameters (position and speed

differences at gate crossing and turn switches) was smaller than the reported performance differences between the fastest and slowest run of a world-class athlete (Spörri et al., 2012a). Thus, the proposed system could be used for between-run performance analysis.

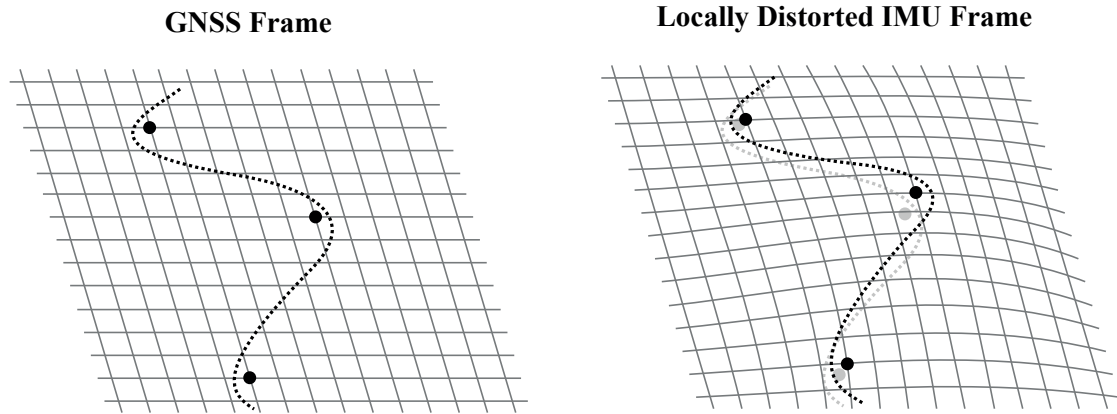


Figure 10.1 – Left: Differential GNSS frame. Right: local distortion created by the non-complete drift cancelling after computing the average gate positions from multiple runs. The very light grey shading illustrates the undistorted trajectory in the GNSS frame.

In order to be able to better cancel out the drift, more runs than analysed in the current study should be recorded per training session. In a regular training, each athlete skis the same course 5-10 times. Therefore, by measuring multiple athletes in parallel, twenty or more runs could be available for computing the estimated gate positions. On a final note, it is worth mentioning that the averaging scheme used was quite simple and assumed linear drift changes over the entire run. However, as drift is movement-dependent and, therefore, is non-linear over the run, more sophisticated averaging procedures might help to better cancel out drift and to obtain more accurate and precise CoM kinematics.

10.5 Conclusion

This study proposed a novel system to compute CoM kinematics for alpine ski racing without the need of terrain surveying and GNSS on the athlete. Mapping individual runs onto a common frame allowed to obtain accurate and precise relative performance parameters for between-run comparison. Thus, the system could be used for performance and relative line analysis in regular training settings. However, due to incomplete drift cancellation caused by slowly changing local coordinate system distortions, absolute CoM kinematics might not be accurate and precise enough for absolute line and speed comparisons. Moreover, since the system did not use GNSS, it would be ideally suited for applications in indoor skiing halls.

11 Applications to performance analysis and injury prevention

Abstract

In the previous chapters, various methods for reducing orientation, velocity, and position drifts in alpine ski racing were presented. The methods took advantage of the movement specificities of skiing and were specifically tailored to movements with high dynamics. Inertial sensors fixed to the lower limbs, trunk, head, and optionally on the upper limbs, allowed to reconstruct the athlete's posture, his joint angles, and his centre of mass (CoM). Further, CoM kinematics (i.e. velocity and trajectory) could be determined with an accuracy and precision close to what could be achieved by differential global navigation satellite system (GNSS)-based solutions. This new system provides a wealth of information on the skiing movement that can be exploited for both performance analysis and injury prevention. The present chapter provides some examples of how the system could be used and which specific parameters it could provide.

Keywords: body sensor networks, inertial sensors, joint angles, sensor fusion, performance analysis, injury prevention, applications

11.1 Performance Analysis

In the alpine skiing literature a large number of different performance factors has been presented (Federolf, 2012; Ferguson, 2010; Hébert-Losier et al., 2014; Spörri et al., 2012a). Hébert-Losier et al. (2014) pointed out in their literature review that the highest performance gains were obtained by reducing the ski-snow friction and aerodynamic drag. Strategies for reducing these two frictional forces could be earlier initiation of the turns, longer but smoother path length (i.e. carving instead of skidding), minimizing the exposed frontal area and optimal positioning of the arms. Race winners were often characterized by a consistently good performance over all sections of the course, independent of terrain and snow conditions.

However, not all performance parameters are well accepted in the literature. The large spectrum of conditions and different skiing disciplines make general conclusions difficult. For example, Supej et al. (2013) reported that for giant slalom aerodynamic drag contributes little to performance gain or loss. Moreover, due to limitations of the measurement systems and complexity of conducting repeatable experiments in-field, the studies were based on small sample sizes (generally less than ten athletes and/or runs) and specific conditions. More general analyses on different conditions and large sample numbers are still lacking.

Especially from a coaching point of view it is important that performance parameters are understandable and can also be used as effective means of feedback to the athletes. For example, the feedback "*for turn X you have to reduce ratio between the mechanical energy difference ΔE_{mech} (Eq. 11.1) and turn entrance speed in order to ski faster*" (Federolf, 2012) is very difficult to understand, even for experts. In addition, it does not provide information about how the athlete should change his way of skiing this particular turn to change this ratio.

$$\Delta E_{\text{mech}} = E_{\text{mech, out}} - E_{\text{mech, in}} \quad (11.1)$$

where $E_{\text{mech, in}}$ and $E_{\text{mech, out}}$ is the mechanical energy at the turn start and end.

Easier to understand performance parameters might therefore work better for efficient feedback to coaches and athletes. For regular trainings coaches use video analysis for feedback purposes. They may compare two runs head-to-head and stop the video at each gate contact. Visually, they determine which run was faster and try to relate the observed time difference to differences in trajectory, speed, and posture. While this approach is highly relevant and provides precious visual feedback it is time-consuming to perform. All runs need to be filmed and the videos need to be synchronized. Moreover, performance changes are difficult to continuously monitor over time, since the performance analysis is most of the time only performed qualitatively but not quantitatively.

Taking into consideration all these aspects, five performance parameters (Table 11.1, Fig. 11.1) were selected to illustrate the possibilities of the proposed system for a gate-to-gate performance analysis: gate-to-gate timing (dt_{seg}), speed variation (dv_{seg}), average speed (v), path length (L), and pre/post ratio ($R_{\text{pre/post}}$). The selected parameters might not be the most sensitive to explain performance differences but have been shown to be

related to performance (Spörri et al., 2012a) and are often used in qualitative performance analysis based on videos.

The course was segmented at each gate, based on the instant of gate crossing. Segment n comprises the trajectory from gate n to gate $n + 1$ and the performance parameters were computed for each segment independently (Fig. 11.1). Each segment contains additionally a turn switch. Gate n was crossed at time t_n and gate $n + 1$ was crossed at time t_{n+1} . Turn switch happened at time t_{TS} and was defined as the instant of time of equal distance between left and right ankle and athlete CoM (Fasel et al., 2016f).

Name	Definition	How to compute
Gate-to-gate timing	Time spent in the segment	$dt_{\text{seg}} = t_{n+1} - t_n$
Speed variation	Difference between the speeds at gate n and $n + 1$. Speed at gate n was denominated as entrance speed and speed at gate $n + 1$ as exit speed.	$dv_{\text{seg}} = v(t_{n+1}) - v(t_n)$
Average speed	Average speed on the segment	$\bar{v} = \text{mean}(v(t))$ $t \in [t_n; t_{n+1}]$
Path length	Total segment length of the CoM trajectory	$L = \int_{t_n}^{t_{n+1}} v(t) dt$
Pre/post ratio	Time ratio between the time spent from gate n to turn switch (t_{TS}) and from t_{TS} to gate $n + 1$	$R_{\text{pre/post}} = \frac{t_{TS} - t_n}{t_{n+1} - t_{TS}}$

Table 11.1 – Definition of the five selected performance parameters.

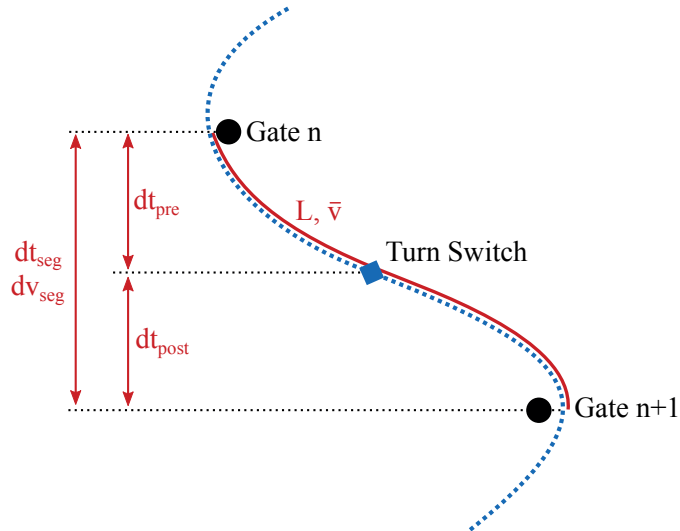


Figure 11.1 – Illustration of the performance parameters for segment n between gate n and gate $n + 1$. The parameter definitions can be found in Table 11.1.

The parameters were computed for a 29-gate giant slalom with irregular gate spacing and changing slope inclination ($2^\circ - 20^\circ$). The same setup and analysis as in Chapter 9 was used: seven inertial sensors were fixed to shanks, thighs, sacrum, sternum and head. The sacrum sensor contained an additional magnetometer. Gate positions were surveyed with a differential GNSS and each gate was equipped with a magnet. After warming up five athletes (European cup level) skied each two runs. Only nine runs were considered for performance analysis and one run had to be discarded due to a sensor failure. A steep 6-gate (i.e. five segments) section ($20^\circ - 7^\circ$) ending in a flat part (5°) at the start of the run (gates 4-9) was selected for performance analysis (Fig. 11.2). Section performance was then defined according to two criteria 1) section time and 2) average speed during the last section analyzed (i.e. average speed between gates 8 and 9). For each criterion, the two runs with the best and worst performance were compared. In addition, a comparison between two randomly selected other runs from two different athletes was performed, emphasizing the importance of detailed performance analysis instead of analyzing performance for entire sections only.

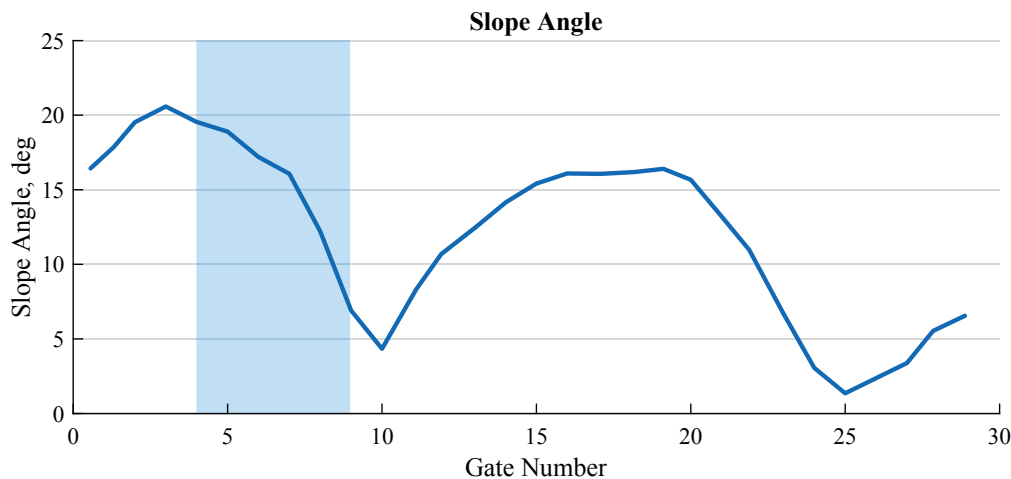


Figure 11.2 – Slope angle at each gate for the giant slalom run considered for performance analysis. The section which is shaded in light blue was selected for the detailed analysis and run comparison.

11.1.1 Performance criterion section time

The performance parameters for the runs with the shortest and highest section time are depicted in Fig. 11.3. Section time was 6.486 seconds for the fastest run and 6.776 seconds for the slowest run. The slowest run consistently lost time in each segment. Path length and speed variations were very similar, with a trend of a relative speed loss for the slowest run and a slightly longer trajectory in segments 6 and 7. Average speed was particularly slower for the slowest run.

These four parameters seem not to explain so much the performance difference: it could simply be concluded that the slowest run was simply slower because of reduced speed.

But what might have led to this reduced speed? The answer might be provided by the pre/post ratio: the slowest run showed a trend for a higher pre/post ratio. This means that the athlete was always somewhat late in his turns and therefore struggled to ski an efficient and fast line. The detailed line differences between the two runs are shown in Fig. 11.4 (top). Especially at gates 4 and 5 the faster run's line was turning earlier and could therefore ski the turns more efficient (i.e. faster). At gate 7 the slower run's line was farther from the gate, resulting in a slightly longer skiing line which further contributed in a loss of time. Fig. 11.4 (bottom) shows the continuous evolution of the skiing speed. This figure might be especially suited for an interactive performance analysis where within-turn speed variations can be well displayed in a zoomed-in view.

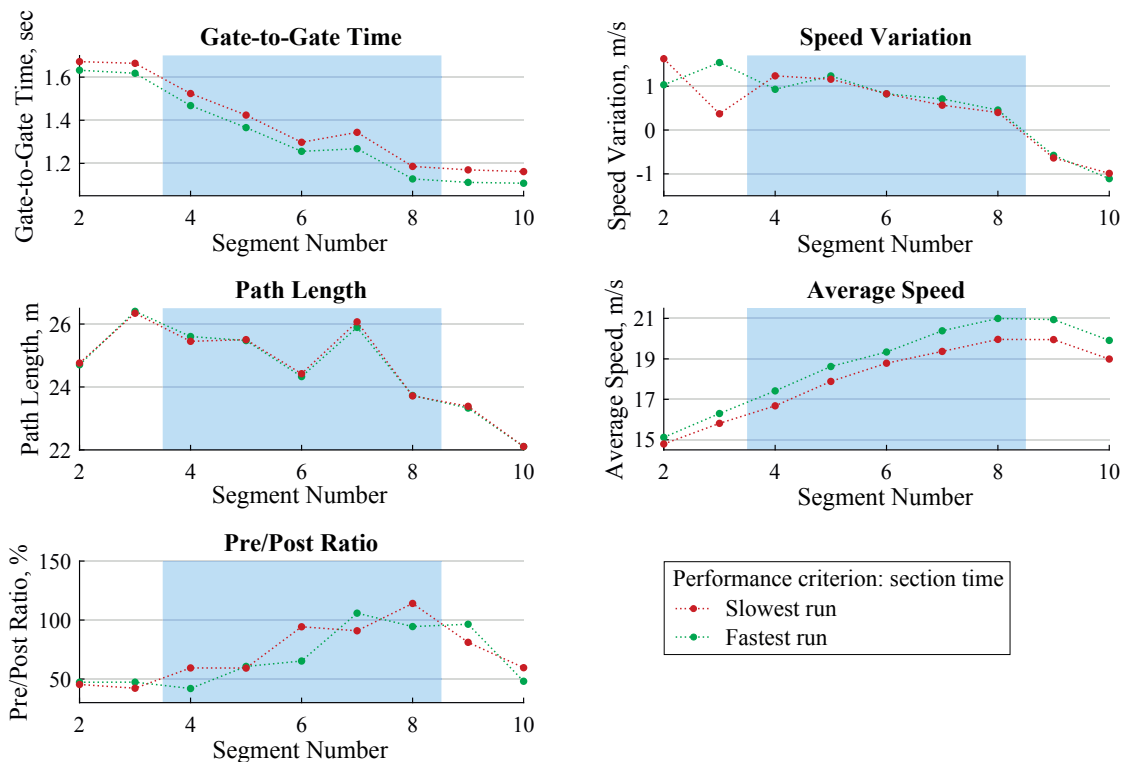


Figure 11.3 – Performance parameters for the two runs with the slowest (red, 6.776 sec) and fastest section times (green, 6.486 sec). The section considered is shaded in blue. Two more segments at the beginning and end are shown for illustration purposes only.

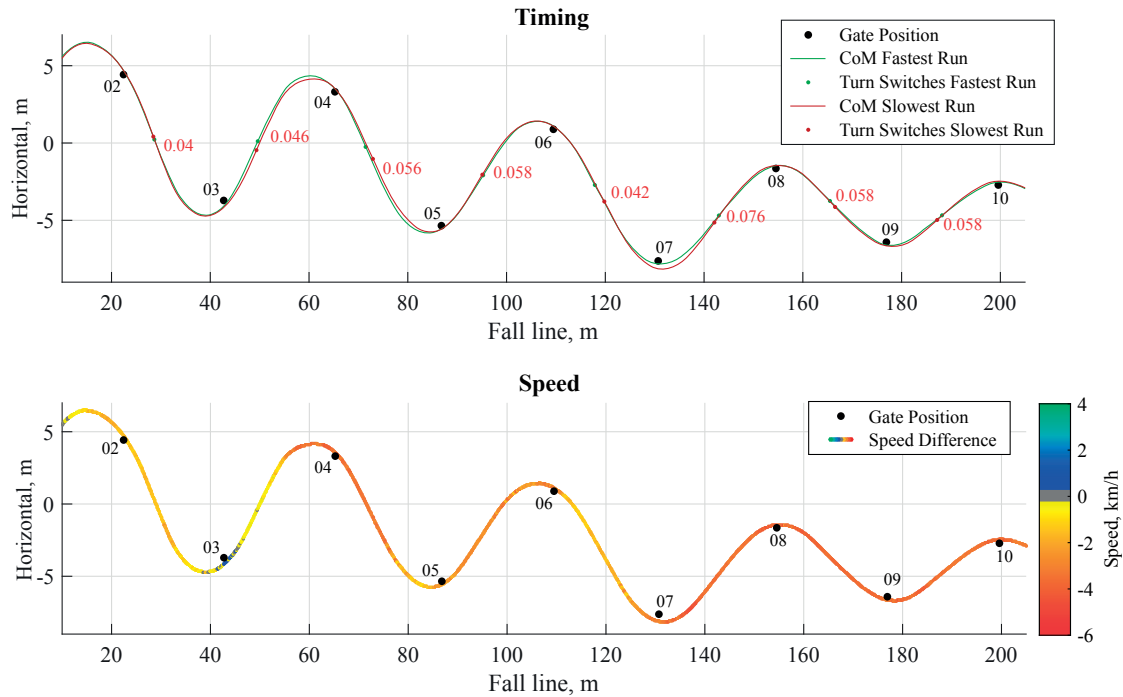


Figure 11.4 – Centre of mass (CoM) trajectory, gate positions, and speed difference for the same two runs and section displayed in Fig. 11.3. The timing graph (top) shows the gate-to-gate time difference between the two runs. The red line is the CoM trajectory of the slowest run and the green line the CoM trajectory of the fastest run. Red, positive, numbers mark a time loss of the slowest run compared to the fastest run. Green, negative, numbers mark a time gain. Units are seconds. The speed difference graph (bottom) shows the color-coded speed difference between the two runs. The trajectory shown is the CoM trajectory of the slowest run. Yellow to red colors mark a negative speed difference (i.e. slower speed for the slowest run). Blue to turquoise colors mark a positive speed difference (i.e. faster speed for the slowest run). The grey color marks no speed difference.

11.1.2 Performance criterion exit speed

Exit speeds were 21.0 m/s for the fastest run and 19.5 m/s for the slowest run. The fastest run was the same as before, i.e. the fastest run had both the shortest section time and highest exit speed. Interestingly, the run with the slowest exit speed was skied by the same athlete who had the longest section time in the previous example. The run selected in this example was his first run and the run selected in the previous example was his second run. In this example, performance differences were much more pronounced and a very interesting phenomenon could be observed: during the first three segments (labelled as 4, 5, 6 in Fig. 11.5) both runs were equally fast. However, during segment 7 something happened and suddenly the average speed of the slowest run stopped to increase. While for the first segments path length was lower for the slowest run it was

higher during segment 7. Again, the pre/post ratio might provide an explanation to what happened: the slowest run had a consistently higher pre/post ratio and showed a peak for segment 7. Probably the skier was always very late, attacking the gates too directly. While this strategy worked for the first few turns it did not anymore for gate 7: the athlete was too late and had to correct his skiing line to come back on track. This "correction" movement can also be seen on Fig. 11.6 (top): CoM trajectories at gate 7 were significantly different – the slowest run was too direct and could not take the turn close to the gate. In Fig. 11.6 (bottom) it can also be observed that at the same time the speed decreased while it increased for the fastest run. Thus, in addition to a longer skiing line there was an additional breaking manoeuvre to allow that the athlete could remain in the course. Overall this manoeuvre cost the athlete 1.5 m/s speed and 0.096 seconds.

This error could also add a further explanation why this athlete's second run was consistently slower: his strategy of directly attacking the gates in the first run did not work. Thus, for the second round he was skiing in a more defensive manner to make sure to have enough time to take all the turns. Interestingly, even though he was slower and would have had more time to choose his ski line his turns were still "late". The athlete was not able to correct this "deficit" and future trainings should probably aim at initiating the turns earlier and attacking the gates less directly.

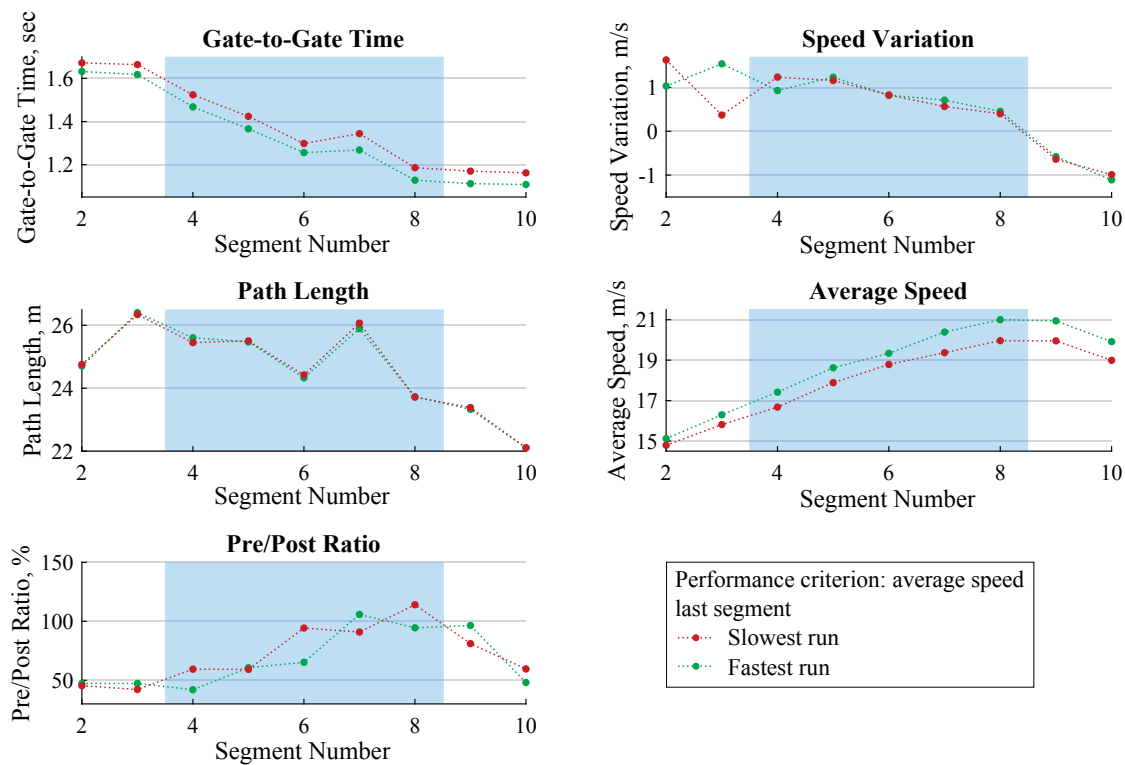


Figure 11.5 – Performance parameters for the two runs with the slowest (red, 19.5 m/s) and fastest (green, 21.0 m/s) section exit speeds. The section considered is shaded in blue. Two more segments at the beginning and end are shown for illustration purposes only.

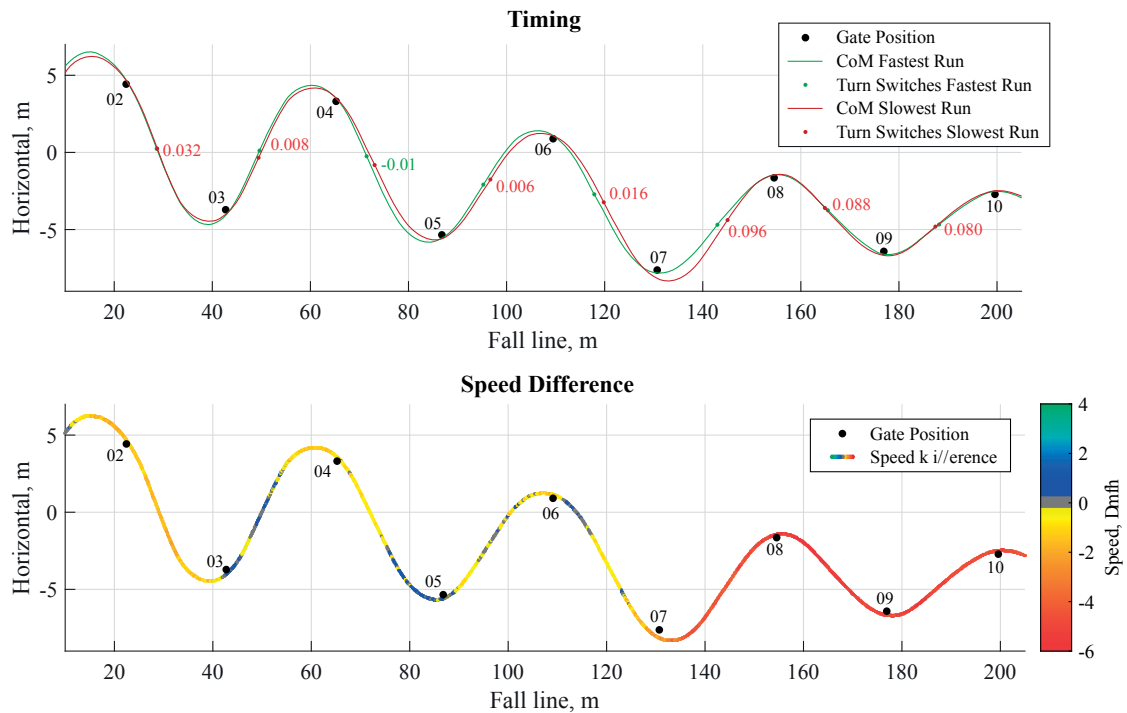


Figure 11.6 – Centre of mass (CoM) trajectory, gate positions, and speed difference for the same two runs and section displayed in Fig. 11.5. The timing graph (top) shows the gate-to-gate time difference between the two runs. The red line is the CoM trajectory of the slowest run and the green line the CoM trajectory of the fastest run. Red, positive, numbers mark a time loss of the slowest run compared to the fastest run. Green, negative, numbers mark a time gain. Units are seconds. The speed difference graph (bottom) shows the color-coded speed difference between the two runs. The trajectory shown is the CoM trajectory of the slowest run. Yellow to red colors mark a negative speed difference (i.e. slower speed for the slowest run). Blue to turquoise colors mark a positive speed difference (i.e. faster speed for the slowest run). The grey color marks no speed difference.

However, such instruction of initiating turns earlier to be faster needs also to be given carefully: for each turn a different "ideal" time of turn switch exists. In other words, initiating turns earlier increases performance up to a certain point only. If turns are initiated too early (i.e. turn switches are in consequence too early too) performance may be decreased again. To illustrate this "optimal" time of turn initiation and turn switch, for all nine runs and turns the pre/post ratio was computed and plotted against the slope angle computed as the arctangent between the gate-to-gate distance and vertical elevation change (Fig. 11.7). Pre/post ratio was dependent on the slope angle, supporting the above hypothesis. For flat terrain turn switch occurred naturally relatively late whereas for steep terrain turn switch occurred relatively early.

These findings are in line with previous studies where different turn cycle structures were observed depending on the course setting or performance. For example Reid (2010)

reported a turn cycle structure difference between a 10 m and 13 m slalom course. Turns were initiated earlier on the 13 m course than on the 10 m course. For giant slalom Spörri et al. (2012a) reported a different turn cycle structure based on the performance: for the same course the analyzed turn for the fastest run was initiated earlier than the slowest run.

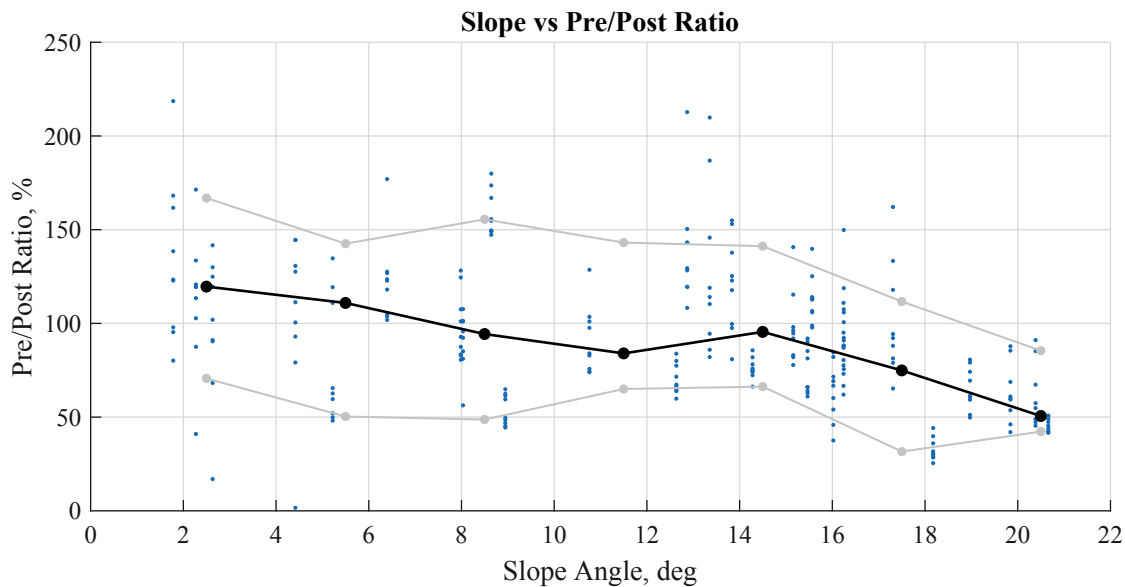


Figure 11.7 – Pre/post ratio in function of slope angle. For each 3-degree section median (black line) and 25th and 75th percentiles (grey lines) were computed.

11.1.3 Comparison of two runs

The above examples illustrated well that the selected performance parameters already allow a very comprehensive performance analysis. Key passages of performance loss and relevant feedback and training hints can be obtained by combining the performance parameters with the ski line and the continuous speed.

The proposed system allows to compute the gate-to-gate crossing times over the entire run. Timing can then be compared between different athletes and runs. While section times are commonly used for performance analysis during trainings they might not provide the necessary time resolution and important details might be missed. Suppose that you have an intermediate and finish time. Suppose further that the intermediate time is taken at gate 17 and that gate 2 was used to set the time difference to zero. When comparing two athletes A and B the timing system shows no time difference for the intermediate time and a 0.12 second time loss for athlete B at the finish. Thus, the conclusion would be made that the athletes had the exact same performance during the first part of the run. When displaying the gate-to-gate timing a completely different picture becomes visible (Fig. 11.8). Athlete B lost almost 0.2 seconds during the first few gates at steep terrain and was then able to speed up to the intermediate flat terrain.

The performances of the two athletes were very different: while athlete A was fast in steep terrain and slow in flat terrain, athlete B was slow in steep terrain and fast on flat terrain. Plotting the ski lines and continuous speed curves (Fig. 11.9) allows to go even further into the details and point out the reasons why athlete B was fast in flat terrain and slow in steep terrain: his line was smoother in the flat part with later turn switches. This allowed him to carve more and keep his speed high. However, for the steeper terrain athlete B might have initiated the turns too early and had an increased path length. This example also shows that very subtle differences may result in large time differences. Choosing a ski line which is 0.5 m longer might in one case be beneficial because a given turn can be skied smoother. Thus, the athlete can keep his speed and gain time because of a faster speed. In other situations it might be impossible to increase speed and a shorter ski line is more beneficial for performance.

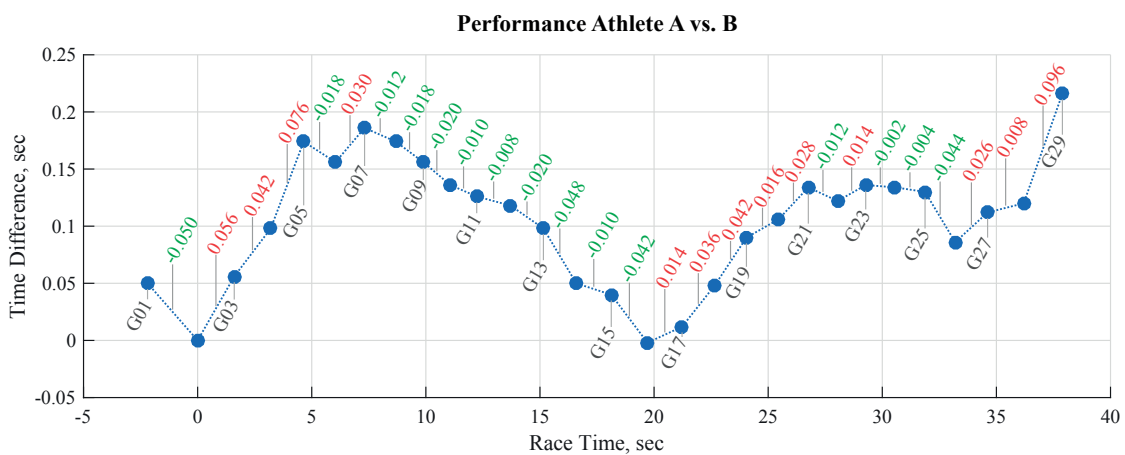


Figure 11.8 – Gate-to-gate timing for two runs from athlete A and B. Athlete B’s gate-to-gate timing difference with respect to athlete A is provided for each segment. A positive red value means that athlete B lost time relative to athlete A and a negative green value means that athlete B gained time relative to athlete A. Time gain/loss is given in seconds.

11.2 Injury prevention

Alpine ski racing is a sport where athletes reach very high speeds of over 120 km/h (Gilgien et al., 2015a). As a consequence, athletes are exposed to high risks of acute and chronic injuries (Flørenes et al., 2009; Haaland et al., 2016). Whereas acute injuries are most likely a direct consequence from falls, chronic injuries are caused by repeated exposure to situations with high loads and pushing the athlete’s body to its limits (Bahr and Krosshaug, 2005; Bahr et al., 2004; Jonasson et al., 2011; Krosshaug et al., 2005). Similar to performance analysis, studies on risk assessment and injury prevention in alpine ski racing were limited by the measurement systems and setups. Therefore, detailed analyses about injury factors and injury risks are still sparse. Nevertheless, the available

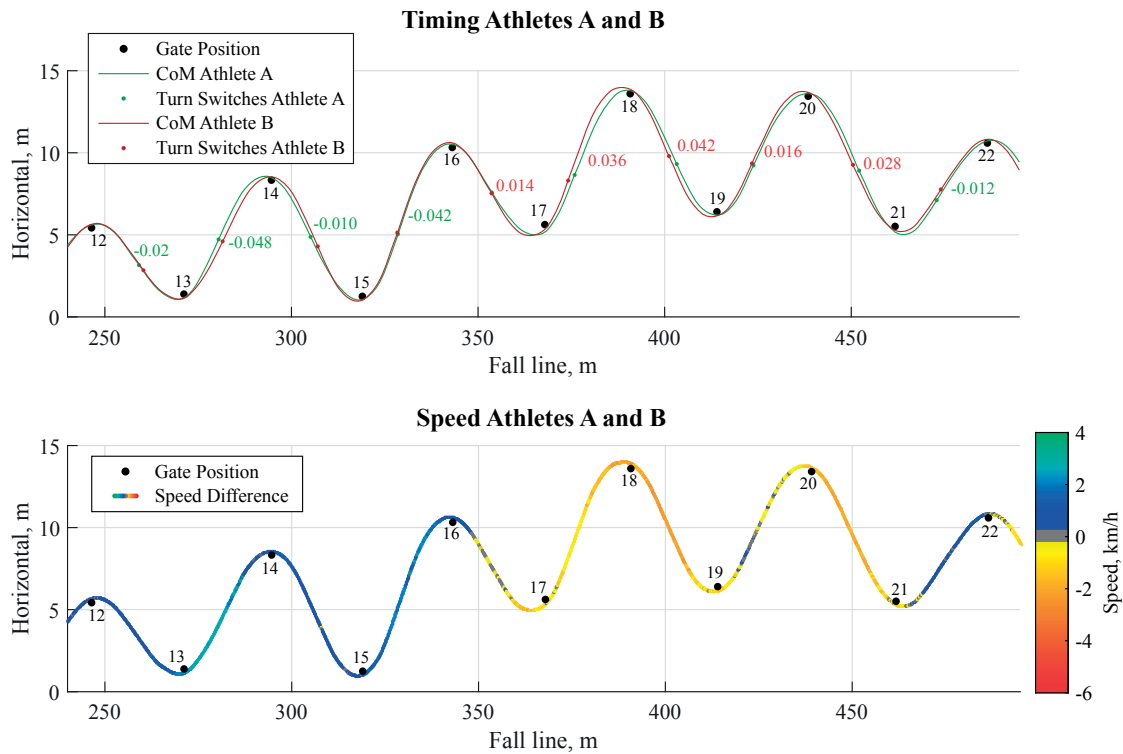


Figure 11.9 – Ski line and CoM speed for the two runs from athlete A and B. Interesting to note is the "inversion" of the CoM line between gates 13-14 and 17-18. For each segment the turns initiated earlier were faster. The timing graph (top) shows the gate-to-gate time difference between the two runs. The green line the CoM trajectory of athlete A and the red line is the CoM trajectory of athlete B. Red, positive, numbers mark a time loss of athlete B compared to athlete A. Green, negative, numbers mark a time gain. Units are seconds. The speed difference graph (bottom) shows the color-coded speed difference between the two athletes. The trajectory shown is the CoM trajectory of athlete B. Yellow to red colors mark a negative speed difference (i.e. slower speed for athlete B). Blue to turquoise colors mark a positive speed difference (i.e. faster speed for athlete B). The grey color marks no speed difference.

studies allowed to obtain valuable insights in the movement of alpine ski racing and associated physiological demands.

This section presents some example curves from in-field measurements performed with the system proposed in this thesis. The aim was to demonstrate its usability and sensitivity to measure kinematic and kinetic differences between slalom (SL) and giant slalom (GS) skiing. Further studies are needed and are in preparation to determine whether these parameters might indeed be related to injury risk or not.

The proposed system allows to measure joint angles with only slightly lower accuracy and precision than currently used 3D video analysis methods while considerably reducing measurement complexity. In addition, the measured accelerations can also be used directly to quantify vibrations and external forces acting on the different segments. For a

better illustration, the following examples (Sections 11.2.1 to 11.2.3) show a comparison between SL and GS skiing. Both measurements for SL and GS were performed on the same slope with a constant inclination of 26° deg. For all gates, horizontal and vertical gate offsets were 3 m and 10 m for SL and 6 m and 25 m for GS. Inertial sensors were fixed to the shanks, thighs, sacrum, and sternum.

11.2.1 Joint flexion angles

For two European-level athletes one representative run of SL with 6 double turns (left – right) and one representative run of GS with 4 double turns was considered for this example. The turns were automatically segmented at each left turn switch and normalized to 200%. Thus, for a cycle the first 100% represent a left turn and the second 100% a right turn. Flexion angles for the right knee, right hip and trunk were analyzed. The angles were computed according to the algorithms presented and validated in Chapter 6. The right knee flexion angles show the typical pattern for the double turn (Fig. 11.10). During the left turn the right leg is the outside leg and its knee was extended. Vice versa, during the right turn the right leg is the inside leg and its knee was flexed. Range of motion for GS was slightly larger with a more extended outside leg. During SL turns the knee flexion for both outside and inside leg are almost constant. At turn switch the athlete has more extended knees in GS than in SL. Hip flexion angle has a considerably higher range of motion in GS than in SL, with less hip flexion at turn switch in GS. Thus, for the analyzed two athletes, the athlete had a more upright posture at turn switch in GS than in SL. A similar pattern is visible for the trunk flexion. In SL the trunk is more flexed with a lower range of motion. Trunk movement is larger in GS and reaches almost full extension shortly after each turn switch. For both disciplines trunk flexion angles are similar for left and right turns.

For the same measurement campaign and complete data set (ten athletes, six runs per athlete) a comprehensive analysis of ground reaction forces and 3D trunk angles was published in Spörri et al. (2016a). An additional study by the same group analyzed ground reaction forces and 3D trunk angles for two different skis for giant slalom (Spörri et al., 2015). In both studies potentially dangerous loads and trunk angles were observed. Higher trunk stability and support from lumbar corsets might help to reduce trunk angles. Equipment intervention, course setting and different snow preparation might help to reduce overall loads.

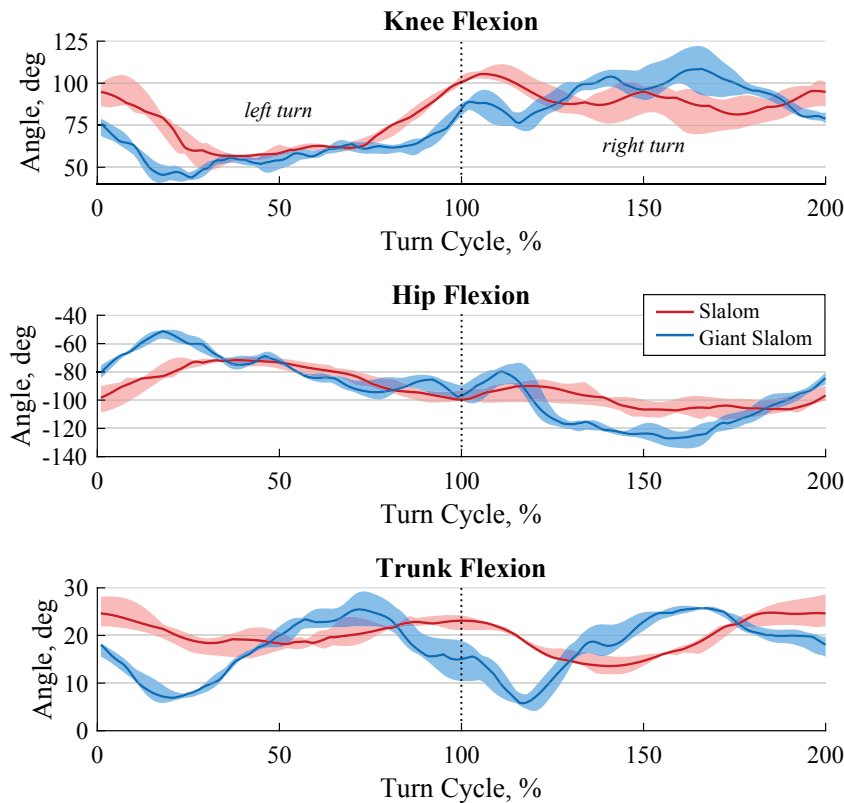


Figure 11.10 – Comparison of the knee, hip and trunk flexion between one representative run of slalom (red) and giant slalom (blue). The dark line is the median angle and the shaded region mark the interquartile ranges over all cycles.

11.2.2 Trunk acceleration

For the same two athletes, runs, and turns, measured acceleration norm of the sacrum sensor was averaged and plotted in Fig. 11.11. In GS acceleration lasted longer and was more constant during each turn. For both disciplines acceleration approached zero at turn switches. It was symmetrical for the left and right turns in SL but accelerations seemed to last longer for right turns in GS. The accelerations are composed from accelerations due to the movement itself (e.g. centripetal acceleration, free-fall motion during turn switches) and vibrations from the ski-snow interactions. The effect of vibrations is especially well visible in GS where several acceleration peaks are reached for each turn. The low interquartile ranges indicate the vibrations were highly repeatable between turns – they started at approximately the same location and had the same effect throughout each turn. Averaged acceleration peaks reached similar values in LS and GS.

The accelerations measure the external forces only and do not allow to estimate joint forces since internal forces (e.g. muscle forces) and ground reaction forces were not quantified. If these parameters (internal forces and ground reaction forces) could be measured reliably inverse kinematics might be used to estimate those joint forces. Nevertheless, the

measured accelerations indicate that acting joint forces may be extremely high due to the centripetal forces and are probably reaching values several times higher than body-weight. There is some evidence that lower forces might reduce injury risk (Haaland et al., 2016; Spörri et al., 2016c) but due to the small sample sizes, a statistical significance could not be demonstrated up to today.

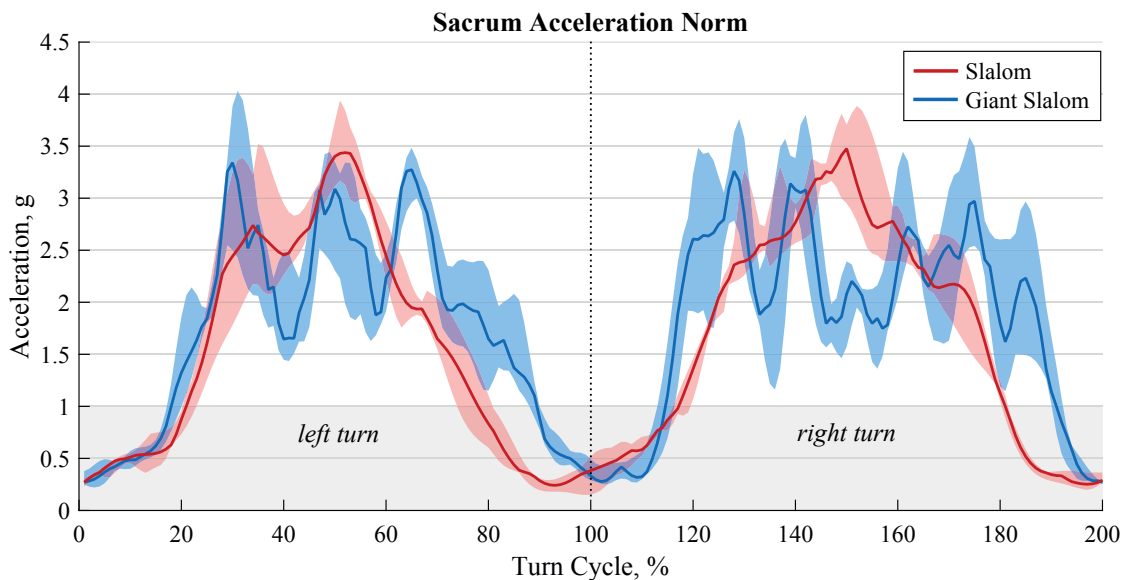


Figure 11.11 – Acceleration norm measured at the sacrum for slalom (red) and giant slalom (blue). The area below 1g acceleration is shaded in grey.

11.2.3 Segment vibrations

To illustrate vibrations from the ski-snow interaction acting on the different segments six runs of SL and six runs of GS were selected. Six European-level athletes were divided into a SL and GS group of equal size depending on their best race results. Each athlete skied two runs on his best discipline. The same SL and GS courses and sensor setup as for the angle and acceleration comparisons above were used. For SL a section of 15 turns was selected and for GS a section of 11 turns was selected. Based on the Fast Fourier Transform (FFT), one single-side amplitude spectrum was computed on the entire section. A variant of the method where the frequency spectrum was computed for each turn independently was presented at the conference 3D-AHM 2017 (Fasel et al., 2016b). Similar studies have been performed before (e.g. Federolf et al. (2009); Supej (2013)) for recreational skiers.

For SL the acceleration frequency spectrum was highest for all frequencies for the shank and was attenuated at each joint, reaching minimum values for the sternum (Fig. 11.12). Vibrations were largest below 15 Hz and again from 18 to 24 Hz. Knee joint was able to attenuate vibrations especially below 20 Hz. The hip joint attenuated the most vibrations above 10 Hz but not below 10 Hz. In the spine, especially vibrations below 8

Hz were attenuated. While there is no evidence that such vibrations and acceleration magnitudes could negatively affect the knee and hip joints the low back pain and spinal disc deformations observed in a large group of alpine ski racers indicate that this might not be the case for the back (Spörri et al., 2016a, 2015).

For GS shank vibrations were largest around 15 Hz and linearly decreased for higher frequencies (Fig. 11.13). Similar vibration transmissions as in SL were observed. However, vibrations were significantly larger, where especially the thigh showed a relatively large and almost constant amplitude from 15Hz to 30Hz. Vibrations at the sacrum were amplified at the hip joint for frequencies below 9Hz, indicating a resonant frequency in the pelvis. In comparison to SL vibrations were more important at the entire frequency spectrum.

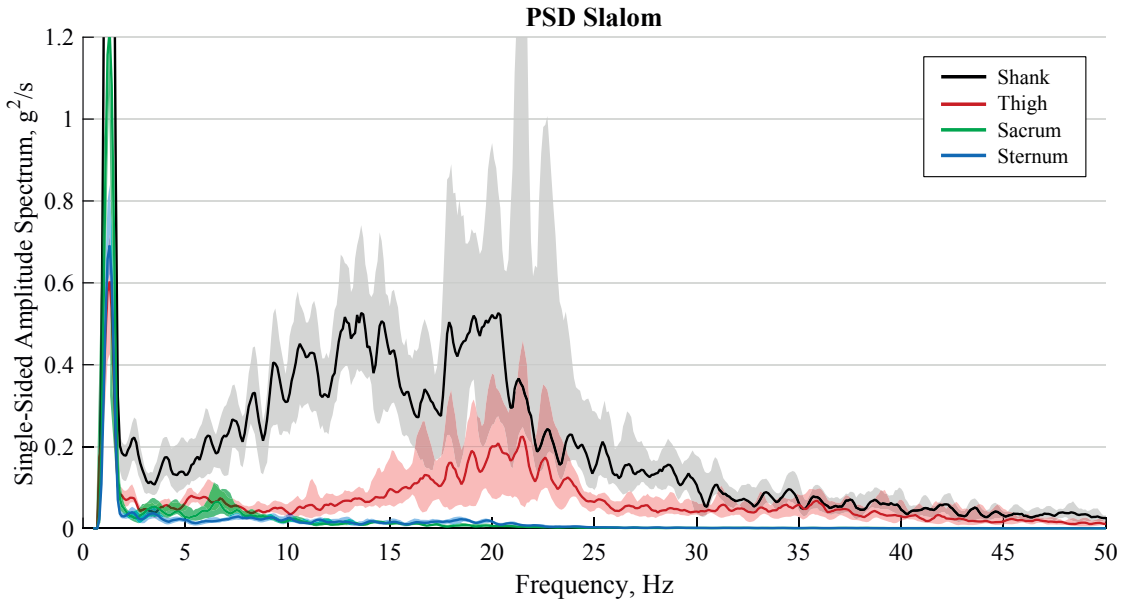


Figure 11.12 – Acceleration frequency spectrum for slalom.

11.3 Conclusion

The system proposed in this thesis allows to obtain a large spectrum of parameters related to performance and injury, even though only inertial and magnetic sensors were used. In the previous chapters the system and its algorithms were presented and technically validated. The illustrations and examples provided in this chapter now demonstrate the in-field applications and efficiency. Results were in agreement to previous studies and the system may allow to obtain new results from large sample sizes with a relatively easy setup. Even though the accuracy and the precision of the proposed system for joint angles and CoM kinematics may be slightly worse in comparison to 3D video analysis and differential GNSS, this loss could be compensated with the simplified setup which allowed to measure larger sample sizes. There are already two published studies based

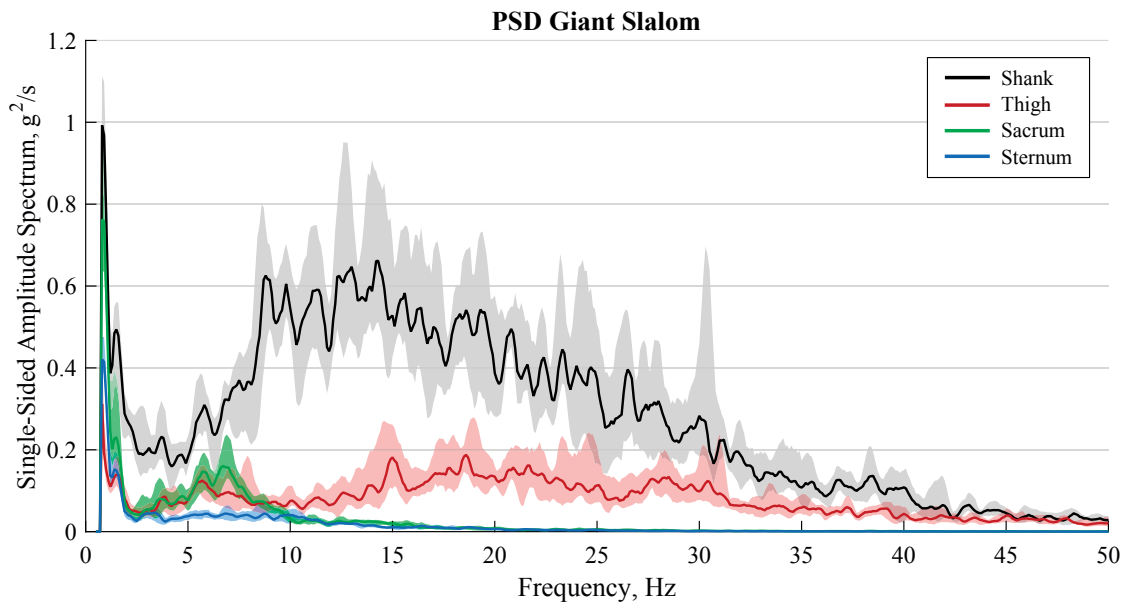


Figure 11.13 – Acceleration frequency spectrum for giant slalom.

on the proposed system that examine injury-related parameters and allowed to measure larger groups (Spörri et al., 2016a, 2015).

For performance analysis the system should be further simplified. For using it during regular trainings the number of sensors need to be minimized. Ideally only one sensor integrated in the athlete's equipment (e.g. back protector) should be used. Such a simplification would open up new ways for a continuous and automatic training monitoring. Performance of every athlete during every training can be recorded and tracked. In combination with traditional video-based analysis coaches could use this additional information to train athletes more specifically and better track their performance. The information can also be used to set up a "performance database" which can be used to identify the fastest skiing strategies under different conditions and to provide valuable inputs to athletes for future races.

From a research point of view there are still many open questions. How can we further reduce injury risk, both acute and chronic? Could the proposed system be used to detect technical errors leading to uncontrolled skiing situations and therefore potentially high injury risk situations? Which interventions are the most efficient while keeping the competition level high and interesting? Could a real-time feedback reduce exposure to potentially dangerous situations? While the proposed system will not help to ask the right questions and cannot find the best movement analysis strategy, it may provide an efficient tool to test the different hypotheses and might also serve to generate new hypotheses. Simplified systems could be used for continuous training monitoring, similar to a performance analysis system. Long-term risk factors for both acute and chronic injuries might be better identified and athletes could be more easily monitored during prospective studies.

Direct Speed Estimation Part IV

12 Direct Estimation of Walking Cadence and Speed

Abstract

In daily life, a person's gait - an important marker for his/her health status - is usually assessed using inertial sensors fixed to lower limbs or trunk. Such sensor locations are not well suited for continuous and long duration measurements. A better location would be the wrist but with the drawback of the presence of perturbative movements independent of walking. The aim of this study was to devise and validate an algorithm able to accurately estimate walking cadence and speed for daily life walking in various environments based on acceleration measured at the wrist. To this end, a cadence likelihood measure was designed, automatically filtering out perturbative movements and amplifying the periodic wrist movement characteristic of walking. Speed was estimated using a piecewise linear model. The algorithm was validated for outdoor walking in various and challenging environments (e.g., trail, uphill, downhill). Cadence and speed were successfully estimated for all conditions. Overall median (interquartile range) relative errors were -0.13% (-1.72 2.04%) for instantaneous cadence and -0.67% (-6.52 6.23%) for instantaneous speed. The performance was comparable to existing algorithms for trunk- or lower limb-fixed sensors. The algorithm's low complexity would also allow a real-time implementation in a watch.

Keywords: inertial sensor, wrist, walking, cadence, speed

12.1 Introduction

Walking cadence (i.e. number of steps per unit time) and walking speed are among the most basic outcome measures of gait analysis (Oberg et al., 1993; Susi et al., 2013; Zijlstra and Hof, 2003). Clinical gait analysis can be used to diagnose diseases, to assess their severity and extent, to monitor the effect of an intervention, and to predict the outcome of an intervention (Baker, 2006; Brand, 1989). In clinical settings, gait speed is used as primary outcome for evaluation of recovery from many diseases (Fulk et al., 2014). In a healthy average population, age affects walking speed (Elble et al., 1991) but not walking cadence (Samson et al., 2001). Boyer et al. (2012) reported the opposite for a fit and healthy population walking at least 7500 steps a day, hypothesizing that walking attenuated the effect of aging on ambulatory mechanics. In elderly persons, walking speed was also associated with fall risk (Quach et al., 2011), fear of falling (Rochat et al., 2010) and survival: increased walking speed implies healthier aging (Studenski et al., 2011).

The field of physical activity monitoring tries to relate everyday life physical activity, including gait, to health status (Butte et al., 2012; Paraschiv-Ionescu et al., 2012; Taraldsen et al., 2012). While precious information about the walking abilities and the risk of falling lies in walking cadence and speed during daily activities (Brodie et al., 2015) most studies tried to estimate energy expenditure, time spent in each activity (e.g. lying, sitting, standing), or to detect activity patterns.

In clinical and research settings, walking cadence is commonly measured using straight walking over force plates (Samson et al., 2001), with foot switches (Morris et al., 1994), or over-ground or treadmill walking using pressure insoles (Hausdorff et al., 1998; Redd et al., 2012). In addition, optical motion capture (Cedervall et al., 2014) or inertial sensors placed on the feet (Jasiewicz et al., 2006; Mariani et al., 2010; Rampp et al., 2015), shank (Aminian et al., 2002; Trojaniello et al., 2014), trunk (Moe-Nilssen and Helbostad, 2004; Zijlstra and Hof, 2003) or a combination of different sensors and sensor placements (Alaqtash et al., 2011; Tao et al., 2012) can estimate both cadence and speed. These measurement systems are generally used in laboratory conditions; they are complex to set up and cannot always be used for gait analysis during long-term monitoring in real life conditions. Gait speed is generally measured in laboratory conditions and the question arises on how this measure reflects the patient's performance and capability in real life (Bonato, 2005). This explains the lack of information on walking cadence and speed in everyday life. Inertial sensors fixed to the wrist provide a good alternative for long-term daily activity monitoring (Mannini et al., 2013). They can be hidden inside a regular watch, not marking the wearer as a person being monitored, thus increasing user compliance. Moreover, the watch can be used as means of real time feedback to the user, for example to increase physical activity. However, since the arm may move independent from the legs, wrist-based activity monitors have a relatively low accuracy and precision (Ahola, 2010; Karuei et al., 2013). Standard approaches for step detection, such as peak detectors used for analyzing data from the trunk or lower limbs,

cannot be used for the wrist: random arm movements may cause additional peaks or the absence of arm swing may hide peaks that could be used for step detection (Susi et al., 2013). Moreover, walking speed cannot be estimated by integration of the measured acceleration. Unlike the foot, for example, no motionless phases exist that could be used for removing integration drift (Elhoushi et al., 2016; Mariani et al., 2010; Susi et al., 2013). Smartwatches were introduced to the mass market in the past years as consumer-oriented activity trackers, providing an easy and non-intrusive solution to monitor activity in real life condition. While the accuracy of step counting is in general reasonable for healthy young persons, it could reach up to 20% of error for some activity trackers (El-Amrawy and Nounou, 2015). These devices do not measure instantaneous walking speed but rather the distance covered using an estimate of step length (Pasolini, 2007; Zhao, 2010). Other technologies such as global navigation satellite systems (GNSS) integrated in a watch were also proposed and provide a proper accuracy for measuring total walking distance (Abraham et al., 2012; Tan et al., 2008; Terrier et al., 2000). However, GNSS chips need a lot of power decreasing battery lifetime drastically and sensors need to be charged at least once per day. Additionally, GNSS signals may be degraded in urban environment or be completely blocked indoors (Elhoushi et al., 2016). Among inertial sensors, accelerometers are the ones with lowest power consumption, and today they allow continuous activity recording up to several months without the need of charging their batteries.

The current study aimed at designing and validating a wrist sensor-based algorithm optimized for long-term measurements of walking cadence and speed with the possibility of real-time implementation. The goal was to obtain a high temporal resolution of 1 Hz for both cadence and speed. To this end, a cadence likelihood measure was proposed based on the acceleration measured at the wrist. The cadence likelihood was then used to estimate the walking cadence and a locally linear model was designed to estimate walking speed. This approach allowed the design of a calibration-free algorithm only needing the person's height as additional input parameter. The algorithm was validated for outdoor walking on a long trail in rural and urban environments for a healthy group of participants.

12.2 Methods

12.2.1 Measurement Protocol

Twenty-nine healthy and active persons (7 women, 22 men, age 39.1 ± 10.8 years, height 175.3 ± 10.9 cm, and weight 71.5 ± 10.5 kg) participated in the study. The measurement protocol consisted of two different datasets. Dataset 1 consisted of walking a total distance of approximately 4.7 km over level and inclined terrain, with different ground surface (tar, grass, gravel), in urban and rural setting, involving different situations of daily life (cellphone, obstacles, carrying bag, hand in pocket) (Fig. 12.1). The total

walking path was segmented into shorter bouts of varying environments where each participant was asked by the accompanying instructor to walk in a specific manner (Table 12.1). Each segment was separated from the next by a short static phase of at least 10 seconds. In Dataset 2, six healthy and active men; age 23.7 ± 18.6 years, height 179.5 ± 12.1 cm, weight 73.9 ± 10.4 kg), none of which participated in Dataset 1 walked another trail of highly inclined surfaces. For each trial the person was asked to walk at normal, self-selected speed and with arms swinging freely (Table 12.2). Dataset 1 was used for training and testing the speed estimation algorithm while Dataset 2 was only used for training the speed estimation model (see validation section 12.2.4). The experimental protocol was explained to the participants and written informed consent was obtained prior to the measurements. The experimental procedure was approved by the Human Research Ethics Committee of Ecole Polytechnique Fédérale de Lausanne (HREC No: 007_13/10/2014).

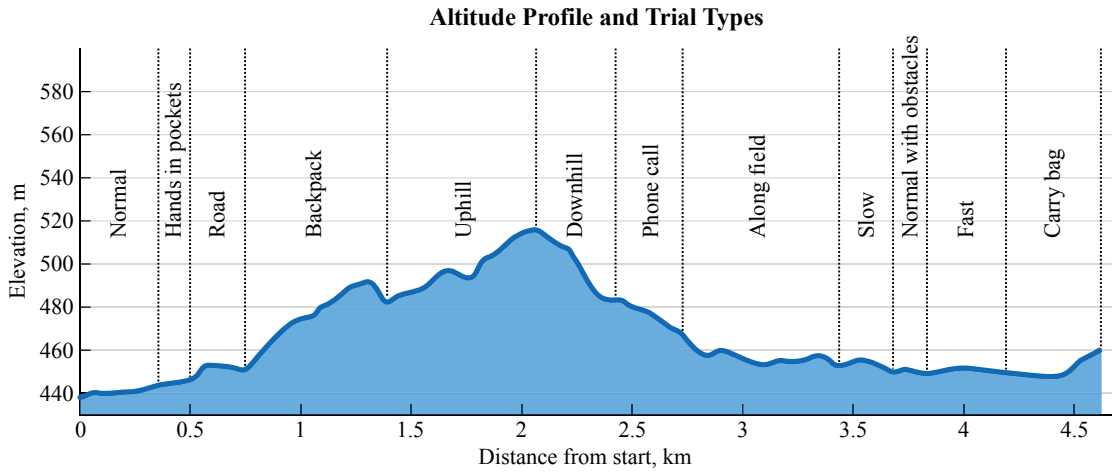


Figure 12.1 – Altitude profile for Dataset 1 with description of the different trial conditions

12.2.2 Materials and Setup

The participants were equipped with an inertial sensor (Physilog IV, Gait Up, Switzerland) placed on the left wrist using an elastic strap. In addition, for validation purpose (see section 12.2.4), three additional time-synchronized inertial sensors (Physilog IV, Gait Up, Switzerland) were placed on the left and right shoes using adhesive tape and on the head using Velcro attached to a cap (Fig. 12.2). All inertial sensors measured tri-axial acceleration and angular velocity at 200 Hz (range ± 16 g, $pm1000$ deg/sec) and barometric pressure at 25 Hz. The head inertial sensor additionally comprised a Global Navigation Satellite System (GNSS) chip (CAM-M8Q, u-blox, Switzerland) sampling at 10 Hz in pedestrian mode with an external active antenna (ANN-MS, u-blox, Switzerland). The GNSS chip was controlled by the inertial sensors. Accelerometer offset and sensitivity were corrected using the method of Ferraris et al. (1995).

Label	Walking surface type and environment	Instructions given to participants	Median distance [95% CI], m	Median altitude change [95% CI], m
Normal	Uneven gravel road with puddles, no traffic	Walk normally, avoid puddles. Move your arms naturally along your body.	351.7 [347.4 355.4]	4.7 [2.8 5.5]
Hands in pockets	Uneven gravel road with puddles, no traffic	Walk with both hands in the pockets of your pants, avoid puddles.	158.5 [151.9 174.0]	2.1 [1.2 3.3]
Road	Sidewalk along busy and noisy road with a lot of trucks driving past	Walk normally on the sidewalk along the road. No restrictions and indications for arm movement.	266.7 [248.00 287.3]	5.6 [4.1 7.0]
Backpack	Tar road with few cars passing (50%) and gravel road in forest (50%)	Walk normally carrying the backpack. No restrictions and indications for arm movement.	692.4 [669.2 700.4]	31.1 [29.2 32.4]
Uphill	Tar road (66%), grass road (34%), no traffic	Walk normally. No restrictions and indications for arm movement.	669.6 [661.0 676.6]	31.9 [29.9 34.0]
Downhill	Grass road (50%), gravel road (50%), no traffic	Walk normally. No restrictions and indications for arm movement.	360.4 [354.5 373.0]	-31.3 [-32.6 -30.6]
Phone call	Tar road, little traffic, crossing of busy road	Walk normally while performing a phone call with the left hand constantly holding the phone to the ear.	304.7 [290.8 308.0]	-16.6 [-17.3 -15.8]
Along field	Tar road (50%), grass trail (50%). No traffic	Walk normally. No restrictions and indications for arm movement.	718.4 [712.5 739.9]	-13.2 [-14.4 -11.7]
Slow	Tar sidewalk in quite neighborhood with little traffic	Walk as slowly as possible, as you would on a Sunday afternoon family stroll with children and grandparents. No restrictions and indications for arm movement.	267.4 [263.4 275.2]	-2.3 [-3.1 -1.5]
Normal with obstacles	Tar road. Passing a busy road. No other cars passing by, few other people	Walk normally, avoid obstacles (street crossing, walking around railings). No restrictions of the arm movement but on two occasions the person was asked to point at landmarks.	126.2 [119.4 130.4]	-1.2 [-2.1 -0.6]
Fast	Tar sidewalk, few other people on sidewalk and few cars passing by.	Walk as fast as possible but without running: you have to catch a train and are very late. No restrictions and indications for arm movement.	407.7 [402.2 411.4]	-0.3 [-1.5 1.0]
Carry bag	Tar sidewalk. Very busy with many people and heavy traffic.	Carry a heavy bag (5kg) with your left hand. Adapt walking speed and direction to avoid walking into other people.	375.8 [368.5 387.1]	11.1 [9.9 12.0]

Table 12.1 – Trial description of Dataset 1 with median and 95% confidence interval (CI, 2.5th and 97.5th percentiles) of reference distance obtained with the GNSS system and altitude change measured using the barometric pressure sensor (Parviainen et al., 2008).

Chapter 12. Direct Estimation of Walking Cadence and Speed

Label	Walking surface type	Median distance [95% CI], m	Median altitude change [95% CI], m
Uphill 13%	Asphalt road	268.8 [265.4 270.1]	33.8 [32.5 36.1]
Downhill -18%	Gravel road	200.7 [197.5 213.6]	-34.5 [-37.2 -32.7]
Uphill 32%	Gravel road	64.9 [62.5 67.0] 19.8	[19.1 20.8]
Downhill -42%	Gravel road	59.4 [58.2 62.9]	-21.4 [-22.5 -20.0]
Uphill 21%	Gravel road	101.3 [98.9 123.1]	20.4 [19.1 23.2]
Uphill 6%	Asphalt road	251.4 [244.7 254.7]	16.4 [15.6 17.2]
Downhill -13%	Asphalt road	159.1 [152.6 162.7]	-21.9 [-22.9 -21.0]
Uphill 23%	Asphalt road	153.3 [150.2 178.4]	33.5 [31.8 35.9]
Downhill -23%	Asphalt road	150.1 [148.6 175.5]	-33.5 [-35.5 -31.9]
Downhill -10%	Asphalt road	99.3 [94.9 102.8]	-9.5 [-10.9 -8.9]
Uphill 18%	Gravel road	195.8 [193.6 199.8]	34.0 [32.6 34.8]

Table 12.2 – Trials in Dataset 2 on highly inclined roads recorded for 6 persons used for the training of the speed estimation model only. Median and 95% confidence interval (CI, 2.5th and 97.5th percentiles) of reference distance was obtained with the GNSS system and altitude change measured using the barometric pressure sensor (Parviainen et al., 2008).

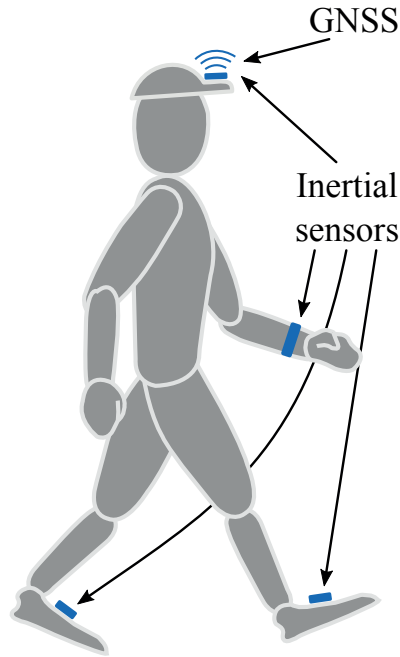


Figure 12.2 – Placement of the wrist inertial sensor and the reference system consisting of three inertial sensors and the GNSS on feet and head

12.2.3 Wrist algorithm

All walking periods were manually segmented, excluding the rest periods at the very beginning and end of each walking trial. For the wrist algorithm, only the acceleration and barometric pressure ($p(t)$) were considered. First, the acceleration was low-pass filtered

at 10 Hz (2nd order Butterworth filter) and then down-sampled to 20 Hz. Next, to be insensitive to sensor placement and orientation, the acceleration norm $\mathbf{a}(t)$ (including the gravity component) was computed. $\mathbf{a}(t)$ was segmented into windows of 6 seconds $W[n]$ (i.e. 120 samples per window) and each window was shifted by 1 second, having an overlap of 5 seconds, to obtain one cadence and speed estimate per second. These estimates were defined to represent the instantaneous walking cadence (i.e. step frequency) $c_{wrist}[n]$ and instantaneous walking speed $v_{wrist}[n]$ where $n \in \mathbb{N}$ denotes the window number.

Cadence estimation

During walking, arm movement (e.g. arm swing combined with up/down movement of the person's center of mass at each step) generates a harmonic pattern in the frequency domain of the wrist's acceleration. While generally the arm swing has a period of stride (two steps), it moves up and down with the trunk at each step. Therefore the hypothesis was that the fundamental frequency of $\mathbf{a}(t)$ corresponded to the stride frequency and its first harmonics to the step frequency (i.e. walking cadence). Depending on the arm movement, the fundamental frequency and some of its harmonics may be weak and below the noise level. Therefore, simple peak detection of the acceleration spectrum would not be sufficient for a robust estimation of walking cadence and a more sophisticated method was needed. The main idea of the algorithm was to emphasize harmonic frequency patterns in the frequency domain of $W[n]$ and to relate the enhanced patterns to walking cadence. For this purpose, comb filters (Smith, 2010) were adapted and a cadence likelihood function $CL_n[f]$ was computed for each window $W[n]$. It was then hypothesized that the location of the maximum likelihood corresponded to the stride frequency. Thus, the walking cadence was equal to twice this value (Eq. 12.1).

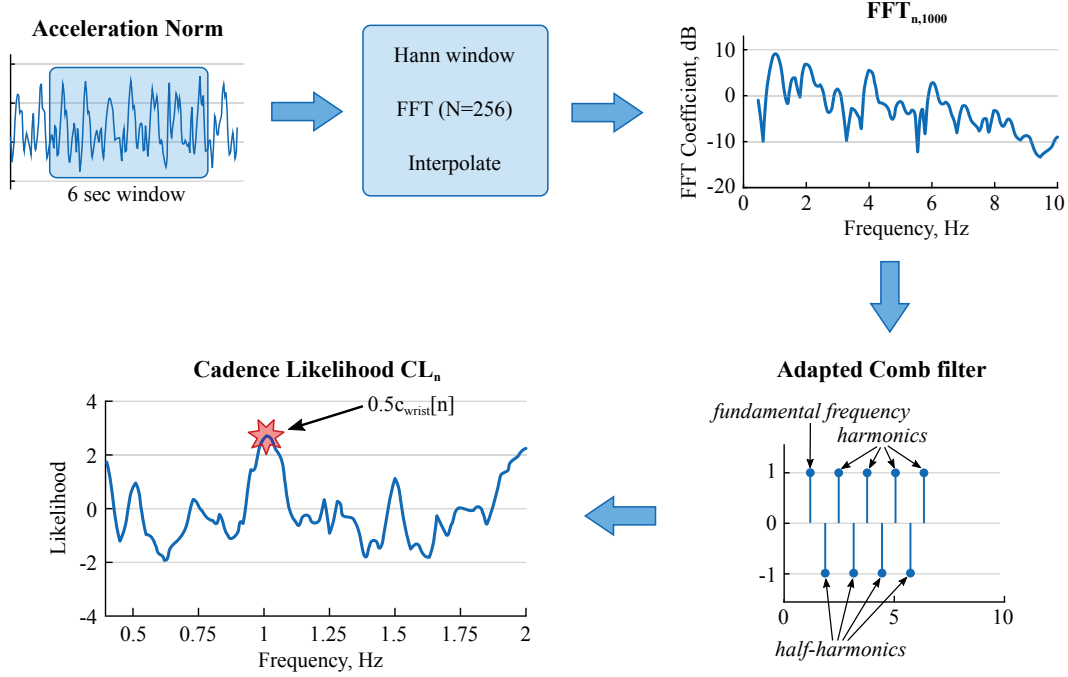
$$c_{wrist}[n] = 2 \arg \max_{0.4 \leq f \leq 2} CL_n[f] \quad (12.1)$$

Fig. 12.3 summarizes the procedure for computing $CL_n[f]$. First, the logarithm of the single-sided amplitude spectrum of $W[n]$ using the Fast Fourier Transform (FFT) of length 256 and the Hann window function (Harris, 1978) was computed. Second, this amplitude spectrum was linearly interpolated to artificially increase the frequency resolution to 0.01 Hz. This new series was denoted as $FFT_{n,1000}[f]$. Third, $CL_n[f]$ was computed using adapted Comb filters, according to Eqs. 12.2 and 12.3.

$$CL_n[f_{test}] = \sum_f FFT_{n,1000}[f] \cdot H_{f_{test}}[f] \quad (12.2)$$

$$H_{f_{test}}[f] = \begin{cases} 1 & \text{if } f = nf_{test}, \quad n \in \{1, 2, 3, 4, 5\} \\ -1 & \text{if } f = mf_{test}, \quad m \in \{1.5, 2.5, 3.5, 4.5\} \\ 0 & \text{else} \end{cases} \quad (12.3)$$

where $f_{test} \in \{0.40, 0.41, 0.42, \dots, 2.00\}$ Hz and $f \in \{0.00, 0.01, 0.02, \dots, 10.00\}$ Hz.


 Figure 12.3 – Flowchart for the computation of $c_{wrist}[n]$

In the case of a stride frequency below 1 Hz, $CL_n[f]$ will have two maxima, one at the stride frequency and one at the step frequency. On the other hand, for vigorous and walking-independent arm movements, multiple local maxima can be found in $CL_n[f]$, which are not matching the stride or step frequency. To avoid detecting a local maximum which does not correspond to the true stride frequency, $c_{wrist}[n]$ was tracked over time. For walking, excluding gait initiation and termination, the stride frequency generally changes slowly between two consecutive windows $W[n-1]$ and $W[n]$. Therefore, if the stride frequency of the current window was too different from the estimate of the past window (empirically selected threshold of 0.07 Hz, based on the data from the foot inertial sensors) and if the stride frequency was below 1 Hz, $CL_n[f]$ was searched for a local maximum near the stride frequency (range A , Eq. 12.4) and near the step frequency (range B , Eq. 12.4). The more prominent maxima was then kept, allowing a robust detection if neither the stride nor step frequency were present (Eq. 12.5).

$$\begin{aligned} A : & \quad 0.5c_{wrist}[n-1] - 0.07 \leq f \leq 0.5c_{wrist}[n-1] + 0.07 \\ B : & \quad c_{wrist}[n-1] - 0.14 \leq f \leq c_{wrist}[n-1] + 0.14 \end{aligned} \quad (12.4)$$

$$c_{wrist}[n] = \begin{cases} 2 \arg \max_{f \in \{A, B\}} CL_n[f] & \text{if } f \in A \\ \arg \max_{f \in \{A, B\}} CL_n[f] & \text{if } f \in B \end{cases} \quad (12.5)$$

Finally, $c_{wrist}[n]$ was low-pass filtered using the filter $c_{wrist}[n] = 0.33c_{wrist}[n-1] + 0.67c_{wrist}[n]$.

Speed estimation model

Instantaneous walking speed $v_{wrist}[n]$ depends mostly on cadence and stride length. In order to account for stride length, the person's height (h) and an estimation of acceleration intensity defined here as the product between average acceleration (interpreted as the person's average movement energy) and its standard deviation (interpreted as energy from arm movement) was used. Walking speed could also change with slope, thus an estimate of altitude change was considered. This lead to four features, computed independently for each window (Eq. 12.6).

$$\begin{aligned} x_1[n] &= \text{mean}(W[n]) \cdot \text{std}(W[n]) \\ x_2[n] &= c_{wrist}[n] \\ x_3[n] &= p(t - 0.5) - p(t - 9.5) \\ x_4[n] &= h \end{aligned} \tag{12.6}$$

where $p(t)$ is the barometric pressure at time t (corresponding to window n) and h is the person's height (in m). Pressure difference was computed for the last nine seconds instead of six in order to reduce sensor noise.

The speed estimation was based on a model using mapping function M between $\mathbf{x}[n] = (x_1[n], x_2[n], x_3[n], x_4[n])$ and the person's reference walking speed $v_{ref}[n]$ such that $v_{ref}[n] = M(\mathbf{x}[n]) + \eta$, where η is Gaussian white noise. To this end, the input feature space was first partitioned into 16 clusters using the k-means clustering technique. A linear model, $g_i(\mathbf{x}[n])$, was then fitted to each of these clusters (Nelles, 2001). The mapping function M was then defined according to Eq. 12.7.

$$\begin{aligned} M(\mathbf{x}[n]) &= g_i(\mathbf{x}[n]) \\ i &= \arg \min_{i=\{1,\dots,16\}} |\mathbf{x}[n] - \mathbf{G}_i| \end{aligned} \tag{12.7}$$

where \mathbf{G}_i is the geometric cluster center of cluster i obtained from the k-means clustering. In addition, the average speed of each trial was computed and the total distance walked per trial was obtained by summing and integrating all speed estimates.

12.2.4 Validation and statistical analysis

Reference values for cadence and speed

The reference system was composed of the two inertial sensors fixed to the feet and of the inertial sensor and GNSS placed on the head (Fig. 12.2). Reference walking cadence $c_{ref}[n]$ was obtained through linear interpolation at 1 second intervals of the walking cadence obtained from the toe-off events of both left and right foot, detected using the feet's medio-lateral angular velocity (Mariani et al., 2013). The precision of this event is given with 14 ms in Mariani et al. (2013). Reference walking speed $v_{ref}[n]$ was obtained

by first low-pass filtering (2nd order Butterworth, 0.25 Hz cutoff frequency) the speed obtained from the GNSS and second by resampling the low-pass filtered speed at 1 Hz. For 10 Hz sampling frequency the data sheet specifies a speed accuracy of 0.05 m/s (50% of the samples are within 0.05 m/s of the true speed, measured at 30 m/s). During the measurements, the GNSS chip reported a median accuracy of 0.057 m/s and 95% confidence interval of 0.040 - 0.094 m/s. Speed samples where the accuracy was above 0.25 m/s were marked as unreliable and were discarded. Inertial data from the head sensor and pressure data from the feet sensors were not used.

Cross validation and statistical analysis

After discarding the first and last two seconds of each walking trial for each participant, estimated and reference cadence and speed were stored for each window. For validation of the wrist algorithm, the leave one out cross validation was used as follows. The training set consisted of Dataset 2 plus the data of the trials "hands in pockets", "backpack", "downhill", "phone call", "along field", "slow", and "fast" for all participants in Dataset 1 except one. The testing set included all the data of the remaining participant in Dataset 1. This procedure was repeated with the data of all participants of Dataset 1. The algorithm error was then defined as the sample-by-sample difference between the estimated and the reference values. Normality of the parameter values and errors was assessed using the Lilliefors test. Median value and the interquartile range of the parameter values obtained with the reference system and the wrist algorithm were computed. Absolute and relative errors were quantified using median values and interquartile ranges. Error plots where average values are plotted against their difference (Bland and Altman, 1999) were generated for each parameter. Since cadence samples were not independent, no limits of agreements were computed. Instead we reported the 5th, 25th, median, 75th, and 95th percentiles. Spearman rank correlation was used for testing for correlations between the error and reference parameter value. Kruskal-Wallis test was performed to check for significant effects of participant and trial condition on speed and cadence errors.

12.3 Results

12.3.1 Overview

In total 94'259 cycles (i.e. 26.18 hours of data, 348 walking trials) were analyzed. For illustration purpose, Fig. 12.4 shows the time series curves of the reference and wrist system for the instantaneous cadence and speed for one typical participant. The different trial conditions allowed measuring a broad range of walking cadences and speeds and different movement types. The instantaneous cadence, speed, and the errors were not normally distributed ($p < 0.001$).

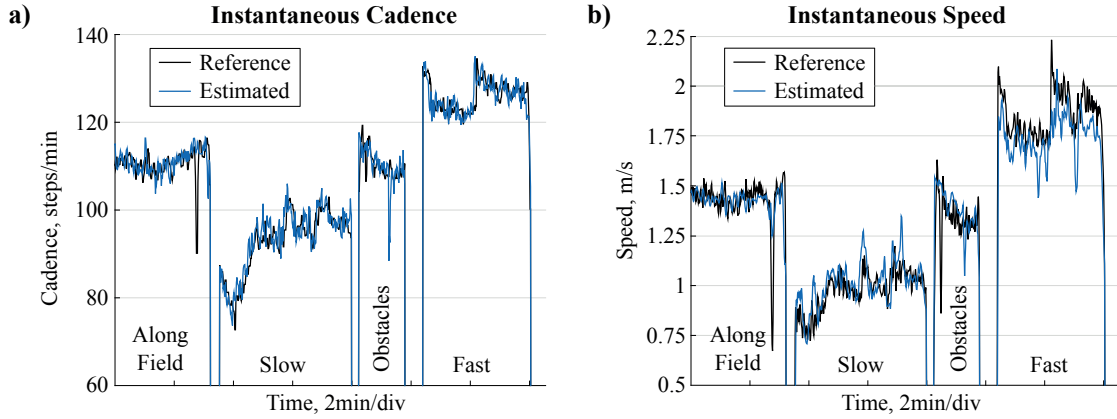


Figure 12.4 – Illustration of a typical time series of reference and wrist cadence (a) and speed (b)

Spearman's correlation coefficient between the reference and wrist system was 0.90 and 0.71 for instantaneous cadence and speed, respectively. For values averaged over each trial the correlation increased to 0.998 for the cadence and 0.83 for the speed. Table 12.3 lists average parameter values for each trial condition and the corresponding error. Overall median [interquartile range] relative errors were -0.13% [-1.72% 2.04%] for instantaneous cadence, and -0.67% [-6.52% 6.23%] for instantaneous speed. Average errors per trial were -0.23% [-0.60% 0.11%] and -0.43% [-4.52% 4.73%] for cadence and speed, respectively. For the total distance per trial, Spearman's correlation coefficient between the reference and wrist system was 0.97, with median [interquartile range] absolute errors of -8.34 m [-23.63 m 6.37 m] and relative errors of -2.73% [-6.28% 2.79%].

12.3.2 Error dependencies

Error plots were generated for the cadence and speed errors (Figs. 12.5, 12.6). The cadence error was weakly correlated to its value ($R^2 = 0.07$, Fig. 12.5). The speed error was slightly correlated to its value ($R^2 = 0.32$, Fig. 12.6). The different conditions allowed measuring walking as it occurs during daily living. Moreover, the heterogeneous participant group allowed testing for error dependencies on their anthropometry. According to the Kruskal-Wallis test, both the trial condition and the participant had a significant influence ($p < 0.001$) on the error for the cadence and speed estimation. For the cadence, the differences between the smallest and largest median errors were 0.78 steps/min for trial conditions (Fig. 12.7a) and 0.48 steps/min for participant. For the speed, the differences between smallest and largest median errors were 0.15 m/s for trial condition (Fig. 12.7b), and 0.28 m/s for participant. The R^2 value for correlations between participant height, weight, and age and both cadence and speed were below 0.01.

Chapter 12. Direct Estimation of Walking Cadence and Speed

Condition	Median cadence [interquartile], steps/min			Median speed [interquartile], m/s		
	Reference	Wrist	Error	Reference	Wrist	Error
Normal	113.7 [110.1 118.8]	114.0 [110.3 118.9]	0.13 [-1.87 2.05]	1.49 [1.41 1.56]	1.45 [1.36 1.53]	-0.032 [-0.106 0.038]
Hands in pockets	113.4 [108.1 118.4]	113.2 [108.1 118.4]	-0.13 [-1.78 1.53]	1.45 [1.37 1.54]	1.48 [1.39 1.59]	0.043 [-0.036 0.135]
Noisy road	114.1 [108.8 119.2]	114.2 [109.1 119.2]	0.03 [-2.03 2.18]	1.49 [1.36 1.58]	1.44 [1.33 1.54]	-0.043 [-0.119 0.040]
Backpack	108.7 [103.6 112.9]	108.9 [103.8 113.3]	0.20 [-2.02 2.25]	1.33 [1.22 1.43]	1.36 [1.26 1.45]	0.035 [-0.055 0.130]
Uphill	109.1 [104.0 114.3]	109.4 [103.8 114.5]	0.11 [-2.02 2.25]	1.41 [1.30 1.50]	1.37 [1.27 1.46]	-0.037 [-0.112 0.044]
Downhill	114.1 [109.9 118.7]	114.5 [110.2 119.3]	0.31 [-1.99 2.73]	1.40 [1.28 1.49]	1.41 [1.34 1.48]	0.015 [-0.086 0.135]
Phone call	116.5 [112.1 120.6]	116.8 [112.5 121.1]	0.21 [-1.75 2.23]	1.50 [1.39 1.57]	1.44 [1.38 1.50]	-0.052 [-0.130 0.039]
Along field	111.9 [107.8 116.0]	112.1 [107.8 116.3]	0.09 [-1.99 2.14]	1.43 [1.33 1.52]	1.42 [1.34 1.49]	-0.011 [-0.097 0.077]
Slow	97.3 [88.6 103.4]	98.6 [90.7 104.7]	0.65 [-1.86 3.42]	1.03 [0.92 1.17]	1.08 [0.94 1.27]	0.044 [-0.034 0.135]
Normal with obstacles	111.4 [107.1 115.5]	112.1 [107.8 116.1]	0.22 [-1.86 2.52]	1.38 [1.26 1.47]	1.40 [1.31 1.48]	0.014 [-0.072 0.098]
Fast	127.1 [122.4 132.8]	127.0 [122.2 133.0]	-0.04 [-1.88 1.73]	1.84 [1.76 1.92]	1.74 [1.64 1.82]	-0.104 [-0.192 -0.018]
Carry bag	114.6 [110.1 120.4]	114.9 [110.0 120.3]	-0.03 [-2.04 1.96]	1.45 [1.30 1.56]	1.45 [1.36 1.58]	0.019 [-0.070 0.127]
Total	112.0 [106.3 117.9]	112.4 [106.5 118.2]	0.15 [-1.95 2.27]	1.42 [1.28 1.53]	1.41 [1.30 1.51]	-0.009 [-0.096 0.084]

Table 12.3 – Median and interquartile range for the parameter values and the instantaneous cadence and speed error (i.e. estimated at each gait cycle) of the wrist algorithm

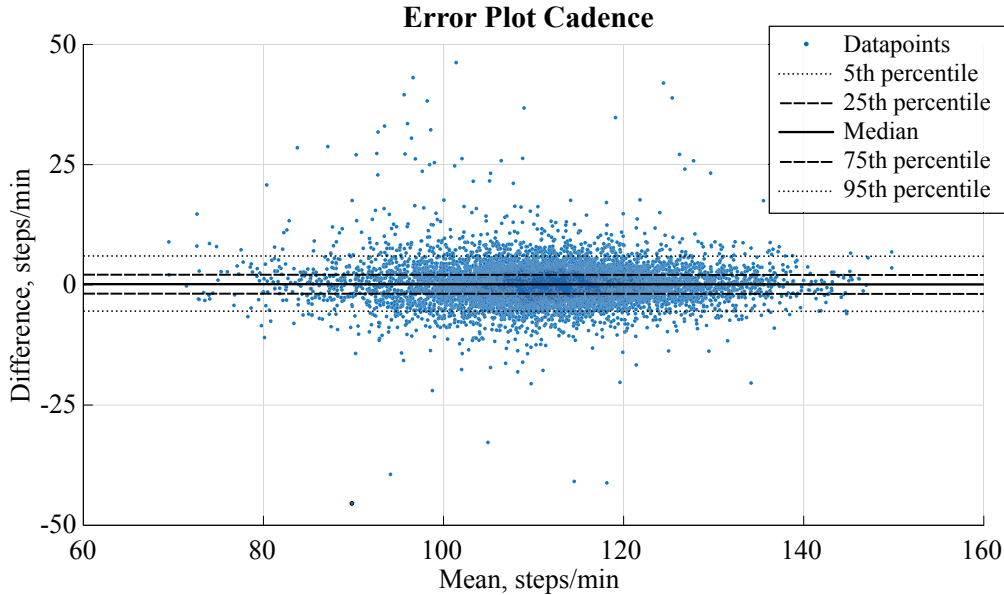
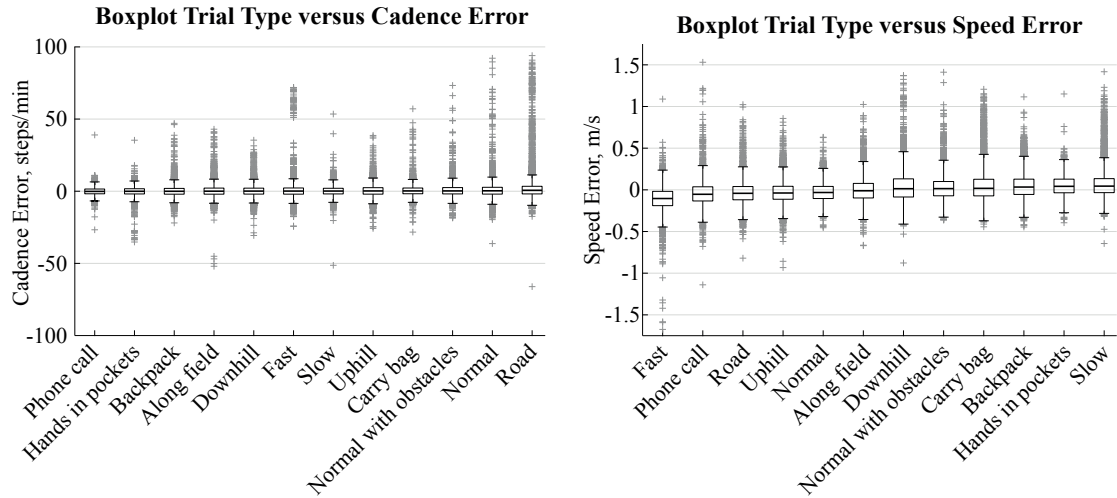


Figure 12.5 – Error plot for the instantaneous cadence. The 5th, 25th, median, 75th and 95th percentiles are -6.1, -2.4, -0.3, 1.8, and 6.0 steps/min, respectively.



Figure 12.6 – Error plot for the instantaneous speed estimate. The correlation adjusted 5th, 25th, median, 75th and 95th percentiles are -0.21, -0.10, -0.01, 0.08, and 0.25m/s, respectively.



(a) Boxplot with the trial condition listed versus the cadence error.

(b) Boxplot with the trial condition listed versus the speed error.

Figure 12.7 – Boxplots for the speed and cadence errors separated by trial types. For each boxplot the trials were ordered in increasing order of median error.

12.4 Discussion

In the present study a wrist sensor based system was proposed for estimating cadence and speed during over-ground walking on different surface, slope, constraints and environments.

The experimental protocol involved different situations of outdoor walking where the arm swing was strongly affected by the type of terrain, speed and daily tasks. In all conditions the norm of wrist acceleration showed to be robust enough to represent both stride and step frequency, though the presence of these frequencies was weak due to changing behavior of arm swing (e.g. hands in pockets, cellphone usage, carrying a bag). Thanks to the proposed cadence detection algorithm, cadence was estimated every second with a median error of -0.13% and the interquartile range of -2.04% – 1.72%. This range of error was close to the error of reference foot sensors which have a precision of 14 ms for the toe-off detection, resulting in approximately 1.4% precision for the cadence (Mariani et al., 2013). Compared to other studies the proposed algorithm performed similarly or better, even though the measurements were more challenging since the sensor was placed on the wrist and walking in outdoor environments and in real conditions added further variability to the data. Henriksen et al. (2004) reported a measurement error (defined as square root of the mean square error term of within-subject variability) of 1.65 steps/min applied to an accelerometer attached to the trunk and for straight indoor walking. For a similar setup but using force insoles to determine cadence, Macleod et al. (2014) found mean errors (standard deviation) of 0.52 steps/min (0.5 steps/min). The proposed system has a better accuracy but approximately half as good precision compared to these studies. The lower precision could be explained by the more challenging outdoor environment that led to more variable gait and walking independent wrist movements. Often participants changed their cadence abruptly, for example for avoiding obstacles or crossing roads. Compared to the reference system, the wrist algorithm was slower to react to those changes due to the averaging effect of the 10 second windows of the wrist algorithm, which could explain the outliers observed in Figs. 12.7a and 12.7b.

In the past, the trajectory of the foot has been used with lower limb attached inertial sensors to estimate the speed. When foot sensors were used, the reported mean error was 1.5% and the precision 5.8% for straight and curved indoor walking (Mariani et al., 2010). With shank and thigh sensors the precision was 0.06 m/s (6.7%) (Aminian et al., 2002). Other studies, based on either gait modeling, neural networks, or integration of accelerations, achieved significantly higher errors of up to 0.5 m/s (corresponding to 35% error at a comfortable walking speed of 1.4 m/s) (Yang and Li, 2012). While lower limb swing is the origin of walking, distance covered, and speed, there is no clear association between speed and arm movement: the person can walk without arm swing. This makes the speed estimation more challenging with a wrist sensor. Nevertheless, this issue affects the cadence estimation not as much, since even in the absence of arm swing, the wrists follow the movement of the trunk at each step. For speed estimation, we divided the parameter space in different clusters and generated a mapping model within each cluster. 16 clusters were selected as a trade-off between sufficient modeling of local non-linearity and over fitting. The clustering mapping model was able to estimate the speed with a median error of -0.67% and the interquartile range of -6.52% – 6.23%. For five participants the estimated walking speed had a positive or negative bias between 0.10 m/s and 0.15 m/s (maximum median error; interquartile range was -0.06 m/s – 0.05

ms/s). Therefore, for walking speed estimation, the proposed system had a performance comparable to the best results obtained in other studies using inertial sensors placed on the lower limbs. The speed error did also depend on the walking speed itself (Fig. 12.6) where fast speeds were underestimated and slow speeds were overestimated. This behavior could come from a biased training data set. Even though only a subset of all trial conditions was selected for training data, there were only two trials at low and high speeds. This data imbalance may have led to a biased estimation where the model fitted less well the low and high speed samples. On the other hand, adding dataset 2, even though it was comparatively small, allowed increasing robustness and precision especially for inclined walking. Different sampling of the training data set and providing means for compensating data imbalance could further reduce the algorithm's error (He and Garcia, 2009). The speed estimation error at lower speeds could also be associated with a decreased coordination between arms and legs at slower speeds (Meyns et al., 2013). Different models or model input parameters for slow speeds might further reduce this error.

Choosing the ideal reference system was challenging. The reference system needed to be portable and usable in-field. Therefore, GNSS and foot-worn inertial sensors were chosen. By placing the GNSS on the person's head and using a high-performance, portable antenna satellite, visibility was maximized. This allowed that on average 17-19 satellites were visible, maximizing the speed estimation precision. The foot-worn inertial sensors allowed detecting the toe-off events with a precision of 14 ms (Mariani et al., 2013) and was supposed to be currently the best available and validated algorithm. The alternative setup of measuring indoors on treadmill with a possibly better reference system could not be applied here since the goal of the project was to measure walking as naturally as possible using different surfaces, avoiding obstacles such as driving cars or other pedestrians, and crossing streets. Further, the barometric pressure sensor for inclined walking cannot be used on treadmill since the person's elevation does not change over time and several walking types such as walking with the hands in the pockets would cause safety issues on the treadmill.

Compared to the proposed algorithm, watches with integrated GNSS may provide more accurate and precise speed and distance estimates. However, as soon as the wearer is in a challenging environment where satellite signals do not pass easily or not at all such as in building, forests, canyons, cities or tunnels, the GNSS watches are not anymore able to measure the walking speed since the satellite signals are degraded or lost. Moreover, GNSS is a very power consuming technology and watches need to be recharged almost daily. The biggest advantage of the proposed wrist system is its high wearability and usability, its low power consumption, which does not require regular recharging, and its functionality in outdoor/indoor environments, offering a simple tool for ubiquitous monitoring. As accelerometer and barometer are low consumption components that are already integrated in many watches, the proposed algorithm can be easily used with many existing watches. The algorithm did not need any calibration; only the user's height needed to be known. The sensor axes did not need to be aligned with any anatomical axes.

Finally, the relatively low sampling rate required (20 Hz) and the short time-window of 6 seconds for feature extraction would allow applying the algorithm also on low-cost devices. The window size of 6 seconds was chosen as a trade-off between sufficient time resolution (quasi instantaneous) and sufficient data for the frequency analysis for estimating the cadence robustly. Decreasing the window size further would lead to a decreased robustness and performance for the cadence estimation.

Computing of quasi-instantaneous walking cadence and speed further allows analyzing cadence and speed distributions. Brodie et al. (2015) showed that elderly persons prone to falling have a different walking cadence distribution while having no significant difference for the mean cadence. They also reported a bi-modal cadence distribution in healthy persons where a person had a first mode at 88 steps/min and a second at 112 steps/min. A system able to quantify such distributions could therefore be a powerful tool for fitness assessment of elderly and could help identifying persons at risk for falling. If applied to large cohort studies it would allow relating cadence and speed distributions for example to gender, age, anthropometry and health. However, care has to be taken when applying the proposed algorithm to elderly or patients: both the cadence and speed estimation may not be valid for those groups since they may have altered gait (i.e. in elderly the relationship between cadence and speed are changed (Elble et al., 1991)). In patients, as for example for Parkinson's disease, the additional hand movement or very slow and irregular gait may mask the true walking cadence in the wrist movement. Thus, before applying the algorithm to a different population than young and healthy it should be tested for validity on the new populations.

In this study, it was assumed that the walking periods were known. Robust and automatic detection of walking periods based on the wrist sensor data was not part of this study. Further work is thus required in order to automatically detect walking periods in daily live and to distinguish arm movement caused by other activities (e.g. brushing teeth, cleaning dishes) from walking. A typical use case for the proposed system integrated in a watch could be, for example, that the person is actively starting and stopping the algorithm at the beginning and end of a walking period by pushing a button on the watch. The system could also be used as a motivation for more walking activities where goals could be set and progress monitored directly in real time on the watch.

In conclusion the proposed algorithm provided a powerful tool for estimating walking cadence and speed in one second intervals. The algorithm's performance was comparable to existing algorithms with sensors placed on the lower limbs or the trunk, despite that wrist movement was analyzed and that the walking took place outdoors in different and sometimes challenging environments. The presented algorithm did not provide means for automatic segmentation of the walking periods. Thus, in future developments, the algorithm should be extended to include an automatic detection of walking periods so that it could truly be used in real life. Thanks to the algorithm's robustness to sensor placement (e.g. the algorithm successfully and precisely estimates the cadence and speed if the sensor is moving similarly than the center of mass) it could also be integrated into smartphones.

Acknowledgements

This study was financed by the CTI Grant No 14787.1 PFNM-NM. The authors would like to thank all participants that agreed walking in various meteorological conditions ranging from cold to hot and from sun to light rain.

Conclusion Part V

13 General Discussion and Conclusion

13.1 Main contributions

The main aim of the thesis was to provide robust methods to correct orientation and position drift for in-field inertial sensor measurements. Although multiple methods to correct both orientation and position drift have been proposed in the past, they were mainly designed for clinical applications and short duration indoor measurements with low movement dynamics (e.g. gait analysis). Studies aiming at providing accurate and precise results for determining orientation or position in-field and with high movement dynamics (e.g. outdoor sports) provided unsatisfactory results. Thus, the thesis focused on correcting drift for in-field measurements on uneven surfaces and in unconstrained environments with potentially long measurement durations and high movement dynamics. Special attention was paid to provide easy-to-use methods that are applicable in-field. In the different chapters various strategies for correction of the drift were proposed and validated in-field. All strategies have in common that they exploit the biomechanical constraints of the activities and that they were specifically tailored to their respective movements.

The thesis was separated in three parts, each part focussing on a different aspect of drift reduction. In the first part static phases were used to correct the drift. A single inertial sensor fixed to the ski allowed to quantify the skiing movement of the diagonal stride in classical cross-country skiing. Orientation and speed drift was corrected during each push phase where the ski was motionless on the ground. The method was further extended to measure the skiing movement of ski mountaineering. In the second part several methods were designed to correct orientation and position drifts for dynamic motions with no motionless instants of time. The algorithms were designed for one of the most challenging sports to analyse: alpine ski racing. Athletes were equipped with a full-body setup: inertial sensors were fixed to their lower limbs, trunk, and head. To correct orientation drift we proposed the concept of joint drift correction. To correct position drift surveyed anchor points were fused with the inertial sensors. In the third part of this thesis a method was proposed to measure a person's walking speed and total

distance covered during long duration outdoor walking. Due to the constraints, i.e. single sensor location and modality (only accelerometer), this project did not allow to use any of the previously designed methods to correct drift. Instead, we proposed to directly estimate walking speed by finding a non-linear mapping between acceleration features of the wrist and walking speed.

13.1.1 Part 1 – Static drift correction

The main contribution of this part was an extension and improvement of the existing motionless drift correction methods for gait analysis to the diagonal stride classical cross-country skiing and ski mountaineering in order to analyse spatio-temporal cycle parameters. The existing methods could not directly be applied for measuring the diagonal stride for several reasons: 1) different movement phases: instead of a swing and stance phase as for walking, the stance and swing phases in the diagonal stride are separated by a gliding phase where the weight on the ski is gradually increased to 100% body weight while at the same time gliding forward. Moreover, the stance phase from walking where the foot lies motionless on the ground is altered to the thrust phase in diagonal stride and is significantly shortened to last less than 15% of a cycle (Nilsson et al., 2004). 2) steadily changing slope inclination: in contrast to clinical gait analysis on flat grounds the diagonal stride is performed uphill and at varying slope inclinations. Thus, during each thrust phase the ski and foot might be in a different inclination and their angle cannot be simply reset to zero degrees. 3) faster speeds: while walking speeds are generally below 6 km/h, top speeds in diagonal stride can exceed 20 km/h (Vähäsöyrinki et al., 2008). Similarly, for ski mountaineering, even though the movement closely resembles the diagonal stride, the phases are different, more closely related to walking with thrust phases lasting between 25% and 60% of a cycle depending on slope inclination and skiing speeds (Praz et al., 2016) and has almost no gliding phase.

In this thesis a measurement system was proposed and validated for a spatio-temporal analysis of the diagonal stride in classical cross country skiing and for ski mountaineering. More specifically, with the motionless and zero-velocity drift correction during each thrust phase the system allowed to:

- automatically align the inertial sensor axes with the ski axes,
- detect the temporal events and phases,
- estimate the slope inclination during each thrust phase,
- estimate the ski orientation for each sampled time instant,
- estimate the instantaneous and per-cycle average skiing speed,
- estimate the horizontal distance and elevation gain for each cycle.

The method used only a single ski-fixed inertial sensor for on-snow skiing and allowed any measurement duration.

13.1.2 Part 2 – Dynamic drift correction

The main contribution of this chapter was the design and validation of 3D drift correction methods for highly dynamic movements without motionless periods. Two methods were proposed: one to correct orientation drifts and the other one to correct position drifts. These methods were targeted at alpine ski racing and allowed to compute the athlete's 3D joint kinematics and his posture and CoM position in relative and absolute frames. Orientation drift was corrected based on the joint drift correction principle: accelerations recorded on two adjacent segments connected by a joint and translated to the joint centre must be equal. Any difference in acceleration orientation was then attributed to measurement errors caused by drift. Even though this idea exists since the 1970s (Morris, 1973), so far it has only been applied to two-dimensional analyses, in most cases limited to the sagittal plane for gait analysis. Moreover, most methods were limited to periods of low accelerations to estimate and correct drift. In this thesis methods were present that allow estimating joint drift in 3D and during periods of high accelerations and the presence of high noise. With the exception of inertial sensor and global navigation satellite system (GNSS) fusion for inertial navigation there are no other methods to correct speed or position drifts for human movement analysis during phases of non-zero or potentially unknown speed. We proposed a method to correct position drift (and therefore also speed drift) based on the fusion of the inertial data with surveyed anchor points. This approach allowed to obtain CoM position accuracies close to what could be obtained with differential GNSS even though the method was only based on inertial sensors and magnetometers.

In this thesis a measurement system was proposed and validated to provide a 3D kinematics analysis of alpine ski racing. More specifically, the joint drift correction and position drift correction allowed to compute:

- 3D joint angles of the knee, hip, and trunk,
- body model and 3D positions of the ankle, knee, hip, lumbar, cervical, shoulder, elbow, and wrist joint centres,
- athlete CoM kinematics (i.e. speed and position) in both a relative, body fixed, and absolute global frame,
- turn switch detection and gate crossing detection.

The method used inertial sensors fixed to the shanks, thighs, lower trunk, upper trunk, head, and optionally arms and wrists for on-snow alpine ski racing. Moreover an optimized functional calibration procedure was proposed to align the inertial sensor axes with the functional segment frames for the lower and upper limbs, trunk, and head. The movements were optimized so that they can be performed in-field with minimal effort and while wearing ski boots restricting ankle joint movement.

13.1.3 Part 3 – Direct speed estimation

The main contribution of this chapter was the design and validation of a method to detect and analyse locomotion periods during every-day living based on a single wrist-worn accelerometer. Existing methods for daily activity monitoring were based on one or multiple foot- or trunk-fixed inertial sensors. They were not practical for analysing the locomotion periods for every-day living and long-duration measurements. Additionally, most methods were designed for clinical gait analysis and activity detection methods were validated with prescribed movements in laboratory settings. We proposed a method which could reliably detect locomotion periods during prolonged over-ground walking in changing environments. Moreover, instantaneous walking cadence and speed were estimated. Since the project goals did not allow any calibration and targeted a low-power embedded implementation on smartwatches the method was designed to work at 20 Hz, quasi-real time, and with minimal computational requirements. Therefore, and since only a single accelerometer worn at the wrist could be used, it was not possible to implement any of the previously designed drift correction methods. Instead the method was based on a non-linear mapping between acceleration features and walking speed which allowed to directly obtain a drift-free speed estimation.

In this thesis a measurement system was proposed and validated to provide instantaneous walking cadence and speed for over-ground outdoor walking. More specifically the method allowed to

- detect locomotion periods,
- estimate walking cadence,
- estimate instantaneous walking speed.

The method was quasi-real-time with a single 3D accelerometer sampling at 20 Hz worn at the wrist and for long-duration walking in dynamically changing environments.

13.1.4 Current uses of the proposed systems and relevance for industry applications

In addition to the scientific contributions in form of published papers and conference presentations, a vast majority of the developments made in this thesis are now used in sports research, clinical research, training of athletes, and in industry.

- The system designed for the spatio-temporal analysis of ski mountaineering has been provided as an executable software to the SAC Swiss Ski Mountaineering Team to monitor their training efficiency and the athlete's performance improvements. The companies Gait Up and Pomoca adapted the algorithm to integrate it in their product Pomocup.

- The system designed for alpine ski racing analysis has been provided to the University of Salzburg who already used the system in multiple measurement campaigns for injury prevention.
- A simplified system for alpine ski racing analysis consisting of a single inertial measurement unit with included GNSS receiver is currently in use by Swiss-Ski for performance feedback purposes in alpine ski racing, snowboard cross, ski cross, and snowboard giant slalom. This system allows to estimate a skier's speed and synchronize it with video streams.
- The system designed for wrist locomotion analysis is being further improved in partnership with the Swiss watch industry and is also used in a cohort-based activity analysis on several thousand persons of the city of Lausanne (CoLaus).
- Two patent applications (EP3090684A1 and EP3090685A1) have been submitted for the wrist-based system.
- One patent application (WO2016174612A1) has been submitted for the simplified system for alpine ski racing analysis. Negotiations are also underway to include the system for gate crossing detection for improved spectator experience in the official time keeping of the FIS ski races.

13.2 Limitations

This thesis proposed multiple methods for estimating and correcting drift or for a direct estimation of speed for fast movements taking place in challenging and sometimes highly variable environments. It allowed to gain precious insights into the origins of drift and the inherent limitations of the current use of inertial sensors for movement analysis. The multiple in-field and in-lab validation measurements allowed to support the system's validity, but also helped to better point out its limitations.

13.2.1 Cross-country skiing and ski mountaineering

Both the cross-country skiing and ski mountaineering methods were validated indoors on treadmill. While the movements closely resemble on-snow skiing, small differences are observable. The biggest difference lying in the ski design: treadmill skiing is performed on roller skis and the floor-ski interactions are not exactly the same as for on-snow skiing. It is generally accepted that in treadmill skiing the skis provide a different gliding and breaking behaviour and require higher balancing capabilities from the athletes. Thus, the algorithm's performance on snow might be different than for treadmill roller skiing. Treadmill speeds were low to medium and the algorithm's performance for high speeds could not be assessed. Nevertheless, on-snow test measurements at different speeds showed that the signals were less affected by noise (unstable roller skis, vibrations of

the treadmill) even at higher speeds and that the events were clearer to define. The ski-mountaineering algorithm has been applied for on-snow measurements (Praz et al., 2016) and qualitatively no negative effects on algorithm performance were observed. Nevertheless, additional on-snow validation measurements on different snow conditions and at different speeds should be performed, for example against a differential GNSS. The proposed methods did not include an automatic technique (style) detection. For treadmill skiing the slope angles can be kept constant and chosen such that the athlete does not need to change techniques. However, especially for cross-country skiing, the technique used (i.e. diagonal stride, double poling, etc.) depends on both snow conditions and slope angles. Therefore, the athletes change technique often and cycles where the diagonal stride was used have to be detected prior to compute the spatio-temporal cycle parameters.

13.2.2 Alpine ski racing

Even though the proposed system considerably reduced the measurement setup complexity compared to 3D camera-based systems it can be used mainly for research purposes and still has some limitations for routine training. Although not time consuming, attaching the inertial sensors to the athletes, instructing the correct calibration movements, and data-segmentation during post-processing requires expert knowledge. However, depending on the selected parameters and required precision the system could be simplified by reducing the number of used sensors. The decrease in performance when removing sensors has not been assessed yet and needs further investigations.

Errors of the 3D joint angles showed an athlete-specific bias. Even though calibration movements were improved and tailored to skiing measurements the issue of zeroing joint angles during the calibration could not be solved. Nevertheless, and despite the higher movement dynamics, the observed errors were similar than what has been reported for gait analysis. To further improve the system's accuracy methods to reduce the athlete-specific joint angle bias should be found.

Soft tissue artefacts appeared to be particularly large for the skiing movements. In contrast to the studies who assessed marker-based soft tissue artefacts for clinical gait analysis based on average populations the magnitude of soft tissue artefacts is increased in alpine ski racing due to two factors: significantly larger muscle masses for athletes, especially for the thigh, higher muscle volume change during contraction, and important vibrations from the ski-snow interaction. Thus, resulting knee and hip angles in all three dimensions are likely to be affected by several degrees from soft tissue artefacts. Although joint angles were validated for all three dimensions (flexion/extension, abduction/adduction, and internal/external rotation) both the reference and our estimations for knee abduction/adduction and internal/external rotation should be interpreted carefully. These angles should therefore not be considered for precise analysis.

The proposed methods were validated based on slalom and giant slalom skiing. Performance of both orientation and position drift correction methods for faster disciplines

with less narrow turns like super-G or downhill might be different. For position drift correction super-G and downhill conditions were simulated and errors did only slightly increase. However, position drift might behave differently for real super-G and downhill runs and further investigations are necessary to confirm the simulation results. Moreover, gate crossings can only be detected if the athlete passes at distances of less than 1 m. In these speed disciplines athletes could be sometimes further away from the gates. Not all gate crossings may be detected and less anchor points could be available for drift correction. Thus, results should be inspected critically and carefully when measuring such disciplines. A solution for increasing the number of anchor points would be to use "anchor lines" by aligning several magnets in a line perpendicular to the skiing line. Since the magnets can be buried under the snow the magnets can be placed where the athlete is skiing over them without any safety risk. With this setup, the skier position can be expressed relative to these lines and used to correct the drift perpendicular to the lines. For the position drift correction a very basic Extended Kalman Smoother was used and the filter and smoother parameters were chosen empirically. It should be possible to further reduce position drift by applying a more appropriate Kalman smoother with automatically trained parameters, more states, and different measurement and state transfer functions which better take into account the origins of position drift.

Orientation drift was estimated deterministically based on the joint drift correction and motionless drift correction during static phases at the start and end of a run. There might be other, additional constraints that could be used for even more efficient orientation drift correction. For example, the magnetometer was only used for gate crossing detection but the recorded magnetic field outside areas of distortions created by the magnets placed at each gate could help to further reduce orientation drift. Moreover, orientation drift was corrected independently from position drift correction. However, as stated in the chapter state of the art (Chapter 2), a large part of speed and position drift is caused by incorrect gravity removal from errors in orientation estimation. Thus, speed and position drift information could also help to better estimate orientation drift. Combining all these information sources will probably need a different algorithm design with more complex fusion algorithms than currently used. Maybe a wisely designed Extended Kalman Smoother might be enough but probably other, more advanced, algorithms will be needed to obtain good results.

Finally, the algorithms were all non-causal. To correct both orientation and position drifts the data from the entire run needed to be available. Therefore, in its current form it could not be used for a real-time feedback. However, the system could be adapted to obtain feedbacks directly after each run. Using inertial sensors capable of downloading their data over Bluetooth the athlete could download the data from the previous run onto his smartphone where it could either be processed in-place or sent to the cloud. Results regarding performance analysis or load surveillance for injury prevention would then be available for the athlete and coach only a few seconds later.

13.2.3 Wrist locomotion detection and analysis

The proposed algorithm was able to reliably detect all locomotion periods during the validation measurements. However, these measurements did only focus on long-duration and outdoor walking activities with short breaks but where other activities were rarely present. Daily living activities (e.g. tooth brushing, vacuum cleaning, dish washing) where the wrist is moving with similar frequencies and amplitudes as during walking might be wrongly detected as locomotion periods. More complex analysis such as between-axis correlation analysis and time-correlations could help to better classify such movements as non-locomotion. Very short locomotion periods of less than 10 – 15 seconds might be missed by the algorithm and interpreted as noise or non-locomotion activities. Thus, the proposed version works very well for a scenario where a user could manually start and stop data recording and processing where breaks would be automatically detected and removed from analysis. Therefore, in future an algorithm for reliably detecting locomotion periods during daily living activities should be devised and validated.

The mapping used to estimate walking speed was found with machine learning techniques. The training group was a healthy group of active persons between 20 and 40 years. To estimate walking speed for other population groups (i.e. obese persons, elderly persons, disabled persons) the mapping might have different performance and would need to be adapted. Moreover, speed was only estimated for walking but not for running. For some persons a bias in speed estimation could also be observed. We hypothesize that these persons had a slightly different walking style that was not well represented by the mapping and a larger training set might be required to obtain more accurate results. A solution to these problems could be to personalize the algorithms. For example, the watch could be equipped with a GNSS module which measures walking speed from time to time and this additional information could be used to adapt the mapping to better match the person's walking characteristics.

13.3 Performance analysis and feedback

Even though this thesis' main topic is rather theoretical concerning different methods to correct drift, all developments were made to allow in-field measurements. The proposed methods for cross-country skiing, ski mountaineering and alpine ski racing could therefore also be used for performance analysis and feedback during regular trainings.

Several test measurements and in-field evaluations have already been conducted for all three sports. These measurements showed that the systems are suitable to use during trainings but development effort is now needed to simplify the systems and completely automatize the analysis. For cross-country skiing and ski mountaineering the system is already as simple as it could be: one single inertial sensor. Nevertheless, the analysis software should be extended by automatic detection of motion periods and techniques used. Extracted parameters are available as tables and simple graphs which is not really useful to coaches or athletes. They need to be presented in more appropriate forms and

should be combined with other parameters, for example to show the dependency of one parameter with respect to slope angle, time (e.g. fatigue), etc.

The alpine skiing system has been designed with the purpose of accurately measuring joint angles, body posture, and CoM kinematics for injury prevention and research-oriented performance analysis. A minimum of seven inertial sensors is needed for computing all these parameters. However, for a use in training, less parameters might be needed and the system could be simplified. Field tests showed that the trainers primarily want to know the skiing speed and would welcome a replacement of the current photocell-based time keeping by an easier-to-use systems such as the magnet-based gate crossing detection. For practical reasons, a single-sensor solution that does not need any calibration and allows a fully automatic data analysis is key. Efforts are currently underway to design such as system based on a single unit consisting of an inertial sensor, a magnetometer, and a GNSS receiver integrated in the lower-back part of the athlete's back protector. The protector additionally contains a high-precision GNSS antenna fixed at the level of the shoulder blades. For the moment this system is able to compute a skiing speed and detect the gate crossings. However, further developments are needed to estimate the skiing speed at the location of the athlete's CoM and also provide an accurate and precise CoM trajectory. CoM speed could for example be obtained similar to the pendulum approach proposed by Gilgien et al. (2015c) and machine-learning approaches could be used to estimate the athlete's posture at gate crossings in order to estimate his distance to the magnet so that an accurate CoM trajectory could be obtained.

13.4 Future developments

The various limitations cited above do all provide future research directions. In short, all methods were able to provide accurate and precise results, but there is clearly room for improvement. Some of the most interesting and promising future research directions are provided in this section. From the point of view of algorithm design, five major aspects could be further investigated: 1) drift correction, 2) soft tissue artefact reduction, 3) functional calibration, 4) integration of other sensor data, and 5) extension to other sports. Finally, from a sports science point of view the problem of data interpretation needs to be solved: with the current sensor technologies almost all aspects of movements can be measured. It is crucial to find smart ways to summarize the recorded data and present the results in an intuitive and interpretable manner.

13.4.1 Drift correction

In the proposed methods drift is modelled, estimated, and corrected in various frames, but never in the sensor frames directly where the true origin of drift lies. Therefore, the proposed methods could be adapted to directly model, estimate, and correct drift in the sensor frames. This would allow that individual sensor offsets, sensitivity, and axis

cross-talk get mapped non-linearly into other frames where they are then a combination of all these factors. Such a fusion scheme would also allow more easily to combine orientation and position drift correction where knowledge of incorrect gravity projection and removal could directly be attributed to the different sensor axes and represented in simpler ways. For example a speed drift in the horizontal plane indicates that sensor inclination may have been wrongly estimated. Through optimization an updated sensor inclination could be found which minimizes this speed drift. Finally, as hinted in Chapter 9 and in this thesis' state of the art (Chapter 2), based on the law of sine and cosine for gravity removal, orientation errors cause different speed drift behaviours along each axis. Thus, for movements with no accelerometer and gyroscope saturation, the behaviour of the estimated speed drift could also help to deduce orientation errors.

13.4.2 Soft tissue artefact reduction

As with the marker-based motion capture methods should be proposed to reduce soft tissue artefacts (STA). Especially sensors fixed to the thigh are prone to such artefacts. An inertial sensor cannot measure a position but measures precisely the acceleration and angular velocity at a given point of a segment. From marker-based STA research we know that for the same segment different locations are affected differently by STA and that STA can be decomposed into a rigid and non-rigid motion component (e.g. Andersen et al. (2012); Barré et al. (2015); Benoit et al. (2015); Camomilla et al. (2015); Dumas et al. (2014)). Models have been proposed to estimate the rigid motion component (Andersen et al., 2012; Camomilla et al., 2015; Dumas et al., 2014) and a study (Benoit et al., 2015) concluded that non-rigid motion components affect total STA little in comparison to the rigid motion component. The above cited studies also found that STA was highly activity- and subject-dependent.

Since inertial sensors can measure acceleration and angular velocity at specific locations of a segment this information could be used to estimate and correct both the rigid and non-rigid motion components. Part of the STA could already be corrected based on the proposed joint drift correction method. In this method the acceleration measured at the sensor is translated to the joint centre along a vector fixed with respect to the sensor. Thus, if the sensor is not moving exactly the same way as the underlying bone is moving due to the STA this vector does no longer point to the joint centre but next to it. Thus, the translated acceleration would no longer match the translated acceleration obtained from a sensor fixed to the adjacent segment. If we assume that STA is minimum on this adjacent segment (e.g. shank if we want to estimate STA at the thigh), this difference could then be used to correct STA. Thus, the high-frequency part of the estimated joint drift which we filtered out to obtain total orientation drift (Fig. 6.3 in Chapter 6) could be used to estimate STA. To further improve such STA estimation multiple sensors could be fixed at different locations on the segment. Joint drift could be estimated for each sensor as well as orientation error between each pair of sensors. Moreover, measured angular velocity must be the same for each sensor and differences must come from local

STA. Based on optimization algorithms all this information could be fused and STA could be at least partly estimated and corrected, leading to more accurate results.

13.4.3 Functional calibration

In order to obtain the best possible results the movements for the functional calibration should be executed with great care. Future efforts should be oriented towards eliminating functional calibrations, for example based on joint and segment motion constraints, similar to Taetz et al. (2016) or based on general movement constraints similar to what has been applied in this thesis for cross-country skiing and ski mountaineering. Methods should also be found to reduce the athlete-specific joint angle bias. This could maybe be achieved by different or additional, redundant, calibration movements (e.g. leg swing, trunk lateral bending) or with more advanced signal processing algorithms that can take into account potential inaccuracies and redundancies in the calibration movements.

13.4.4 Integration of other sensor data

The proposed systems are all entirely based on inertial sensors only. For alpine ski racing we have also shown methods to integrate absolute speed and position information obtained with low-cost or differential GNSS. Such a fusion could also be helpful for both the cross-country skiing and wrist methods. In cross-country skiing speed and position drifts could be further reduced with periodic position updates and the skier's trajectory could also be displayed in an absolute frame for better visualization and athlete feedback. For the wrist method a low-cost GNSS could be sporadically used in order to automatically fine-tune and personalize the initial, general, mapping between acceleration features and walking speed.

For the skiing applications (cross-country, mountaineering, and alpine) information about kinetics is currently missing. Such information could be useful for both performance analysis (e.g. is the poling force in the optimal direction?) and injury prevention (e.g. are the knee forces too high?). The proposed system could either be combined with existing force measurement systems or new systems could be designed.

Finally, a very promising sensory input could be barometric pressure. For example, in a recent Master project at the laboratory of movement analysis and measurement we demonstrated that such sensors could be used to estimate air drag. The relative pressure differences from multiple sensors fixed to the athletes was proportional to air drag. Linear mappings were used to successfully estimate total air drag based on these pressure differences and the athlete's posture. The project was based on measurements from a single athlete and numerical simulations. Future work would need to generalize the algorithm to multiple athletes and also evaluate its use for in-field measurements, for example for gliding tests.

13.4.5 Extensions to other sports

The methods were initially designed for the diagonal stride in classical cross-country skiing and for alpine ski racing. The work for ski mountaineering has shown that the proposed methods can be adapted to other, similar, sports without much effort. The diagonal stride method could be extended to the other classical cross-country skiing styles. Combined with the alpine skiing method it could also be applied to the skating techniques as demonstrated in the proof-of-concept paper in Fasel et al. (2016a).

Since the alpine skiing algorithm is largely constraint free (e.g. no joint motion constraints, no motionless constraints) and deals especially well with fast movements in all three dimensions it can be applied to almost any other movement. Depending on the movement dynamics certain thresholds for drift estimation might need to be adapted. Short in-lab tests showed that with slightly lower acceleration thresholds joint drift could be corrected during walking, stair-climbing, and stair-descent over several minutes without breaks. It could also be applied to the various other skiing and snowboarding disciplines such as, for example, freestyle, cross, moguls. The position drift correction could also be used to track athletes in environments where no or only reduced GNSS signal reception are present such as in forests for mountain bike races or hurdling where athletes also pass points (e.g. trees, hurdles) which could serve as anchor points. Since the algorithms don't have any joint motion constraints the system could also be used to track pathological gait with abnormal joint motions. In contrast, other systems where joint motions are optimized along certain axes to correct drift might not be applicable for such cases. Nevertheless, before applying the system to any other sports or activities it should be carefully validated.

13.4.6 Data visualization and interpretation

As already stated above, inertial sensors allow motion capture relatively easy and without the constraints imposed by traditional measurement systems such as 3D cameras. Thus, a wealth of data is provided and users of such systems also expect that inertial sensors could replace the traditional systems. Since inertial sensors cannot directly measure positions and orientations it is unlikely that they will ever be able to provide more accurate results than cameras and would actually replace cameras. For the moment, inertial sensors should be considered as an additional measurement system. Kinematics can be obtained from inertial sensors but they are more ideally suited also for other type of analyses, which can only be performed with considerable effort if other measurement systems are to be used. For example, inertial sensors are ideally suited to detect events, analyse movement variability or movement asymmetries. Together with the "approximately correct" kinematics the main difficulty now lies in the efficient and intuitive way of data presentation. Key questions that still need to be answered are: How can I represent the data efficiently? Based on the data, what feedback should I give to athletes? What can I do not to get lost in the amount of data and focus on the relevant data only?

These questions should be answered in close collaboration with coaches. Constant efforts from both sides are required so that we, as scientists, can understand the challenges of coaching and that coaches can also understand the challenges of science.

13.5 The End

The combination of metrology with engineering allowed to propose novel methods for inertial sensor-based motion capture. The developments made in this thesis allow a more accurate measurement of a person's motion in winter sports or for daily living and demonstrated that innovative and targeted algorithms can efficiently reduce drift in multiple and challenging environments. The proposed systems are applicable in-field and can now be used to gain further insights in performance analysis and injury prevention.

Bibliography

- P. Abraham, B. Noury-Desvaux, M. Gernigon, G. Mahé, T. Sauvaget, G. Leftheriotis, and A. Le Faucheur. The inter- and intra-unit variability of a low-cost GPS data logger/receiver to study human outdoor walking in view of health and clinical studies. *PloS one*, 7(2):e31338, 2012. doi:10.1371/journal.pone.0031338.
- C. M. el Achkar, C. Lenoble-Hoskovec, A. Paraschiv-Ionescu, K. Major, C. Büla, and K. Aminian. Instrumented shoes for activity classification in the elderly. *Gait & Posture*, 44:12–17, 2016. doi:10.1016/j.gaitpost.2015.10.016.
- R. Adelsberger, S. Aufdenblatten, M. Gilgien, and G. Tröster. On bending characteristics of skis in use. *Procedia Engineering*, 72:362–367, 2014. doi:10.1016/j.proeng.2014.06.063.
- P. Aggarwal, Z. Syed, X. Niu, and N. El-Sheimy. A Standard Testing and Calibration Procedure for Low Cost MEMS Inertial Sensors and Units. *Journal of Navigation*, 61(2008):323–336, 2008. doi:10.1017/S0373463307004560.
- T. Ahola. Pedometer for Running Activity Using Accelerometer Sensors on the Wrist. *Medical Equipment Insights*, page 1, 2010. doi:10.4137/MEI.S3748.
- M. Alaqtash, H. Yu, R. Brower, A. Abdelgawad, and T. Sarkodie-Gyan. Application of wearable sensors for human gait analysis using fuzzy computational algorithm. *Engineering Applications of Artificial Intelligence*, 24(6):1018–1025, 2011. doi:10.1016/j.engappai.2011.04.010.
- K. Aminian. Human movement capture and their clinical applications. In R. K. Begg and M. Palaniswami, eds., *Computational Intelligence for Movement Sciences: Neural Networks, Support Vector Machines and other Emerging Techniques*, chapter 3, pages 101–138. Idea Group Inc., USA, 2006.
- K. Aminian, B. Najafi, C. Büla, P.-F. Leyvraz, and P. Robert. Spatio-temporal parameters of gait measured by an ambulatory system using miniature gyroscopes. *Journal of biomechanics*, 35(5):689–99, 2002.
- R. Anacleto, L. Figueiredo, A. Almeida, and P. Novais. Localization system for pedestrians based on sensor and information fusion. *17th International Conference on Information Fusion (FUSION). IEEE. 2014*, page 8, 2014.

Bibliography

- M. S. Andersen, M. Damsgaard, J. Rasmussen, D. K. Ramsey, and D. L. Benoit. A linear soft tissue artefact model for human movement analysis: Proof of concept using in vivo data. *Gait & Posture*, 35(4):606–611, 2012. doi:10.1016/j.gaitpost.2011.11.032.
- E. Andersson, B. Pellegrini, Ø. Sandbakk, T. Stüggli, and H.-C. Holmberg. The effects of skiing velocity on mechanical aspects of diagonal cross-country skiing. *Sports Biomechanics*, 13(3):267–284, 2014. doi:10.1080/14763141.2014.921236.
- R. Bahr, S. O. Andersen, S. Løken, B. Fossan, T. Hansen, and I. Holme. Low back pain among endurance athletes with and without specific back loading—a cross-sectional survey of cross-country skiers, rowers, orienteers, and nonathletic controls. *Spine*, 29(4):449–54, 2004.
- R. Bahr and T. Krosshaug. Understanding injury mechanisms: a key component of preventing injuries in sport. *British journal of sports medicine*, 39(6):324–9, 2005. doi:10.1136/bjsm.2005.018341.
- R. Baker. Gait analysis methods in rehabilitation. *Journal of neuroengineering and rehabilitation*, 3:4, 2006. doi:10.1186/1743-0003-3-4.
- T. M. Barbosa, R. J. Fernandes, K. L. Keskinen, and J. P. Vilas-Boas. The influence of stroke mechanics into energy cost of elite swimmers. *European Journal of Applied Physiology*, 103(2):139–149, 2008. doi:10.1007/s00421-008-0676-z.
- A. Barré, B. M. Jolles, N. Theumann, and K. Aminian. Soft tissue artifact distribution on lower limbs during treadmill gait: Influence of skin markers’ location on cluster design. *Journal of Biomechanics*, 48(10):1965–1971, 2015. doi:10.1016/j.jbiomech.2015.04.007.
- R. Bartlett and M. Bussey. *Sports Biomechanics: Reducing Injury Risk and Improving Sports Performance*. Routledge, 2, revised edition, 2013. ISBN 9781135282257.
- D. Benoit, M. Damsgaard, and M. Andersen. Surface marker cluster translation, rotation, scaling and deformation: Their contribution to soft tissue artefact and impact on knee joint kinematics. *Journal of Biomechanics*, 48(10):2124–2129, 2015. doi:10.1016/j.jbiomech.2015.02.050.
- H. E. Berg, O. Eiken, and P. A. Tesch. Involvement of eccentric muscle actions in giant slalom racing. *Medicine and science in sports and exercise*, 27(12):1666–1670, 1995.
- E. Bergamini, G. Ligorio, A. Summa, G. Vannozzi, A. Cappozzo, and A. M. Sabatini. Estimating orientation using magnetic and inertial sensors and different sensor fusion approaches: Accuracy assessment in manual and locomotion tasks. *Sensors (Switzerland)*, 14(10):18625–18649, 2014. doi:10.3390/s141018625.
- E. Bergamini, P. Picerno, H. Pillet, F. Natta, P. Thoreux, and V. Camomilla. Estimation of temporal parameters during sprint running using a trunk-mounted inertial measurement unit. *Journal of biomechanics*, 45(6):1123–6, 2012. doi:10.1016/j.jbiomech.2011.12.020.

- B. Bilodeau, M. R. Boulay, and B. Roy. Propulsive and gliding phases in four cross-country skiing techniques. *Medicine and science in sports and exercise*, 24(8):917–25, 1992.
- B. Bilodeau, K. W. Rundell, B. Roy, and M. R. Boulay. Kinematics of cross-country ski racing. *Medicine and science in sports and exercise*, 28(1):128–38, 1996.
- J. Bland and D. Altman. Agreement between methods of measurement with multiple observations per individual. *Journal of Pharmaceutical Statistics*, 17(4):571–582, 2007. doi:10.1080/10543400701329422.
- J. M. Bland and D. G. Altman. Measuring agreement in method comparison studies. *Statistical methods in medical research*, 8(2):135–60, 1999.
- T. Blumenbach. High Precision Kinematic GPS Positioning Of Ski Jumpers. In *Proceedings of the 17th International Technical Meeting of the Satellite Division of The Institute of Navigation (ION GNSS 2004)*, pages 761–765. Long Beach, CA, 2004.
- P. Bonato. Advances in wearable technology and applications in physical medicine and rehabilitation. *Journal of NeuroEngineering and Rehabilitation*, 2(2), 2005. doi:10.1186/1743-0003-2-2.
- S. Bonnet, C. Bassompierre, C. Godin, S. Lesecq, and A. Barraud. Calibration methods for inertial and magnetic sensors. *Sensors and Actuators A: Physical*, 156:302–311, 2009. doi:10.1016/j.sna.2009.10.008.
- V. Bonnet, C. Mazzà, J. McCamley, and A. Cappozzo. Use of weighted Fourier linear combiner filters to estimate lower trunk 3D orientation from gyroscope sensors data. *Journal of neuroengineering and rehabilitation*, 10(29):29, 2013. doi:10.1186/1743-0003-10-29.
- N. A. Borghese, L. Bianchi, and F. Lacquaniti. Kinematic determinants of human locomotion. *The Journal of physiology*, 494(3):863–79, 1996.
- K. A. Boyer, T. P. Andriacchi, and G. S. Beaupre. The role of physical activity in changes in walking mechanics with age. *Gait & Posture*, 36(1):149–153, 2012. doi:10.1016/j.gaitpost.2012.02.007.
- R. A. Brand. Can Biomechanics Contribute to Clinical Orthopaedic Assessments? *Iowa Orthopaedic Journal*, 9:61–64, 1989.
- A. Brennan, K. Deluzio, and Q. Li. Assessment of anatomical frame variation effect on joint angles: A linear perturbation approach. *Journal of Biomechanics*, 44(16):2838–2842, 2011. doi:10.1016/j.jbiomech.2011.09.006.
- M. Brodie, S. Lord, M. Coppens, J. Annegarn, and K. Delbaere. Eight weeks remote monitoring using a freely worn device reveals unstable gait patterns in older fallers. *IEEE Transactions on Biomedical Engineering*, 9294(c):1–1, 2015. doi:10.1109/TBME.2015.2433935.

Bibliography

- M. Brodie, A. Walmsley, and W. Page. Fusion motion capture: a prototype system using inertial measurement units and GPS for the biomechanical analysis of ski racing. *Sports Technology*, 1(1):17–28, 2008. doi:10.1002/jst.6.
- N. F. Butte, U. Ekelund, and K. R. Westerterp. Assessing physical activity using wearable monitors: measures of physical activity. *Medicine and science in sports and exercise*, 44(1 Suppl 1):S5–12, 2012. doi:10.1249/MSS.0b013e3182399c0e.
- V. Camomilla, T. Bonci, R. Dumas, L. Chèze, and a. Cappozzo. A model of the soft tissue artefact rigid component. *Journal of Biomechanics*, 48(10):1752–1759, 2015. doi:10.1016/j.jbiomech.2015.05.007.
- A. Cappello, A. Cappozzo, P. F. La Palombara, L. Lucchetti, and A. Leardini. Multiple anatomical landmark calibration for optimal bone pose estimation. *Human Movement Science*, 16:259–274, 1997. doi:10.1016/S0167-9457(96)00055-3.
- A. Cappozzo, U. Della Croce, A. Leardini, and L. Chiari. Human movement analysis using stereophotogrammetry Part 1 : theoretical background. *Gait and Posture*, 21(2):186–196, 2005. doi:10.1016/j.gaitpost.2004.01.010.
- Y. Cedervall, K. Halvorsen, and A. C. Åberg. A longitudinal study of gait function and characteristics of gait disturbance in individuals with Alzheimer’s disease. *Gait & Posture*, 39(4):1022–1027, 2014. doi:10.1016/j.gaitpost.2013.12.026.
- J. Chardonens. *In-field objective evaluation and analysis in ski jumping using interial sensors*. Ph.D. thesis, Ecole Polytechnique Fédérale de Lausanne, 2012.
- J. Chardonens, J. Favre, F. Cuendet, G. Gremion, and K. Aminian. A system to measure the kinematics during the entire ski jump sequence using inertial sensors. *Journal of biomechanics*, 46(1):56–62, 2013. doi:10.1016/j.jbiomech.2012.10.005.
- J. Chardonens, J. Favre, F. Cuendet, G. Gremion, and K. Aminian. Measurement of the dynamics in ski jumping using a wearable inertial sensor-based system. *Journal of sports sciences*, 32(6):591–600, 2014. doi:10.1080/02640414.2013.845679.
- J. Chardonens, J. Favre, B. Le Callennec, F. Cuendet, G. Gremion, and K. Aminian. Automatic measurement of key ski jumping phases and temporal events with a wearable system. *Journal of sports sciences*, 30(1):53–61, 2012. doi:10.1080/02640414.2011.624538.
- F. Cignetti, F. Schena, and a. Rouard. Effects of fatigue on inter-cycle variability in cross-country skiing. *Journal of biomechanics*, 42(10):1452–9, 2009. doi:10.1016/j.jbiomech.2009.04.012.
- J. Cohen. *Statistical power analysis for the behavioral sciences*. Lawrence Erlbaum Associates, 2 edition, 1988. ISBN 0-8058-0283-5.

- G. Cooper, I. Sheret, L. McMillan, L. McMillian, K. Siliverdis, N. Sha, D. Hodgins, L. Kenney, and D. Howard. Inertial sensor-based knee flexion/extension angle estimation. *Journal of biomechanics*, 42(16):2678–85, 2009. doi:10.1016/j.jbiomech.2009.08.004.
- F. Dadashi, F. Crettenand, G. Millet, L. Seiffert, J. Komar, and K. Aminian. Automatic front-crawl temporal phase detection using adaptive filtering of inertial signals. *Journal of sports sciences*, 2013a.
- F. Dadashi, F. Crettenand, G. P. Millet, and K. Aminian. Front-crawl instantaneous velocity estimation using a wearable inertial measurement unit. *Sensors (Basel, Switzerland)*, 12(10):12927–39, 2012. doi:10.3390/s121012927.
- F. Dadashi, G. Millet, and K. Aminian. Gaussian process framework for pervasive estimation of swimming velocity with body-worn IMU. *Electronics Letters*, 49(1):44–45, 2013b. doi:10.1049/el.2012.3684.
- G. Dalleau, a. Belli, M. Bourdin, and J. R. Lacour. The spring-mass model and the energy cost of treadmill running. *European journal of applied physiology and occupational physiology*, 77(3):257–263, 1998. doi:10.1007/s004210050330.
- H. Dejnabadi, B. M. Jolles, E. Casanova, P. Fua, and K. Aminian. Estimation and visualization of sagittal kinematics of lower limbs orientation using body-fixed sensors. *IEEE transactions on bio-medical engineering*, 53(7):1385–93, 2006. doi:10.1109/TBME.2006.873678.
- U. Della Croce, A. Cappozzo, and D. C. Kerrigan. Pelvis and lower limb anatomical landmark calibration precision and its propagation to bone geometry and joint angles. *Medical & biological engineering & computing*, 37(2):155–161, 1999. doi:10.1007/BF02513282.
- A. V. Dowling, J. Favre, and T. P. Andriacchi. A wearable system to assess risk for anterior cruciate ligament injury during jump landing: measurements of temporal events, jump height, and sagittal plane kinematics. *Journal of biomechanical engineering*, 133(7):071008, 2011. doi:10.1115/1.4004413.
- A. V. Dowling, J. Favre, and T. P. Andriacchi. Inertial sensor-based feedback can reduce key risk metrics for anterior cruciate ligament injury during jump landings. *The American journal of sports medicine*, 40(5):1075–83, 2012. doi:10.1177/0363546512437529.
- V. Drenk. Bildmessverfahren für schwenk- und neigbare sowie in der Brennweite variierbare Kameras. *Schriftenreihe zur Angewandten Trainingswissenschaft*, 1:130 – 142, 1994.
- C. Duc, P. Salvia, A. Lubansu, V. Feipel, and K. Aminian. A wearable inertial system to assess the cervical spine mobility: Comparison with an optoelectronic-based motion capture evaluation. *Medical Engineering and Physics*, 36(1):49–56, 2014. doi:10.1016/j.medengphy.2013.09.002.

Bibliography

- S. Duc, J. Cassirame, and F. Durand. Physiology of ski mountaineering racing. *International journal of sports medicine*, 32(11):856–63, 2011. doi:10.1055/s-0031-1279721.
- R. Dumas, V. Camomilla, T. Bonci, L. Cheze, and A. Cappozzo. Generalized mathematical representation of the soft tissue artefact. *Journal of Biomechanics*, 47(2):476–481, 2014. doi:10.1016/j.jbiomech.2013.10.034.
- R. Dumas, L. Chèze, and J.-P. Verriest. Adjustments to McConville et al. and Young et al. body segment inertial parameters. *Journal of biomechanics*, 40(3):543–53, 2007. doi:10.1016/j.jbiomech.2006.02.013.
- M. H. A. Eames, A. Cosgrove, and R. Baker. Comparing methods of estimating the total body centre of mass in three-dimensions in normal and pathological gaits. *Human Movement Science*, 18(5):637–646, 1999. doi:10.1016/S0167-9457(99)00022-6.
- F. El-Amrawy and M. I. Nounou. Are currently available wearable devices for activity tracking and heart rate monitoring accurate, precise, and medically beneficial? *Healthcare Informatics Research*, 21(4):315–320, 2015. doi:10.4258/hir.2015.21.4.315.
- R. J. Elble, S. S. Thomas, C. Higgins, and J. Colliver. Stride-dependent changes in gait of older people. *Journal of Neurology*, 238(1):1–5, 1991. doi:10.1007/BF00319700.
- M. Elhoushi, J. Georgy, A. Noureldin, and M. J. Korenberg. Motion Mode Recognition for Indoor Pedestrian Navigation Using Portable Devices. *IEEE Transactions on Instrumentation and Measurement*, 65(1):208–221, 2016. doi:10.1109/TIM.2015.2477159.
- P. Esser, H. Dawes, J. Collett, and K. Howells. IMU: Inertial sensing of vertical CoM movement. *Journal of Biomechanics*, 42(10):1578–1581, 2009. doi:10.1016/j.jbiomech.2009.03.049.
- B. Fasel, C. Duc, F. Dadashi, F. Bardyn, M. Savary, P.-A. Farine, and K. Aminian. A wrist sensor and algorithm to determine instantaneous walking cadence and speed in daily life walking. *Medical & Biological Engineering & Computing*, 2017a. doi:10.1007/s11517-017-1621-2.
- B. Fasel, J. Favre, J. Chardonens, G. Gremion, and K. Aminian. An inertial sensor-based system for spatio-temporal analysis in classic cross-country skiing diagonal technique. *Journal of Biomechanics*, 48(12):3199–3205, 2015a. doi:10.1016/j.jbiomech.2015.07.001.
- B. Fasel, C. Göpfert, W. Rapp, S. J. Lindinger, and K. Aminian. Validation of relative CoM displacement in V2 skating obtained with inertial sensors - a feasibility study. In *Abstract Book of the 7th International congress on science and skiing*. 2016a.
- B. Fasel, C. Lehot, J. Spörri, E. Müller, and K. Aminian. Body vibration and its transmission in alpine ski racing. In *XIV International Symposium on 3D Analysis of Human Movement*. 2016b.

- B. Fasel, C. Praz, B. Kayser, and K. Aminian. Measuring spatio-temporal parameters of uphill ski-mountaineering with ski-fixed inertial sensors. *Journal of Biomechanics*, 49(13):3052–3055, 2016c. doi:10.1016/j.jbiomech.2016.06.017.
- B. Fasel, J. Spörri, and K. Aminian. Improving the accuracy of low-cost GNSS by fusion with inertial and magnetic sensors in alpine ski racing. In *34th International Conference on Biomechanics in Sports*. Tsukuba, 2016d.
- B. Fasel, J. Spörri, J. Chardonens, M. Gilgien, J. Kröll, E. Müller, and K. Aminian. 3D measurement of lower limb kinematics in alpine ski racing using inertial sensors. In *International congress on science and skiing 2013*. 2013.
- B. Fasel, J. Spörri, J. Chardonens, J. Kröll, E. Müller, and K. Aminian. Joint Inertial Sensor Orientation Drift Reduction for Highly Dynamic Movements. *IEEE Journal of Biomedical and Health Informatics*, 2017b. doi:10.1109/JBHI.2017.2659758.
- B. Fasel, J. Spörri, M. Gilgien, G. Boffi, J. Chardonens, E. Müller, and K. Aminian. Three-Dimensional Body and Centre of Mass Kinematics in Alpine Ski Racing Using Differential GNSS and Inertial Sensors. *Remote Sensing*, 8(671), 2016e. doi:10.3390/rs8080671.
- B. Fasel, J. Spörri, M. Gilgien, N. Gerber, M. Falbriard, E. Müller, and K. Aminian. IMU and GNSS-based turn switch detection in alpine ski racing. In *Abstract Book of the 7th International congress on science and skiing*. 2016f.
- B. Fasel, J. Spörri, J. Kröll, and K. Aminian. Alpine ski racing gate crossing detection using magnetometers. In *Abstract Book of the 7th International congress on science and skiing*. 2016g.
- B. Fasel, J. Spörri, J. Kröll, E. Müller, and K. Aminian. Using inertial sensors for reconstructing 3D full-body movement in sports - possibilities and limitations on the example of alpine ski racing. In *International Conference on Biomechanics in Sports 2015*. 2015b.
- J. Favre, R. Aissaoui, B. M. Jolles, J. A. de Guise, and K. Aminian. Functional calibration procedure for 3D knee joint angle description using inertial sensors. *Journal of biomechanics*, 42(14):2330–5, 2009. doi:10.1016/j.jbiomech.2009.06.025.
- J. Favre, B. Jolles, O. Siegrist, and K. Aminian. Quaternion-based fusion of gyroscopes and accelerometers to improve 3D angle measurement. *Electronics Letters*, 42(11):612, 2006. doi:10.1049/el:20060124.
- J. Favre, B. M. Jolles, R. Aissaoui, and K. Aminian. Ambulatory measurement of 3D knee joint angle. *Journal of biomechanics*, 41(5):1029–35, 2008. doi:10.1016/j.jbiomech.2007.12.003.

Bibliography

- P. Federolf, P. Scheiber, E. Rauscher, H. Schwameder, A. Lüthi, H. U. Rhyner, and E. Müller. Impact of skier actions on the gliding times in alpine skiing. *Scandinavian Journal of Medicine and Science in Sports*, 18(6):790–797, 2008. doi:10.1111/j.1600-0838.2007.00745.x.
- P. Federolf, V. von Tscharnern, D. Häufle, B. Nigg, M. Gimpl, and E. Müller. Vibration exposure in alpine skiing and consequences for muscle activation levels. In E. Müller, S. Lindinger, and T. Stöggl, eds., *Science and Skiing IV*, pages 19–25. Meyer & Meyer Sport (UK), 2009. ISBN 978-1-84126-255-0.
- P. A. Federolf. Quantifying instantaneous performance in alpine ski racing. *Journal of sports sciences*, 30(10):1063–8, 2012. doi:10.1080/02640414.2012.690073.
- R. a. Ferguson. Limitations to performance during alpine skiing. *Experimental physiology*, 95(3):404–10, 2010. doi:10.1113/expphysiol.2009.047563.
- F. Ferraris, U. Grimaldi, and M. Parvis. Procedure for effortless in-field calibration of three-axis rate gyros and accelerometers. *Sensors and Materials*, 7(5):311–30, 1995.
- C. Finch. A new framework for research leading to sports injury prevention. *Journal of Science and Medicine in Sport*, 9(1-2):3–9, 2006. doi:10.1016/j.jsams.2006.02.009.
- T. W. Flørenes, T. Bere, L. Nordsletten, S. Heir, and R. Bahr. Injuries among male and female World Cup alpine skiers. *British journal of sports medicine*, 43(13):973–8, 2009. doi:10.1136/bjsm.2009.068759.
- E. Foxlin. Pedestrian tracking with shoe-mounted inertial sensors. *IEEE Computer Graphics and Applications*, 25(6):38–46, 2005. doi:10.1109/MCG.2005.140.
- G. D. Fulk, S. A. Combs, K. A. Danks, C. D. Nirider, B. Raja, and D. S. Reisman. Accuracy of 2 Activity Monitors in Detecting Steps in People With Stroke and Traumatic Brain Injury. *Physical Therapy*, 94(2):222–229, 2014. doi:10.2522/ptj.20120525.
- E. P. Furlani. *Permanent magnet and electromechanical devices : materials, analysis, and applications*. Academic, 2001. ISBN 9780122699511.
- M. Gietzelt, S. Schnabel, K.-H. Wolf, F. Büsching, B. Song, S. Rust, and M. Marschollek. A method to align the coordinate system of accelerometers to the axes of a human body: The depitch algorithm. *Computer methods and programs in biomedicine*, 106(2):97–103, 2012. doi:10.1016/j.cmpb.2011.10.014.
- M. Gietzelt, K. H. Wolf, M. Marschollek, and R. Haux. Performance comparison of accelerometer calibration algorithms based on 3D-ellipsoid fitting methods. *Computer Methods and Programs in Biomedicine*, 111(1):62–71, 2013. doi:10.1016/j.cmpb.2013.03.006.

- M. Gilgien, P. Crivelli, J. Spörri, J. Kröll, and E. Müller. Characterization of Course and Terrain and Their Effect on Skier Speed in World Cup Alpine Ski Racing. *PLOS ONE*, 10(3):e0118119, 2015a. doi:10.1371/journal.pone.0118119.
- M. Gilgien, P. Crivelli, J. Spörri, J. Kröll, and E. Müller. Correction: Characterization of Course and Terrain and Their Effect on Skier Speed in World Cup Alpine Ski Racing. *PLOS ONE*, 10(5):e0128899, 2015b. doi:10.1371/journal.pone.0128899.
- M. Gilgien, J. Spörri, J. Chardonens, J. Kröll, P. Limpach, and E. Müller. Determination of the centre of mass kinematics in alpine skiing using differential global navigation satellite systems. *Journal of Sports Sciences*, 33(9):960–969, 2015c. doi:10.1080/02640414.2014.977934.
- M. Gilgien, J. Spörri, J. Chardonens, J. Kröll, and E. Müller. Determination of external forces in alpine skiing using a differential global navigation satellite system. *Sensors (Basel, Switzerland)*, 13(8):9821–35, 2013. doi:10.3390/s130809821.
- M. Gilgien, J. Spörri, J. Kröll, P. Crivelli, and E. Müller. Mechanics of turning and jumping and skier speed are associated with injury risk in men’s World Cup alpine skiing: a comparison between the competition disciplines. *British journal of sports medicine*, 48(9):742–7, 2014a. doi:10.1136/bjsports-2013-092994.
- M. Gilgien, J. Spörri, J. Kröll, and E. Müller. Effect of ski geometry and standing height on kinetic energy: equipment designed to reduce risk of severe traumatic injuries in alpine downhill ski racing. *British Journal of Sports Medicine*, 50(1):8–13, 2016. doi:10.1136/bjsports-2015-095465.
- M. Gilgien, J. Spörri, P. Limpach, A. Geiger, and E. Müller. The effect of different Global Navigation Satellite System methods on positioning accuracy in elite alpine skiing. *Sensors (Basel, Switzerland)*, 14(10):18433–53, 2014b. doi:10.3390/s141018433.
- S. Godha, G. Lachapelle, and M. Cannon. Integrated GPS/INS System for Pedestrian Navigation in a Signal Degraded Environment. In *Proceedings of the 19th International Technical Meeting of the Satellite Division of The Institute of Navigation (ION GNSS 2006)*, September, pages 2151 – 2164. 2006.
- C. M. Gosling, B. J. Gabbe, and A. B. Forbes. Triathlon related musculoskeletal injuries: The status of injury prevention knowledge. *Journal of Science and Medicine in Sport*, 11(4):396–406, 2008. doi:10.1016/j.jsams.2007.07.009.
- D. Gouwanda and S. M. N. A. Senanayake. Emerging trends of body-mounted sensors in sports and human gait analysis. *IFMBE Proceedings*, 21 IFMBE(1):715–718, 2008. doi:10.1007/978-3-540-69139-6-178.
- R. Gray and D. Neuhoff. Quantization. *IEEE Transactions on Information Theory*, 44(6):2325–2383, 1998. doi:10.1109/18.720541.

Bibliography

- M. Grewal and A. Andrews. How good is your gyro: Ask the experts. *IEEE Control Systems Magazine*, 30(1):12–15, 2010a. doi:10.1109/MCS.2009.935122.
- M. S. Grewal and A. P. Andrews. Applications of Kalman filtering in aerospace 1960 to the present. *IEEE Control Systems Magazine*, 30(3):69–78, 2010b. doi:10.1109/MCS.2010.936465.
- M. S. Grewal, A. P. Andrews, and C. G. Bartone. *Global Navigation Satellite Systems, Inertial Navigation, and Integration*. John Wiley & Sons, 3 edition, 2013. ISBN 9781118523506.
- E. S. Grood and W. J. Suntay. A joint coordinate system for the clinical description of three-dimensional motions: application to the knee. *Journal of biomechanical engineering*, 105(2):136–44, 1983.
- B. Haaland, S. E. Steenstrup, T. Bere, R. Bahr, and L. Nordsletten. Injury rate and injury patterns in FIS World Cup Alpine skiing (2006–2015): have the new ski regulations made an impact? *British Journal of Sports Medicine*, 50(1):32–36, 2016. doi:10.1136/bjsports-2015-095467.
- F. Harris. On the use of windows for harmonic analysis with the discrete Fourier transform. *Proceedings of the IEEE*, 66(1):51–83, 1978. doi:10.1109/PROC.1978.10837.
- J. Hartikainen, A. Solin, and S. Särkkä. Optimal filtering with Kalman filters and smoothers – a Manual for Matlab toolbox EKF / UKF. 2011.
- J. M. Hausdorff, M. E. Cudkowicz, R. Firtion, J. Y. Wei, and A. L. Goldberger. Gait variability and basal ganglia disorders: stride-to-stride variations of gait cycle timing in Parkinson’s disease and Huntington’s disease. *Movement Disorders*, 13(3):428–437, 1998. doi:10.1002/mds.870130310.
- C. Hausswirth, A. Bigard, and C. Guezennec. Relationships between Running Mechanics and Energy Cost of Running at the End of a Triathlon and a Marathon. *International Journal of Sports Medicine*, 18(05):330–339, 1997. doi:10.1055/s-2007-972642.
- H. He and E. A. Garcia. Learning from imbalanced data. *IEEE Transactions on Knowledge and Data Engineering*, 21(9):1263–1284, 2009. doi:10.1109/TKDE.2008.239.
- K. Hébert-Losier, M. Supej, and H.-C. Holmberg. Biomechanical factors influencing the performance of elite alpine ski racers. *Sports medicine*, 44(4):519–33, 2014. doi:10.1007/s40279-013-0132-z.
- M. Henriksen, H. Lund, R. Moe-Nilssen, H. Bliddal, and B. Danneskiold-Samsøe. Test–retest reliability of trunk accelerometric gait analysis. *Gait & Posture*, 19(3):288–297, 2004. doi:10.1016/S0966-6362(03)00069-9.
- K. Hottenroot and V. Urban. *Das grosse Buch von Skilanglauf*. Meyer&Meyer Verlag, 2 edition, 2011. ISBN 9783898996976.

- J. Husa-Russell, T. Ukelo, R. List, S. Lorenzetti, and P. Wolf. Day-to-day consistency of lower extremity kinematics during stair ambulation in 24-45 years old athletes. *Gait and Posture*, 33(4):635–639, 2011. doi:10.1016/j.gaitpost.2011.02.009.
- C. Jakob, P. Kugler, F. Hebenstreit, S. Reinfelder, U. Jensen, D. Schuldhaus, M. Lochmann, and B. Eskofier. Estimation of the Knee Flexion-Extension Angle During Dynamic Sport Motions Using Body-worn Inertial Sensors. *Proceedings of the 8th International Conference on Body Area Networks*, pages 289–295, 2013. doi:10.4108/icst.bodynets.2013.253613.
- J. M. Jasiewicz, J. H. J. Allum, J. W. Middleton, A. Barriskill, P. Condie, B. Purcell, and R. C. T. Li. Gait event detection using linear accelerometers or angular velocity transducers in able-bodied and spinal-cord injured individuals. *Gait & posture*, 24(4):502–9, 2006. doi:10.1016/j.gaitpost.2005.12.017.
- P. Jonasson, K. Halldin, J. Karlsson, O. Thoreson, J. Hvannberg, L. Swärd, and A. Baranto. Prevalence of joint-related pain in the extremities and spine in five groups of top athletes. *Knee Surgery, Sports Traumatology, Arthroscopy*, 19(9):1540–1546, 2011. doi:10.1007/s00167-011-1539-4.
- M. P. Kadaba, H. K. Ramakrishnan, and M. E. Wootten. Measurement of lower extremity kinematics during level walking. *Journal of orthopaedic research : official publication of the Orthopaedic Research Society*, 8(3):383–92, 1990. doi:10.1002/jor.1100080310.
- M. P. Kadaba, H. K. Ramakrishnan, M. E. Wootten, J. Gainey, G. Gorton, and G. V. Cochran. Repeatability of kinematic, kinetic, and electromyographic data in normal adult gait. *Journal of orthopaedic research : official publication of the Orthopaedic Research Society*, 7(6):849–60, 1989. doi:10.1002/jor.1100070611.
- I. Karuei, O. S. Schneider, B. Stern, M. Chuang, and K. E. MacLean. RRACE: Robust realtime algorithm for cadence estimation. *Pervasive and Mobile Computing*, 2013. doi:10.1016/j.pmcj.2013.09.006.
- A. E. Kedgley, T. Birmingham, and T. R. Jenkyn. Comparative accuracy of radiostereometric and optical tracking systems. *Journal of Biomechanics*, 42(9):1350–1354, 2009. doi:10.1016/j.jbiomech.2009.03.018.
- S. Kim and M. A. Nussbaum. Performance evaluation of a wearable inertial motion capture system for capturing physical exposures during manual material handling tasks. *Ergonomics*, 56(2):314–26, 2013. doi:10.1080/00140139.2012.742932.
- R. W. Kipp, R. C. Reid, M. Gilgien, T. Moger, H. Tjørhom, P. Haugen, and G. Smith. Slalom Performance in Elite Alpine Ski Racing can be Predicted by Fore / Aft Movement Dynamics. *Medicine and science in sports and exercise*, 40(5):S165, 2008.
- M. Klous, E. Müller, and H. Schwameder. Collecting kinematic data on a ski/snowboard track with panning, tilting, and zooming cameras: is there sufficient accuracy for

Bibliography

- a biomechanical analysis? *Journal of sports sciences*, 28(12):1345–53, 2010. doi:10.1080/02640414.2010.507253.
- M. Klous, E. Müller, and H. Schwameder. Three-dimensional knee joint loading in alpine skiing: a comparison between a carved and a skidded turn. *Journal of applied biomechanics*, 28(6):655–64, 2012.
- D. P. Kroese, T. Brereton, T. Taimre, and Z. I. Botev. Why the Monte Carlo method is so important today. *Wiley Interdisciplinary Reviews: Computational Statistics*, 6(6):386–392, 2014. doi:10.1002/wics.1314.
- J. Kröll, E. Müller, J. G. Seifert, and J. M. Wakeling. Changes in quadriceps muscle activity during sustained recreational alpine skiing. *Journal of Sports Science and Medicine*, 10:81–92, 2011.
- J. Kröll, J. Spörri, B. Fasel, E. Müller, and H. Schwameder. Type of muscle control in elite Alpine skiing - Is it still the same than in 1995 ? *Science and Skiing VI*, 2015.
- J. Kröll, J. Spörri, M. Gilgien, J. Chardonens, and E. Müller. Verletzungsprävention innerhalb eines internationalen Sportverbandes – Eine Prozessbeschreibung am Beispiel des alpinen Skirennsports. *Sport-Orthopädie - Sport-Traumatologie - Sports Orthopaedics and Traumatology*, pages 1–9, 2013. doi:10.1016/j.orthtr.2013.09.002.
- J. Kröll, J. Spörri, M. Gilgien, H. Schwameder, and E. Müller. Effect of ski geometry on aggressive ski behaviour and visual aesthetics: equipment designed to reduce risk of severe traumatic knee injuries in alpine giant slalom ski racing. *British journal of sports medicine*, 50(1):20–5, 2016a. doi:10.1136/bjsports-2015-095433.
- J. Kröll, J. Spörri, M. Gilgien, H. Schwameder, and E. Müller. Sidecut radius and kinetic energy: equipment designed to reduce risk of severe traumatic knee injuries in alpine giant slalom ski racing. *British Journal of Sports Medicine*, 50(1):26–31, 2016b. doi:10.1136/bjsports-2015-095463.
- J. Kröll, J. M. Wakeling, J. G. Seifert, and E. Müller. Quadriceps Muscle Function during Recreational Alpine Skiing. *Medicine and science in sports and exercise*, 42(8):1545–56, 2010. doi:10.1249/MSS.0b013e3181d299cf.
- T. Krosshaug, T. E. Andersen, O. E. Olsen, G. Myklebust, and R. Bahr. Research approaches to describe the mechanisms of injuries in sport: limitations and possibilities. *Br J Sports Med*, 39(6):330–339, 2005. doi:10.1136/bjsm.2005.018358.
- A. Krüger and J. Edelmann-Nusser. Biomechanical analysis in freestyle snowboarding: application of a full-body inertial measurement system and a bilateral insole measurement system. *Sports Technology*, 2:17–23, 2009. doi:10.1002/jst.89.
- A. Krüger and J. Edelmann-Nusser. Application of a full body inertial measurement system in alpine skiing: a comparison with an optical video based system. *Journal of applied biomechanics*, 26(4):516–21, 2010.

- G. Lachapelle, A. Morrison, and R. Ong. Ultra-Precise Positioning for Sport Applications. In *13th IAIN World Congress*. Stockholm, 2009.
- J. C. Lagarias, J. A. Reeds, M. H. Wright, and P. E. Wright. Convergence Properties of the Nelder–Mead Simplex Method in Low Dimensions. 1998. doi:10.1137/S1052623496303470.
- S. Lambrecht, S. L. Nogueira, M. Bortole, A. A. G. Siqueira, M. H. Terra, E. Rocon, and J. L. Pons. Inertial sensor error reduction through calibration and sensor fusion. *Sensors (Switzerland)*, 16(2):1–16, 2016. doi:10.3390/s16020235.
- P. Läubli and J. Spörri. *Ski Alpin Racing Concept*. Swiss-Ski, Muri b. Bern, 2014.
- A. Leardini, L. Chiari, U. Della Croce, A. Cappozzo, A. Chiari, U. Della Croce, and A. Cappozzo. Human movement analysis using stereophotogrammetry Part 3. Soft tissue artifact assessment and compensation. *Gait and Posture*, 21(2):212–25, 2005. doi:10.1016/j.gaitpost.2004.05.002.
- A. Leardini, J. J. O’Connor, F. Catani, and S. Giannini. Kinematics of the human ankle complex in passive flexion; A single degree of freedom system. *Journal of Biomechanics*, 32(2):111–118, 1999. doi:10.1016/S0021-9290(98)00157-2.
- J. B. Lee, R. B. Mellifont, and B. J. Burkett. The use of a single inertial sensor to identify stride, step, and stance durations of running gait. *Journal of science and medicine in sport / Sports Medicine Australia*, 13(2):270–3, 2010. doi:10.1016/j.jsams.2009.01.005.
- J. K. Lee and E. J. Park. A fast quaternion-based orientation optimizer via virtual rotation for human motion tracking. *IEEE Transactions on Biomedical Engineering*, 56(5):1574–1582, 2009. doi:10.1109/TBME.2008.2001285.
- R. Y. W. Lee, J. Laprade, and E. H. K. Fung. A real-time gyroscopic system for three-dimensional measurement of lumbar spine motion. *Medical Engineering and Physics*, 25(10):817–824, 2003. doi:10.1016/S1350-4533(03)00115-2.
- P. de Leva. Adjustments to Zatsiorsky-Seluyanov’s segment inertia parameters. *Journal of biomechanics*, 29(9):1223–30, 1996.
- S. J. Lindinger, C. Göpfert, T. Stöggl, E. Müller, and H.-C. Holmberg. Biomechanical pole and leg characteristics during uphill diagonal roller skiing. *Sports biomechanics / International Society of Biomechanics in Sports*, 8(4):318–33, 2009. doi:10.1080/14763140903414417.
- R. List, T. Gülay, M. Stoop, and S. Lorenzetti. Kinematics of the trunk and the lower extremities during restricted and unrestricted squats. *Journal of strength and conditioning research*, 27(6):1529–38, 2013. doi:10.1519/JSC.0b013e3182736034.

Bibliography

- H. J. Luinge and P. H. Veltink. Measuring orientation of human body segments using miniature gyroscopes and accelerometers. *Medical & biological engineering & computing*, 43(2):273–82, 2005.
- H. J. Luinge, P. H. Veltink, and C. T. M. Baten. Ambulatory measurement of arm orientation. *Journal of Biomechanics*, 40(1):78–85, 2007. doi:10.1016/j.jbiomech.2005.11.011.
- C. A. Macleod, B. A. Conway, D. B. Allan, and S. S. Galen. Development and validation of a low-cost, portable and wireless gait assessment tool. *Medical Engineering & Physics*, 36(4):541–546, 2014. doi:10.1016/j.medengphy.2013.11.011.
- S. O. H. Madgwick, A. J. L. Harrison, and R. Vaidyanathan. Estimation of IMU and MARG orientation using a gradient descent algorithm. *IEEE International Conference on Rehabilitation Robotics*, 2011. doi:10.1109/ICORR.2011.5975346.
- A. Mannini, S. S. Intille, M. Rosenberger, A. M. Sabatini, and W. Haskell. Activity recognition using a single accelerometer placed at the wrist or ankle. *Medicine and Science in Sports and Exercise*, 45(11):2193–2203, 2013. doi:10.1249/MSS.0b013e31829736d6.
- B. Mariani, C. Hoskovec, S. Rochat, C. Büla, J. Penders, and K. Aminian. 3D gait assessment in young and elderly subjects using foot-worn inertial sensors. *Journal of biomechanics*, 43(15):2999–3006, 2010. doi:10.1016/j.jbiomech.2010.07.003.
- B. Mariani, H. Rouhani, X. Crevoisier, and K. Aminian. Quantitative estimation of foot-flat and stance phase of gait using foot-worn inertial sensors. *Gait and Posture*, 37(2):229–234, 2013. doi:10.1016/j.gaitpost.2012.07.012.
- F. L. Markley, Y. Cheng, J. L. Crassidis, and Y. Oshman. Averaging Quaternions. *Journal of Guidance, Control, and Dynamics*, 30(4):1193–1197, 2007. doi:10.2514/1.28949.
- J. Marshall. Magnetic Field Swimmer Positioning. *IEEE Sensors Journal*, 15(1):172–179, 2015. doi:10.1109/JSEN.2014.2339400.
- F. Marsland, K. Lyons, J. Anson, G. Waddington, C. Macintosh, and D. Chapman. Identification of cross-country skiing movement patterns using micro-sensors. *Sensors (Basel, Switzerland)*, 12(4):5047–66, 2012. doi:10.3390/s120405047.
- H. Martin, P. Groves, and M. Newman. The Limits of In-Run Calibration of MEMS Inertial Sensors and Sensor Arrays. *Navigation, Journal of the Institute of Navigation*, 63(2):127–143, 2016. doi:10.1002/navi.135.
- C. Mazzà, M. Donati, J. McCamley, P. Picerno, and A. Cappozzo. An optimized Kalman filter for the estimate of trunk orientation from inertial sensors data during treadmill walking. *Gait and Posture*, 35(1):138–142, 2012. doi:10.1016/j.gaitpost.2011.08.024.

- J. Mester. Diagnostik der Lageregulation im Alpinen Skirennlauf. In *Diagnose von Wahrnehmung und Koordination im Sport*, pages 27–67. Verlag Karl Hofmann, Schorndorf, 1992.
- P. Meyns, S. M. Bruijn, and J. Duysens. The how and why of arm swing during human walking. *Gait & posture*, 38(4):555–62, 2013. doi:10.1016/j.gaitpost.2013.02.006.
- M. Miezal, B. Taetz, and G. Bleser. On inertial body tracking in the presence of model calibration errors. *Sensors (Switzerland)*, 16(7):1–34, 2016. doi:10.3390/s16071132.
- M. Miezal, B. Taetz, N. Schmitz, and G. Bleser. Ambulatory inertial spinal tracking using constraints. In *Proceedings of the 9th International Conference on Body Area Networks*, volume 1, pages 131–134. ICST, 2014. ISBN 978-1-63190-047-1. doi:10.4108/icst.bodynets.2014.256955.
- G. P. Millet, D. Boissiere, and R. Candau. Energy cost of different skating techniques in cross-country skiing. *Journal of Sports Sciences*, 21(1):3–11, 2003. doi:10.1080/0264041031000070903.
- A. E. Minetti, C. Moia, G. S. Roi, D. Susta, and G. Ferretti. Energy cost of walking and running at extreme uphill and downhill slopes. *Journal of applied physiology (Bethesda, Md. : 1985)*, 93(3):1039–46, 2002. doi:10.1152/jappphysiol.01177.2001.
- R. Moe-Nilssen and J. L. Helbostad. Estimation of gait cycle characteristics by trunk accelerometry. *Journal of Biomechanics*, 37(1):121–126, 2004. doi:10.1016/S0021-9290(03)00233-1.
- P. Mognoni, G. Rossi, F. Gastaldelli, A. Canclini, and F. Cotelli. Heart rate profiles and energy cost of locomotion during cross-country skiing races. *European Journal of Applied Physiology*, 85(1-2):62–67, 2001. doi:10.1007/s004210100432.
- J. Morris. Accelerometry—A technique for the measurement of human body movements. *Journal of Biomechanics*, 6(6):729–736, 1973. doi:10.1016/0021-9290(73)90029-8.
- M. E. Morris, R. Iansek, T. A. Matyas, and J. J. Summers. Ability to modulate walking cadence remains intact in Parkinson’s disease. *Journal of neurology, neurosurgery, and psychiatry*, 57(1968):1532–1534, 1994. doi:10.1136/jnnp.57.12.1532.
- H. Myklebust, O. Gloersen, and H. Jostein. Validity of Ski Skating Center of Mass Displacement Measured by a Single Inertial Measurement Unit. *Journal of applied biomechanics*, 31(6):492–8, 2015. doi:10.1123/jab.2015-0081.
- H. Myklebust, T. Losnegard, and J. Hallén. Differences in V1 and V2 ski skating techniques described by accelerometers. *Scandinavian journal of medicine & science in sports*, 24(6):882–893, 2014. doi:10.1111/sms.12106.
- O. Nelles. *Nonlinear System Identification*. Springer Berlin Heidelberg, Berlin, Heidelberg, 2001. ISBN 978-3-642-08674-8. doi:10.1007/978-3-662-04323-3.

Bibliography

- B. Nemec, T. Petrič, J. Babič, and M. Supej. Estimation of Alpine Skier Posture Using Machine Learning Techniques. *Sensors*, 14(10):18898–18914, 2014. doi:10.3390/s141018898.
- J. Nilsson, P. Tveit, and O. Eikrehagen. Effects of speed on temporal patterns in classical style and freestyle cross-country skiing. *Sports biomechanics / International Society of Biomechanics in Sports*, 3(1):85–107, 2004. doi:10.1080/14763140408522832.
- T. Oberg, a. Karsznia, and K. Oberg. Basic gait parameters: reference data for normal subjects, 10-79 years of age. *Journal of rehabilitation research and development*, 30(2):210–23, 1993.
- O. Ohtonen, S. Lindinger, and V. Linnamo. Effects of Gliding Properties of Cross-Country Skis on the Force Production During Skating Technique in Elite Cross-Country Skiers. *International Journal of Sports Science and Coaching*, 8(2):407–416, 2013. doi:10.1260/1747-9541.8.2.407.
- E. Palermo, S. Rossi, F. Marini, F. Patanè, and P. Cappa. Experimental evaluation of accuracy and repeatability of a novel body-to-sensor calibration procedure for inertial sensor-based gait analysis. *Measurement*, 52(1):145–155, 2014. doi:10.1016/j.measurement.2014.03.004.
- A. Paraschiv-Ionescu, C. Perruchoud, E. Buchser, and K. Aminian. Barcoding human physical activity to assess chronic pain conditions. *PloS one*, 7(2):e32239, 2012. doi:10.1371/journal.pone.0032239.
- J. Parviainen, J. Kantola, and J. Collin. Differential barometry in personal navigation. In *2008 IEEE/ION Position, Location and Navigation Symposium*, pages 148–152. IEEE, 2008. ISBN 978-1-4244-1536-6. doi:10.1109/PLANS.2008.4570051.
- F. Pasolini. Pedometer device and step detection method using an algorithm for self-adaptive computation of acceleration thresholds. 2007.
- B. Pellegrini, C. Zoppirolli, L. Bortolan, H.-c. Holmberg, P. Zamparo, and F. Schena. Biomechanical and energetic determinants of technique selection in classical cross-country skiing. *Human movement science*, 32(6):1415–29, 2013. doi:10.1016/j.humov.2013.07.010.
- J. Perry and J. Burnfield. *Gait analysis: normal and pathological function*. Slack Incorporated, 2 edition, 2010. ISBN 9781556427664.
- N. Peyrot, D. Thivel, L. Isacco, J.-B. Morin, P. Duche, and A. Belli. Do mechanical gait parameters explain the higher metabolic cost of walking in obese adolescents? *Journal of Applied Physiology*, 106(6):1763–70, 2009. doi:10.1152/jappphysiol.91240.2008.
- T. Pfau, T. H. Witte, and A. M. Wilson. A method for deriving displacement data during cyclical movement using an inertial sensor. *The Journal of experimental biology*, 208(13):2503–14, 2005. doi:10.1242/jeb.01658.

- S. J. Piazza and P. R. Cavanagh. Measurement of the screw-home motion of the knee is sensitive to errors in axis alignment. *Journal of biomechanics*, 33(8):1029–34, 2000. doi:10.1016/S0021-9290(00)00056-7.
- P. Picerno, A. Cereatti, and A. Cappozzo. Joint kinematics estimate using wearable inertial and magnetic sensing modules. *Gait and Posture*, 28(4):588–595, 2008. doi:10.1016/j.gaitpost.2008.04.003.
- A. Plamondon, A. Delisle, C. Larue, D. Brouillette, D. McFadden, P. Desjardins, and C. Larivière. Evaluation of a hybrid system for three-dimensional measurement of trunk posture in motion. *Applied Ergonomics*, 38(6):697–712, 2007. doi:10.1016/j.apergo.2006.12.006.
- M. H. Pope. Giovanni Alfonso Borelli - The Father of Biomechanics. *Spine*, 30(20):2350–2355, 2005. doi:10.1097/01.brs.0000182314.49515.d8.
- C. Praz, B. Fasel, P. Vuistiner, K. Aminian, and B. Kayser. Optimal slopes and speeds in uphill ski mountaineering : a field study. *European Journal of Applied Physiology*, 2016. doi:10.1007/s00421-016-3455-2.
- C. Praz, B. Léger, and B. Kayser. Energy expenditure of extreme competitive mountaineering skiing. *European Journal of Applied Physiology*, 114(10):2201–2211, 2014. doi:10.1007/s00421-014-2939-1.
- L. Quach, A. Galica, R. Jones, E. Procter-Gray, B. Manor, M. Hannan, and L. Lipsitz. The Non-linear Relationship between Gait Speed and Falls:The Mobilize Boston Study. *Journal of American Geriatrics Society*, 59(6):1069–1073, 2011. doi:10.1111/j.1532-5415.2011.03408.x.The.
- A. Rampp, J. Barth, S. Schüle, K. G. Gaßmann, J. Klucken, and B. M. Eskofier. Inertial Sensor-Based Stride Parameter Calculation From Gait Sequences in Geriatric Patients. *IEEE Transactions on Biomedical Engineering*, 62(4):1089–1097, 2015. doi:10.1109/TBME.2014.2368211.
- J. O. Ramsay. Functional Data Analysis. In *Encyclopedia of Statistical Sciences*. John Wiley & Sons, Inc., Hoboken, NJ, USA, 2006. doi:10.1002/0471667196.ess3138.
- C. B. Redd, S. Member, S. J. M. Bamberg, and S. Member. A Wireless Sensory Feedback Device for Real-Time Gait Feedback and Training. *Mechatronics IEEEASME Transactions on*, 17(3):425–433, 2012.
- R. Reid, M. Gilgien, T. Moger, H. Tjørhom, P. Haugen, R. Kipp, and G. Smith. Mechanical Energy Dissipation , Technique and Performance in Alpine Skiing. *Medicine & Science in Sports & Exercise*, 40(5):S165, 2008.
- R. C. Reid. *A kinematic and kinetic study of alpine skiing technique in slalom*. Ph.D. thesis, Norwegian School of Sport Sciences, 2010.

Bibliography

- S. Rochat, C. J. Büla, E. Martin, L. Seematter-Bagnoud, A. Karmaniola, K. Aminian, C. Piot-Ziegler, and B. Santos-Eggimann. What is the Relationship Between Fear of Falling and Gait in Well-Functioning Older Persons Aged 65 to 70 Years? *Archives of Physical Medicine and Rehabilitation*, 91(6):879–884, 2010. doi:10.1016/j.apmr.2010.03.005.
- D. Roetenberg, H. Luinge, and P. Slycke. Xsens MVN : Full 6DOF Human Motion Tracking Using Miniature Inertial Sensors. *Xsens Technologies*, pages 1–9, 2013.
- D. Roetenberg, H. J. Luinge, C. T. M. Baten, and P. H. Veltink. Compensation of magnetic disturbances improves inertial and magnetic sensing of human body segment orientation. *IEEE Transactions on Neural Systems and Rehabilitation Engineering*, 13(3):395–405, 2005. doi:10.1109/TNSRE.2005.847353.
- H. Rouhani, J. Favre, X. Crevoisier, and K. Aminian. Measurement of multi-segment foot joint angles during gait using a wearable system. *Journal of biomechanical engineering*, 134(6):061006, 2012. doi:10.1115/1.4006674.
- A. M. Sabatini. Quaternion-based strap-down integration method for applications of inertial sensing to gait analysis. *Medical & biological engineering & computing*, 43(1):94–101, 2005.
- A. M. Sabatini. Quaternion-based extended Kalman filter for determining orientation by inertial and magnetic sensing. *IEEE Transactions on Biomedical Engineering*, 53(7):1346–1356, 2006. doi:10.1109/TBME.2006.875664.
- A. M. Sabatini, G. Ligorio, and A. Mannini. Fourier-based integration of quasi-periodic gait accelerations for drift-free displacement estimation using inertial sensors. *BioMedical Engineering OnLine*, 14(1):106, 2015. doi:10.1186/s12938-015-0103-8.
- A. M. Sabatini, C. Martelloni, S. Scapellato, and F. Cavallo. Assessment of walking features from foot inertial sensing. *IEEE transactions on bio-medical engineering*, 52(3):486–94, 2005. doi:10.1109/TBME.2004.840727.
- S. Salehi, G. Bleser, A. Reiss, and D. Stricker. Body-IMU autocalibration for inertial hip and knee joint tracking. *Proceedings of the 10th EAI International Conference on Body Area Networks*, 1:51–57, 2015. doi:10.4108/eai.28-9-2015.2261522.
- M. M. Samson, A. Crowe, P. L. de Vreede, J. A. Dessens, S. A. Duursma, and H. J. Verhaar. Differences in gait parameters at a preferred walking speed in healthy subjects due to age, height and body weight. *Aging (Milan, Italy)*, 13(1):16–21, 2001. doi:10.1007/BF03351489.
- O. Sandbakk, G. Ettema, and H.-C. Holmberg. Gender differences in endurance performance by elite cross-country skiers are influenced by the contribution from poling. *Scandinavian journal of medicine & science in sports*, pages 1–6, 2012. doi:10.1111/j.1600-0838.2012.01482.x.

- P. Scheiber, J. Seifert, and E. Müller. Relationships between biomechanics and physiology in older, recreational alpine skiers. *Scandinavian journal of medicine & science in sports*, 22(1):49–57, 2012. doi:10.1111/j.1600-0838.2010.01146.x.
- K. Schenk, M. Faulhaber, H. Gatterer, M. Burtscher, and M. Ferrari. Ski Mountaineering Competition: Fit for It? *Clinical Journal of Sport Medicine*, 21(2):114–118, 2011. doi:10.1097/JSM.0b013e31820f903e.
- H. M. Schepers, D. Roetenberg, and P. H. Veltink. Ambulatory human motion tracking by fusion of inertial and magnetic sensing with adaptive actuation. *Medical and Biological Engineering and Computing*, 48(1):27–37, 2010. doi:10.1007/s11517-009-0562-9.
- C. Schiefermüller, S. Lindinger, and E. Müller. The skier’s centre of gravity as a reference point in movement analysis for different designated systems. *Science and Skiing III*, pages 172–185, 2005.
- M. T. Scott, T. J. Scott, and V. G. Kelly. The Validity and Reliability of Global Positioning Systems in Team Sport. *Journal of Strength and Conditioning Research*, 30(5):1470–1490, 2016. doi:10.1519/JSC.0000000000001221.
- T. Seel, J. Raisch, and T. Schauer. IMU-based joint angle measurement for gait analysis. *Sensors (Basel, Switzerland)*, 14(4):6891–909, 2014. doi:10.3390/s140406891.
- R. Shiavi. *Introduction to applied statistical signal analysis: Guide to biomedical and electrical engineering applications*. Elsevier/Academic Press, Burlington, MA, 3 edition, 2007. ISBN 978-0-12-088581-7.
- K. Shoemake. Animating rotation with quaternion curves. *ACM SIGGRAPH Computer Graphics*, 19(3):245–254, 1985. doi:10.1145/325165.325242.
- G. L. Smidt, J. S. Arora, and R. C. Johnston. Accelerographic analysis of several types of walking. *American Journal of Physical Medicine*, 50(6):285–300, 1971.
- G. L. Smidt, R. H. Deusinger, J. Arora, and J. P. Albright. An automated accelerometry system for gait analysis. *Journal of Biomechanics*, 10(5-6):367–375, 1977. doi:10.1016/0021-9290(77)90009-4.
- J. O. Smith. *Physical Audio Signal Processing*. W3K Publishing, 2010. ISBN 978-0-9745607-2-4.
- J. F. Soechting and B. Ross. Psychophysical determination of coordinate representation of human arm orientation. *Neuroscience*, 13(2):595–604, 1984.
- J. Spörri, J. Kröll, B. Fasel, K. Aminian, and E. Müller. Course Setting as a Prevention Measure for Overuse Injuries of the Back in Alpine Ski Racing: A Kinematic and Kinetic Study of Giant Slalom and Slalom. *Orthopaedic Journal of Sports Medicine*, 4(2):1–8, 2016a. doi:10.1177/2325967116630719.

Bibliography

- J. Spörri, J. Kröll, B. Fasel, K. Aminian, and E. Müller. Rehabilitation following ACL-Reconstruction in alpine ski racing - can indoor carpet skiing build the bridge between ... In *Abstract Book of the 7th International congress on science and skiing*. 2016b.
- J. Spörri, J. Kröll, M. Gilgien, and E. Müller. Sidecut radius and the mechanics of turning—equipment designed to reduce risk of severe traumatic knee injuries in alpine giant slalom ski racing. *British Journal of Sports Medicine*, 50(1):14–19, 2016c. doi:10.1136/bjsports-2015-095737.
- J. Spörri, J. Kröll, C. Haid, B. Fasel, and E. Müller. Potential Mechanisms Leading to Overuse Injuries of the Back in Alpine Ski Racing: A Descriptive Biomechanical Study. *The American Journal of Sports Medicine*, 43(8):2042–2048, 2015. doi:10.1177/0363546515588178.
- J. Spörri, J. Kröll, H. Schwameder, and E. Müller. Turn Characteristics of a Top World Class Athlete in Giant Slalom: A Case Study Assessing Current Performance Prediction Concepts. *International Journal of Sports Science and Coaching*, 7(4):647–660, 2012a. doi:10.1260/1747-9541.7.4.647.
- J. Spörri, J. Kröll, H. Schwameder, C. Schiefermüller, and E. Müller. Course setting and selected biomechanical variables related to injury risk in alpine ski racing: an explorative case study. *British journal of sports medicine*, 46(15):1072–7, 2012b. doi:10.1136/bjsports-2012-091425.
- J. Spörri, C. Schiefermüller, and E. Müller. Collecting Kinematic Data on a Ski Track with Optoelectronic Stereophotogrammetry: A Methodological Study Assessing the Feasibility of Bringing the Biomechanics Lab to the Field. *PLOS ONE*, 11(8):e0161757, 2016d. doi:10.1371/journal.pone.0161757.
- T. Stöggl, A. Holst, A. Jonasson, E. Andersson, T. Wunsch, C. Norström, and H.-C. Holmberg. Automatic Classification of the Sub-Techniques (Gears) Used in Cross-Country Ski Skating Employing a Mobile Phone. *Sensors*, 14(11):20589–20601, 2014. doi:10.3390/s141120589.
- T. Stöggl, W. Kampel, E. Müller, and S. Lindinger. Double-Push Skating versus V2 and V1 Skating on Uphill Terrain in Cross-Country Skiing. *Medicine & Science in Sports & Exercise*, 42(1):187–196, 2010. doi:10.1249/MSS.0b013e3181ac9748.
- T. Stöggl, S. Lindinger, and E. Müller. Analysis of a simulated sprint competition in classical cross country skiing. *Scandinavian journal of medicine & science in sports*, 17(4):362–72, 2007. doi:10.1111/j.1600-0838.2006.00589.x.
- T. Stöggl, E. Müller, M. Ainegren, and H.-C. Holmberg. General strength and kinetics: fundamental to sprinting faster in cross country skiing? *Scandinavian journal of medicine & science in sports*, 21(6):791–803, 2011. doi:10.1111/j.1600-0838.2009.01078.x.

- T. Stöggl, E. Müller, and S. Lindinger. Biomechanical comparison of the double-push technique and the conventional skate skiing technique in cross-country sprint skiing. *Journal of Sports Sciences*, 26(11):1225–1233, 2008a. doi:10.1080/02640410802027386.
- T. L. Stöggl and E. Müller. Kinematic determinants and physiological response of cross-country skiing at maximal speed. *Medicine and science in sports and exercise*, 41(7):1476–87, 2009. doi:10.1249/MSS.0b013e31819b0516.
- T. L. Stöggl, J. Stöggl, and E. Müller. Competition analysis of the last Decade (1996 - 2008) in cross-country skiing. In E. Müller, S. J. Lindinger, and T. L. Stöggl, eds., *4th International Congress on Skiing and Science (ICSS)*, pages 657–677. Meyer&Meyer Verlag, Sankt Anton an Arlberg, Austria, 2008b.
- S. Studenski, S. Perera, K. Patel, C. Rosano, K. Faulkner, M. Inzitari, J. Brach, J. Chandler, P. Cawthon, E. B. Connor, M. Nevitt, M. Visser, S. Kritchevsky, S. Badinelli, T. Harris, A. B. Newman, J. Cauley, L. Ferrucci, and J. Guralnik. Gait speed and survival in older adults. *JAMA : the journal of the American Medical Association*, 305(1):50–58, 2011. doi:10.1001/jama.2010.1923.
- M. Supej. 3D measurements of alpine skiing with an inertial sensor motion capture suit and GNSS RTK system. *Journal of sports sciences*, 28(7):759–69, 2010. doi:10.1080/02640411003716934.
- M. Supej. Vibrations in recreational alpine skiing: a pilot study. In *International Conference on Biomechanics in Sports 2013*. 2013.
- M. Supej, K. Hébert-Losier, and H.-C. Holmberg. Impact of the steepness of the slope on the biomechanics of World Cup slalom skiers. *International journal of sports physiology and performance*, 10(3):361–8, 2015. doi:10.1123/ijsp.2014-0200.
- M. Supej, R. Kipp, and H.-C. Holmberg. Mechanical parameters as predictors of performance in alpine World Cup slalom racing. *Scandinavian journal of medicine & science in sports*, 21(6):e72–81, 2011. doi:10.1111/j.1600-0838.2010.01159.x.
- M. Supej, O. Kugovnik, and B. Nemec. Kinematic determination of the beginning of a ski turn. *Kinesiologie Slovenica*, 9(1):11–17, 2003.
- M. Supej, L. Saetran, L. Oggiano, G. Ettema, N. Šarabon, B. Nemec, and H.-C. Holmberg. Aerodynamic drag is not the major determinant of performance during giant slalom skiing at the elite level. *Scandinavian journal of medicine & science in sports*, 23(1):e38–47, 2013. doi:10.1111/sms.12007.
- M. Susi, V. Renaudin, and G. Lachapelle. Motion mode recognition and step detection algorithms for mobile phone users. *Sensors (Basel, Switzerland)*, 13(2):1539–62, 2013. doi:10.3390/s130201539.

Bibliography

- B. Taetz, G. Bleser, and M. Miezal. Towards self-calibrating inertial body motion capture. In *19th International Conference on Information Fusion (FUSION)*, pages 1751–1759. 2016. ISBN 9780996452748.
- H. Tan, A. M. Wilson, and J. Lowe. Measurement of stride parameters using a wearable GPS and inertial measurement unit. *Journal of Biomechanics*, 41(7):1398–1406, 2008. doi:10.1016/j.jbiomech.2008.02.021.
- W. Tao, T. Liu, R. Zheng, and H. Feng. Gait analysis using wearable sensors. *Sensors (Basel, Switzerland)*, 12(2):2255–83, 2012. doi:10.3390/s120202255.
- K. Taraldsen, S. F. M. Chastin, I. I. Riphagen, B. Vereijken, and J. L. Helbostad. Physical activity monitoring by use of accelerometer-based body-worn sensors in older adults: a systematic literature review of current knowledge and applications. *Maturitas*, 71(1):13–9, 2012. doi:10.1016/j.maturitas.2011.11.003.
- P. Terrier, Q. Ladetto, B. Merminod, and Y. Schutz. High-precision satellite positioning system as a new tool to study the biomechanics of human locomotion. *Journal of Biomechanics*, 33(12):1717–1722, 2000. doi:10.1016/S0021-9290(00)00133-0.
- P. Terrier and Y. Schutz. How useful is satellite positioning system (GPS) to track gait parameters? A review. *Journal of neuroengineering and rehabilitation*, 2:28, 2005. doi:10.1186/1743-0003-2-28.
- P. Tosi, A. Leonardi, and F. Schena. The energy cost of ski mountaineering: effects of speed and ankle loading. *The Journal of sports medicine and physical fitness*, 49(1):25–9, 2009.
- P. Tosi, A. Leonardi, L. Zerbini, A. Rosponi, and F. Schena. Energy cost and efficiency of ski mountaineering. A laboratory study. *The Journal of sports medicine and physical fitness*, 50(4):400–6, 2010.
- A. D. Townshend, C. J. Worringham, and I. B. Stewart. Assessment of Speed and Position during Human Locomotion Using Nondifferential GPS. *Medicine & Science in Sports & Exercise*, 40(1):124–132, 2008. doi:10.1249/mss.0b013e3181590bc2.
- D. Trojaniello, A. Cereatti, E. Pelosin, L. Avanzino, A. Mirelman, J. M. Hausdorff, and U. Della Croce. Estimation of step-by-step spatio-temporal parameters of normal and impaired gait using shank-mounted magneto-inertial sensors: application to elderly, hemiparetic, parkinsonian and choreic gait. *Journal of neuroengineering and rehabilitation*, 11(1):152, 2014. doi:10.1186/1743-0003-11-152.
- J. R. Turnbull, A. Kilding, and J. W. L. Keogh. Physiology of alpine skiing. *Scandinavian journal of medicine & science in sports*, 19(2):146–55, 2009. doi:10.1111/j.1600-0838.2009.00901.x.

- P. Vähäsöyrinki, P. V. Komi, S. Seppälä, M. Ishikawa, V. Kolehmainen, J. a. Salmi, and V. Linnamo. Effect of skiing speed on ski and pole forces in cross-country skiing. *Medicine and science in sports and exercise*, 40(6):1111–6, 2008. doi:10.1249/MSS.0b013e3181666a88.
- A. Veicsteinas, G. Ferretti, V. Margonato, G. Rosa, and D. Tagliabue. Energy cost of and energy sources for alpine skiing in top athletes. *Journal of applied physiology (Bethesda, Md. : 1985)*, 56(5):1187–1190, 1984.
- A. Waegli and J. Skalous. Optimization of two GPS/MEMS-IMU integration strategies with application to sports. *GPS solutions*, 13(4):315–326, 2009. doi:DOI10.1007/s10291-009-0124-5.
- M. Waldron, P. Worsfold, C. Twist, and K. Lamb. Concurrent validity and test–retest reliability of a global positioning system (GPS) and timing gates to assess sprint performance variables. *Journal of Sports Sciences*, 29(15):1613–1619, 2011. doi:10.1080/02640414.2011.608703.
- S. Wang, C. Cao, P. Fei, and A. Zhang. High-G accelerometer dynamic calibration by a laser differential Doppler technique. *Review of Scientific Instruments*, 67(5):2022–2025, 1996. doi:10.1063/1.1146963.
- S. M. Warner, T. O. Koch, and T. Pfau. Inertial sensors for assessment of back movement in horses during locomotion over ground. *Equine Veterinary Journal*, 42(SUPPL. 38):417–424, 2010. doi:10.1111/j.2042-3306.2010.00200.x.
- M. W. Whittle. Clinical gait analysis: A review. *Human Movement Science*, 15(3):369–387, 1996. doi:10.1016/0167-9457(96)00006-1.
- M. W. Whittle. Three-dimensional motion of the center of gravity of the body during walking. *Human Movement Science*, 16(2-3):347–355, 1997. doi:10.1016/S0167-9457(96)00052-8.
- A. T. M. Willemsen, J. A. van Alsté, and H. B. K. Boom. Real-time gait assessment utilizing a new way of accelerometry. *Journal of Biomechanics*, 23(8):859–863, 1990. doi:10.1016/0021-9290(90)90033-Y.
- M. Windolf, N. Götzen, and M. Morlock. Systematic accuracy and precision analysis of video motion capturing systems-exemplified on the Vicon-460 system. *Journal of Biomechanics*, 41(12):2776–2780, 2008. doi:10.1016/j.jbiomech.2008.06.024.
- P. Wolf, R. List, T. Ukelo, C. Maiwald, and A. Stacoff. Day-to-Day Consistency of Lower Extremity Kinematics During Walking And Running. *Journal of Applied Biomechanics*, 25(4):369–376, 2009.
- S. H. P. Won, W. W. Melek, and F. Golnaraghi. A kalman/particle filter-based position and orientation estimation method using a position sensor/inertial measurement unit

Bibliography

- hybrid system. *IEEE Transactions on Industrial Electronics*, 57(5):1787–1798, 2010. doi:10.1109/TIE.2009.2032431.
- T. A. L. Wren, G. E. Gorton, S. Öunpuu, and C. A. Tucker. Efficacy of clinical gait analysis: A systematic review. *Gait and Posture*, 34(2):149–153, 2011. doi:10.1016/j.gaitpost.2011.03.027.
- G. Wu and P. R. Cavanagh. ISB Recommendations in the Reporting for Standardization of Kinematic Data. *Journal of Biomechanics*, 28(10):1257–1261, 1995. doi:10.1016/0021-9290(95)00017-C.
- G. Wu, S. Siegler, P. Allard, C. Kirtley, A. Leardini, D. Rosenbaum, M. Whittle, D. D. D’Lima, L. Cristofolini, H. Witte, O. Schmid, and I. Stokes. ISB recommendation on definitions of joint coordinate system of various joints for the reporting of human joint motion—part I: ankle, hip, and spine. *Journal of Biomechanics*, 35(4):543–548, 2002. doi:10.1016/S0021-9290(01)00222-6.
- G. Wu, F. C. T. Van Der Helm, H. E. J. Veeger, M. Makhsous, P. Van Roy, C. Anglin, J. Nagels, A. R. Karduna, K. McQuade, X. Wang, F. W. Werner, and B. Buchholz. ISB recommendation on definitions of joint coordinate systems of various joints for the reporting of human joint motion - Part II: Shoulder, elbow, wrist and hand. *Journal of Biomechanics*, 38(5):981–992, 2005. doi:10.1016/j.jbiomech.2004.05.042.
- D. Xia, C. Yu, and L. Kong. The development of micromachined gyroscope structure and circuitry technology. *Sensors (Switzerland)*, 14(1):1394–1473, 2014. doi:10.3390/s140101394.
- S. Yang and Q. Li. Inertial sensor-based methods in walking speed estimation: a systematic review. *Sensors (Basel, Switzerland)*, 12(5):6102–16, 2012. doi:10.3390/s120506102.
- A. D. Young. Use of body model constraints to improve accuracy of inertial motion capture. *2010 International Conference on Body Sensor Networks, BSN 2010*, pages 180–186, 2010. doi:10.1109/BSN.2010.30.
- X. Yun and E. Bachmann. Design, Implementation, and Experimental Results of a Quaternion-Based Kalman Filter for Human Body Motion Tracking. *Robotics, IEEE Transactions on*, 22(6):1216–1227, 2006. doi:10.1109/TRO.2006.886270.
- J.-t. Zhang, A. C. Novak, B. Brouwer, and Q. Li. Concurrent validation of Xsens MVN measurement of lower limb joint angular kinematics. *Physiological measurement*, 34(8):N63–9, 2013. doi:10.1088/0967-3334/34/8/N63.
- N. Zhao. Full-featured pedometer design realized with 3-Axis digital accelerometer. *Analog Dialogue*, 44(6):1–5, 2010.

- R. Zhu, D. Sun, Z. Zhou, and D. Wang. A linear fusion algorithm for attitude determination using low cost MEMS-based sensors. *Measurement*, 40(3):322–328, 2007. doi:10.1016/j.measurement.2006.05.020.
- W. Zijlstra and A. L. Hof. Assessment of spatio-temporal gait parameters from trunk accelerations during human walking. *Gait & posture*, 18(2):1–10, 2003.
- M. Zorko, B. Nemec, J. Babič, B. Lešnik, and M. Supej. The Waist Width of Skis Influences the Kinematics of the Knee Joint in Alpine Skiing. *Journal of sports science & medicine*, 14(3):606–19, 2015.

Benedikt Fasel

Allmend 8
1719 Zumholz
Switzerland

+41 79 736 89 49

benedikt.fasel@gmail.com

Date of birth: December 6th 1986

Nationality: Swiss



Education and Work Experience

Doctoral Assistant

2013 - 2017

Ecole Polytechnique Fédérale de Lausanne (EPFL), Switzerland

Laboratory of movement analysis and measurement (LMAM)

Supervisor: Prof. K. Aminian

Drift Reduction for Inertial Sensor Based Orientation and Position Estimation in the Presence of High Dynamic Variability During Competitive Skiing and Daily-Life Walking

- Supervision of 16 semester projects and 3 master projects
- Teaching assistant for “Analysis and Modelling of Human Locomotion”, “Design of Ultra-low Power Wearable Wireless Systems”

Master in Communication Systems

2010 - 2012

Ecole Polytechnique Fédérale de Lausanne (EPFL), Switzerland

Specialization in Wireless Communications

Master thesis at Stanford University (USA) under the supervision of Prof. T. Andriacchi:

Quantification, Modeling and Scoring of Changes in Cartilage Morphology with Knee Osteoarthritis Using Three-dimensional Statistical Analysis of Magnetic Resonance Images

Bachelor in Communication Systems

2007 - 2010

Ecole Polytechnique Fédérale de Lausanne (EPFL), Switzerland

Third year exchange at McGill University (Canada), extended with optional undergraduate semester project under the supervision of Prof. J. Bajcsy: *Waveform Channels and Faster-than-Nyquist Signaling*

Academic Awards

Best Poster Award – EPFL Bioengineering Day

2015

Young Investigator Award – Category Oral Presentations – 6th International Congress on Science and Skiing

2013

Non-academic Work Experience

Web and back-end development of www.sdis-chamberonne.ch

2015 - present

Internship in Software Engineering at AdNovum Informatik AG, Zurich

Summer 2011

Co-founder and manager of the web-development division of futech it GmbH, Plaffeien

2005 - 2011

Activities and Interests

- Firefighter volunteer and first responder (rank: corporal)
- Politics: multiple times candidate for the parliament of the Canton of Fribourg
- President of the EPFL's Mountain Club with over 500 members from 2010 – 2011
- Over 14 years of piano courses at the music academies of Fribourg and Lausanne.
- Ultimate Frisbee, hiking, ski-touring, and mountaineering

Languages

- German and Swiss German: first language
- French: fluent in speaking and good in writing
- English: fluent in speaking and good in writing. Cambridge Advanced Certificate in 2008

Journal Publications

- J. Favre, J. C. Erhart-Hledik, K. Blazek, **B. Fasel** and G. E. Gold et al. *Anatomically-standardized maps reveal distinct patterns of cartilage thickness with increasing severity of medial compartment knee osteoarthritis*, in Journal of Orthopaedic Research, 2017.
- B. Fasel**, C. Duc, F. Dadashi, F. Bardyn and M. Savary et al. *A wrist sensor and algorithm to determine instantaneous walking cadence and speed in daily life walking*, in Medical & Biological Engineering & Computing, 2017.
- B. Fasel**, J. Spörri, J. Chardonens, J. Kröll and E. Müller et al. *Joint Inertial Sensor Orientation Drift Reduction for Highly Dynamic Movements*, in IEEE Journal of Biomedical and Health Informatics, 2017.
- C. Praz, **B. Fasel**, P. Vuistiner, K. Aminian and B. Kayser. *Optimal slopes and speeds in uphill ski mountaineering: a field study*, in European Journal of Applied Physiology, vol. 116, num. 10, p. 2017-2024, 2016.
- B. Fasel**, J. Spörri, M. Gilgien, G. Boffi and J. Chardonens et al. *Three-Dimensional Body and Centre of Mass Kinematics in Alpine Ski Racing Using Differential GNSS and Inertial Sensors*, in Remote Sensing, vol. 8, num. 671, 2016.
- B. Fasel**, C. Praz, B. Kayser and K. Aminian. *Measuring spatio-temporal parameters of uphill ski mountaineering with ski-fixed inertial sensors*, in Journal of Biomechanics, vol. 49, num. 13, p. 3052-3055, 2016.
- C. Praz, **B. Fasel**, P. Vuistiner, K. Aminian and B. Kayser. *Optimal slopes and speeds in uphill ski mountaineering: a laboratory study*, in European Journal of Applied Physiology, vol. 116, num. 10, p. 2017-2024, 2016.
- J. Spörri, J. Kröll, **B. Fasel**, K. Aminian and E. Müller. *Course setting as a prevention measure for overuse injuries of the back in alpine ski racing*, in Orthopaedic Journal of Sports Medicine, vol. 4, num. 2, 2016.
- B. Fasel**, J. Favre, J. Chardonens, G. Gremion and K. Aminian. *An inertial sensor-based system for spatio-temporal analysis in classic cross-country skiing diagonal technique*, in Journal of Biomechanics, vol. 48, num. 12, p. 3199-3205, 2015.

J. Spörri, J. Kröll, C. Haid, **B. Fasel** and E. Müller. *Potential Mechanisms Leading to Overuse Injuries of the Back in Alpine Ski Racing - A Descriptive Biomechanical Study*, in The American Journal of Sports Medicine, 2015.

Conference Papers

- B. Fasel**, M. Gilgien, J. Spörri and K. Aminian. *Estimation of the centre of mass kinematics in alpine ski racing using inertial and magnetic sensors*. 35th International Conference on Biomechanics in Sports, Cologne, Germany, June 14 – 18, 2017.
- L. Rosso, L. Gastaldi, W. Rapp, S. Lindinger, Y. Vanlandewijck, **B. Fasel**, D. Pernot and V. Linnamo. *Performance and perturbation tests in elite paralympic sit-skiers*. 7th International Congress on Science and Skiing (ICSS), St. Christoph am Arlberg, Austria, December 10-15, 2016.
- J. Spörri, J. Kröll, **B. Fasel**, K. Aminian and E. Müller. *Back overuse injuries in alpine ski racing - what do we know and how to prevent them?* 21th Annual Congress of the European College of Sport Science (ECSS), Vienna, Austria, July 6-9, 2016.
- B. Fasel**, C. Göpfert, W. Rapp, S. Lindinger and K. Aminian. *Validation of relative CoM displacement in V2 skating obtained with inertial sensors - a feasibility study*. 7th International Congress on Science and Skiing (ICSS), St. Christoph am Arlberg, Austria, December 10-15, 2016.
- B. Fasel**, J. Spörri, J. Kröll and K. Aminian. *Alpine ski racing gate crossing detection using magnetometers*. 7th International Congress on Science and Skiing (ICSS), St. Christoph am Arlberg, Austria, December 10-15, 2016.
- M. Falbriard, **B. Fasel**, J. Spörri and K. Aminian. *A ski racer's turn cycle structure depends on slope inclination, speed and gate off-set*. 7th International Congress on Science and Skiing (ICSS), St. Christoph am Arlberg, Austria, December 10-15, 2016.
- J. Spörri, J. Kröll, **B. Fasel**, K. Aminian and E. Müller. *Rehabilitation following ACL-Reconstruction in alpine ski racing - can indoor carpet skiing build the bridge between ski-specific off-snow training and return-to-ski?* 7th International Congress on Science and Skiing (ICSS), St. Christoph am Arlberg, Austria, December 10-15, 2016.
- B. Fasel**, J. Spörri, M. Gilgien, N. Gerber and M. Falbriard et al. *IMU and GNSS-based turn switch detection in alpine ski racing*. 7th International Congress on Science and Skiing (ICSS), St. Christoph am Arlberg, Austria, December 10-15, 2016.
- F. Bardyn, M. Savary, S. Grassi Pauletti, P.-A. Farine and **B. Fasel** et al. *MEMS Inertial Motion Sensing Watch for Measuring Walking and Running Activities*. 2016 IEEE International Workshop on Signal Processing Systems (SIPS), Dallas, Texas, USA, October 26-28, 2016.
- B. Fasel**, C. Lehot, J. Spörri, E. Müller and K. Aminian. *Body vibration and its transmission in alpine ski racing*. XIV International Symposium on 3D Analysis of Human Movement, Taipei, Taiwan, July 18-21, 2016.
- B. Fasel**, J. Spörri and K. Aminian. *Improving the accuracy of low-cost GNSS by fusion with inertial and magnetic sensors in alpine ski racing*. 34th International Conference on Biomechanics in Sports, Tsukuba, Japan, July 18-22, 2016.
- B. Ulrich, **B. Fasel**, J. Spörri, E. Müller and K. Aminian. *Using inertial sensors to compute an alpine ski racing specific full body kinematic model – an application to track the distance between ankle joint and athlete's center of mass*. 7th Annual Congress of the Swiss Society of Sports Sciences, Lausanne, Switzerland, February, 2015.

- B. Fasel**, F. Dadashi and K. Aminian. *Instantaneous walking speed estimation for daily life activity monitoring based on wrist acceleration*. 4th International Conference on Ambulatory Monitoring of Physical Activity and Movement (ICAMPAM), Limerick, Ireland, June 10-12, 2015.
- B. Fasel** and K. Aminian. *Stride-to-stride gait variability in daily life measured using accelerometers attached to the wrist*. 4th International Conference on Ambulatory Monitoring of Physical Activity and Movement (ICAMPAM), Limerick, Ireland, June 10-12, 2015.
- B. Fasel**, J. Spörri, J. Kröll, E. Müller and K. Aminian. *Using inertial sensors for reconstructing 3D full-body movement in sports - possibilities and limitations on the example of alpine ski racing*. 33rd International Conference on Biomechanics in Sports, Poitiers, France, June 29 - July 3, 2015.
- B. Fasel**, C. Duc and K. Aminian. *Stride count and frequency measured with a wrist-worn inertial sensor*. 13th International Symposium on 3D Analysis of Human Movement, Lausanne, Switzerland, July 14-17, 2014.
- B. Fasel**, J. Spörri, J. Chardonnnens, M. Gilgien and J. Kröll et al. *3D measurement of lower limb kinematics in alpine ski racing using inertial sensors*. 6th International Congress on Science and Skiing, St. Christoph am Arlberg, Austria, December 14-19, 2013.
- B. Fasel**, J. Favre, J. Chardonnnens and K. Aminian. *A wearable system to measure speed and phase durations during each cycle of classical cross-country skiing*. 6th International Congress on Science and Skiing, St. Christoph am Arlberg, Austria, December 14-19, 2013.

Patent Applications

- B. Fasel**, K. Aminian. *High precision trajectory and speed sensor and measuring method*. W02016174612A1, 2016.
- B. Fasel**, K. Aminian. *Pedometer and method for analyzing motion data*. EP3090685A1, 2016.
- B. Fasel**, C. Duc, F. Dadashi, K. Aminian. *Pedometer and method for analyzing motion data*. EP3090684A1, 2016.

